TECHNISCHE UNIVERSITÄT
CHEMNITZ

A Partitioned FSI Approach to Study the Interaction between Flexible Membranes and Fluids

Dissertation for Obtaining the Academic Degree

Doctor of Engineering

Dr.-Ing.

Faculty of Mechanical Engineering at the Chemnitz University of Technology

M.Sc. Mahtab Makaremi Masouleh

Born in Khorram Abad, Iran

Submitted on 30. April 2021

Reviewer:

Prof. Dr.-Ing. habil. Günter Wozniak, TU Chemnitz

Prof. Dr.-Ing. Janusz Szymczyk, FH Stralsund

Chairman: Prof. Dr.-Ing. Michael Gehde, TU Chemnitz

The day of defense: 08. November 2021

Web link: https://nbn-resolving.org/html/urn:nbn:de:bsz:ch1-qucosa2-785297

Zusammenfassung

Diese Arbeit ist Teil eines interdisziplinären Forschungsprojekts zum Entwurf einer leichten, temporären Struktur als Hochwasserschutz. Motivation für diese Arbeit ist die Notwendigkeit, Leichtstrukturen zum Schutz der Küstengebiete vor schädlichen Auswirkungen eines schnellen Wasseranstieges anzuwenden. Das Hauptziel der Dissertation ist die numerische Analyse der Wechselwirkung zwischen dünnen flexiblen Strukturen und dem freien Oberflächenwasserfluss und starren Strukturen, die eine wichtige Rolle für zuverlässige Leistungen der beabsichtigten Systeme spielen.

In den letzten Jahrzehnten führte der Bedarf an Leichtstrukturen zu weitreichenden Studien über FSI-Probleme mit Fluid-Struktur-Wechselwirkungen, bei denen die numerische Analyse für eine effiziente, wirtschaftliche und sichere Fertigung von Vorteil ist.
Die gebräuchlichsten Anwendungen der FSI-Analyse sind in der Schiffahrts-, Luftfahrt- und Automobilindustrie zu erkennen, während ihr Beitrag auch in der Medizin- und Unterhaltungsindustrie immer bedeutender wird.

Wenn eine Fluidströmung mit einer Struktur in Wechselwirkung tritt, wird die aus der Fluidströmung resultierende Druckbelastung auf die Struktur ausgeübt, gefolgt von Deformationen, Spannungen und Dehnungen der Struktur. Abhängig von der resultierenden Verformung und der Variationsrate kann eine Einweg- oder Zweiweg-Kopplungsanalyse durchgeführt werden.
Die Fluid-Struktur-Interaktion (FSI) ist durch die Wechselwirkung einer beweglichen oder deformierbaren Struktur mit einer inneren oder umgebenden Strömung gekennzeichnet.
In einer Fluid-Struktur-Interaktion (FSI) werden die Gesetze, die die Fluiddynamik und die Strukturmechanik beschreiben, gekoppelt.

Um ein ausreichend genaues Verhalten zu modellieren, gibt es viele Aspekte, die berücksichtigt werden sollten. Die Beschreibung der Leichtstrukturen in Bezug auf Materialeigenschaften, Geometrie, Diskretisierungstypen kombiniert mit der Definition von Fluidbereichen sind entscheidende Parameter. Darüber hinaus stellten die Stabilität und Robustheit der entsprechenden numerischen Algorithmen, die sich dem Verhalten jeder Komponente und den Kopplungsansätzen sowie deren Grenzen und Widersprüchen widmen, eine große Herausforderung für numerische Simulationen dar. Das bekannteste Problem in Bezug auf FSI-Studien entstand aus einem zusätzlichen Masseneffekt, der auf die Kopplungsmethode zwischen Fluid- und Strukturgerüsten

zurückzuführen war. Dieses Problem vergrößerte sich, wenn schwere Flüssigkeiten wie Wasser und flexible Strukturen miteinander interagierten.

Die numerische Arbeit wurde mit Hilfe der Finite-Volume-Löser von Star CCM+, einem Produkt von Siemens PLM Software, durchgeführt. Innerhalb des FV-Rahmens wurde das Strukturverhalten über verfügbare Netze und Algorithmen angenähert, die an Konvergenz und Stabilitätsproblemen litten. Als nächstes wurde eine aufgeteilte Strategie eingeführt, um sowohl Strukturen als auch Flüssigkeiten mit geeigneten Formulierungen und Lösungsmethoden diskretisieren und lösen zu können.

Um Fluiddomänen zu lösen, wurde der nicht mischbare Wasser-Luft-Fluss innerhalb des Kanals durch das Volumen-Fluid-Modell (VOF-Modell) modelliert, das auf dem Euler-Euler-Modell für Mehrphasenflüsse basiert. Darüber hinaus implementiert das VOF-Modell das High Resolution Interface Capturing (HRIC) -Schema zum Erfassen der freien Oberfläche.

Um das turbulente Verhalten der Strömungen zu erfassen, wurde das „Realizable k-ε Model“ als Turbulenzmodell gewählt. In diesem Modell ist ein kritischer Koeffizient in der Transportgleichung für die turbulente Dissipationsrate eine Funktion der mittleren Strömungs- und Turbulenzeigenschaften und erfüllt die Physik der Turbulenz (Realisierbarkeit).

Bei der Methode des finiten Volumens (FV) werden die maßgebenden Gleichungen über ein Volumen oder eine Zelle integriert, wobei eine stückweise lineare Variation der abhängigen Variablen angenommen wird. Mithilfe dieser Integrationen müssen Flüsse über die Grenzen der einzelnen Volumina hinweg ausgeglichen werden, wobei die Flüsse in der Mitte zwischen den einzelnen Knoten in der Domäne berechnet werden.

In diesem Zusammenhang wurde die Finite-Elemente-Analyse Software von Abaqus ausgewählt, welche ein Produkt vom Simulia-Unternehmen ist und ausschließlich aus fünf Hauptprodukten besteht, nämlich dem Abaqus-Standard, dem Abaqus-Explicit, dem Abaqus CAE, dem Abaqus-CFD und dem Abaqus-Electromagnetic, um die Strukturen zu lösen, die mit der durch das Star CCM+ analysierten Fluiddomäne gekoppelt waren.

In der vorliegenden Arbeit wurden der Abaqus-Standard, Abaqus explicit und Abaqus CAE verwendet, um das Verhalten flexibler Strukturen mit der Finite-Elemente-Methode (FEM) numerisch zu untersuchen. Die Strukturdomäne wurde in Abaqus CAE erstellt und als Eingabedatei geschrieben, die mit dem automatischen Kommunikationstool CSE „Simulia Co-Simulation Engine” mit der Fluiddomäne verbunden wer-

den kann. Als geeigneterer Algorithmus für nichtlineare Probleme wurde Abaqus explicit ursprünglich implementiert, um den strukturellen Bereich zu lösen. Trotzdem wurde der Löser aufgrund von Stabilitätsproblemen des entsprechenden Kopplungsalgorithmus explizit von Abaqus auf Abaqus-Standard umgestellt.

Die Finite-Elemente-Methode (FE) basiert im Allgemeinen auf Galerkins Methode der gewichteten Residuen, bei der die maßgeblichen partiellen Differentialgleichungen nach Multiplikation mit einer Gewichtsfunktion über ein Element oder Volumen integriert werden. Die abhängigen Variablen werden durch eine Formfunktion auf das Element angewendet, die mit der Gewichtsfunktion identisch ist (nach der Methode von Galerkin).

Schließlich ermöglichte die Implementierung einer effektiven partitionierten Strategie in Form eines impliziten Kopplungsalgorithmus, dass partitionierte Domänen kraftvoll verknüpft werden konnten. Um zu ermöglichen, dass die gekoppelten Bewegungsgrenzen innerhalb der Fluiddomäne der von der Strukturdomäne (berechnet von Abaqus) vorgegebenen Bewegung folgen, wurde ein Morphing-Bewegungsmodell in die physikalische Modellkonfiguration innerhalb des Fluidcodes von Star CCM+ integriert.
Das angewandte Verfahren gewährleistete Stabilität und Konvergenz bei der Lösung dieser komplizierten Probleme, jedoch mit hohem Rechenaufwand.

Die numerischen Modelle wurden mit experimentellen Modellen verglichen und validiert. In dieser Hinsicht wurden zwei verschiedene Fälle für verfügbare experimentelle Aufzeichnungen diskutiert und verglichen, wobei die numerischen Ergebnisse eine gute Übereinstimmung mit experimentellen Ergebnissen zeigten.

Erstere verdeutlichten, wie sich die flexible Flutabwehr im ganzen Maßstab verhält, wenn sie von einem beschleunigten massiven Treibgut angefahren und beeinflusst wird. Die Hauptkomplexität dieser Studie beruht auf dem Netzkriterium im Flüssigkeitsbereich, wenn sich zwei Strukturen sehr nahe kommen. Die Fluiddomäne wurde sowohl durch die Standard-Vernetzungstechniken als auch durch ein Overset Mesh diskretisiert.

Letzteres veranschaulichte die Wechselwirkung zwischen einer Membran im unteren Maßstab mit einer ausgebreiteten Wasserwelle, die durch Kolbenbewegung erzeugt wurde. Dieser Beitrag stellt die Ansätze für die Festlegung einer konvergenten numerischen Lösung vor und vergleicht die Ergebnisse mit den experimentellen Ergebnissen.

ABSTRACT

This work is part of an interdisciplinary research project concerning the design of a light temporary installable textile flood control structure. The motivation for this work is the great need of applying light structures for the protection of coastal areas from detrimental effects of rapid water runoff. The prime target of the thesis is the numerical analysis of the interaction between slender shaped pliable structures, free surface water flow and surrounding rigid structures, playing an influential role in the reliable performance of the investigated systems.

In the last decades, the need for light structures motivated wide-ranging studies on FSI problems „fluid-structure interaction“, where numerical analysis is advantageous for efficient, economical and secure manufacturing.
Fluid-structure interaction (FSI) is characterized by the interaction of some movable or deformable structure with an internal or surrounding fluid flow.
In a fluid-structure interaction (FSI), the laws that describe fluid dynamics and structural mechanics are coupled.
The most common application of the FSI analysis can be found in marine, aircraft and the automotive industries, while its contribution in medicine and entertainment continues to gain in popularity.

In order to model sufficiently the accurate behavior of the structures, there are many aspects which should be taken into account. The descriptions of light structures in terms of material properties, geometry, and discretization types in conjunction with the definition of fluid regions are decisive parameters.

When a fluid flow interacts with a structure, the pressure load arising from the fluid flow is exerted on the structure, followed by deformations, stresses, and strains of the structure. Depending on the resulting deformation and the rate of the variations, a one-way or two-way coupling analysis can be conducted.

Moreover, the stability and robustness of the corresponding numerical algorithms which approximate the behavior of each component and coupling approaches, their limitations and contradictions with each other pose a huge challenge for numerical simulations. The most known issue regarding FSI studies is imposed by an added mass effect which stems from the coupling method between fluid and structure frameworks. This matter is deteriorated when heavy fluids such as water and a flexible structure are interacting.

The numerical work was launched by means of the finite volume solvers of the Star CCM+, which is a product of Siemens PLM Software. Within the FV framework, a par-

titioned approach was implemented to solve the FSI problem. The behavior of both structures and fluids was approximated via available meshes and algorithms based on the FV framework which suffered from convergence and stability issues.

To solve fluid domains, the immiscible water-air flow within the channel was modeled by the volume of fluid model (VOF model) which is based on the Euler-Euler model for multiphase flows. Moreover, the VOF model implements the high resolution interface capturing (HRIC) scheme to capture the free surface.
In order to capture the turbulent behavior of the flows, the „Realizable k-ε model“ was chosen as a turbulence model. In this model, a critical coefficient in the transport equation for the turbulent dissipation rate is a function of mean flow and turbulence properties and satisfies the physics of turbulence (realizability).

In the finite volume method (FV), the governing equations are integrated over a volume or cell, where a piece-wise linear variation of the dependent variables is supposed. Using these integrations, fluxes across the boundaries of the individual volumes have to be balanced, where the fluxes are computed at the mid-point between the discrete nodes in the domain.

To solve the issue regarding convergency, another partitioned strategy was imposed to discretize and solve both structures and fluids with appropriate formulations and solvers.

In this context, the finite element analysis software of Abaqus which is a product of Simulia companies and solely comprised of five main products, i.e. the Abaqus standard, the Abaqus explicit, the Abaqus CAE (complete Abaqus environment), the Abaqus CFD, and the Abaqus Electromagnetic was selected to solve the structures which were coupled with the fluid part analyzed by Star CCM+.

In the current work, the Abaqus standard, Abaqus explicit and Abaqus CAE were utilized to investigate numerically the behavior of flexible structures by the finite element method (FEM). The structure domain was prepared within Abaqus CAE and written as an input file which can be interconnected with the fluid domain by the automatic communication tool CSE „Simulia co-simulation engine”. As a more appropriate algorithm for nonlinear problems, Abaqus explicit was initially implemented to solve the structural domain. Nevertheless, the solver was switched from Abaqus explicit to Abaqus standard due to stability problems of the corresponding coupling algorithm.
The finite element method (FEM) is generally based on Galerkin's method of weighted residuals, where the governing partial differential equations are integrated over an element or volume after having been multiplied by a weight function. The

dependent variables are introduced on the element by the shape function which is identical to the weight function introduced in Galerkin's method.

Finally, the implementation of an effective partitioned strategy in the form of an implicit coupling algorithm made it possible for the partitioned domains to be linked powerfully. In order to allow the coupled moving boundaries within the fluid domain to follow the motion dictated by the structural domain (computed by Abaqus), a morphing motion model was incorporated into the physical model setup for the fluid within the software of the Star CCM+.
The applied procedure ensures stability and convergence in the solution of these complicated issues, albeit with high computational cost.

The FSI numerical models were compared and validated by experimental models. In this regard, two different cases were discussed and compared with available experimental records, where numerical results have exhibited a good agreement with experimental findings.

The former illustrated how the full-scale flexible flood barrier behaved when approached and impacted by an accelerated massive flotsam. The principal complexity of this study stemmed from the mesh criterion in the fluid domain when two structures approached each other very closely. The fluid domain was discretized by both the standard meshing techniques and the overset mesh, respectively.

The latter illustrated the interaction between the down-scale membrane and the propagated water wave which was generated by a one-way movement of a piston type wave generator.

This contribution presents the approaches for the establishment of a convergent numerical solution and compares the results with experimental data.

Key words

FSI analysis, finite element method, finite volume method, flexible light structure, free surface flow

ACKNOWLEDGEMENTS

In the current thesis, I give an overview of the main results of my research at the Institute of Mechanics and Thermodynamics of the TU Chemnitz since 2013.

This work is financed partially by die Arbeitsgemeinschaft industrieller Forschungsvereinigungen“(AiF) and the „Deutscher Akademischer Austauschdienst“(DAAD). Moreover, the support of Siemens industry regarding academic licenses is gratefully acknowledged.

At this point I thank my supervisor Prof.Dr.-Ing.habil.Günter Wozniak for his guidance. Many thanks go to my colleagues Mr. Carsten Heinich and Mr. Ebram Boshra for their supportive and friendly assistance. With their technical collaboration regardind experimental investigation, this work progresses as smoothly as possible. Furthermore, I appreciate the other colleagues at professorship of fluid mechanics for the good working atmosphere, trusting cooperation and their mutual help with everyday problems.
In addition, the support of the light construction institute at the Technical University of Chemnitz for modal experimental investigation is gratefully aknowledged.

The years I spent during my thesis, remain as good memories in my mind forever.

Last but least I would like to express my special thanks to my parents for their energetic emotional support and financial helps.

Contents

Nomenclature

Latin Letters

Symbol	***Description***	***Dimensions***	***Unit***
$[C]$	*Damping Matrix*	-	-
$[K]$	*Stiffness Matrix*	-	-
$[M]$	*Mass Matrix*	-	-
A	*Cross Section Area of Projectile*	L^2	m^2
B21, B22, B23, B31, B32, and B33	*Beam Elements in Abaqus*	-	-
B31	*Linear Interpolated Timoshenko Beam Element*	-	-
C	*Phase Fraction Function, Initial Velocity of Projectiles at Impact Time*	-, LT^{-1}	-, m/s
Cn()	*Jacobian elliptic function*	-	-
CO	*Courant Number*	-	-
CO_{max}	*Maximum Courant Number*		
d_1	*Damping Ratio*	-	-
E	*Young modulus*	$ML^{-1}T^{-2}$	$kg/(m.s^2)$
B_M	*Bending Stiffness of Membrane*	ML^2T^{-2}	$kg.m^2/s^2$
B_{beam}	*Bending Stiffness of Steel Cord*	ML^3T^{-2}	$kg.m^3/s^2$
f	*Mathematical Function for Contact Length, Slope, Displacements*	L, -, L	m, degree, m
f, f_0, f_1, f_2	*Frequency*	T^{-1}	Hz
$f(x,k,d)$	*Function of Parameters* x, k, d	-	-
$F(X_1, X_2, \ldots., X_k)$	*Function* F *of* k *Variables* $X_1, X_2, \ldots., X_k$	-	-
$F(x), F1(x), F2(x)$	*Cumulative Distribution Functions*	-	-
g	*Gravitational Acceleration*	LT^{-2}	m/s^2
$G(\pi_1, \pi_2, \ldots., \pi_{k-r})$	*Function* G *of* $(k\text{-}r)$ *Variables* $\pi_1, \pi_2, \ldots \pi_{k-r}$.	-	-
h	*Water Flow Depth, Membrane Height, Validity of Null Hypothesis*	L, L, -	m, m, -
h_w	*Water Flow Depth*	L	m
H	*Wave Height*	L	m
H1	*Amplitude*		dB
I	*Moment of Inertia*	L^4	m^4
k	*Wave Number, turbulent kinetic energy, Kolmogorov-Smirnov statistic*	-, L^2T^{-3}, -	-, m^2/s^3, -
K, K_R	*Curvature*	-	-
l, b, a and ha	*Geometrical Dimensions of Membrane*	L	m
L	*Wave Length, Fundamental Dimension of Length*	L, L	m, m
m	*Bending Moment*	ML^2T^{-2}	$kg.m^2/s^2$
M	*Mass of Projectile, Fundamental Dimension of Mass*	M	kg
M3D3	*Three-Dimensional, 3-Node Membrane*	-	-

	Element		
M3D4	*Three-Dimensional, 4-Node Membrane Element*	-	-
n_1	*The Local (1) Beam Section Axis, Sample Size*	-, -	-, -
n_2	*The Local (2) Beam Section Axis, Sample Size*	-, -	-, -
p_1, p_2, p_3, a_1,.., a_4, b_1,.., b_4, c_1,.., c_4	*Function Coefficients*	-	-
P	*Hydrostatic Pressure of Water*	$ML^{-1}T^{-2}$	$kg/(m.s^2)$
PIPE21, PIPE22, PIPE31, and PIPE32	*Pipe Elements in Abaqus*	-	-
r	*Radius, Sum of Squared Residuals*	L, L^2	m, m^2
R	*Radius of Curvature of Beam*	L	m
R3D4	*Three-Dimensional Rigid Element With 4-Node*	-	-
S	*Stroke of Wavemaker, Scale Factor*	L, -	m, -
S(Y)	*Stroke of Wavemaker*	L	m
t	*Time, Thickness*	T, L	s, m
t	*Local Tangent along the Beam Element*	-	-
T	*Fundamental Dimension of Time, Period of Water Wave*	T	s
u	*Water Velocity*	LT^{-1}	m/s
U, U1,U2,U3	*Displacements*	L	m
v	*Velocity at Interface*	LT^{-1}	m/s
v	*The Vector Approximating the n1 Orientation of a Beam Element*	-	-
V	*Wave Propagation Speed*	LT^{-1}	m/s
W_M	*Weight of Membrane per Area*	$ML^{-1}T^{-2}$	$kg/(m.s^2)$
W_s	*Weight of Steel Cord per Length*	MT^{-2}	kg/s^2
x,y	*Position Variables*	L	m
x_1, x_2	*Vector for sample Data*	-	-
X, Y, Z	*Axes of a Cartesian Coordinate System*	-	-
Y, U_1, U_2, U_3	*Data Samples for Displacements*	L	m

Greek Letters

Symbol	***Description***	***Dimensions***	***Unit***
Δt	*Time Step*	T	s
Δx	*Length Interval*	L	m
Δf	*Frequency Difference*	T^{-1}	Hz
α	*Mass Proportional Damping Coefficient*	-	-
β	*Material Stiffness Proportional Damping Coefficient*	-	-
ε	*Turbulent Dissipation Rate*	L^2T^{-3}	m^2/s^3
μ	*Fluid Viscosity*	$ML^{-1}T^{-1}$	kg/(m.s)
ν	*Poisson Ratio, Fluid Kinematic Viscosity*	-, L^2T^{-1}	1, m^2/s
ζ	*Damping Ratio*	-	-

π	*Pi Number*	-	-
$\pi_1, \pi_2, \ldots, \pi_{k-r}$	*Dimensionless Numbers*	-	-
ρ	*Density*	ML^{-3}	kg/m^3
σ	*Angular Frequency of Wavemaker, Surface Tension*	T^{-1}, MT^{-2}	rad/s, kg/s^2
σ/ρ	*Kinematic Surface Tension*	L^3T^{-2}	M^3/s^2
ω	*Dissipation Rate per Unit Turbulent Kinetic Energy, Angular Frequency*	T^{-1}, T^{-1}	1/s, rad/s

Mathematic Operators

Symbol	***Description***	***Dimensions***	***Unit***
$\cdot$	*Scalar Product Operator*	-	-
x	*Cross Product Operator*	-	-
∂	*Partial Differential Operator*	-	-
∇	*Nabla Operator*	-	-
$\nabla \cdot$	*Divergence Operator*	-	-

Abbreviations

Symbol	***Description***
1-D, 2-D, 3-D	*One Dimensional, Two Dimensional, Three Dimensional*
AiF	*Arbeitsgemeinschaft industrieller Forschungsvereinigungen*
ALE	*Arbitrary Lagrangian Eulerian*
AMR	*Adaptive Mesh Refinement*
BEM	*Boundary Element Method*
BIM	*Boundary Integral Method*
CAD	*Computer-Aided Design*
CAE	*Complete Abaqus Environment*
CFL	*Courant-Friedrichs-Lewy*
CPU	*Central Processing Unit*
CSE	*Simulia Co-simulation Engine*
DAAD	*Deutscher Akademischer Austauschdienst*
DEM	*Discrete Element Method*
DSD	*Deforming Spatial Domain*
DTW	*Dynamic Time Warping*
FD	*Fictitious Domain*
FD/adap	*Fictitious Domain with adaptive meshing*
FE	*Finite Element*
FEM	*Finite Element Method*
FSI	*Fluid-Structure Interaction*
FPM	*Finite Pointset Method*
FRF	*Frequency Response Function*
FV	*Finite Volume*
HOBEM	*Higher Order Boundary Element Model*

HRIC	*High Resolution Interface Capturing*
IAC	*Interface Artificial Compressibility*
IB	*Immersed Boundary*
IBM	*Immersed Boundary Method*
ITTC	*International Towing Tank Conference*
JONSWAP	*Joint North Sea Wave Observation Project*
ktest2	*Cumulative Distribution Function Test*
LBM	*Lattice Boltzmann Method*
LES	*Large Eddy Simulation*
MAC	*Marker-and-Cell*
MOR	*Model Reduction Order*
NURBS	*Non-Uniform Rational B-Spline*
NVD	*Normalized Variable Diagram*
NWT	*Numerical Wave Tank*
OpenFOAM	*Open Field Operation and Manipulation*
PCM	*Partial Curve Mapping*
PDE	*Partial Differential Equation*
PE	*Polyethylene*
PIC	*Particle-in-Cell*
PIV	*particle image velocimetry*
PVC	*Polyvinyl Chloride*
RANS	*Reynolds-averaged Navier-Stokes*
RBF	*Residual Basis Functions*
ROM	*Reduced-Order Model*
RST	*Reynolds Stress Tensor*
SPH	*Smoothed Particle Hydrodynamics*
SST	*Stabilized Space Time*
UDF	*User Defined Function*
VOF	*Volume of Fluid*

Subscripts

Symbol	***Description***
e	*Experimental Data Sample*
n	*Numerical Data Sample*
$beam$	*Subscript for Beam Elements*
k	*Physical Variables Used in Buckingham Pi Theorem*
M	*Subscript for Membrane*
m	*Subscript for Down-Scale Model, Bending Moment*
max	*Subscript for Maximum*
p	*Subscript for Prototype, Subscript for Progressive Wave*
R	*Subscript for Resting Configuration*
r	*The Number of the Fundamental Dimensions Used in Buckingham Pi Theorem*
s	*Standing Wave, Steel Cord*
w	*Subscript for Water Wave or Water*

Superscripts

Symbol	***Description***
e	*Experimental Data Sample*
n	*Numerical Data Sample*

1 Introduction

An abrupt increase in river water level triggers dire aftereffects on coastal ecosystems and renders coastal inhabitants defenceless (Figure 1.1). Although the protection against floods can be achieved by rigid permanent structures, such structures not only disturb local natural landscapes and views but also are very expensive. A surge in the vital demand for the development of a temporary protective system against flood provides the motivation for conducting the current research.

Figure 1.1: A catastrophical aftereffect of a flood in the Lower Bavarian district of Rottal-Inn (Hoppe 2016) [1]

Figure 1.2: Exemplary experimental impact analysis for flood barrier flexible structures in TU Hamburg-Harburg (Wibbeler 2016) [2]

A key challenge in the advent of such a flood protection system that is characterized by low cost, quick and easy assembly capability is the answer to the question how far it can resist against hydropower, flotsam and so on (Figure 1.2).

In this work, we study numerically and experimentally the fluid-structure interaction comprising a flexible slender shaped structure, free surface flow and potentially interacting rigid structures, categorized in flood protection applications, whereas more emphasis is given to numerical analysis. Objectives of this study are defined in detail as follows:

The initial aim is the numerical analysis of the behavior of a down-scale membrane loaded by hydrostatic pressures, where the numerical results have to be validated against available experimental data.

A further case which has to be investigated is how the full scale flexible flood barrier behaves when approached and impacted by an accelerated massive flotsam. The numerical model has to be built so as to replicate the same physical phenomenon investigated experimentally. It enables a comparison between the numerical and experimental analyses to be drawn.

A more complicated case where the flexible down-scale membrane interacts with a propagated water wave is a further target area to study. Moreover, an experimental investigation is required to validate the numerical results by way of comparison.

The ultimate goal is to perform a similitude analysis upon which a correlation between the full-scale prototype and the down-scale model can be formed. The implementation of the similarity laws enables the behavior of the full scale prototype to be quantitatively assessed on the basis of the available data for the down-scale model. In addition, in order to validate the accuracy of the similitude analysis, numerical analyses have to be carried out.

1.1 Work overview

This thesis is structured into eight chapters. Chapter 1 outlines briefly the objectives and application areas of the thesis and a review of relevant literature.

In chapter 2, the history of the work and the research methodology are presented, where numerical damping models are emphasized. Also, the reason why the fluid-structure analysis is partitioned into two domains is explained, wherein the applied solvers and coupling methods are discussed in detail.

Chapter 3 is targeted to examine the validity of the structural model setup including discretization, solvers, interactions, and so on. What are described in this chapter are the down-scale model setup, the results based on a hydrostatic load, and the validation of the numerical results by comparison with the experimental data.

In chapter 4, impact analysis on the full-scale prototype is under debate, where two co-simulation cases are represented. In both cases, the co-simulation analyses represent a scenario where the full-scale prototype loaded by a water flow is attacked by a heavy flotsam. In the former co-simulation case, the fluid domain is discretized with a standard mesh, whereas the latter exhibited results with an overset mesh. In order to gain a better insight regarding the overset mesh, further cases are simulated within the Star CCM+ environment, where the geometrical parameters of the flotsam and the discretization specifications are subjected to change.

To verify the behavior of the down-scale membrane in response to hydrodynamic forces, a channel was constructed, where a wave is generated by the movement of a wooden body which replicates the behavior of a piston-type wavemaker.
With this intention, the numerical wave generation and comparison with analytical results is demonstrated in chapter 5.

Afterwards, the experimental and numerical model setups regarding the down-scale membrane are introduced in chapter 6. Experimental and numerical model results are then compared and validated.

Chapter 7 contains a structural similitude or a dimensionless analysis for the full-scale membrane. Furthermore, to verify the accuracy of the dimensional analysis, two different numerical simulations are conducted. While the first analysis is performed for the full-scale membrane, the membrane downscaled based on the dimensionless analysis results is analyzed in the second one.

Finally, in Chapter 8, conclusions of the thesis are drawn and the contributions made by the investigation to numerical fluid-structure analysis are outlined and some recommendations for future work are given.

1.2 Literature review

The interaction between fluids and structures, which is an interdisciplinary problem, has gained importance in a wide range of scientific and engineering applications. Thanks to new advances in computer technology, the numerical analysis of multiphysics phenomena has aroused growing interest.

Fluid-structure interactions have been numerically and experimentally studied by many researchers and published by several books, papers, and review papers.

For instance, different numerical models for the interaction of elastic structures with internal fluids for sloshing, hydroelasticity and structural acoustics applications were proposed by Morand and Ohayon (1995) [3].

Furthermore, a variety of numerical works with emphasis on ocean engineering was collected by Chakrabarti (2005) [4]. FSI numerical works on the basis of the immersed boundary formulation were reviewed by Mittal and Iaccarino (2005) [5].

Hou et al. (2012) [6] have also published a review paper entitled “Numerical methods for fluid-structure interaction”, which provides useful knowledge about different approaches for FSI analysis.

In spite of the potential for the description of a fluid motion within Langrangian coordinates, a fluid domain is generally viewed based on an Eulerian frame of reference, where fluid fields are solved within the mesh points that are fixed in space.

The key challenge encountered in any FSI analysis is the coupling between the two independent domains with clear distinctions. For example, a structure domain requires discretizing by a Lagrangian mesh where the mesh is fixed to the mass and follows the mass motion. In fact, the Lagrangian mesh is able to deform and follows an individual structural mass as it moves through space and time. Nonetheless, the fluid mesh remains intact within the space, where the fluid flows as time passes.

The numerical approaches with regard to FSI phenomena can be divided into two main categories, namely the monolithic approach and the partitioned approach.

In the former, a single system equation for the whole problem is solved simultaneously by a unified algorithm; however, in the latter, the fluid and the structure are discretized with their proper mesh and solved separately by different numerical algorithms.

There is also another classification for FSI problems on the basis of mesh methods: conforming methods and non-conforming methods. In the first method, the interface condition is regarded as a physical boundary (interface boundary) moving during the solution time, which imposes the mesh for the fluid domain to be updated in conformity with the new position for the interface.

In contrast, the implementation of the second method eliminates a need for the fluid mesh-update on the account of the fact that the interface requirement is enforced by constraints on the system equations instead of the physical boundary motion.

Most of the FSI studies with the partitioned approach are discretized on the basis of the conforming mesh, while the immersed methods classified within FSI monolithic approach-based methods utilize non-conforming mesh methods.

Further alternatives to deal with FSI problems are the particle based methods which can be used to solve numerically the partial differential equations for the simulation of particulate flows. The work is based on a Lagrangian description to model the motion of nodes (particles) in the fluid domain.

The particle based methods include the Lattice Boltzmann, the smoothed particle hydrodynamics and the finite pointset method as illustrations which are explained in detail as follows.

The Lattice Boltzmann method (LBM) is another approach to fluid dynamics where mass and momentum conservation laws are enforced to a solution, but not on a continuum velocity and a pressure field. The fluid flow is depicted as a discrete set of particles instead of the representation as the continuous flow governed by the Navier-Stokes equations. The merit of the Lattice Boltzmann method is low computational time, albeit with a drastic reduction in the number of degrees of freedom.

One application related to LBM is the Leonardi et al.'s work (2016) [7] on the flexible barriers as protection tools against debris flow in mountainous terrain. Different computational frameworks, including the finite element method (FEM), the discrete element method (DEM) and the Lattice Boltzmann method (LBM) were applied. The behavior of the flexible barrier was solved by the former, whereas the impacts on the structure exerted by the debris flow with fluid-grain mixture were computed by coupling between the two other solvers. In detail, the motion of the grains was modeled by the DEM, while the LBM provided the solution for the free surface non-Newtonian fluid.

There is also another method similar to LBM, termed the smoothed particle hydrodynamics (SPH). It was developed by Gingold and Monaghan (1977) [8] and Lucy (1977) [9] and can be utilized to model a fluid motion.
A typical work done on this method is Schörgenhumer et al.'s study (2013) [10] on the interaction of flexible multibody systems with fluids, where the SPH solved the fluid part in combination with the finite element method and model reduction techniques for the structural parts. The interaction between the fluids and the structures was imposed by a distributed potential over the structural boundary segments shared by the fluid particles.

The SPH is a Lagrangian method for the solution of partial differential equations regarding to mass, momentum, and energy conservation laws, where PDEs are spatially discretized by particles with material properties. The interaction between the particles is determined by a smoothing, or kernel, function with compact support. These

particles move according to inter-particle interactions and external forces. For small velocity/pressure gradients, a single resolution process with uniform spaced particles can be applied, while the multiple resolution method populating the computational domain with particles by locally refinement assists to capture the near field for high velocity/pressure gradient phenomena (Hu et al. 2017) [11].

Another meshfree method for the simulation of a fluid flow on the basis of the Lagrangian approach to fluid dynamics is the finite pointset method (FPM). This method was examined by Tiwari et al. (2007) [12] for different FSI applications, where the spatial derivatives at an arbitrary point were approximated with regard to its surrounding neighbor particles by the weighted least squares method.

The following provides details on FSI numerical analysis regarding the mesh type.

1.2.1 The non-conforming methods

The immersed methods are well known approaches within the category of the non-conforming methods (the framework of monolithic approach), where the interaction between two distinct continua is implemented by the incorporation of Lagrangian force-equivalent terms into the fluid equations.

The formulation for the immersed boundary method was originally proposed by Peskin (1977) [13] to study blood flow through a beating heart. In this method, the immersed boundary (IB) equations are discretized spatially by a fixed Cartesian mesh for the Eulerian variables and a moving curvilinear mesh for the Lagrangian variables, where the curvilinear mesh moves freely through the fixed Cartesian mesh of the fluid domain. The free movement has no effect on the fluid mesh, which exempts the mesh from update as the solution advances in time.
Both variables are linked by the Dirac delta function which is approximated over a band of cells surrounding the immersed boundary (IB) in the numerical scheme. As a result, the sharp interface is numerically represented by a thin layer of finite depth.

In Figure 1.3 and Figure 1.4, the procedure involving the FSI study by means of the immersed boundary method and a typical representation of IB are depicted, respectively.

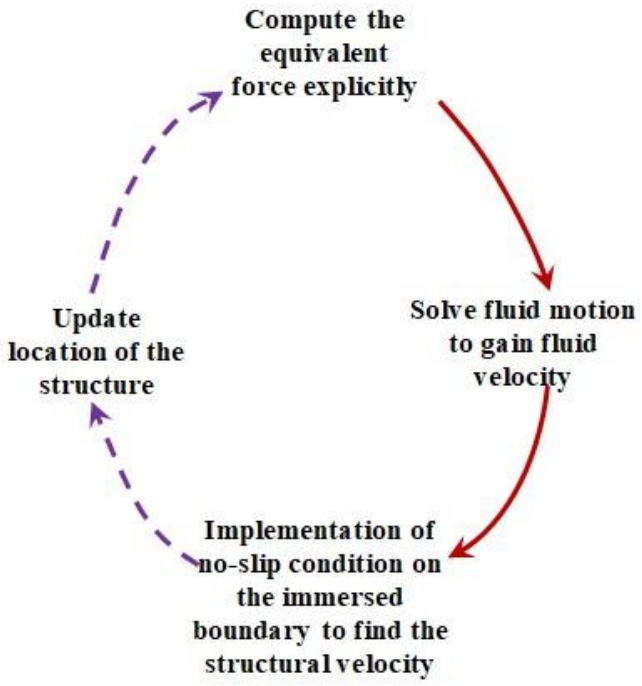

Figure 1.3: Immersed boundary procedure

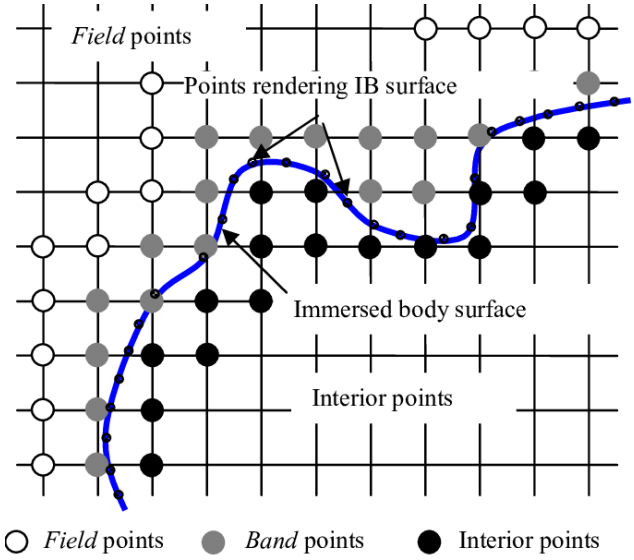

Figure 1.4: Immersed boundary representation (Ghosh et al. 2012) [14]

In principle, an immersed boundary can be a substitution for a structure without a finite volume (a closed curve in 2-D space or a membrane in 3-D space). The original immersed boundary was first order in space, which has the leakage disadvantage, notwithstanding the possibility for an improvement in the mass conservation.

The immersed domain method was a further development for the immersed bulk structures occupying a finite volume, where the artificial fluid covering the structural domain was introduced to extend the fluid domain to the entire computational domain.

The immersed thick boundary method stemmed also from the original immersed boundary method (IBM) introduced by Peskin to simulate 3-D membranes with finite thickness like an aortic valve, in which a finite volume flow solver was coupled with a finite element solid mechanics solver (Sigüenza et al. 2016) [15].

The other method in this category is the direct forcing method developed by Mohd-Yusof (1997) [16], which uses a discrete time immersed boundary method to simulate three-dimensional complex flow domains.

With the aim of a better volume conservation, an immersed interface method was developed by Leveque and Li (1997) [17], and Li and Lai (2001) [18]. The method enjoys a second-order approximation using the jump condition and the normal derivatives of the velocity in the solution instead of discrete delta functions. Nevertheless, this method was not applicable for embedded bulk structures and was limited to cases with a closed surface (3-D) or a closed curve (2-D).

The mirroring immersed boundary method (Mark and van Wachem 2008) [19] is another method to improve local mass preservations regarding the cases where a closed surface represents an immersed boundary. The method worked based on two interior and exterior points nearby the immersed boundary, where the velocity of the interior point was linearly interpolated to find the velocity of the exterior point by the fluid momentum equation.

The distributed Lagrange multiplier method, categorized in the immersed boundary methods family, achieves popularity when immersed rigid structures are concerned. In this regard, there are two sub categories based on the inclusion of the velocity constraint condition into the solution procedure before or after the time discretization of the FSI equations. The latter is named also as the fictitious domain method or domain embedding method and was investigated by many researchers, Glowinski et al. (1999, 2000, 2001) [20]–[22], Patankar (2001) [23], Yu (2005) [24] and Yu and Shao (2007) [25].

For both the immersed boundary methods and the fictitious domain method, source terms in the momentum equations of the fluid represent the contribution of the structure on the solution.

Glowinski and his co-workers (1999, 2000, 2001) [20]–[22] worked on a solution for the motion of many rigid bodies within an incompressible flow, where the repelling force between the rigid bodies, resulted from collision, was appended to the rigid body motion equation. Whereas the immersed boundary method used a finite difference framework, the fictitious domain method was formulated based on the finite

element method. The fluid and each of the rigid bodies were coupled at the interface by a distributed Lagrange multiplier to impose the constraint on the inner body.

Baaijens (2001) [26] has extended the fictitious domain method for compliant bodies, but only with slender shape, which has been further utilized to model flexible heart valve simulations (De Hart et al. 2000, 2003) [27], [28].

The fictitious domain method has been further extended for flexible structures, being not restricted to slender shapes, where Lagrange multipliers were incorporated across the whole solid body rather than only along its boundaries.

Van Loon et al. (2006, 2007) [29], [30] combined the fictitious domain method with an improved adaptive meshing to compute the structures behavior in response to fluid pressures without a need for a conforming connection between the fluid and structure mesh.

Van Loon et al. (2006) [29] took advantage of different techniques, such as Lagrange multipliers, adaptive meshing, and ALE methods, enabling both an accurate motion of the structure and a more precise estimation for the fluid behavior near the fluid-structure interface. They utilized finite element formulations for both the structure and fluid domains within two-dimensional frameworks, followed by the claim for possible extension to three dimensions.

Van Loon et al. (2007) [30] compared the distinction between the arbitrary Lagrangian Eulerian (ALE) methods (explained later in detail), the fictitious domain (FD) and the fictitious domain with adaptive meshing (FD/adap) approaches.
Applying the FD method, there was no change for the fluid mesh when the structure was updated in a Lagrangian way; hence, the mesh generation occurred only before the analysis.
Both the ALE and the FD/adap methods worked based on the coupling along the centerline curve of the structure, which necessitated a remeshing algorithm; however, in the FD/adap method, the fluid mesh was only aligned with the centerline of the structure mesh, but discretized in a different way. In fact, the mutual conformity was not imposed within the FD/adap method, which made it computationally inexpensive in comparison with the ALE method.

Furthermore, the extended immersed boundary method (Wang and Liu 2004) [31] and the immersed finite element method (Zhang et al. 2004) [32] implemented the finite element method for the structure coupled with the fluid domain by the discrete dirac delta functions that found their origin in the meshless reproducing kernel parti-

cle method (RKPM). The fluid domain would also be discretized by either the finite difference method or the finite element method.

Kamensky et al. (2015) [33] presented a solely finite element based formulation for both the flow and the structural equations, applying the immersogeometric FSI approach to analyze the interaction of a bioprosthetic heart valve with a straight aorta. The immersogeometric FSI approach computes directly a spline-based surface representation of the structure by immersing it into a non-boundary-fitted discretization of the surrounding fluid domain.

There are many parameters influencing the accuracy and stability of the immersed methods, such as the mesh size, time step size, and the coupling way as explicit, semi implicit or implicit. Furthermore, how the shared data are interpreted for the counterpart domain plays a crucial role.

For instance, Zhao et al. (2008) [34] compared three ways to transfer the forces from the structure Lagrangian mesh to the underlying fluid Eulerian mesh. He applied the distributed force method, the discrete momentum equation for the interface jump conditions with a minimized truncation error, and the finite element Galerkin projection method. His results exhibited success to maintain a sharp interface in addition to ensured momentum conservation across the interface.

The work of Glowinski et al. (1999) [20] related to an analysis on finite element errors recommended the ratio of the structural mesh size to the fluid mesh size between one and two to reach a compromise between stability and accuracy.

The adaptive mesh refinement (AMR) was examined in many investigations, which represented an improvement in the precision of the results.

To estimate the forces on the rigid body surface more accurately, a dense overlapping mesh around the interface was used by Tai et al. (2005, 2007) [35], [36]. Altogether, the whole domains were discretized by three mesh types, including the stationary fluid mesh, the sub-domain with the dense overlapping mesh around the body, and the rigid mesh inside the rigid body. The cycle implementing an algorithm to distinguish the status type of fluid points is shown in Figure 1.5.

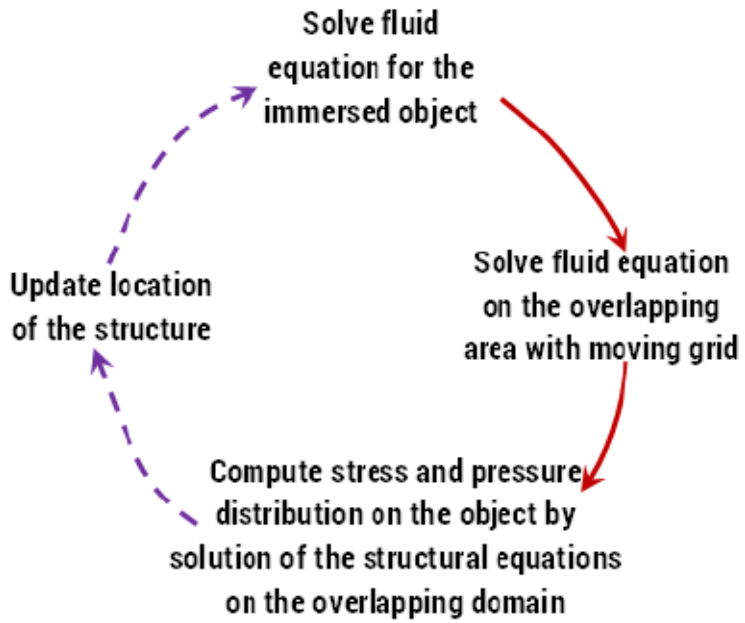

Figure 1.5: A loosely coupled iterative procedure for FSI analysis of rigid bodies introduced by Tai et al. (2007) [36]

The overlapping grid approach has been first used by Starius (1977, 1980) [37], [38] to compute elliptic and hyperbolic problems with moving bodies. The overlapping structured grids were utilized by Steger et al. (1983) [39] and Benek et al. (1985) [40] to solve flows around complex geometries.

A general algorithm for the generation of the overlapping grids was proposed by Chesshire and Henshaw (1990) [41] to solve elliptic and time-dependent PDEs „partial differential equation“ on composite meshes.

The implementation of a nonlinear weighted average method was also an exemplary effort to estimate the boundary layer velocity nearby the interface, Luo et al. (2007) [42]. In this regard, several investigations were also done using ghost cells for the direct forcing method, e.g. Ghias et al. (2004) [43], and Iaccarino and Verzicco (2003) [44].

1.2.2 The conforming (partitioned) approaches

The partitioned approach is very useful for integration between multiphysics aspects problems because it takes advantage of the available codes equipped with appropriate discretization strategies and numerical algorithms for each discipline. Nevertheless, a challenging and fallible characteristic is an update of the new position of the interface between two domains. In fact, the interface is required to be tracked due to the fact that it changes with time.

The FSI studies can be split in two groups based on the direction of the data transfer:

- „One-way" interactions
- „Two-way" interactions

The one-way interaction is applicable in cases when the integration of the structural displacement into the fluid domain has low impact on the flow fields sending back to the structure. The one-way interaction can also be utilized the other way around to reduce the required computational time. In other words, the fluid flow patterns are strongly affected by the structural motion, whereas the change in the counterpart domain in response to updated fluid flow can be ignored. The second alternative has been used rarely.

On the other hand, the fluid and structure domains must interact in two ways if the motion of the structure necessitates the flow motion and vice versa. The two-way interaction can be in turn branched into two classifications related to the frequency of the information exchange during each time step.

FSI problems can also be grouped by the kind of coupling used:

- Weak coupling
- Strong coupling

In a weak coupling, the data transfer happens once within each time step, no matter whether the data converge. This coupling strategy, referred as staggered coupling or loose coupling, is performed in an explicit sequential manner. As a result, it runs faster than a strong coupling, but with the expense of less accurate answers. Furthermore, there are many FSI scenarios, especially when the response time of each code to the other is comparable or the flexibility of the structure is high, where a loose coupling algorithm such as the block Gauss-Seidel method may not converge and suffers from instability issues.

While the FSI model involves large deformation or high frequency dynamic events, the strong coupling method can resolve some of these issues, albeit with more computational effort. Thanks to the new advances in technology, there are many applications for relatively low density or flexible structures interacting with a relatively heavy, almost incompressible fluid. Similarly, many structures in interaction with fluid flows can be regarded as light structures when their weight is lighter than the replaced fluid. These cases tend to be unstable unless they become solved by a powerful communication method between the partitioned physics. In the strong coupling, the fluid and structure solvers can be accommodated in the processor memory simultaneously, allowing the data exchange between the codes more than once per time

step, which is known as implicit, iterative staggered, iterative successive substitution, or multiple iterative coupling.

The arbitrary Lagrangian Eulerian method (ALE) is one of the famous methods in this category for the fluid-structure interaction analysis, being a proper approach to capture the details of the flow near the boundary. It implements the convection of mesh points, allowing the points to move arbitrary with respect to their frame of reference.

A certain merit with the ALE method is a strong coupling, whereas huge rotations, translations and/or deformations of the structure domain work to the disadvantage of the method. In fact, if the deformation of the structure violates the allowed threshold, ill-shaped fluid cells are produced, which force remeshing within the fluid domain.
Nonetheless, the transfer of the solution from the degenerated mesh to the new mesh renders artificial diffusions and decreases the precision.

ALE methods for the solution of the Navier-Stokes equations were first introduced by the discretization of moving fluid domains on the framework of the finite difference method. ALE methods represented accuracy and robustness for hemodynamics applications when small mesh displacements were predicted.

Farhat and Lakshminarayan (2014) [45] suggested an ALE formulation utilizing a so-called embedded boundary approach to analyze compressible FSI problems for external aerodynamics applications at high Reynolds numbers. They enforced the finite volume approach and the finite element method to solve the fluid equations and the structural equations, respectively.

An illustrative example for the partitioned approach is the work of Schäfer et al. (2010) [46], where the fluid-structure-acoustics interaction resulting from a fluid flow over a thin flexible structure was of interest.
It was carried out with an implicit, strong coupling between the finite volume CFD solver of FASTEST-3D (developed at the institute of fluid mechanics, University of Erlangen-Nuremberg) and the finite element multiphysics solver of CFS (developed at the department of sensor technology, University of Erlangen). The former was used to simulate the fluid domain, while the structural mechanics and the acoustics computations were modeled by the latter. To compute flow-induced noise (fluid-acoustics coupling), the Lighthill's analogy was implemented.

Another investigation on fluid-structure-acoustics interactions was conducted on a two-dimensional basis with the application to human phonation (Link et al. 2009) [47]. The finite element code of the CFS++, equipped with a fluid solver as well, was

selected to solve all physical aspects, where fluid and acoustics fields were coupled again by Lighthill's analogy.

Moreover, an implicit coupling method between a research code of CARAT (developed by Technical University of Munich) and the control volume based software of Ansys CFX was implemented for an analysis on free form membranes, promoting the solution for structure and fluid domains, respectively (Wüchner et al. 2006) [48].

The other toolkits for FSI analysis in a partitioned fashion are the FE-based solver of CARAT and the FV code of FASTEST-3D, coupled by the CoMA (developed by Technical University of Munich), which were utilized to study on the structure placed in a fluid flow by the LES turbulent model „Large Eddy Simulation" (Breuer et al. 2011) [49].

The investigation on hemodynamic patterns in large blood vessels by a coupling between the FE software of Abaqus and the FV software of the Star CCM+ would be a sample in a biological context (Sotelo 2013) [50]. A one-dimensional closed loop electrical circuit system was used as a tool for the generation of a dynamic pressure pulse. The pressure pulse generation tool and FSI solvers were coupled explicitly, where the pressure pulse and the mass flow rates became updated at the end of the periodic solution within the FSI analysis.

The other work regarding aorta artery was performed based on control volume solvers for both structural and fluid domains within the Star CCM+, where the effect of the wall elasticity of an idealized aorta artery on the Dean vortices of a secondary flow was studied (De Andrade 2014) [51].

A hydro-elastic analysis on the behavior of the flexible (composite) marine propeller blade design exposed to environmental loads was conducted based on the boundary element method-finite element method (BEM-FEM) by a two-way coupling between the panel code of KPA14 and the Abaqus Standard, respectively (Lee et al. 2014) [52]. To address the instability issues regarding the added mass effect, an acoustic medium field was incorporated into the model to generate a pressure component. The pressure load stemming from the acoustic medium field was imposed directly on the blade surface.

To provide a perspective for the simulation of insect flights, the tumbling and fluttering motion of the 2-D Rigid and deformable structures interacting with heavy Stokes flow was studied by the Star CCM+ and Abaqus co-simulation (Gomes 2014) [53].

The performance enhancement of a racing car established also a motive for the FSI analysis which was investigated by the Abaqus as a solver for the analysis of the structure, where both OpenFOAM and Star CCM+ provided the solution for the fluid domain (Landvogt 2016) [54].

The investigation on hypersonic deployable re-entry systems necessitated the fluid-thermal-structural analysis which was conducted by the coupling between the Star CCM+ and the Abaqus. The solution for the thermal and structural aspects was provided by the Abaqus, while the Star CCM+ added information from the fluid domain (Pasolini et al. 2015) [55].

The study on dropped lifeboats (Handeland 2015) [56], surface effect ship bow seal (Bloxom 2014) [57], offshore environments (Oliveira et al. 2016) [58], and thin plates regarding application for low enriched uranium fuel in reactors (Jesse et al. 2015) [59] were further interesting areas investigated by the data exchange between the Star CCM+ and the Abaqus for a two-dimensional model.

The model reduction order (MOR) is a way to alleviate the complexity of a dynamic system with lower computational cost as a consequence. A decrease in the number of degrees of freedom (the order of the model) in the target system in comparison with the source system promotes an analysis of complex dynamics with less effort.

An illustration for this method would be referred to Neumann's work (2016) [60] with an application for the turbines whose kinematics were simulated with a multi-body approach modeling flexible bodies. The solution for the fluid domain was based on RANS equations (Reynolds-averaged Navier-Stokes) by open source codes available in the OpenFOAM joined with an actuator-line method. The actuator-line method represented an order-reduced model for the blade by imposing external forces on the momentum equations in a two-way iterative coupling fashion.

To investigate the reason for the epiglottic folds collapse due to the ventilation-induced inspirational pressure difference, especially during strenuous exercise, the Star CCM+ was selected as the software equipped with solvers for both the structure and the fluid. The work was focused on the relation between the Young's modulus of the epiglottic fold and the displacement of the fold, which changes the volume flow at lungs (Lied 2017) [61].

1.2.2.1 Interface data transfer

A possible numerical barrier for data transfer on fluid-structure interfaces would be the mismatches and even the gaps resulting from the inconsistency between the meshes for the fluid and structure domains on the interface.
To solve the issue, the point match method and the artificial interface structure method were proposed.

After matching mesh points for both domains, they could be connected based on the shortest distances between the points (Brown 1997) [62] or the normal projection (Onishi et al. 1998) [63].

A rigid element connecting the matched points (Brown 1997 [62], Cebral et al. 1997 [64], [65], Onishi et al. 1998 [63], Farhat et al. 1998 [66]) was responsible for the displacement of the fluid surface mesh point on the interface according to the structural deformation. The rest of the fluid surface mesh points could be redistributed by local or global interpolation (Raveh and Karpel 1998 [67], Brown 1997 [62], Farhat et al. 1998 [66]).

In the Samareh's approach (1996, 1998, 1999) [68]–[71], after constructing a non-uniform rational B-spline (NURBS) representation for the structure, the structural displacements are projected onto the NURBS model (instead of the direct transmission to the matched fluid surface mesh points). The new fluid dynamic surface mesh can be constructed based on the new NURBS for the deformed structure.

In the mortar method (Appa 1989 [72], Guruswamy and Byun 1995 [73], Kapania et al. 1996 [74], Hou and Satyanarayana 2000 [75]), an artificial thin shell structure represents the fluid-structure interface to transfer the load and the displacement data between the fluid and structural domains.

1.2.2.2 Accuracy, stability and efficiency

In order to increase accuracy, stability, and efficiency, several methods have been developed, improving the treatment of interface conditions.

To predict the interface locations, Farhat et al. (2006) [76] proposed two algorithms with second-order accuracy in time without sub-iterations. To solve the fluid field, a three-point backward difference method was implemented.
In both algorithms, the interface velocity was predicted by a structural analysis, which updates the interface location and the fluid domain mesh. The solution for the fluid domain resulted in the updated velocity and pressure, followed by an updated equiv-

alent load of the fluid domain on the fluid-structure interface to correct the structural response.

Moreover, Zhang et al. (2007) [77] proposed two second-order algorithms without sub-iterations, where an external blackbox CFD code computed the pressure load.
In the first algorithm, the standard fourth-order Runge-Kutta method was applied to compute the structural domain, which required the fluid pressures at the last three time steps.
In contrast, the multi-step, implicit second order Adams scheme was implemented in their second algorithm to solve the structural dynamic equation, where the fluid pressures within the last four time steps were needed.

The sub-iterations between the fluid and structure solutions are influential factors for stability and convergency of the FSI numerical analysis.

For stabilization purposes, Vierendeels et al. (2000, 2002) [78], [79] incorporated an artificial compressibility in the fluid solver during the coupling iterations for partitioned procedures in blood vessels analyses.

A further technique to stabilize the coupling iterations between a black box fluid and a structural solver is the Aitken acceleration method (Mok et al. 2001) [80].

Reduced-order models (ROM) were applied by many researchers. To stabilize the partitioned procedure implemented between fluid and structure black box solvers, Vierendeels et al. (2007) [81] introduced linear reduced order models of two black box solvers, applied only within a coupling algorithm. They have analyzed the fluid domain by the software of Fluent 6.2, where the Abaqus 6.5 executed the structural domain. Two cases including pressure wave propagation in a blood vessel and the growth and the detachment of a gas bubble from a vertical needle submerged in a liquid were investigated to verify the accuracy of the applied methods.

Vierendeels et al. (2008) [82] introduced a reduced-order model (ROM) method to solve a heart valve dynamics problem. The heart valve was modeled by a chain of rigid linkages joined by hinges along with torsional compliance.
The commercial CFD package of Fluent was used as a tool to solve the fluid domain. The use of a commercial solver confirmed that the new algorithm has the capability to work with a black box fluid solver.

To solve an unsteady blood flow in a flexible tube, Degroote et al. (2008) [83] applied strategies to update the interface location. In the first part of the paper for a 1-D example, they derived an extra linear relation which updated the interface location in

response to the fluid pressure in order to improve convergency for a very flexible structure.
To solve complex problems, they implemented the ROM method to maintain the convergency and stability with an iterative algorithm. They used black box codes to solve fluid and structure domains, where ROMs for both the domains were built after two sub-iterations.
In the first sub-iteration, a multistep predictor was applied to estimate the interface location used in the fluid solution based on the solution of the structural domain.
The interface location was corrected in the second iteration by the Aitken under-relaxation factor (Irons and Tuck 1969) [84]. The ROM was built on the basis of the displacement modes relating to two above-estimated interface locations.

Degroote et al. (2008) [83] made a comparison between the stability of coupling techniques for partitioned solvers in FSI applications, where the coupling scheme with reduced-order models (with and without Aitken underrelaxation) and a fixed point iterative coupling with an added artificial compressibility coupling term were compared against each other.

Moreover, Degroote et al. (2010) [85] implemented the interface artificial compressibility (IAC) method by the source term appended to the continuity equation in the fluid domain next to the fluid-structure interface. The applied method was aimed at overcoming the barrier imposed by an added mass effect. The incompressibility within the fluid flow interacting with a carotid artery was the leading cause of the added mass effect. The results were generated by the flow software of Fluent and the structural software of Abaqus.

1.2.2.3 Modification of interface conditions: Robin transmission conditions

To achieve better convergency, Badia et al. (2008) [86] implemented the conventional block Gauss-Seidel scheme for a partitioned FSI problem, albeit with a modification on the interface condition.
In general, partitioned FSI problems necessitate sharing not only the same interface location but also the equal velocity (on account of the no-slip condition), and the similar normal stress. As a result, the Dirichlet condition has to be imposed onto the fluid field (the common velocity condition), whereas the Neumann condition constrains the structure field (the similar stress condition). What was modified in their work includes a replacement of the standard Dirichlet and Neumann interface conditions by the general Robin Transmission. The Robin transmission condition was composed based on a weighted, linear combination of the mentioned Dirichlet and Neumann conditions. Different weighted coefficients for a simplified FSI problem were exam-

ined, which introduced the Robin-Neumann procedure as a convergent and insensitive algorithm to mitigate the added mass effect. The Robin-Neumann algorithm imposes the Robin transmission condition on the fluid field and the Neumann transmission condition on the structure field.

1.3 Concluding remarks

Due to the multidisciplinary nature of FSI problems, there are many further publications which were not mentioned in this work. Moreover, a great emphasis was placed on the numerical procedures aimed at treating the interface conditions between fluids and structures. In this regard, two different classes of methods for FSI numerical procedures were reviewed.

The former is based on the immersed methods implementing non-conforming mesh. This class of methods solves the issue regarding the interface between two different Eulerian and Lagrangian frameworks by the incorporation of Lagrangian force-equivalent terms into the fluid equations.

The latter applies the partitioned approach which permits the fluid and structure domains involved in the FSI problems to be solved separately by their respective algorithms and discretizations. Furthermore, the data were shared between two domains in the specified intervals. On account of the added flexibility in spatial meshing, the partitioned approach is able to capture the detailed physics along the fluid-structure interface.

In the next chapter, the applied algorithms for solvers, and the discretization approaches will be discussed in detail. Furthermore, some extra models which are need to be incorporated into the physics of the fluid or structure domains like turbulence models for fluid or damping models for structure will be reviewed in-depth.

2 Methodology-numerical methods for fluid-structure interaction analysis (FSI)

In this chapter, the partitioned approaches such as single FV, and coupled FV-FE frameworks will be explained, where they can in turn implement explicit or implicit time integration solvers. Moreover, the coupling methods, which are key parameters in FSI analyses, will be discussed.

The further topics which will be described are the damping models appended into the physics of the structure and the turbulence models integrated into the physics of the fluid. Structural discretization elements like beam elements, membrane elements which require detailed descriptions will be also reviewed here. Likewise, the overset grid techniques implemented to discretize the fluid domains by splitting them into sub-domains according to hole-cutting and donor searching will be presented in detail.

On the whole, the methods used in this research fall in two broad categories, a single FV framework computed by the FV solvers available in the Star CCM+ and two partitioned FV and FE frameworks. The latter solution was achieved by an automatic communication between the FV solvers for the execution of the fluid side and the FE solvers used for the structural analysis. Whereas each method enjoyed advantages, it imposed some inherent limitations which had to be taken into account.

There are also some program packages equipped with general purpose grid-based flow solvers with free surface capabilities such as the OpenFOAM, the Star CCM+, the CFX, and the FLOW-3D.

The OpenFOAM (open field operation and manipulation), a free and open source CFD software, is based on the finite volume approach which offers both surface tracking and surface capturing methods for free surface flows.

The Star CCM+ is a finite volume based program package introduced by the computer software company CD-adapco and developed further by Siemens AG. Star CCM+ applies the volume of fluid (VOF) approach by a high resolution interface capturing (HRIC) scheme to track sharp interfaces.

The CFX is developed by the engineering simulation software company Ansys, where a hybrid finite element based control volume method is implemented to solve the Navier-Stokes equations. In the CFX, the Navier-Stokes equations are discretized in a collocated way and solved by a parallel, implicitly coupled multigrid.

The FLOW-3D is a multiphysics CFD tool based on a finite volume/finite difference approach. To solve free surface flows, an adapted version of the volume of fluid method namely TruVOF claims to implement the three ingredients of the original VOF method, recommended for the successful treatment of free surfaces. It uses an interface tracking scheme to locate the free surface, where boundary conditions at the free surface have to be applied.

2.1 Single FV framework

The first simulations were conducted by means of FV solvers in the Star CCM+, where the entire fluid-structure problem was discretized with finite volume based meshing tools and solved by finite volume based models and solvers in a single integrated software environment. In this context, the fluid flow took advantage of the appropriate solvers and the volume meshing methods.

Nevertheless, the finite volume solid stress model was attributed to the thin flexible structure which was meshed by a thin mesher as a solely available meshing type for thin solid structures.

As mentioned in the previous chapter, the fluid domain is generally presented in an Eulerian frame of reference, which results in solution fields for the mesh points that are fixed in space.
There is no problem with the Eulerian framework for geometrically fixed fluid domains; however, when the fluid domain changes shape or when moving interfaces are present inside the domain, a remedy to mimic the movement has to be taken.

In this regard, a mesh morpher model was assigned to the movement of the fluid domain, which allows the fluid interior vertices to follow the deformation of the fluid-structure interface (imposed by a finite volume solid stress solver). The mesh motion in the Star CCM+ uses a multi-quadric morphing model resting upon radial basis functions. Besides, more improved robustness was enforced by the incorporation of the cell quality remedy model into the physics of the simulation.

A certain drawback of this approach was the impossibility to append the contact interaction model which introduced the contact between the bottom of the channel and the deformable membrane. Nevertheless, the contact interaction model was necessary to prevent the structure from falling below the specified level (the channel bottom level).

In order to eliminate the artificial barriers associated with default numerical methods, two types of loads were defined on the structure region as a body force and also an additional load on the fluid-structure interface.
Within the membrane, the part which was vulnerable to make contact with the bottom boundary was defined with the help of some complex user field functions and cell sets.

Unfortunately, initial simulations of the flexible membrane with an arbitrary initial form showed that the quality of the deformed cells became poor. This issue caused the program to stop running when the bad cells appeared. The resulting failure could not be circumvented even if solver parameters were altered.

In order to prevent a huge mesh modification of the fluid region in compliance with the structure deformation, the two-dimensional deformed form of the membrane clamped at the two ends with the same Young's modulus, Poisson ratio, and density under its own weight and hydrostatic pressure was calculated according to the Pozrikidis' proposed method (2009) [87] and applied as the initial form of the membrane.

To achieve a robust, convergent simulation, a further availability in the Star CCM+ by applying overset mesh and a morphing motion model, enabling the motion of the fluid region in response to the deformation in the structure, was examined. The overset technology was used with the hope for maintaining a good mesh quality and a prospective solution.

Although successful coupling of the overset mesh was ensured, applying fixed conditions in any boundaries of the structure region did not prevent them from movement.
The reason why the prescribing boundary conditions could not constrain the relevant degree of freedom of boundaries was that they were interfaced with the fluid (as against to the previous measure). This interfacing created a dependency on intersected boundaries, while a boundary condition could only be imposed on the unconstrained boundaries, not the dependent boundaries. As a result, the whole structure floated free, no matter some boundaries were fixed.
So, although the overset mesh works generally better in FV applications in conjunction with the morphing motion, helping in maintaining good quality cells in this type of FSI simulation and increased convergence as a result, it demonstrated no competence in our case. It was evident that the overset mesh could not fulfill the expectation for an improvement of the mesh cell quality for the FSI problem to maintain the target convergency.

Overall, FSI simulations including thin flexible membrane have exhibited that the single FV-based numerical algorithm suffered from convergence problems and the mesh was distorted in such a way that the element quality became unacceptable.

The fact prompted us to solve the aimed complex FSI problem via coupling between the FE software of Abaqus and the FV software of Star CCM+. There were obvious advantages with the Abaqus and Star CCM+ co-simulation.

For instance, contact interactions were supported in the Abaqus contrary to the Star CCM+. As a consequence, there was no need to define the contact interaction between the membrane and the bottom of the channel by applying virtual loads on the contact-prone part of the membrane, which was both strenuous and not precise. Instead, the desired contact interaction could be imposed on the structural model in a simple and precise manner by the available algorithms within the Abaqus.

Besides, structural elements such as beams, membranes (explained in section 2.3 in detail) and algorithms for the computation of the structural domains available in the FE Codes had no counterparts in FV based codes such as the Star CCM+. Despite a thin structure could be discretized as three-dimensional cells by means of a thin mesher or an embedded thin mesher, some care in terms of the cell aspect ratio, the number of cells across the thickness of the structure and so on had to be taken. Acceptable stiffness behavior can be thereby gained, giving rise to a marked increase in the mesh number and consequently the numerical cost.

Last but not least, the main reason why the discretization of a slender membrane or a beam by three-dimensional cells could not be encouraged is the fact that the resulted model suffered significantly from the shear locking effect. As there were not enough cells across the thickness, the stiffness of the structure was significantly over predicted. Therefore, the bending deformation was under estimated, which gave rise to wrong results.

Altogether, the applied numerical measurement proved that an advanced partnership of the Star CCM+ with a FE-based code is unavoidable, in which the Star CCM+ provided the fluid domain solution and a third-party code such as the Abaqus solves for the structure region of the problem. Two partitioned regions had to be coupled with each other so that the solution data on the interface were imparted between two codes at specified intervals.

Within the whole fluid domain introduced in the thesis, the prism layer mesh, and a turbulence model were applied, which will be discussed in the following sections.

2.1.1 The prism layer mesher

The prism meshing model can be activated together with a core volume mesh, generating orthogonal prismatic cells close to wall boundaries as a default.
The meshing model is aimed at resolving the boundary layer next to wall surfaces, where no-slip flow condition has been imposed. The feature of high aspect ratio cells for prism layers is very useful to reduce the number of cells in many scenarios.

The Prism layers also reduce the numerical diffusion near the wall. Numerical diffusion, a discretization error, triggers discontinuities and steep gradients in a finite volume advection scheme and can be decreased if the flow would be aligned with the mesh by means of the prism layers.

They represent large velocity gradients in the direction normal to the surface, which are suitable to predict the flow solution more accurately.
Enabling the prism meshing model, a subsurface is created offset from the starting wall surface based on the user defined prism layer thickness. This subsurface is used to build the core mesh. The extrusion of the cell faces from the core mesh to the original starting target surface completes the prism layer mesh generation.

It is recommended (Siemens AG 2019) [88] that the prism layer mesh has to be built in such a way that the viscous sublayer can be resolved directly based on the turbulence model (low y+$\sim$1). Alternatively, for coarser meshes, a non-dimensional wall distance y+ bigger than 30 permits the code to implement a sufficiently precise wall function treatment.

A variety of parameters such as the number of cells, the thickness of the cell nearest the wall, and the expansion rate of the prism cell thickness can all be adjusted to capture the desired boundary.

2.1.2 Turbulence modeling

Irregular fluctuating flow is the common feature observed in a wide range of engineering applications.

Analysis of such high frequency fluctuations can be achieved at huge computational costs when utilising the exact governing equations of turbulent flows.

To alleviate numerical efforts, various turbulence models were proposed to solve for averaged or filtered quantities of flow and approximate the influence of fluctuation terms on the physical phenomena of turbulence.

To solve the Navier-Stokes equations based on the RANS solution approach „Reynolds-averaged Navier-Stokes“, the Star CCM+ is equipped with a wide range of turbulence modeling options, such as:

• Spalart-Allmaras
• $k-\omega$
• $k-\varepsilon$
• Reynolds stress transport

Spalart-Allmaras models

Spalart-Allmaras models are popular for the aerospace industry, where flows over a wing, fuselage or other aerospace external-flow are investigated.
They can be used for the applications in which the boundary layers are largely attached and separation is mild. In contrast, they are not suited to approximate flows involving free-shear layers, body forces (such as buoyancy), and complex recirculation.

The Spalart-Allmaras turbulence model is the one-equation model computing a transport equation for the modified diffusivity to define the turbulent eddy viscosity.

K-Epsilon models

K-Epsilon models are the industry-oriented approaches leading to a compromise between robustness, computational cost and accuracy.
The K-Epsilon turbulence model is a two-equation model, where the turbulent eddy viscosity is defined by a solution of the transport equations for the turbulent kinetic energy (k) and the turbulent dissipation rate (ε).

High Reynolds number approach

The original K-Epsilon turbulence model was introduced by Jones and Launder (1972) [89], where wall function laws were implemented on high Reynolds number grids.
Various approaches were later proposed to improve the accuracy of the original model.

Low Reynolds number approach

The approach introduces damping functions to some or all of the coefficients in the model according to the Reynolds number and the wall distance.

Two-layer approach

An alternative to the low Reynolds number approach was first proposed by Rodi (1991) [90] to predict the turbulence in the viscous-affected layers including the viscous sub-layer and the buffer layer.

Realizable K-Epsilon model

Shih et al. (1995) [91] applied a new transport equation for the turbulent dissipation rate in addition to a change in a critical coefficient of the model from a constant value (as in the standard model) to a coefficient as a function of mean flow and turbulence properties.
As a result, certain mathematical constraints on the normal stresses would match the physics of turbulence (realizability). This model exhibits more accurate results than the standard K-Epsilon model for many applications.

Realizable two-layer K-Epsilon model

The realizable two-layer K-Epsilon model is a combination of the realizable K-Epsilon model with the two-layer approach and enjoys the added flexibility of an all-wall treatment.

K-Omega models

K-Omega models resemble to K-Epsilon models, where two transport equations for the turbulent kinetic energy (k) and the specific dissipation rate (ω) are solved to compute the turbulent eddy viscosity, where ω ($\omega \propto k/\varepsilon$) represents the dissipation rate per unit turbulent kinetic energy.

However, they are different from each other in terms of the second transported turbulence variable (ω instead of ε in the k-Epsilon model). These models would be mostly used in the aerospace industry (like the Spalart-Allmaras models).

The biggest cons of the K-Omega model in its original form proposed by Wilcox (1998) [92] stems from sensitivity of boundary layer computations to the values of ω in the free-stream.
To overcome this shortcoming, various efforts have been made, where the SST (shear-stress transport) K-Omega model proposed by Menter (1994) [93] is an example.

Reynolds stress transport models

The Reynolds stress transport models, known also as second-moment closure models, approximate complex flows more accurately than the eddy viscosity models, but at the expense of complexity and numerical costs. Good results for the situations where turbulence is strongly anisotropic, such as the swirling flow in a cyclone separator can be achieved by a calculation of the components of the specific Reynolds stress tensor directly from the governing transport equations.

Seven equations including six equations for the Reynolds stresses (symmetric tensor) and one equation for the isotropic turbulent dissipation have to be solved (contrary to the two equations for either a K-Epsilon model or a K-Omega model). In addition to the extensive computational time required to solve the governing equations, the numerical stiffness of the RST equations imposes likely more iterations to reach a converged solution.

Weighing up the pros and cons of each turbulent model motivated us to select the realizable two-layer K-Epsilon turbulence model to simulate the free surface flow. This model which is used in many engineering applications proved to give good results for all-layer, especially for viscous sub-layer (low y+∼1), and the logarithmic area (y+ > 30).

2.2 Preparation of the standalone Abaqus model

In the first simulations of the structure, the dynamic explicit scheme was picked up to solve the structure on account of the fact that an analysis of such flexible slender structure in the Abaqus is an inherently highly nonlinear phenomenon which could be solved more efficiently by the Abaqus explicit solver.
Furthermore, the dynamic explicit analysis would add more comfort to incorporate contact interactions to the model.

The direct-integration dynamic procedure within the Abaqus standard implements the implicit Hilber-Hughes-Taylor operator (by default) which is an extension of the Newmark β method and unconditionally stable.
The approach imposes no limitation on the size of the time increment and the time increment size is selected by a user. In an implicit dynamic approach, the integration operator matrix must be inverted when solving a set of nonlinear equilibrium equations at each time increment.

In comparison, the Abaqus explicit uses the central-difference operator which presents stability only conditionally.

Furthermore, the time incrementation is fully automatic without user intervention.
The highest eigenvalue of the entire model, estimated by the maximum element dilatational mode of the mesh, governs the stability bound for the analysis.
Time incrementation relies closely upon the time needed for the propagation of a stress wave across the smallest element in the model.
That means that the time increment can be very short either if there exists a small mesh element or if the stress wave speed in the material is very high. This issue escalated when activating a Rayleigh damping (especially stiffness related damping).
However, the displacements and the velocities are known at the beginning of an increment.
As a result, there is no need for the construction or the inversion of the global mass and stiffness matrices.
In other words, each increment in the Abaqus explicit is less expensive than the increment in an implicit approach.

Nonetheless, numerical results within the Abaqus exhibited an oscillatory behavior for the thin structure, as evidenced by prior numerical models within the single framework of the Star CCM+, so that there was no decrease in amplitude of oscillations over time if no damping model was activated.

In reality, the oscillations of the thin membrane can be dissipated due to the internal resistances of the membrane and the friction between the membrane and the channel bottom.
Furthermore, the extent of water was practically unbounded which resulted in dissipation of a major amount of the oscillations, whereas in the numerical analysis it added more undesired artificial instabilities to the solution, well known as inevitable side effects for FSI numerical approaches.

That is why some measures had to be taken to suppress these oscillations, which mimicked the inherent damping behavior of the system. Otherwise, the simulations experienced neither a quasi steady state nor stability.

2.2.1 Damping by bulk viscosity

The linear and quadratic bulk viscosities were included by default in the Abaqus explicit with a default damping coefficient value of 0.06 and 1.2, respectively. The bulk viscosity created damping in proportion to the volumetric straining aimed at stability and the elimination of unwanted high frequency oscillations, which incorporated a numerical effect without any influence on the material point stresses. Although the damping coefficients could be modified, an increase of the damping coefficient was not able to prohibit the membrane from the oscillations.

2.2.2 Coulomb friction damping

The Coulomb friction damping was suitable to model damping arising from the friction between the outer surface of the membrane and the bottom of the channel. The damping force was equal to the product of the normal force and the friction coefficient, as set to 0.1, and acted in opposite direction of the membrane motion on the channel bottom and imposed a prohibitive force (against the motion) on the membrane. It was clear that the damping force grew with an increase in the friction coefficient. Nevertheless, there was a limitation upon the rise in the friction coefficient because applying a big coefficient was far from reality. Furthermore, the selection of a high friction coefficient increased the possibility for a failure in the simulation.

2.2.3 Rayleigh damping

Rayleigh damping is a mathematical damping model to damp low frequencies and high frequencies, where the effects of mass and stiffness are approximated by two damping coefficients. Moreover, it is assumed that the damping matrix $[C]$ for a system is proportional to the sum of the mass $[M]$ and stiffness $[K]$ matrices.

$$[C] = \alpha[M] + \beta[K] \tag{2.1}$$

α: Mass proportional damping coefficient (for low frequencies)

β: Material stiffness proportional damping coefficient (for high frequencies)

To define these coefficients, the basic requirement is to obtain the damping ratios corresponding to the first few modes, which can be computed by numerical modal analysis within the Abaqus.

Despite all efforts, there was no possibility for the definition of the damping ratios with numerical modal analysis due to the discretization of the light flexible structure by the membrane elements which lacked bending stiffness. Hence, these elements could not resist against the static load which had to be imposed in the modal analysis. Furthermore, an experimental modal analysis is a more precise method than a numerical modal analysis.
As a result, an experimental modal study was inevitable to be conducted.

2.2.4 Determination of the Rayleigh damping parameters based on the Chowdhury procedure

By means of the orthogonal transformation, the Rayleigh damping equation reduces to a formulation of the damping ratio (ζ) in terms of the angular frequency (ω):

$$\zeta = \frac{\alpha}{2\omega} + \frac{\beta\omega}{2} \tag{2.2}$$

Since there are two unknown coefficients in the formulation of the damping ratio, two known damping ratios are required, one corresponding to the first mode and the other regarding to a higher mode (m^{th} mode), to compute the Rayleigh damping coefficients. In the Chowdhury's method (Chowdhury and Dasgupta 2003) [94], three curves based on three data sets are needed to be plotted.

- On the basis of the damping ratios for the first mode and the m^{th} mode and the associated angular frequencies
- On the basis of the damping ratios for the first mode and 2.5 times of the m^{th} mode and the associated frequencies
- Based on the average values of the previously calculated Rayleigh damping ratios

The Rayleigh damping coefficients corresponding to the data set which fits best with a linear interpolated curve for the first m significant modes can be selected.
The experimental modal analysis was aimed to estimate the natural frequencies, the damping ratio, and ultimately damping parameters. The following steps had to be taken:

First, the frequency-response function curves had to be determined by an experimental investigation. Next, the natural frequencies were defined in the local maxima and the damping ratios are evaluated using the half-power bandwidth method. Finally, the Rayleigh damping coefficients could be calculated based on the Chowdhury's approach; however, because the significant modes were difficult to determine, more than three curves were plotted to find the curve best suited to experimentally collected data.

2.2.5 The frequency response function (FRF) measurement

Modal analysis was performed on a membrane prototype, where the boundary conditions, geometrical dimensions and material properties corresponding to the full-scale prototype membrane were observed, whereby frequency-response function curves of the artificially excited membrane (via an impact hammer) were plotted. The membrane prototype and the experimental FRF curves are depicted based on different water levels in Figure 2.1 and Figure 2.2, respectively.

Figure 2.1: The textile flexible membrane prototype and the impact hammer

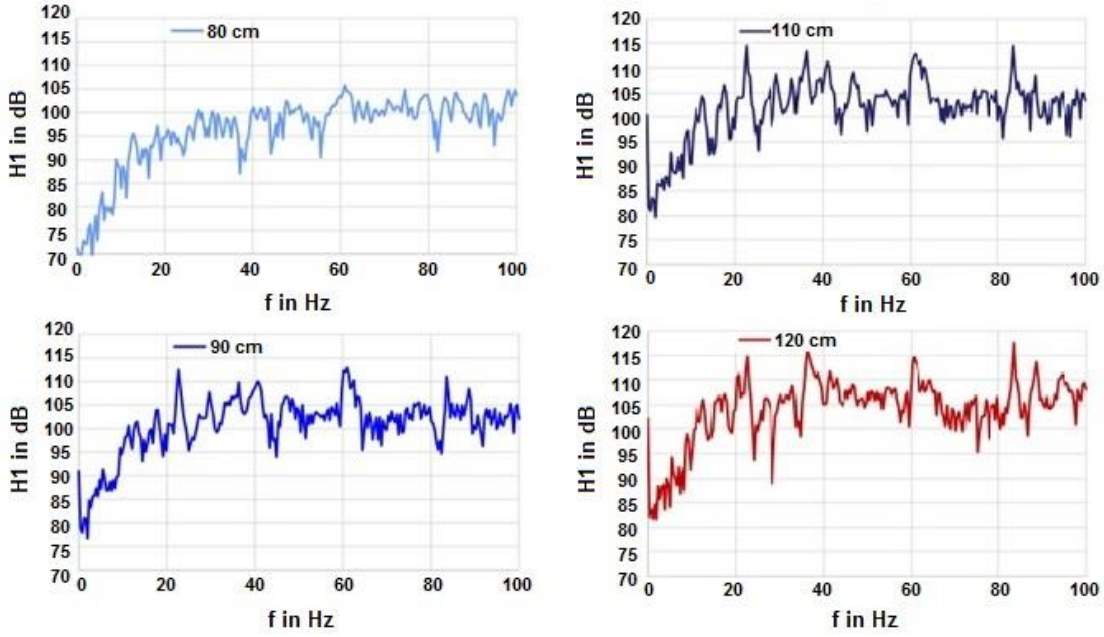

Figure 2.2: The frequency-response function curves for the membrane under hydrostatic load resulting from water levels of 80 cm, 90 cm, 110 cm, and 120 cm (H1 and f represent the amplitude in dB and the frequency in Hz, respectively).

2.2.6 The half-power bandwidth method

The half-power bandwidth method is a common procedure to evaluate the damping ratios by the frequency response data resulting from forced vibration modal analysis. In the forced vibration analysis, the excited system exhibits the maximum responses corresponding to its' natural frequencies falling steeply on either side of these natural frequencies. The bandwidth represents the width of frequency-response function curves when the amplitude is 3 dB lower than the peak value or reaches $\frac{\sqrt{2}}{2}$ times the maximum value, where energy falls into 50 % of peak energy. The damping ratio can be determined based on eq. (2.3) if the damping ratio is smaller than 0.1 or according to eq. (2.4) if the damping ratio is between 0.1 and 0.3827.

$$\zeta = \frac{f_2 - f_1}{2f_0} \tag{2.3}$$

$$\zeta = \frac{d_1}{\sqrt{1 + 4d_1^2}} \tag{2.4}$$

Here, d_1 is calculated by eq. (2.5).

$$d_1 = \frac{f_2 - f_1}{2f_0} \tag{2.5}$$

The exemplary Figure 2.3 explains how the damping ratio is estimated by the half-power bandwidth method.

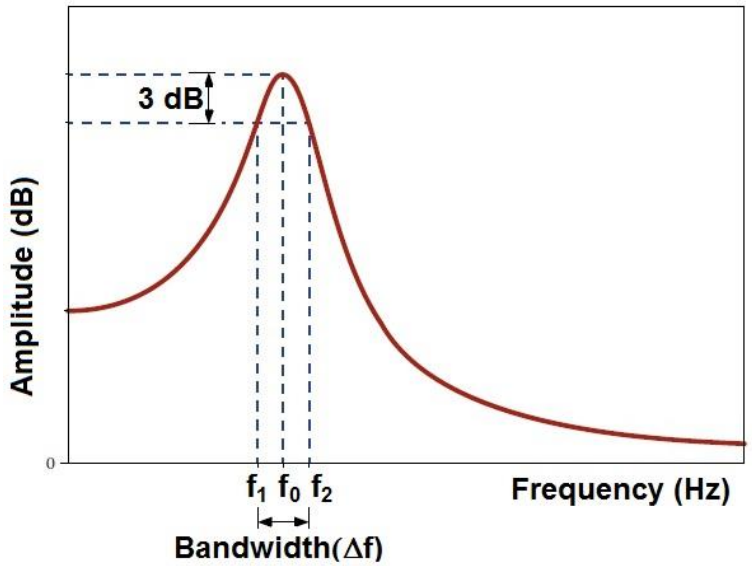

Figure 2.3: Graph to explain the half-power bandwidth method for the estimation of the damping ratio

Figure 2.4 demonstrates clearly the applied procedures to determine the Rayleigh damping coefficients, as mentioned in section 2.2.4.

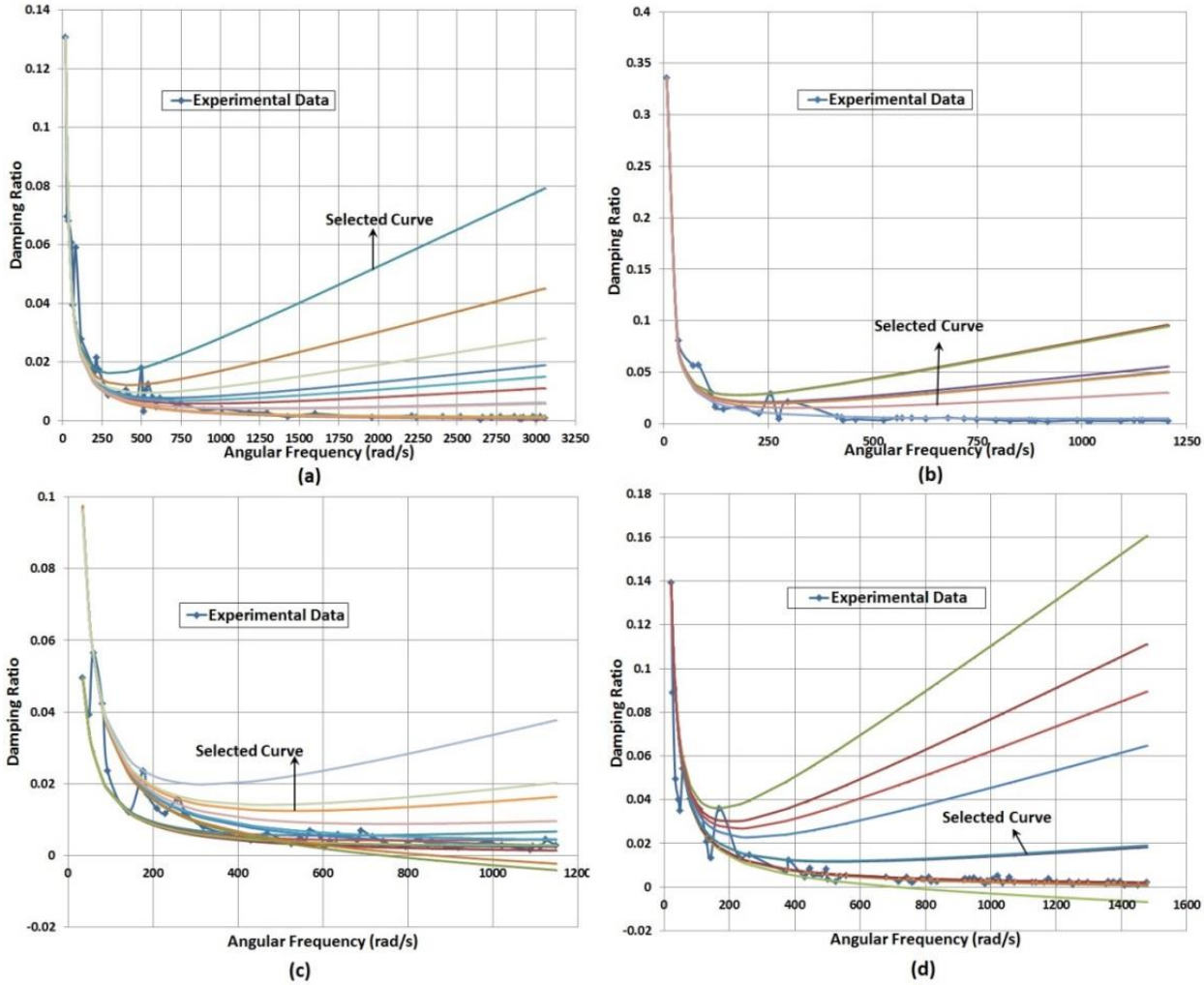

Figure 2.4: Damping ratio vs. angular frequency curves for water levels of 80 cm (a), 90 cm (b), 110 cm (c), and 120 cm (d)

The validity of the applied methods for the structure model will be later verified in chapter 3 by drawing an analogy between the numerical and experimental results for different hydrostatic pressures based on the specified water levels.

2.3 Explicit partitioned coupling

In the first co-simulation analysis, the original prototype was modeled (Figure 2.5).

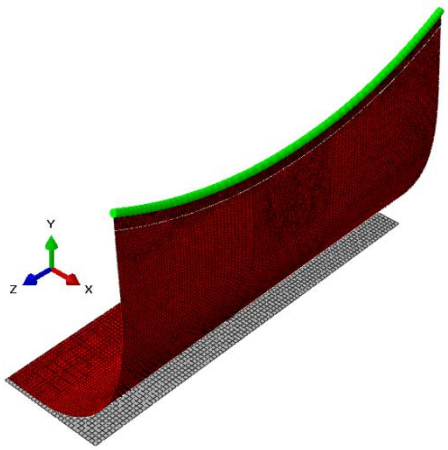

Figure 2.5: Configuration of the full-scale prototype (the membrane (red), and the steel cord (green))

The explicit coupling scheme was used to exchange data on account of the fact that the Abaqus explicit solver (suitable for nonlinear problems as mentioned in section 2.2) had been selected as a solver for the structure domain, enforcing an explicit weak way of communication across the interface as a coupling scheme. For an explicit coupling scheme, two different scenarios could appear. The data could be exchanged between the Abaqus and the Star CCM+ either by the Jacobi (explicit parallel coupling) or the Gauss-Seidel (explicit serial coupling) scheme. The latter was preferred because it is more stable than the former.

Abaqus was selected by means of the scheme modifier in the Abaqus input file and also within the Star CCM+ to lead the co-simulation with the serial coupling algorithm.

The Abaqus element library is equipped with several different types of structural elements with a wide range of spatial dimensionality. The pertinent element types are explained in detail as follows.

Membrane elements belong to the shell elements group, which can be utilized in situations where the wall thickness of the structure is not more than 1/10th of the overall dimension and the stress in the thickness direction can be ignored (based on the Abaqus recommendation (Dassault Systèmes 2013) [95]).

Membrane elements in Abaqus are named based on the following convention.

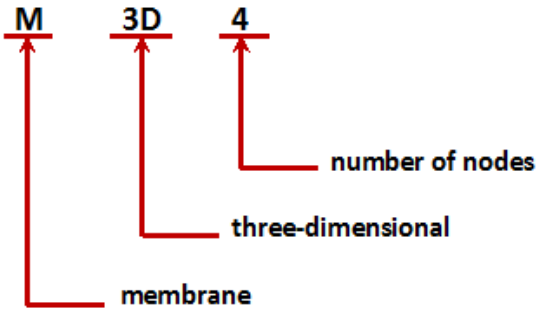

In order to model the reinforcement at the upper boundary, a stringer bonded to the selected edge was introduced, followed by the specification of its engineering properties, like a beam section, beam cross section axes, material orientation, and beam element tangent direction. The stringer was modeled with the line elements which add more simplicity to the analysis and model definition.

There are several levels of complexity in the assumed formulation for the elements available in Abaqus, where the required degree of freedom based on the application guides us to select the best assumption behind the elements. Before proceeding further, it would be appropriate to gain an overview of the elements for the modelling of the stringer.

Truss elements are one-dimensional line elements which own solely axial stiffness. The truss elements lack initial stiffness to bear loading perpendicular to their axis. As a result, numerical singularities and lack of convergence is inevitable when a stress-free line of the truss element is loaded perpendicular to the centerline. In fact, the truss elements are not appropriate for bending problems because moments or forces upright to their axis are not supported.

This requirement leads us to choose the elements which introduce rotational degrees of freedom.

In contrast, the beam elements present additional flexibility regarding transverse shear deformation between the beam's axis and its cross-section directions.
The beam element is defined as a one-dimensional line element in the three-dimensional space or in the X-Y plane, which offers stiffness with regard to deformations of the beam's axis (including axial stretch, curvature change (bending) or torsion).

Geometrical simplicity and few degrees of freedom put beam elements at advantage. The formulation for beam elements causes the member's deformation to be computed totally from the variables which are functional to position along the beam axis only and reduce the computational effort as a result.

Element types B23, B33, etc. with cubic interpolation scheme use the classical Euler-Bernoulli assumption which is the simplest approach to beam theory. This approach assumed that plane cross-sections (initially normal to the beam's axis) stay plane, normal to the beam axis, and undistorted during the analysis.

The beam elements with linear and quadratic interpolation (B21, B22, B31, B32, PIPE21, PIPE22, PIPE31, PIPE32, etc.) are based on such a formulation, but with added allowance for transverse shear strain. These elements are formulated according to the Timoshenko beam theory, where the cross-section may not necessarily maintain to be normal to the beam axis. These elements are the most effective beam elements in the Abaqus on account of the fact that they work well to model both thick beams with a possibly important shear flexibility and thin beams. The transverse shear behavior of Timoshenko beams is supposed to be linear elastic with a fixed modulus no matter how the beam section responses to axial stretch and bending.

For Timoshenko beams made of uniform material, useful results can be achieved for cross-sectional dimensions up to 1/8 of typical axial distances or the wavelength of the highest natural mode that plays a significant role for the response. Beyond this ratio, the simplicity is no longer valid and the approximation of the member's behavior only based on axial position does not lead to sufficiently precise results.

Beam elements in Abaqus are named conventionally as follows.

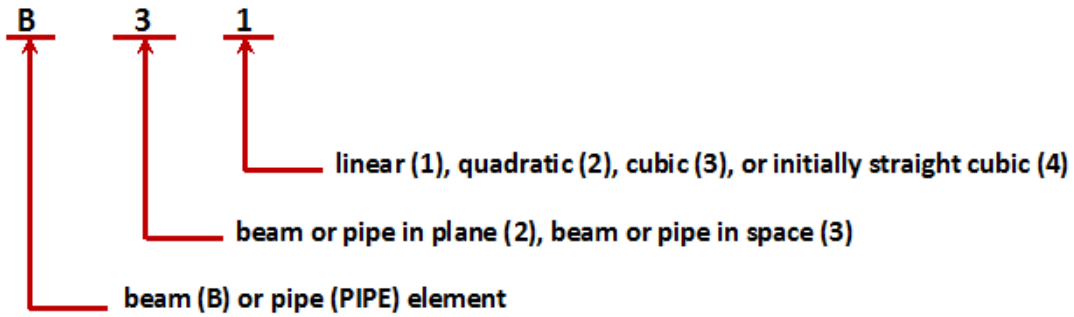

The linear Timoshenko beam elements like B31 applies a lumped mass formulation, while a consistent mass formulation is used for quadratic Timoshenko beam elements such as B32 imposes in the Abaqus standard. Nevertheless, a lumped mass formulation with a 1/6, 2/3, 1/6 distribution is imposed for quadratic Timoshenko beam elements in the Abaqus explicit and in the Abaqus standard dealing with dynamic procedures.

All masses in the finite element method have to be attributed to the nodes of the elements. In order to convert the continuously distributed mass of the elements to an equivalent set of masses at the nodes, there are two methods: the consistent and the lumped mass approximations.

The lumped mass method in which the distributed mass is lumped to the nodal masses in such a manner that the sum of these nodal masses equals the total mass of the structure includes usually only translational inertias directly at the nodes.

However, in the consistent mass approach, the distributed mass is so lumped to the nodal masses that both translational and rotational inertias are represented, where the same integrations computing the element stiffness matrix are implemented to distribute the mass.

After taking an overview of available elements within the Abaqus, the membrane elements and linear beam elements were selected to discretize the flexible membrane and the steel stringer, respectively. Not only do these elements enjoy simplicity, but also they are able to capture details of the physical model.

Coming back to the target problem, an important issue, however, arose due to beam elements on the upper boundary when conducting the co-simulation (either by explicit coupling or implicit coupling). Beam elements in the structure domain are not allowed to be wetted by the fluid domain due to an incompatibility between the discretizations for the beam elements and the fluid. To overcome this limitation, a small part of the structure nearby the steel cord including beam elements of B31 on the top boundary of the structure was selected as a further part, and not included as a surface interface. In other words, the interface was reduced to the original membrane (without the steel cord) tied with the further small part (new defined as a separate part in the structural model including the steel cord).
As a result, the incompatibility of the beam elements with the discretized fluid domain was resolved when the beam elements were excluded from the defined interface. The problem and solution will be discussed in chapter 4 as well.

Moreover, only one side of the membrane which was located inside of the channel was modeled as a wall boundary and coupled with its counterpart in scope of the Abaqus. In other words, the membrane underwent the loads merely from the free surface flow within the channel since the influence of the air environment on the membrane was assumed to be negligible.

A common approach to prevent the co-simulation from destabilization is to initialize the co-simulation with the solution achieved by the freeze of the co-simulation and the mesh morpher solvers, which renders the flexible structure as a rigid one.

In the co-simulation, there are some other possibilities such as grid flux under-relaxation, pressure ramping parameters, traction clipping parameters, and traction

field multiplier to adjust, ramp or limit loading conditions in order to increase robustness of the co-simulation.

To suppress destabilization, a one way co-simulation was applied by means of traction clipping parameters, where only geometric data (displacement) from the Abaqus were passed to the Star CCM+, while no load data from the Star CCM+ was transferred to the Abaqus. In fact, the loads imposed on the membrane including the weight of the membrane in addition to the hydrostatic pressure were specified within the Abaqus input file through the user defined field functions decoupled from the fluid domain. Afterwards, a two way co-simulation was released, where the computed traction via the Star CCM+ (instead of applying the pressure load through a field function) was imported and mapped to the interface within the Abaqus.
Remeshing at the realm of the Star CCM+ domain was besides executed as soon as either the cell quality or skew angle was beyond the allowable limit. The remeshing process was comprised of the extraction of the volume domain boundaries, the previous surface representations removal, and an introduction of the extracted boundaries as the new input.

Conducted co-simulations experienced numerical instabilities owing to high inertia of the added mass stemming from the fluid medium, high flexibility level in the structure. As a result, the default setting had to be adjusted with the hope for the realization of a stable and convergent solution.

Notwithstanding all efforts, the results regarding the interaction of the structure with the fluid domain have exhibited numerical instabilities ensuing from high inertia of added mass, the high compliant membrane still persisted and a fully convergent solution was never accomplished.

In fluid mechanics, added mass or virtual mass is attributed to the inertia added to a FSI system due to asynchronous motion of the surrounding fluid with regard to the structure. Nevertheless, from the numerical viewpoint, the added mass effect represents an extra mass exerting on the formulation of the structure, which stems from the interaction between the fluid and the structure. Consequently, it alters the natural frequencies of the structure, setting off the numerical instabilities in the simulation. The added mass effect within the fluid region gives rise to dilatation waves which propagate through the flexible structure. The propagation of the dilatation waves triggers an abrupt distortion in the structural domain, which will be exacerbated when the simulation forwards in time.

Implementation of the viscous pressure damping in some numerical FSI problems have been published, which was targeted at the suppression of the instabilities due

to the added mass side effect. Azaouzi et al.'s (2012) [96], Baek and Karniadakis's (2012) [97], and Liaghat et al.'s work (2014) [98] are examples of the application of the viscous pressure damping to dissipate disturbances.

The viscous pressure damping is integrated in the structural domain to exert a resistance against the motion of the structure, resulting in the energy dissipation. Contrary to the Rayleigh damping which dissipates the oscillation in the interior of the body, the viscous pressure damping imposes a load on the surface of the structure. The load renders the pressure waves crossing the free surface to be absorbed. To what extent the energy can be worn down is dependent on many characteristic parameters in the fluid and structure domain.

This method can be successful if the instabilities dissipate before the added mass effect leads to a failure due to enormous displacement in the structure domain.

However, how far the energy should be dissipated in such a way that the energy delivered to the fluid never returns back to the structure, while no important dynamic effects will be ignored, is a matter of concern.

2.4 Implicit partitioned coupling

Hence, further investigations were needed to be performed with a change in the viscous damping parameter to achieve a convergent and robust model. The other alternative was to switch to the other coupling algorithm, namely an implicit coupling scheme, which results in more realistic deformation and stresses in the membrane. As a further approach, the former was abandoned in favor of the precision, albeit with more computational cost.

Causin et al. (2005) [99] justified instabilities under the choice of an explicit coupling scheme if the fluid and the structure are comparable in terms of density or if dealing with a slender shape structure. Contrary to the explicit coupling scheme, the strongly coupled implicit algorithm fulfills convergence criteria under the same circumstance. They also provided a mathematical explanation why the partitioned time marching algorithms implementing a loosely coupled (explicit) algorithm can cope with computational modeling of FSI problems within the scope of aeroelasticity.

However, using the implicit coupling scheme dictated some changes in the structure domain.

For instance, the implicit coupling scheme would not present compatibility with the Abaqus explicit solver. Instead, the Abaqus implicit solver could be selected to compute the deformation of the structure.

Moreover, within the Star CCM+, the flexible membrane was modeled as zero thickness baffle interface, necessitating the air environment model on the other side of the membrane. This model resembled more closely the surrounding environment around the membrane than one introduced before. In detail, it included the immiscible water-air flow inside the channel on one side, while the effect of the surrounding air environment on the other side was also taken into account.

2.5 Overset mesh

The problem regarding moving grids with large motion results in such a mesh distortion that a single mesh of a specified topology can no more be applicable. To overcome the issue, overlapping techniques (known as Chimera or overset grid techniques) can be implemented. The underlying algorithm for the overlapping techniques is based on hole-cutting and donor searching. The principle of the overlapping techniques is to split the fluid domain into the sub-domains which are discretized by different meshes. The sub-domains have to be meshed in such ways that overlap each other sufficiently to couple the solutions between the regions.
The major drawback of this approach is the difficulty in ensuring the conservation of the computed variables/quantities across the grid interfaces.

The meshes related to moving bodies (overset regions' grid) move with the bodies whereas the rest of the mesh (covering the background region) stays fixed.
The grids around the moving bodies have not to be adjusted unless the bodies deform. The interpolation for flow variables between the overlapped grids happens to exchange the information. In order to reduce interpolation errors, the overset interfaces can be selected in the areas far from moving bodies where a change in the flow characteristics is smoother.

In an overlapping grid, cells are divided into active, inactive and acceptor cells. The status of the cells changes dependent on new positions for moving bodies. The inactive cells become excluded from the solution domain, whereas the governing equations for the flow have to be solved for the active cells. The acceptor cells, connected to the overset boundary of the overset region, segregate active and inactive cells within the background region. They are responsible for the exchange of data between two overlapping grids, where the values at the donor cells region are interpolated. In fact, the donor cells are the active cells in the counterpart region in an immediate vicinity of the acceptor cells, providing variable values for the acceptor cells.

There are some algorithms to search host cells for a given point such as the bruteforce algorithm which is a simple but expensive technique. Within an exhaustive

search, all possibilities are taken into account and checked until the right solution is found.
The neighbor-to-neighbor searching algorithm (Löhner 1995) [100] and the Shimarat's algorithms (Milgram 1989) [101] are further available search algorithms.

During the hole-cutting process, all cells excluded from the computational domain are identified, which determines the status of involving cells as active or inactive as a result.

The grid hierarchy affects the hole-cutting process, where the grids on a higher level region are prior to the grids belonging to the other overlapping region pair.
In detail, the cells associated with lower priority have to be inactive in the overlapping zone, while the cells with higher level of priority are active. The lowest level of priority belongs always to the background region.
The maximum allowable movement during a time step depends on the time integration scheme. It is not permitted to be bigger than the smallest cell in the overlapping zone for the first order Euler scheme. It would be halved if a second order implicit time integration scheme is utilized.

The inaccuracies arising from a duplicate integral computation in the overlapping areas for volumes, surfaces and boundaries are issues regarding the overset approach. The second and third ones happen if the boundaries of two overlapping grids cover each other.

Another issue with regard to the overset mesh techniques is rooted at the fact that the mass conservation is not strictly ensured. As a result, an extra treatment is required to be applied to the pressure correction equation. If incompressible flows are enclosed by walls, an additional source term has to be introduced to the pressure correction equation to make residuals converged and reasonable results could be achieved as a consequence.
The mass conservation is enforced at the overset interface by a flux correction at the interface in such a manner that their sum reaches zero. The flux correction is needed for compressible and incompressible, non-closed flow cases such as the simulation of rotating gear pumps or moving cars.

According to the recommendation of Siemens AG (2019) [88], the minimum number of 4-5 cells within the overlapping zone guaranties a successful exchange of data between the overset and the background meshes.

There are some interpolation options to approximate the variable value at the acceptor cells known as distance-weighted interpolation, linear interpolation, and least squares interpolation.

Distance-weighted interpolation uses the interpolation factor which is in inverse proportion with the distance from the acceptor to the donor cell center.

Linear interpolation (activated by default) is more accurate, but at the expense of more computational time. This method applies the shape functions which stretch over a triangle (in 2-D) or a tetrahedron (in 3-D) based on centroids of donor cells.

Least squares interpolation introduces the interpolation functions into the coefficient matrix of the governing equation, which enables an implicit coupling of the overset meshes.

Overlapping techniques can be applied to model two different scenarios either with or without background region. The dynamic overset behavior of wall boundaries can be enabled after the implementation of the overset interfaces. This option would be useful for cases with/without background region when an automatic switch from a wall boundary type to an overset boundary type (or vice versa) is necessary.

If the moving body approaches a physical boundary of the background region very closely, the overlapping areas within the overset mesh can extend over the boundary. The cells in the overset region with a vertex outside the boundary would be deactivated unless the option of the close vicinity is enabled. In this case, each cell will be considered active if the cell centroid is located inside the background region.

As an alternative to the overset interface, the overset mesh zero gap can be implemented to promote the simulations with the above mentioned scenario. The gap between wall boundaries of the overset region and the background region is measured always during the assembly process. If the number of cells within the gap is detected to be less than the specified criteria, the cells become inactive. The criteria for the cells placed within the zero gap can not be set to less than two layers.

2.6 Concluding remarks

In this chapter, the partitioned approaches applied for the current work were discussed. In this regard, two different partitioned methods including a single FV framework, and coupled FV-FE methods were explained.

Nevertheless, each of FV and FE frameworks can be solved by explicit or time integration procedures. Throughout the current work, an implicit time integration procedure

was applied to solve the FV framework of the fluid domain whereas both FE explicit and implicit approaches were implemented within the structural domain.

The FE dynamic explicit scheme is a better choice for inherently highly nonlinear phenomenon. That is why this approach was firstly selected to provide a solution for structural domain (refer to chapter 3).

Furthermore, the FV and FE frameworks can be coupled with two different coupling schemes, either explicit or implicit. Nonetheless, the numerical simulation of the FSI problems connected by a loosely coupled (explicit) algorithm suffers from convergency issues when the target problem deals with a high degree of flexibility for the structure or comparable heavy fluids. As a result, the initial explicit coupling scheme was exchanged with the strong coupling (implicit) algorithm which will be explained in chapters 4 and 6.

However, the implementation of the implicit coupling scheme imposed some changes on the structural domain. For example, the dynamic explicit solver which is a better alternative relative to the dynamic implicit solver for nonlinear problems had to be replaced with its implicit counterpart on account of the incompatibility between a dynamic explicit solver (for structure) and an implicit coupling scheme.

Further topics for discussion were options like turbulence models which will be added to the physics of the fluid domain in all FV numerical simulations conducted in this work.
On the other side, the damping models which will be incorporated into the physics of the structure in order to dissipate any oscillations in the structure were described.
The further subjects dealt with are the discretization models, cells, and elements like the overset mesh, the prism layer mesh, the membrane elements, the beam elements which will be implemented in the next chapters.

In the next chapter, the behavior of the down-scale membrane loaded by a water pressure will be analyzed by a dynamic explicit solver, where the damping models, and the discretization elements explained in this chapter will be put in practice.

3 Verification and validation of the structural model

Due to the lack of a quantitative research on the full-scale model, the numerical analysis was carried out on a down-scale model in order to assess accuracy and reliability of the applied measures.
This chapter discusses the down-scale membrane loaded by water pressure, where its numerical model setup and the implemented solver are thoroughly described. Moreover, the achieved numerical results will be compared against the observed experimental data.

3.1 Numerical model setup of the down-scale membrane

The membrane was made of flexible PE with Young's modulus, density, Poisson's ratio and thickness of 258 MPa, 865.51 kg/m^3, 0.48 and 0.06381 mm, respectively.
In addition, a so-called steel cord was attached to the upper edge of the flexible PE membrane. The steel cord was designed as a steel circular stringer with a diameter of 0.6 mm, a Young's modulus of 2100 GPa, a density of 7850 kg/m^3, and a Poisson's ratio of 0.3. The mass proportional and stiffness proportional damping coefficients for Rayleigh damping were guessed based on the results of the experimental modal analysis and set to 4.0 and 0, respectively.

The configuration and the dimensions of the undeformed down-scale membrane (before loading) are presented in Figure 3.1 and Figure 3.2.

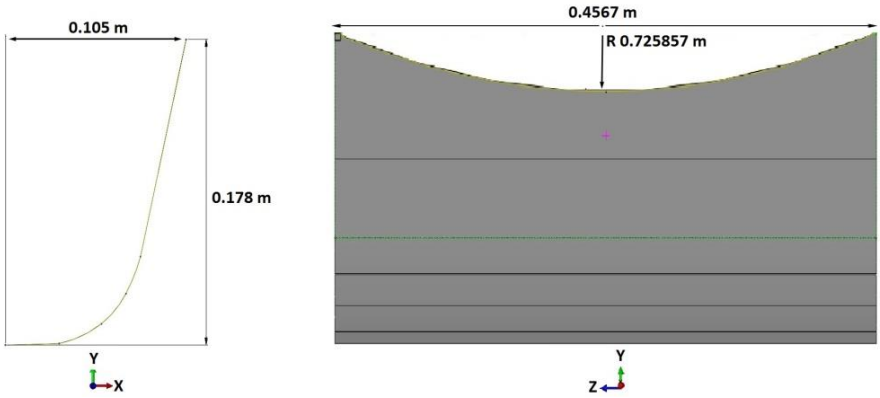

Figure 3.1: Dimensions of the initial configuration of the membrane (the cross section (left) and longitudinal view (right))

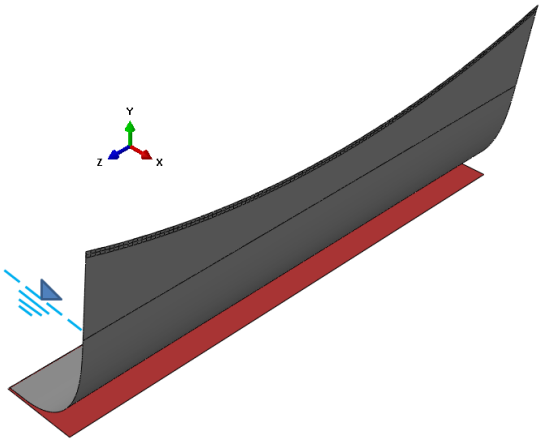

Figure 3.2: Three-dimensional configuration of the down-scale membrane

The discretization of the membrane was performed by membrane type of elements, either M3D4 (a three-dimensional, 4-node membrane element) or M3D3 (a three-dimensional, 3-node membrane element), exhibiting just membrane stiffness without additional bending stiffness. On the other hand, the steel cord was discretized under assumption of one-dimensional beam theory by linear interpolated Timoshenko beam elements of B31 because the dimensions in the cross-section of the beam were supposed small compared with the typical dimension along the beam axis. Moreover, three-dimensional rigid elements of R3D4 with 4 nodes were used to discretize the bottom of the channel.

The contact between the membrane and the bottom of the channel was simulated through the interaction module (surface-to-surface contact model) in the Abaqus with a friction coefficient of 0.1. A penalty contact method was dedicated to the mechanical constraint formulation, with the applied finite sliding.

The applied loads on the membrane were introduced as the hydrostatic pressure caused by specified water level by means of user defined field functions in addition to the weight of the flexible membrane and the steel cord.

Because no co-simulation analysis was conducted in the current analysis, the Abaqus explicit triggers no problem with the coupling (no coupling was demanded).

To deal with nonlinearity in the model (as mentioned in section 2.2), the Abaqus explicit executed the structural model, which used the central-difference operator. As a result, the size of the time increment in the analysis is automatically defined by the Abaqus so that a stabilized simulation can be achieved.

In order to access the suitability of both the underlying applied algorithms and the discretization models, the numerical results will be compared against experimental

results with respect to different water levels when the membrane undergoes the hydrostatic pressure.

However, before drawing comparisons between results, the next section offers an overview of available statistical techniques to compare data samples or curves (here numerical and experimental data samples).

3.2 Comparing similarity between numerical and experimental results

There are some statistical functions such as mean, median, standard deviation which are used to describe data samples. However, they are not suitable to compare two data samples in terms of distribution, similarity to provide meaningful descriptions for the data. In this section, some kinds of techniques used commonly to draw an analogy between two data samples will be explained.

3.2.1 Hypothesis test terminology

To get started, some statistical terms which are used to make assumptions requires to be define.

The null hypothesis is the original assertion which will be examined, where there are also other possibilities for the alternative hypothesis.

The significance level depends on the degree of certainty which is needed to reject the null hypothesis, which is set to 5 % as a default.

The p-value is the probability of observing the given sample result provided that the null hypothesis is true. In other words, the null hypothesis will be rejected unless the probability of observing the null hypothesis (p-value) is greater than the significance level.

There are some different measures belonging to the hypothesis test categories, where they varied in terms of underlying assumptions and application areas. Two different measures which are available in Matlab will be discussed as follows:

Two-sample t-test

The two-sample t-test conducts a t-test to examine if two samples of X and Y with normal distributions share the same mean when the standard deviations in each samples are unknown but supposed identical. T-test is a hypothesis testing to compare the mean values of two samples. The result demonstrates whether the null hypothesis that the means are equal can be rejected at the 0.05 significance level.

Two-sample Kolmogorov-Smirnov test

The two-sample Kolmogorov-Smirnov test compares the distributions of values in two data sets represented by vectors x_1 and x_2, respectively. Moreover, the data sets can have different lengths of n_1 and n_2 respectively while they are not restricted to be normally distributed. The following syntax in Matlab can be applied in order to verify the distributions of two samples.

$$[h, p, k] = ktest2(x_1, x_2)$$

The null hypothesis for this test is that both x_1 and x_2 own the same continuous distributions. The alternative hypothesis is that they are distributed in different ways.
The null hypothesis can be rejected provided that the test is significant at the (100*alpha) % level, where the default value for the alpha is 0.05. In detail, the resulted h equal to 1 rejects the null hypothesis indicating the same distributions for both datasets.

The p-value represents the probability that the null hypothesis is true.
For instance, if the value of the p-value is 0.90, a 90 % probability for the identical distribution of two datasets is ensured. For large sample sizes, p-value has proved to be very accurate. Nonetheless, it is reasonably precise for sample sizes n_1 and n_2 provided that $(n_1 n_2)/(n_1 + n_2)$ is bigger or equal to 4.
The Kolmogorov-Smirnov statistic (k) is the maximum difference between cumulative distribution functions for x_1 and x_2 datasets, which can be written mathematically as follows:

$$max(|F1(x) - F2(x)|)$$

For each potential value of x, the Kolmogorov-Smirnov test compares the $F1(x)$ against $F2(x)$, where $F1(x)$ and $F2(x)$ represent the proportions of x_1 and x_2 values respectively which are less than or equal to x.

In the next step to compare similarity between curves, the curve fitting tool in Matlab will be employed to describe data points based on a mathematical model function in the best possible way.

3.2.2 Curve fitting

A linear model is the simplest case, where the coefficients of k and d for the first degree polynomial are determined according to the least squares method, as eq. (3.1).

$$f(x, k, d) = kx + d \tag{3.1}$$

The least squares method is a standard approach in the regression analysis to determine the best fit for a data set. The method works on the principle that the sum of the offsets or residuals of data points from the selected curve have to be minimized.
A key step in the curve fitting is to select the proper model function. In some cases, underlying physical models like vibration, damping, and theoretical formulation provide a good guidance for the selection of the mathematical function.

The curve fitting toolbox offers a wide range of functions such as linear or nonlinear regression, interpolation, smoothing, and custom equations to fit curves and surfaces to data. It is equipped with a flexible interface, where curves and surfaces can be interactively adjusted to the data set.

Furthermore, after choosing the function from the available library, a curve based on the data and the selected function form will be plotted and statistical information like confidence intervals and residuals can be viewed. After comparing multiple curve fits, a code can be generated according to the curve fitting and used in the workspace for further post processing.

3.2.3 Similarity measures between two curves

In order to quantify the difference or similarity between two curves or datasets, there are some widely used methods which are presented as follows:

The Frechet distance method

The Frechet distance is a well-known measure of similarity between two curves. The Frechet distance is determined as the minimum cord-length connecting a point traveling forwards along one curve and one proceeding forwards along another curve, where the traveling speed for either point does not have to be necessarily uniform.
The Frechet distance is generally explained by walking a man and his dog on a leash Figure 3.3. The man walks on one curve whereas the dog walks on the other. The dog and the man are allowed to vary their speeds, or even stop, while backtracking is not permitted. The Frechet distance is the minimum leash length needed to traverse both curves.

Figure 3.3: Two curves, and a man walking his dog on a leash (Alt and Godau 1995)[102]

The discrete Frechet distance method

There is another alternative to the Frechet distance method to approximate the exact Frechet distance value, which is named the discrete Frechet distance method. The discrete Frechet distance between two curves is calculated by ordered discrete points, where two sets of connected points represent two directed polygonal lines.

Dynamic Time Warping

Dynamic Time Warping is a popular method to compare the similarity between two arrays or time series with different lengths. The similarity or dissimilarity of two-time series is computed by a non-linear (elastic) alignment which permits similar features to be matched even if they are out of phase.
The dynamic time warping measure, verifying similarity between two sequences which may vary in time or rate, works through the following steps:

- Division of two series into equal points
- Computation of the Euclidean distance between the first point in the first series and every point in the second series and storage of the minimum distance (time warp stage)
- Repetition of the second step for all points along the series
- Repetition of the second and third steps but with reference points along the second series
- Summation of all the minimum distances stored

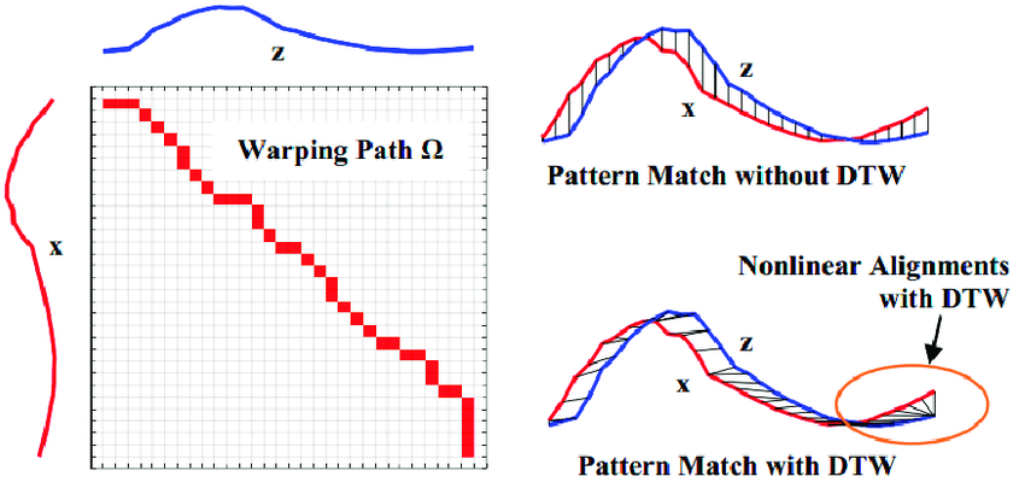

Figure 3.4: Dynamic time warping (Yang et al. 2019) [103]

DTW, which has been implemented in Matlab, aligns two sequences in an optimal sense under certain constraints. The algorithm returns the warping path in such a manner that the sum of the Euclidean distances between corresponding points will be minimized (Figure 3.4).

Partial curve mapping

The partial curve mapping (PCM) method defines the similarity between curves with the help of arc length together with area. Figure 3.5 shows the implementation of PCM method, where arc-length of the experimental curve is longer than the numerical curve. After imposing the arc-length of the shorter curve on a section on the longer curve, trapezoids will be built between the curves and the areas of the trapezoids are added up. Impose of the short arc length on the curve with the longer arc length will be iterated with various offsets. The minimum computed area for all iterations returns the PCM value.

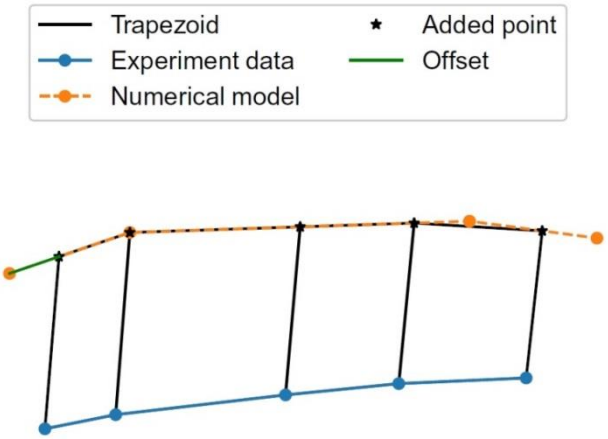

Figure 3.5: PCM method and trapezoids constructed between two curves for an arbitrary offset (green) (Jekel et al. 2019) [104]

Curve length

In the curve length method, every point on one curve is compared against the location of its corresponding curve length on the other curve.
Figure 3.6 demonstrates the procedure which must be taken in the curve length method. The numerical curve is discretized at the equivalent curve lengths of the corresponding data points on the experimental curve. The residual values are squared as a function of both the dependent and independent variables. The sum of the squared residuals is an indicator of the difference between an experimental and a numerical curve.

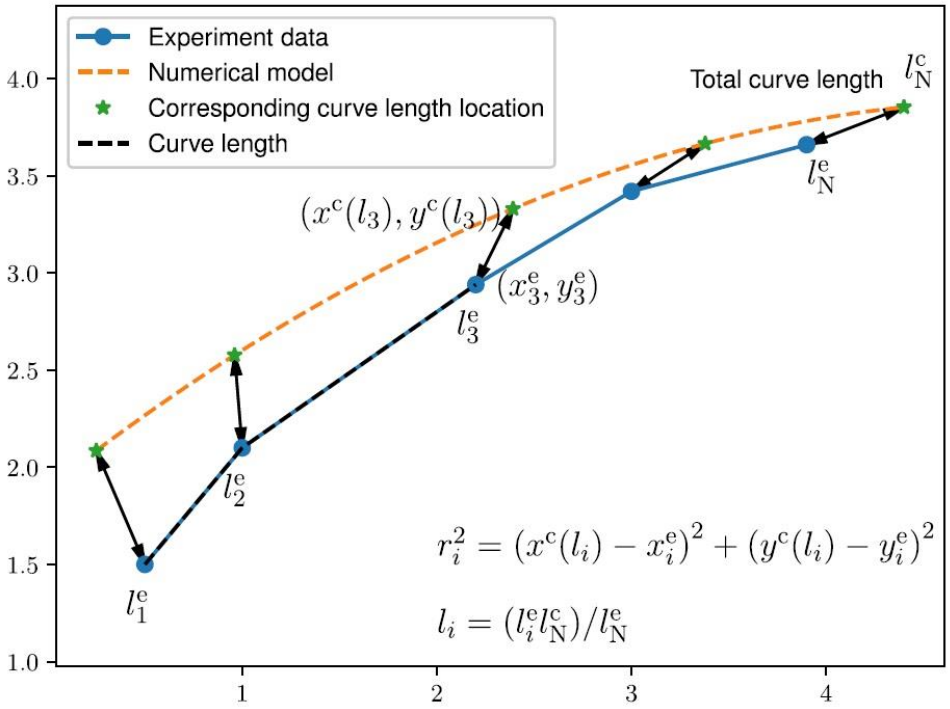

Figure 3.6: curve length method (Jekel et al. 2019) [104]

Area between two curves

In this method, quadrilaterals are constructed between two curves which are discretized based on the relevant data points. The area between curves results from the sum of the quadrilateral areas.

The equality in the number of data points for two curves is a requirement for the application of this method. If two curves own different data points, data points are added to the curve with fewer data points until both curves share the same number of data points.
Figure 3.7 exhibits the construction of quadrilaterals between experimental and numerical data sets.

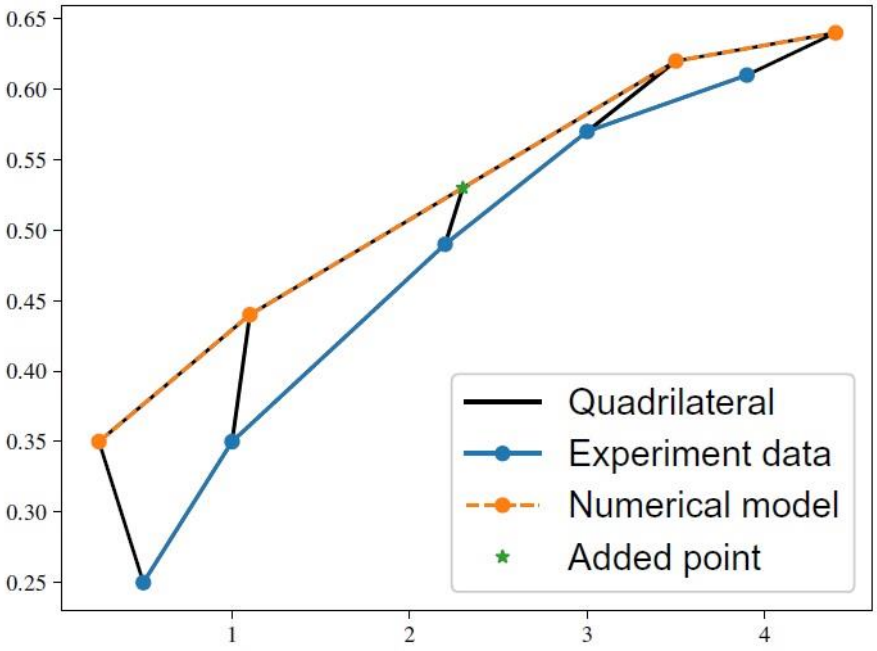

Figure 3.7: Area between two curves (Jekel et al. 2019) [104]

Weighing up the advantages and limitations of each model, while the two-sample Kolmogorov-Smirnov test has been preferred to compare the distributions of values within each pair of the numerical and experimental results, the Frechet distance, discrete Frechet distance, and dynamic time warping will be used to define the similarity between each pair of experimental and numerical curves.

3.3 Results (down-scale membrane)

Figure 3.9 compare the numerical and experimental results of selected distinguishing quantities with respect to different water levels when the membrane undergoes the hydrostatic pressure. The experimental results for the Y-displacements are based on the work published by Schade et al. (2016) [105].

Within the experimental analyses, the uncertainties for the contact length and the slope are ±0.25 mm and ±0.5 degree respectively. Whereas the contact length and the slope are measured on the middle line of the membrane, the measurement for the Y-displacements is performed on a point on the middle line of the membrane as Figure 3.8.

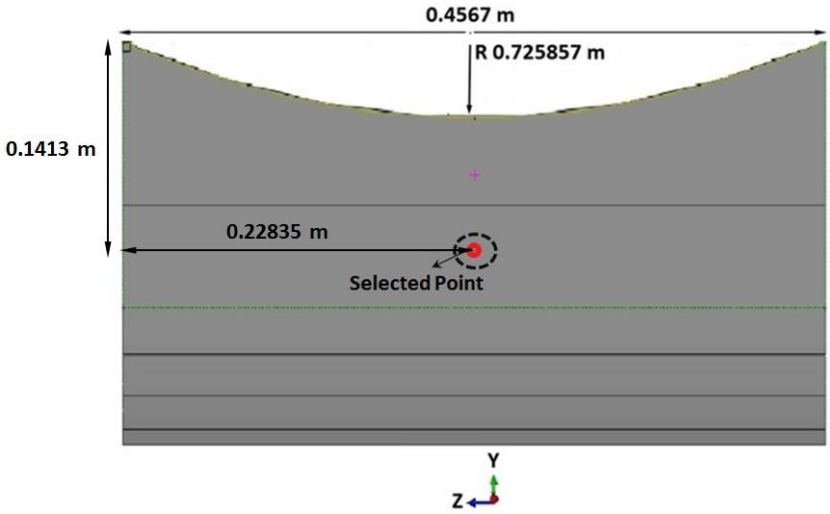

Figure 3.8: The point on the membrane selected for the Y-displacement measurement

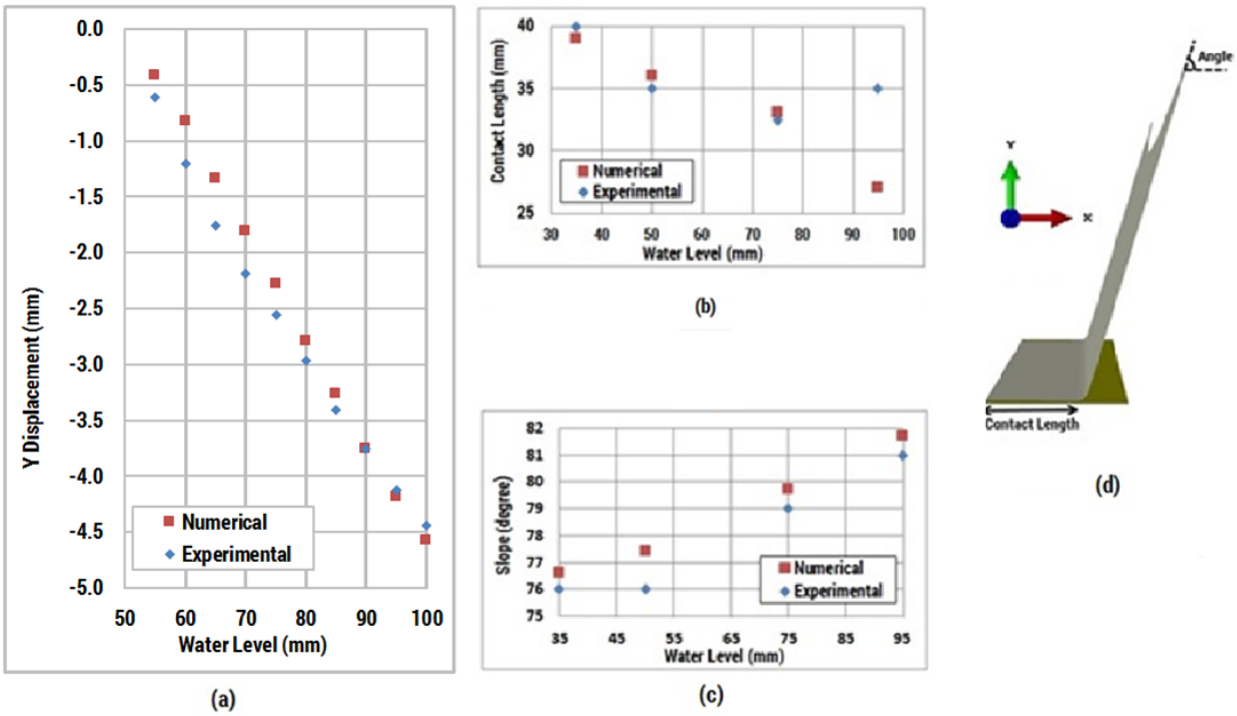

Figure 3.9: Comparison between the numerical and experimental results of displacement in Y direction (a), the contact length (b) and the slope of membrane (c) in accordance with water level and an illustration of the contact length (between the membrane and the bottom of the channel) and the slope of the membrane (d)

In both numerical and experimental methods, there is an increase in the absolute value of the Y directional displacement and the slope of the membrane proportional to a rise in the water level, whereas the contact length decreases at the same time.

The last data point for the contact length violates the above conclusion drawn from the trend dominant for the numerical and experimental results. This data point will

be excluded from the data points which are used to perform similarity test for the contact length.

It is clear that the numerical model represents the physical model well, not only qualitatively but also quantitatively; however, slight differences can be attributed to a minor discrepancy in the parameter setup and some errors associated with both the experimental measurement and the applied numerical solvers.

Here, the user defined field functions represent the hydrostatic pressure on the model, which is dependent on the initial undeformed geometry of the membrane. The user defined field functions, i.e. hydrostatic pressure, cannot be updated, while the membrane deforms. Later, the hydrostatic pressure has been imposed by the subroutine of DLOAD, which are kept up-to-date during an Abaqus standard standalone analysis.

In the next chapters, all standalone Abaqus simulations were conducted with the help of the subroutine of DLOAD which was responsible to update the hydrostatic pressure imposed on the structure. The reason why the subroutine of DLOAD was not applied within the co-simulation input files (in a preload step) is incompatibility between the Abaqus input file and the subroutine of DLOAD.

In order to compare the distributions of values within each pair of the numerical and experimental results, two-sample Kolmogorov-Smirnov test has been performed. However, only the comparison for the Y directional displacement are presented on account of the fact that the number of data points for the other samples (the contact length and the slope) do not satisfy the criteria provided in section 3.2.1.

Next, the data points for each sample are formulated on the basis of a mathematical model function in the best possible way by the curve fitting tool in Matlab.

Moreover, the Frechet distance, the discrete Frechet distance, and the dynamic time warping are used to measure the similarity between each pair of experimental and numerical curves. While the Frechet distance is computed by the function of the Frechet distance calculator developed by Ursell (2020) [106], the function of discrete Frechet distance proposed by Danziger (2020) [107] is responsible for the calculation of the discrete Frechet distance. In the following sections, the comparisons made for the contact length, the slope, and the Y directional displacement will be presented.

3.3.1 Similarity tests for the contact length

Before proceeding with the similarity tests, the mathematical formulations for the datasets have to be found.

In this regard, the fitting curve is depicted in Figure 3.10 based on a linear function as eq. (3.2) for the numerically computed contact lengths:

$$f(h) = p_1 h + p_2 \tag{3.2}$$

Where the coefficients (with 95 % confidence bounds) are as follows:
$p_1 = -0.174\ (-0.2425, -0.1056)$
$p_2 = 45.35\ (40.71, 49.98)$
h: water level (mm)
f: the contact length (mm)

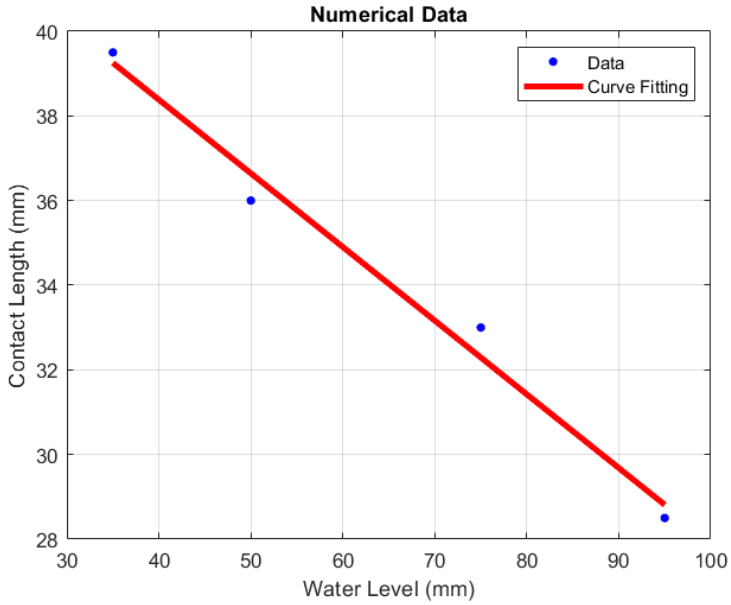

Figure 3.10: The raw data for the numerical result of the contact length (blue) and the fitting curve (red)

Likewise, a linear function as eq. (3.2) introduces a mathematical formulation for the experimental contact length, exhibited by Figure 3.11.
Where the coefficients (with 95 % confidence bounds) are as follows:
$p_1 = -0.1797\ (-1.001, 0.6419)$
$p_2 = 45.48\ (-0.3894, 91.35)$
h: water level (mm)
f: the contact length (mm)

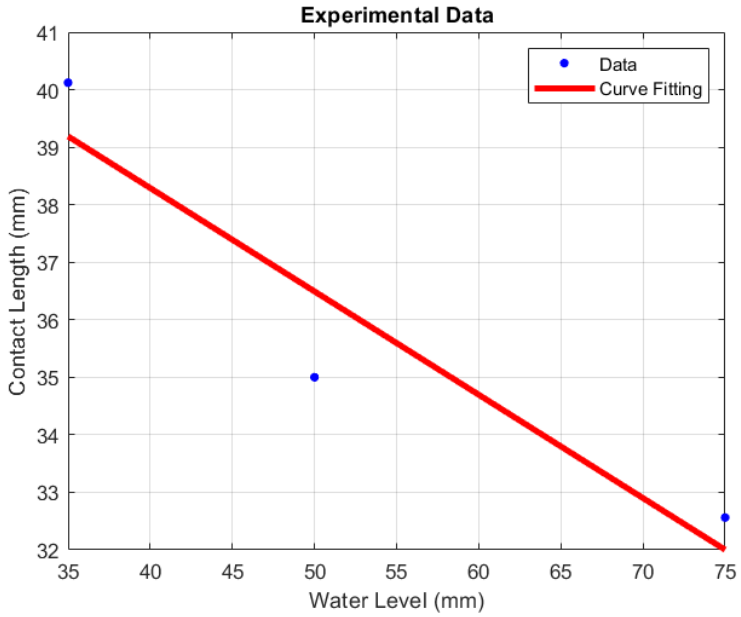

Figure 3.11: The raw data for the experimental result of the contact length (blue) and the fitting curve (red)

Whereas the numerical and experimental results for the contact length exhibits a Frechet distances of 0.3086 mm and 0.4305 mm for three and four data points, respectively, the discrete Frechet distance method depicts a higher difference of 1 mm between the results for three data points. Nevertheless, considering the range of data from 28 mm to 40 mm, a high similarity between the curves can be recognized.

In the same manner, the cumulative distance for three points of curves (Figure 3.12) is computed as 0.5059 mm by the dynamic time warping method (DTW), which reveals the similarity between curves. The cumulative distance between two curves reaches 0.9099 mm if four points of the each curve are taken into account (Figure 3.13).
Furthermore, DTW is aimed at finding a path (warping path) between two curves which minimizes the cumulative distance between points.
By warping based on the warping path, the two curves can be aligned in time (Figure 3.12 and Figure 3.13), which results in transformations of the original data points to warped data points.

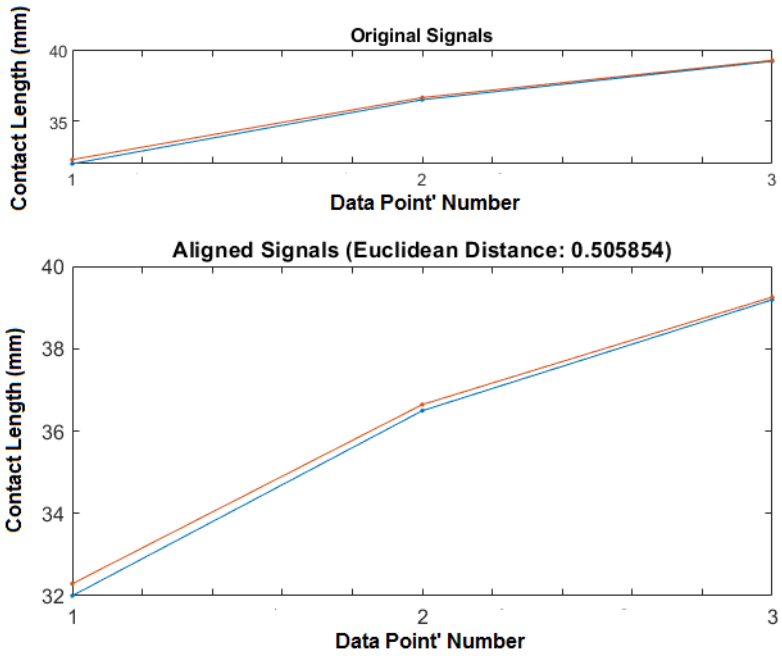

Figure 3.12: Two original sets of three data points (up) and the warped sets of the data points (down) (Horizontal and vertical axes exhibit the data points number, and the contact length (mm), respectively).

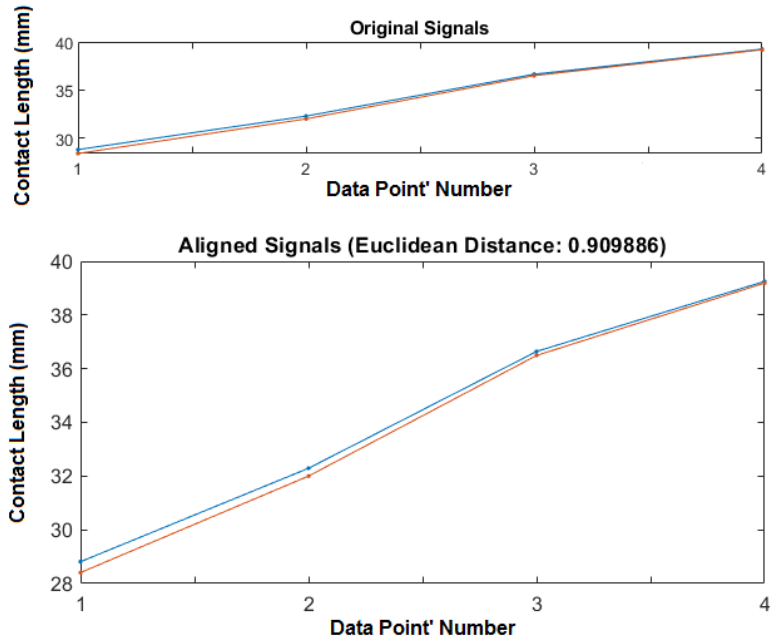

Figure 3.13: Two original sets of four data points (up) and the warped sets of the data points (down) (Horizontal and vertical axes exhibit the data points number, and the contact length (mm), respectively).

3.3.2 Similarity tests for the slope

Similar to what is done in section 3.3.1, a second degree polynomial function fitting best with the numerical data points (Figure 3.14) for the slope is expressed as eq. (3.3):

$$f(h) = p_1 h^2 + p_2 h + p_3 \tag{3.3}$$

Where the coefficients (with 95 % confidence bounds) are as follows:
$p_1 = 0.0004141\ (-0.002405, 0.003233)$
$p_2 = 0.03304\ (-0.3366, 0.4027)$
$p_3 = 74.88\ (63.99, 85.76)$
h: water level (mm)
f: the slope (degree)

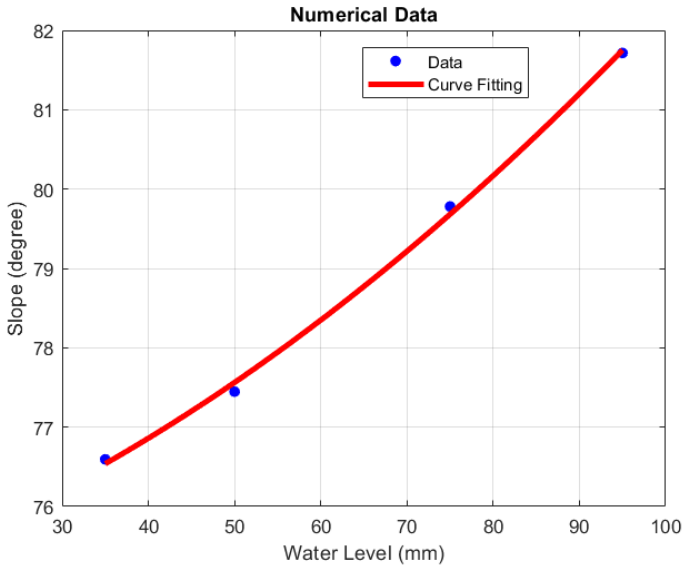

Figure 3.14: The raw data for the numerical result of the slope (blue) and the fitting curve (red)

In the same manner, the curve matching the experimental data points for the slope (Figure 3.15) introduces a second degree polynomial function as eq. (3.3).
Where the coefficients (with 95 % confidence bounds) are as follows:
$p_1 = 0.0008542\ (-0.01044, 0.01215)$
$p_2 = -0.01965\ (-1.5, 1.461)$
$p_3 = 75.28\ (31.69, 118.9)$
h: water level (mm)
f: the slope (degree)

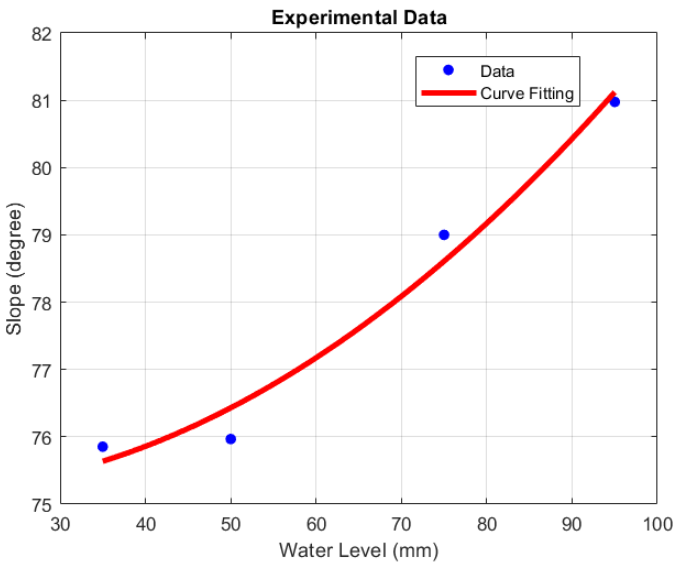

Figure 3.15: The raw data for the experimental result of the slope (blue) and the fitting curve (red)

In comparison to the contact length, the Frechet distance of the numerical and experimental results for the slope is clearly higher. In detail, the Frechet distance and the discrete Frechet distance for four data points are 1.1683 degree and 1.4797 degree, respectively.
Although the Frechet distance and the discrete Frechet distance depict lower similarity for the slope compared to the contact length, they are reasonable in consideration of the range of data from 75 to 82 degrees.

Likewise, the cumulative distance for four points on the curves plotted for the slope (Figure 3.16) is 3.7398 degree which indicates less similarity compared to the contact length.
Moreover, the original data points and the warped data points for the slope are plotted in Figure 3.16.

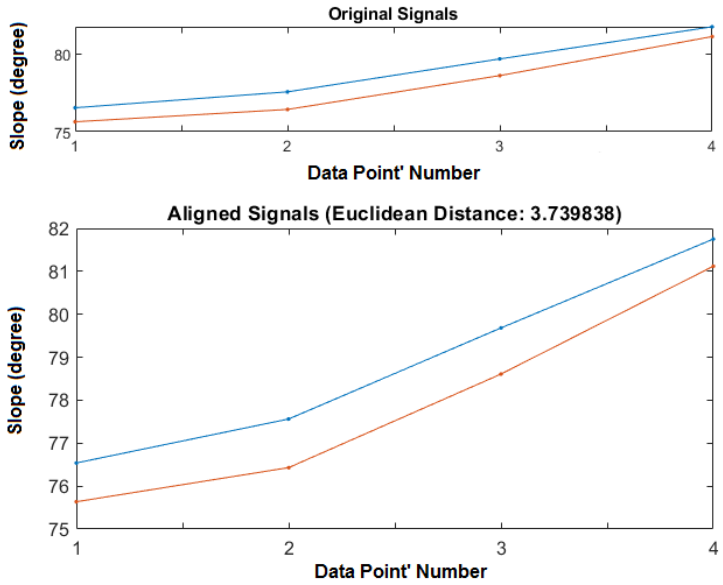

Figure 3.16: Two original sets of four data points (up) and the warped sets of the data points (down) (Horizontal and vertical axes exhibit the data points number, and the slope (degree), respectively).

3.3.3 Similarity tests for the displacement in Y direction

In addition, a linear function best suited to the experimental data points for the displacement in Y direction is described according to eq. (3.4), represented by Figure 3.17.

$$f(h) = p_1 h + p_2 \tag{3.4}$$

Where the coefficients (with 95 % confidence bounds) are as follows:
$p_1 = -0.08359\ (-0.08909, -0.0781)$
$p_2 = 3.775\ (3.343, 4.208)$
h: water level (mm)
f: displacement in Y direction (mm)

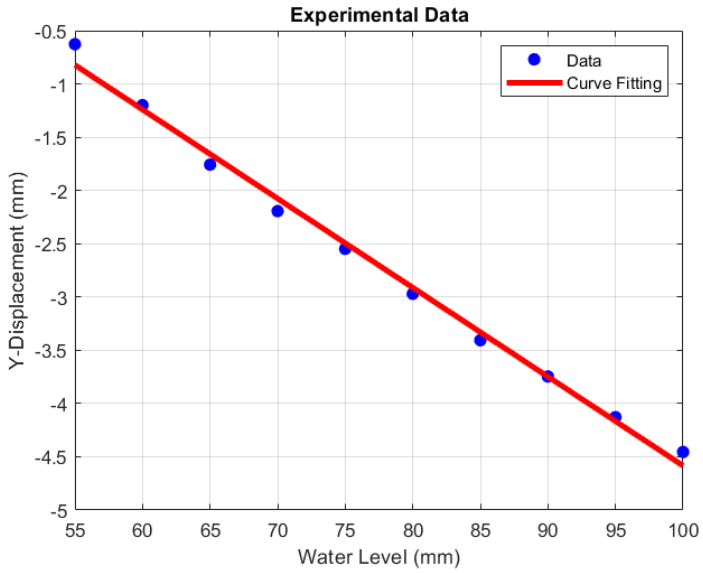

Figure 3.17: The raw data for the experimental result of the Y displacement (blue) and the fitting curve (red)

Likewise, the numerical datapoints for the displacement in Y direction (Figure 3.18) can be formulated based on a linear function as eq. (3.4).

Where the coefficients (with 95 % confidence bounds) are as follows:

$p_1 = -0.09448\ (-0.09639, -0.09257)$

$p_2 = 4.804\ (4.653, 4.955)$

h: water level (mm)

f: displacement in Y direction (mm)

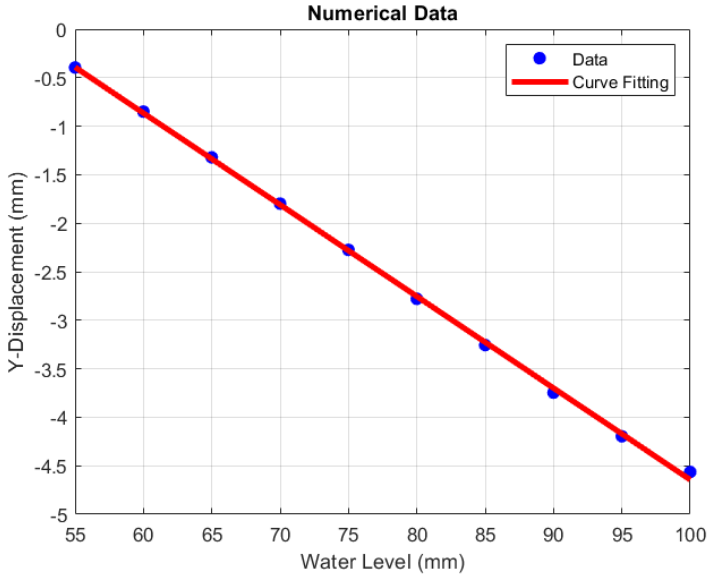

Figure 3.18: The raw data for the numerical result of the Y displacement (blue) and the fitting curve (red)

The results for the cumulative distribution function test (ktest2) which compares the distributions of the experimental and numerical data points is shown according to eq.

(3.5). It reveals a similar distribution (Figure 3.19) for both data series, where the computed values for h and p represent the validity of the null hypothesis (similar distribution) and probability of 100 % for the similarity.
Moreover, the maximum difference for the cumulative distribution function of $F(x)$ equals the k value.

$$[h, p, k] = ktest2(Y_e\ ,\ Y_n) \tag{3.5}$$

$h = 0\ (logical)$
$p = 1.0000$
$k = 0.1000$
Y_n: numerical data sample for the displacement in Y direction
Y_e: experimental data sample for the displacement in Y direction

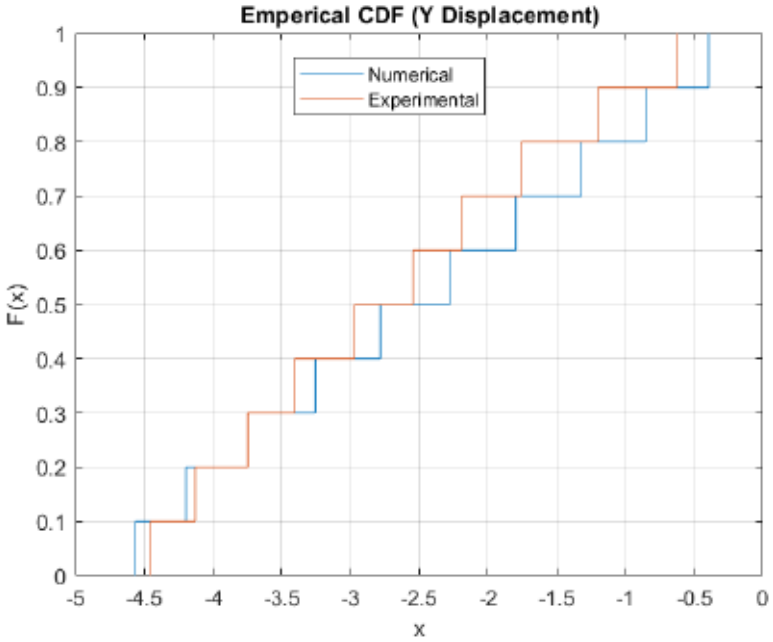

Figure 3.19: Cumulative distribution function (Horizontal and vertical axes exhibit the displacement in Y direction, and the cumulative distribution function, respectively).

In an analogous manner, the Frechet distance and the discrete Frechet distance of the numerical and experimental results for the displacement in Y direction are 0.4577 mm and 0.8193 mm, where ten data points for each data sample were compared.

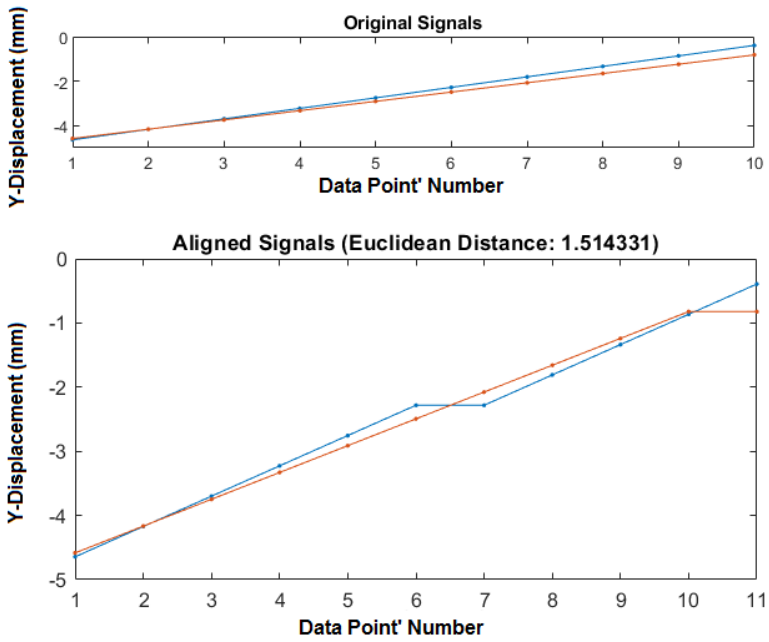

Figure 3.20: Two original sets of ten data points (up) and the warped sets of the data points (down) (Horizontal and vertical axes exhibit the data points number, and the Y displacement (mm), respectively).

Likewise, the cumulative distance for ten points on the curves for the displacement in Y direction (Figure 3.20) is computed as 1.5143 mm, which proves a similarity between two curves.

In addition, Figure 3.20 shows the original data points and the warped data points for the displacement in Y direction.

3.4 Concluding remarks

This chapter makes a contribution to analyze numerically the behavior of the downscale membrane loaded by water pressure by the finite element dynamic explicit solver, where the numerical results hold the possibility to be compared against experimental observations.

The material properties like the density, the Young's modulus, the Poisson's ratio and the thickness of the membrane were measured experimentally (Table 3.1) and applied for the numerical model. Moreover, the reinforcing steel cord on the upper boundary of the numerical model membrane was set up based on the manufacturing material specification (Table 3.2)

In addition to the similarity in the material characteristics, the numerical model and the experimental membrane shared common boundary conditions, which enabled a valid comparison between numerical and experimental results.

Density	865.51 kg/m^3
Young's modulus	258 MPa
Poisson's ratio	0.48
Thickness	0.06381 mm

Table 3.1: Material for flexible PE

Density	7850 kg/m^3
Young's modulus	2100 GPa
Poisson's ratio	0.3
Diameter of the circular cross section of the stringer	0.6 mm

Table 3.2: Material for steel circular stringer

In this regard, the numerical and experimental results for the Y directional displacement, the contact length of the membrane with the channel ground level and the slope of the membrane (relative to the Y-axis) were compared with respect to the different water levels which imposed the hydrostatic pressures on the membrane. While there is a decrease in the contact length of the membrane with the channel ground level with regard to a rise in the water level, the absolute value of Y-displacement and the slope of the membrane exhibit a proportional increase.

Moreover, the mathematical formulations fitting best with the datasets were found by the curve fitting tool in Matlab.

In addition, the similarities between each pair of experimental and numerical curves were discussed with the Frechet distance, the discrete Frechet distance, and the dynamic time warping (section 3.3).

Likewise, the distributions of the experimental and numerical data points for the Y-displacement were compared with the two-sample Kolmogorov-Smirnov test, which exhibited a similar distribution (Figure 3.19) for both data series.

Apart from the trivial discrepancy accountable to the parameter setup difference and some errors regarding both experimental measurement and the applied numerical solvers, numerical models are in satisfying agreement with the experimental observations and the collected data. Future work is still needed to provide an optimized structure model which represents all characteristics of the physical model, where an improvement in the imposed boundary conditions is a good example. For simplicity reasons, two hanging points on the upper boundary were assumed as fixed in every direction, while they have small displacements according to the slight deformation of supports, which were not included in the model.

Promising numerical results verify the validity of the structural model setup of the flexible membrane which promotes conducting further researches in order to investigate other possible scenarios which add complexity into the model setup.

The next chapter deals with a complicated case where the original prototype interacting with a low speed water flow is attacked by a heavy flotsam. After preparing the structural model setup for the original prototype, two couplings are obviously inevitable components which are added to the numerical model setup. The movement of the flotsam within the fluid domain, and the issue regarding the mesh criteria, especially when the flotsam makes contact with the original prototype are potential causes for concern. The transfer of data between two software is without doubt the further subject which deserves special care.

4 Numerical model setup of the original membrane for impact analysis

With the advent of light structures for flood defense purposes, there are challenges upon their safety, durability, and so on. In case of windy or stormy weather conditions, light structures are extremely vulnerable to be attacked by floating debris and even tree trunks. To meet the safety criteria, estimation of these impulsive forces on light structures is of great importance. This matter provides the motivation to investigate numerically impact phenomena.

This chapter will present the numerical model setups for the impact analysis, where the fluid domain is discretized by both the standard meshing and overset meshing techniques. Both numerical model setups replicate the same physical phenomenon which was investigated experimentally. There are no clear differences in the material properties, boundary conditions between two numerical simulations and even experimental impact test. Therefore, it makes sense to compare the results of the experiments and two simulations. Both numerical simulations need to be conducted by two-way co-simulations between the Abaqus and the Star CCM+, where a data transfer between two software provides the desired results.

In this respect, the impact analyses were executed at the presence of the free surface water flow which interacted with both the rigid and flexible structures. The flexible structure representing the full-scale prototype membrane deformed notably when it was impacted by an accelerated heavy flotsam.

The following figure shows the dimensions of the prototype membrane.

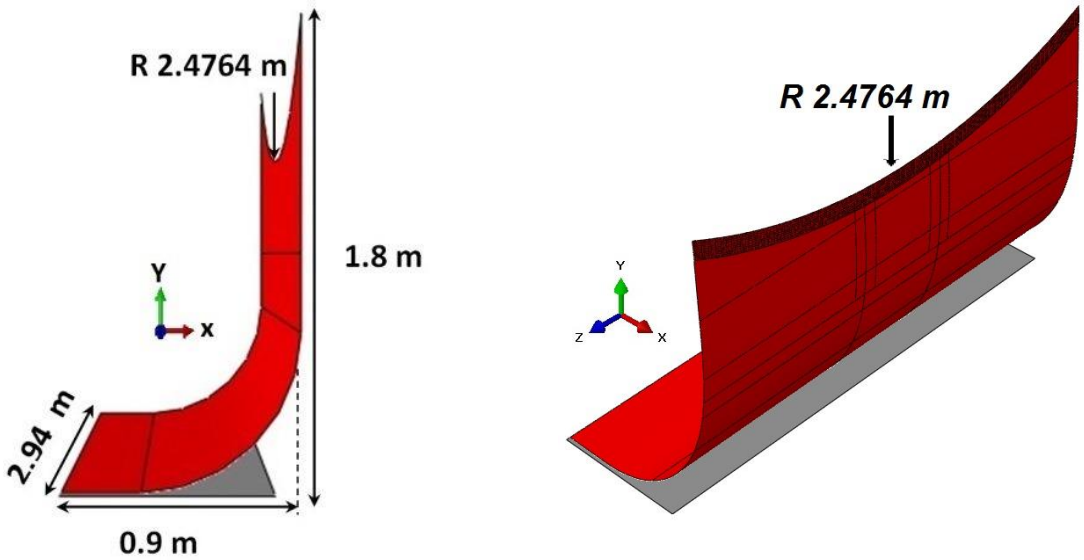

Figure 4.1: Dimensions of the prototype membrane

On account of inherent high nonlinearities involving in the solution of the target dynamic tasks, and more convenience in integration of contact conditions to the model compared to dynamic implicit analysis, dynamic explicit analysis was more suited. However, as mentioned in sections 2.3 and 2.4, the coupling algorithm (here an implicit algorithm) enforced the dynamic implicit analysis, which is solved by the Abaqus standard, on the structure domain.

To prepare a co-simulation case, two separate models were needed to be built for the fluid and structure domains so that they shared some boundaries in common. The structure model was constructed within the complete Abaqus environment (Abaqus CAE) and written as the Abaqus input file which is supported by the Star CCM+ solvers.

4.1 Structure domain

The structure domain consisted of four parts assembled in Abaqus CAE. The inner and outer sides of the flexible membrane were the surface boundaries shared by both sub domains. The Flotsam was the further shared boundary between two software, but introduced as a rigid part within the Abaqus; however, because of a rigidity of the flotsam, the flotsam boundary surface on the fluid side could be linked with a selected point on the flotsam defined on the structure side. To create the flexible membrane, the initial rough geometry for the membrane was estimated based on the total length and boundary settings and then deformed under the influence of stationary water and gravity loads within a standalone analysis. The water pressure load was imposed on the structure by the subroutine of DLOAD, which could be updated in each iteration based on a new deformed shape. The deformed membrane could be imported to the structure and fluid domains and incorporated in them.

As mentioned in section 2.3, the beam elements representing the steel cord on the upper boundary of the structure (refer to Figure 4.4) cause a problem with the coupling between two software.

To prevent these disadvantageous elements from the interaction with the fluid, the steel cord had to be excluded from the part interfacing directly with the fluid domain. But rather a new part including a PVC band and the steel cord (shown in Figure 4.3 and Figure 4.4) could be tied to the membrane which had surfaces (inner and outer surfaces) in common with the fluid. This model provided a solution to the inconsistency problem on one hand and replicated more accurately the full-scale prototype membrane.

The deformed parts comprising the membrane and its attached band were read within the Abaqus output database file and written as a new part with the stl format, but without a geometry feature in the Abaqus standard model. Then the geometry feature could be built by the mesh plugin toolbar, while the option of try to add volumes was deactivated. In the mesh module, by using the virtual topology, the old mesh faces could be removed, while some important feature like the edges which define the partition of the membrane tied with the PVC band could be again restored.

Nonetheless, an important issue had remained unsolved how to deal with the initial orientation of the beam elements in the deformed model. The new problem was rooted at the fact that the orientation of the stringer was missed when importing the deformed membrane. Warning regarding disorientation of the stringer could not be easily ignored. Otherwise, it would result in wrong results even if the analysis procedure would not be terminated due to a disorientation error.

As a result of deformation, the new beam elements were located in different surfaces, which caused the definition of the orientation to be a laborious task. So, the normal vectors for the beam elements on the upper edge of the membrane were computed mathematically based on new positions of the nodes on the band and entered manually in a CAE model. The manually user defined changes for the beam element could be easily written in an input file as n_1 orientation of the beam elements.

Abaqus uses a local, right-handed (t, n_1, n_2) axis system to specify the orientation of a beam cross-section, where t, n_1, and n_2 represent the orientation of the beam element tangent, and the beam section axes, respectively. Figure 4.2 represents the local coordinate system of the beam cross-section.

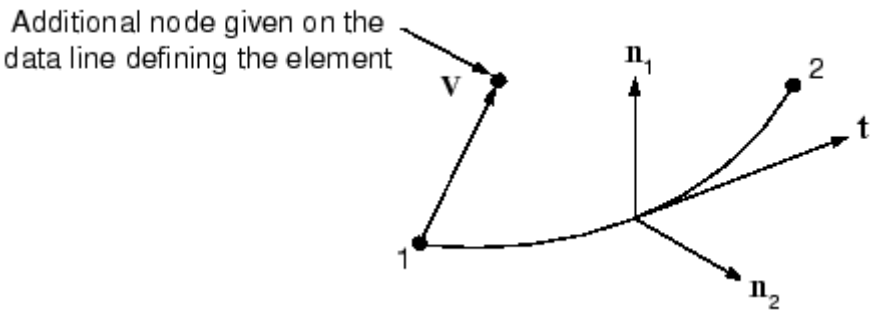

Figure 4.2: Local coordinate system for a beam element (Dassault Systèmes 2013) [95]

The default negative Z axis for n_1 (shown in Figure 4.2) can be remained intact when all the beam elements are located in the X-Y plane. If all the beam elements do not lie in the same plane, several ways are available to determine the vector of n_1.

Having specified an additional node (node 3) in the element entry for the beam, the direction connecting node 1 to node 3 stands for the v direction in Figure 4.2. The v direction is used to approximate the n_1 direction. The Abaqus computes the n_2 direction as the cross product of two vectors of t and v (t x v). The cross product (t x v) is a vector which is perpendicular to both vectors of t and v and thus normal to the plane comprising them. The resulting vector of n_2 is used to define the actual n_1 direction as the cross product of two vectors of n_2 and t (n_2 x t). This procedure ensures that the local tangent and the local beam section axes are orthogonal to each other. Alternatively, the n_1 direction can be approximated and entered either in the input file by the user or in beam section properties in the Abaqus CAE.

The same procedure described above as the second way was followed in the thesis in order to calculate the actual beam section axes.

The membrane was made of flexible PVC with Young's modulus, density, Poisson's ratio and thickness of 1400 MPa, 1500 kg/m^3, 0.1 and 0.075 mm, respectively. The band attached to membrane is consisted of PVC, and an additional steel cord on the upper boundary.

The steel cord was modeled as a steel stringer with a diameter of 10 mm, a Young's modulus of 2100 GPa, a density of 7850 kg/m^3, and a Poisson's ratio of 0.3.

The flotsam and the part representing the ground level were assembled as three-dimensional discrete rigid parts.

The flotsam was represented as a cylinder with a diameter of 0.4 m and a length of 3 m. A mass of 330 kg was attributed to the flotsam at the flotsam center of gravity.

As the membrane was bonded with the other similar membranes on left and right sides, the shared edges on the membrane and its tied band were defined as symmetric boundaries in Z direction. The fixed boundary conditions in three directions were applied for the bottom edge of the membrane, whereas two hanging points on the upper boundary of the band were fixed. The motion of the flotsam was constrained in all directions except the X direction. The flotsam movement towards the membrane was implemented by a velocity boundary type ramped to 4 m/s for the center of gravity of the flotsam. The ground level was fixed completely without any rotational freedom. The prescribed boundary conditions are shown in Figure 4.3.

The discretization of the membrane and its tied band containing the flexible PVC was performed by membrane elements, either M3D4 (a three-dimensional, 4-node membrane element) or M3D3 (a three-dimensional, 3-node membrane element), whereas

the steel cord appended to the band was discretized with linear interpolated beam elements of B31 (the Timoshenko (shear flexible) beams in space).

To discretize both the rigid bodies (the flotsam and the bottom of the channel), three-dimensional rigid elements of R3D4 (with 4 nodes) were used. In case the mass of the rigid body needed to be defined (the mass of the flotsam for instance), in the Abaqus standard, rigid elements do not support an attribute of the mass. Using a point mass is a way to assign the mass distribution to the rigid body.

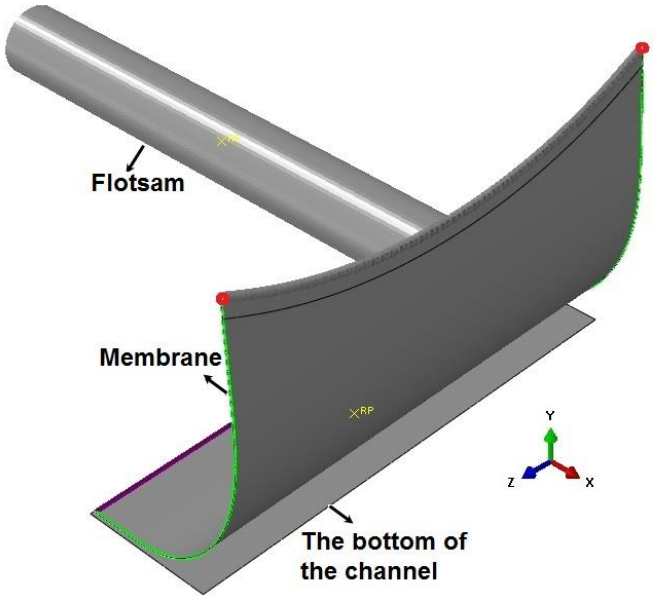

Figure 4.3: Scheme of the full-scale prototype membrane in the Abaqus standard and boundary conditions, including two fixed hanging points (red), and the bottom edge of the membrane as fixed boundaries in three directions (violet), side edges of the membrane as symmetric boundaries in Z direction (green)

Figure 4.4 depicts the discretization for the structural domain. The stringer (grey) in Figure 4.3 and relating beam elements (green) in Figure 4.4 were scaled to be seen clearly.

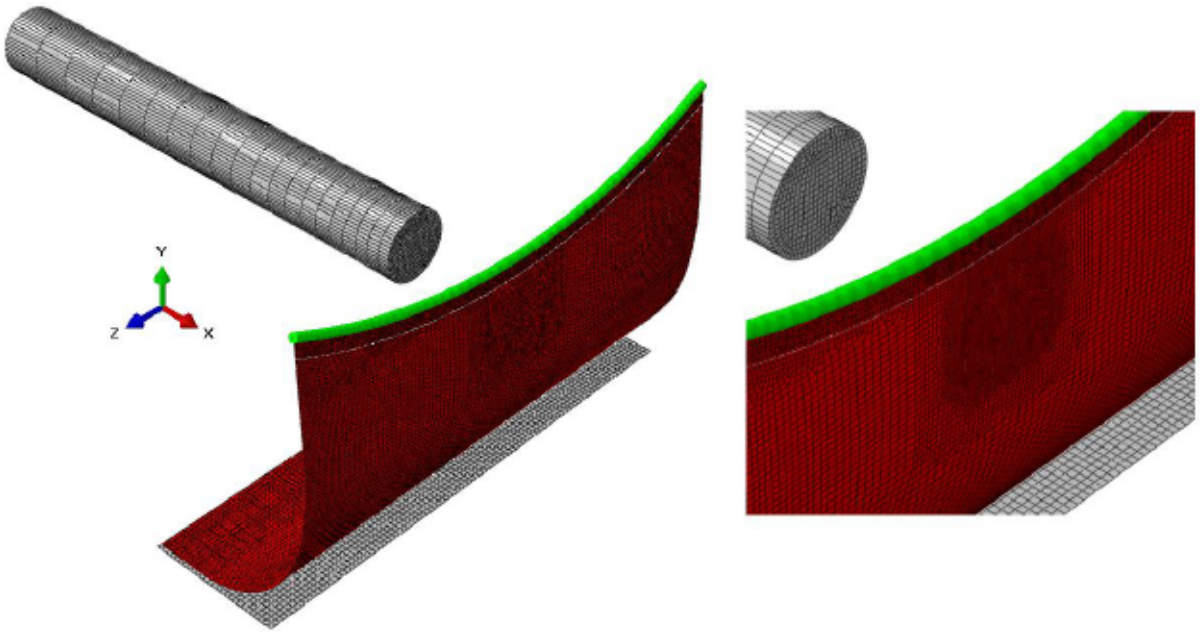

Figure 4.4: Discretization of the full-scale model with local refinement: membrane elements of M3D4 and M3D3 (red), beam elements of B31 (green), and rigid elements of R3d4 (grey)

The mass proportional and stiffness proportional damping coefficients for Rayleigh damping can be generally computed by a numerical modal analysis within the Abaqus; however, as mentioned in section 2.2.3, a lack of bending stiffness in the membrane elements rendered the modal analysis impractical. Therefore, the empirical results including frequency-response function curves, the half-power bandwidth method, followed by relevant damping ratios are deciding factors to define two Rayleigh damping coefficients.

The mass proportional and stiffness proportional damping coefficients for Rayleigh damping were set as 6.15237 and 2.18341e-5, respectively.

Two contact interactions were specified throughout the Abaqus model by the interaction module (surface-to-surface contact model). One was accounted for the contact between the membrane and the bottom of the channel with a friction coefficient of 0.1, while the latter stands for the contact between the membrane and the flotsam with a friction coefficient of 0.01 when colliding. The penalty contact method was assigned to the mechanical constraint formulation, with the applied finite sliding.

The model transient behavior was executed by the default Hughes-Taylor implicit time integration method with second order accuracy.

This procedure was implemented with the same initial and maximum time increment sizes of 0.00005 s, where the time increment sub-cycling was activated. When enabling the time increment sub-cycling, the Abaqus implicit is allowed to apply its own

time incrementation to approach the target coupling time, contributing to a convergent simulation. In fact, the specified time increment is divided to smaller sub-increments, when needed, to increase the stability of the simulation.

4.2 Fluid domain

The fluid domain was discretized by both the standard meshing and overset meshing techniques which shared some pre-processing steps. To start with similarity within the Star CCM+, the flexible membrane had to be modeled as the zero thickness baffle interface detaching the immiscible water-air flow inside the channel on one side and surrounding air environment on the other side.

When the membrane approached the ground level on the air side (shown in Figure 4.5), which was created only in the structure domain, the mesh between the interfaces and lower boundary on the air side would be squeezed. Therefore, the lower boundary in the air side was designed to be deeper than the ground level in order to maintain mesh criteria requirements in the squeezed area.

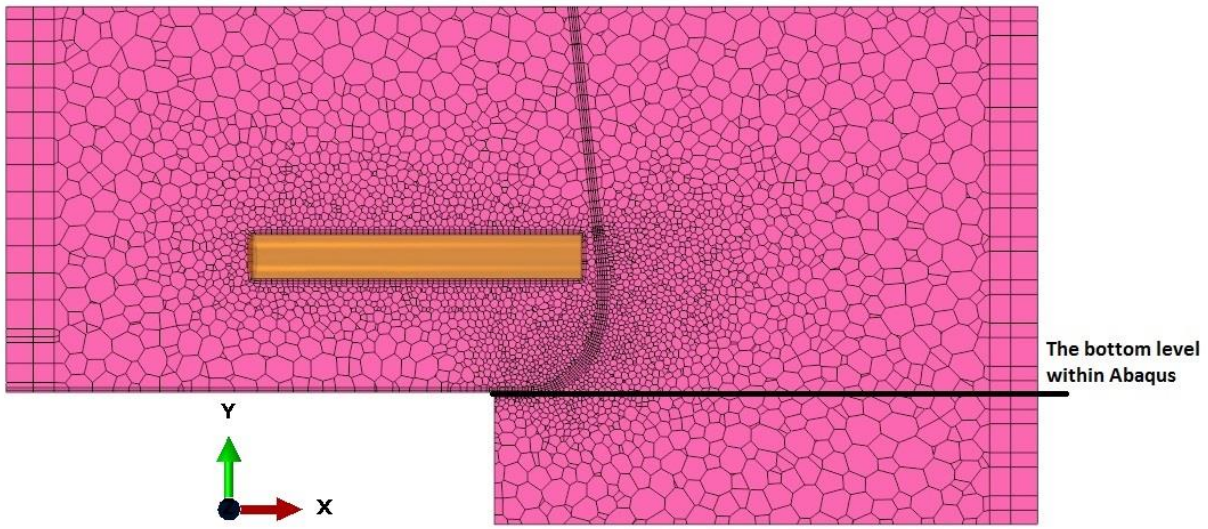

Figure 4.5: Presentation of the actual bottom level in the fluid domain

One part including the channel and the surrounding environment on the other side of the membrane was constructed by means of 3D-CAD model tools available in the Star CCM+. The deformed membrane was imported from the Abaqus into the Star CCM+ with the stl format and inserted into the previous part as a baffle. The further baffle was appended to stop water inside the channel from permeating into air surroundings on the other side. This could be carried out by both Boolean operations and a repair surface tool, making the new baffle by connection of the membrane with the rest of the fluid domain.

The immiscible water-air flow in the channel was modeled by a volume of fluid multiphase model (VOF model) which uses the high resolution interface capturing (HRIC) scheme to obtain the free surface.

In this model, all phases are modeled as one flow, where properties change based on the volume of fraction. The VOF model is a segregated flow model, where the pressure and velocity fields are coupled by means of the SIMPLE algorithm (originally proposed by Caretto et al. (1973) [108]).

The realizable k-ε two-layer turbulence model was enforced to exhibit the turbulent behavior of the fluid domain.

A gap between the membrane and the flotsam could not be avoided in both strategies. As a result, the flotsam in the fluid region had to be located a little behind its counterpart inside the structure domain for the impact analysis.

In fact, the impact between two structures happened solely in the Abaqus model, while they approached each other very closely within the fluid domain.

A trimmer mesh was the more appropriate mesh than a polyhedral mesh for the discretization of the VOF fluid domain, where the precision of the free surface could be captured by anisotropic mesh refinement in the vicinity of the free surface. Nonetheless, a polyhedral mesh was preferred as the volume mesh ensuring a conformal mesh across the interfaces. Prism layers with a stretching factor of 1.2 were created on the wall boundaries, resolving accurately the near wall flow. To prevent the prism layer around the baffles from thinning, an internal baffle was defined within the repair surface tool by the extension of the membrane and the further baffle up to the top boundary.

A morphing motion model permits the coupled moving boundaries (including the membrane and the flotsam) to follow the motion dictated by the Abaqus.

An implicit unsteady solver was set to second order temporal discretization scheme, releasing the discretized grid flux of second order, with a step size of 0.00005 s.

However, there are discrepancies in the geometry, the mesh and the boundary conditions of the fluid domain discretized by both the standard meshing techniques and the overset mesh. Sections 4.2.1 and 4.2.2 explain the differences for the preparation of the fluid domain discretized by the standard meshing technique and the overset mesh, respectively.

4.2.1 Standard mesh and results

The volume of the flotsam was subtracted from the part, remaining the outer surface of the flotsam as an external boundary of the fluid domain. The resultant geometry was attributed to one region.

Two prism layers were established on the inner and outer walls of the baffles, respectively. The internal baffles which were added to inhibit the prism layers from thinning could be fused after meshing to reduce the number of interfaces within one region. Moreover, any mesh refinement of the water free surface and in the vicinity of the membranes and baffles was avoided in order to minimize the risk involved with a negative cell when the flotsam approached the membrane. Furthermore, the lag between the positions of the flotsam in the Abaqus and its counterpart within the Star CCM+ had to be relatively big.

A sheet was inserted into the fluid domain at the free surface location, which was assigned as an internal baffle. By this means, the solvers also enjoyed having cell faces perpendicular to the main gradients of the flow in the presence of the added plane surfaces which could be fused after meshing.

In addition to the polyhedral mesh and prism mesh models, the extruder mesh was applied to extend the inlet boundary, the outlet boundary and the side wall in the channel side.

Two ends of the channel were selected as the inlet and outlet boundaries, respectively. The boundary conditions for the inlet and outlet boundaries were attributed to typical standard models of the velocity inlet and the pressure outlet, respectively.

The bottom of the channel within the channel side, the membrane, the baffles and the flotsam were defined as wall boundaries, while the side boundary in the channel side was selected as a symmetry boundary.

The remaining boundaries were assigned to the velocity inlet (see Figure 4.6).

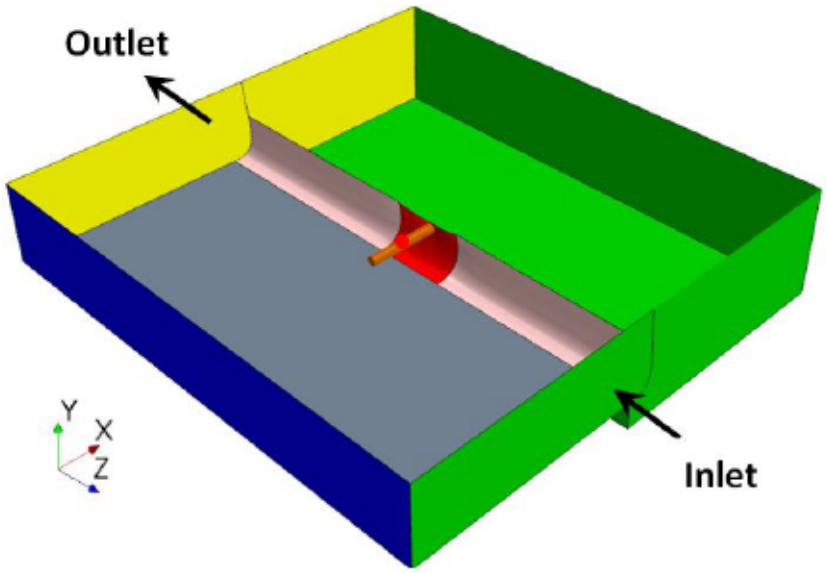

Figure 4.6: Schematic of the fluid model: the coupled membrane (red), the baffle (pink) mimicking the channel wall, the coupled flotsam (brown), the bottom of the channel (grey) and the boundary conditions including velocity inlet (green), pressure outlet (yellow), symmetric boundary (blue) (The red point exhibits the position of the node (within the Abaqus) interfacing with the brown flotsam surfaces).

There was a further issue corresponding to the initialization of the fluid domain. Due to the variable curvature of the baffles, the definition of fraction of cells as either water or air was rendered impossible by means of position-dependent user defined field functions in order to initialize the fluid domain with the VOF continua.

To solve the problem, cell surfaces could be generated, which exhibit all the cells adjacent or intersected by the desired input boundaries. The membrane, the baffle and the internal baffles were selected as input boundaries. Likewise, within derived parts, two cell surface parts were created based on the volume mesh inside and outside of the input boundaries separating the interior water flow from the exterior air, respectively. The respecting cell IDs were extracted as tabular data and used to specify two cell sets. When growing these cell sets, the surrounding air medium was recognized as distinct from the water flow inside the channel. These cell sets could be utilized within the user defined field functions to introduce the initial flow field. The cell sets could be generated only after meshing and they were dependent on meshing; thus, they should be regenerated after remeshing or any change in the mesh continua.

In order to enforce the coupled membrane imported as a deformed surface at the beginning to follow the motion dictated by the Abaqus, a morphing motion model had to be attributed to the region. In addition, the further created baffle was allowed to float based on control points on the adjacent boundaries. A fixed morphing model was set to the other boundaries except the symmetry boundary (refer to Figure 4.7).

In Figure 4.7, the black point exhibits the position of the node (within the Abaqus) interfacing with the red flotsam surfaces.

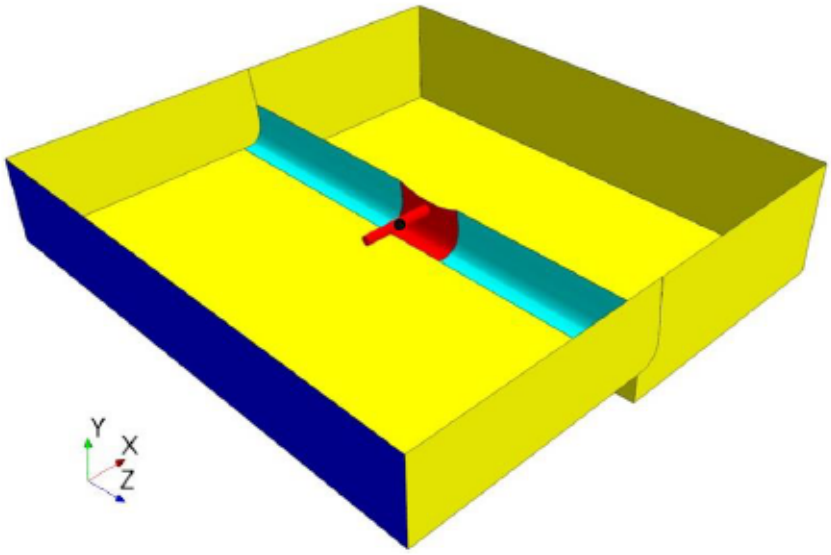

Figure 4.7: Morphing motion model specification: displacement by the co-simulation method (red), fixed model (yellow), the symmetric side (blue), the floating model (cyan)

The execution of the simulation demonstrated restrictions regarding the discretization of the fluid domain by the standard mesh strategy. The strategy was limited to the applications where two structures neither tend to make contact nor have a big movement. In case of a big movement, a remeshing could be implemented in order to enhance the cell quality. Nevertheless, the fluid volume fractions of cells for the new generated mesh had to be interpolated from the old mesh. For this reason, there was some discrepancy between the fluid volume fractions of cells compared to the previous mesh, which was neither desirable nor precise.

Figure 4.8 and Figure 4.9 exhibit the X-Y cross section of the mesh before and after impact, respectively.

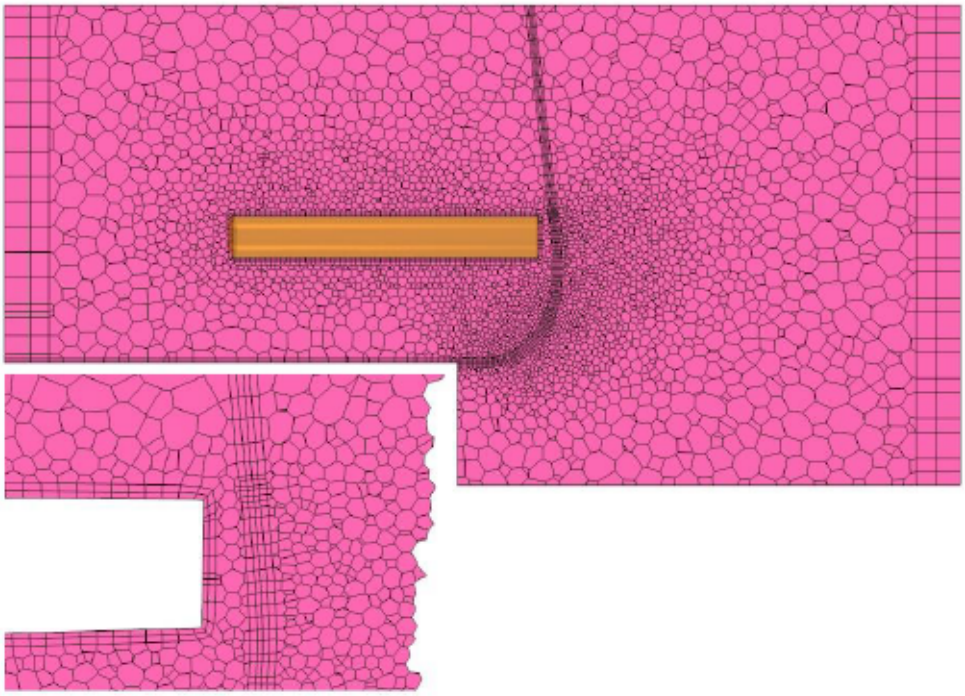

Figure 4.8: The X-Y cross section of the mesh before impact

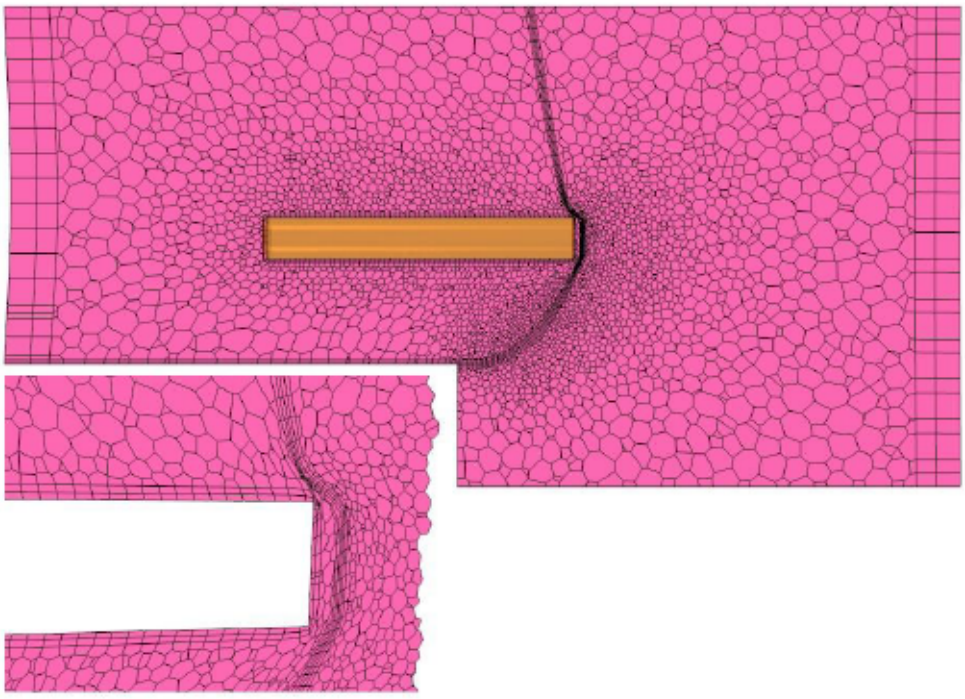

Figure 4.9: The X-Y cross section of the deformed mesh after impact

Figure 4.10, Figure 4.11, and Figure 4.13 represent the total displacement and the displacement in X direction for the prototype membrane after preload step at the

time of impact and 0.104 s after impact (when the maximum deformation for the membrane was observed), respectively.

The simulation depicts subtle differences for the water flow at the time of impact (Figure 4.12) and 0.104 s afterwards (Figure 4.14). There is also little change in the water flow even in the areas where were expected to be affected by impact.

Figure 4.12 and Figure 4.14 exhibit the velocity field on the water free surface and the relative pressure load on the prototype membrane at the time of impact and 0.104 s after impact, respectively.
There is no clear increase in water height either within the gap closure or nearby the impacted zone of the membrane. In these figures, the maximum relative pressures are almost the same, although a slightly higher relative pressure field within the impacted zone can be seen.

In order to verify whether either a close initial distance between the membrane and the flotsam or an inevitable final big gap closure within the fluid region at the time of impact (to maintain the mesh criteria) distorted the results, the impact analysis was also conducted by an overset mesh (refer to section 4.2.2).

Furthermore, the managed velocity of 4 m/s was not disabled at the time of impact, and the flotsam moved without any decrease in pace for about 0.0005 s (Figure 4.11). Therefore, there are low differences in the displacements (particularly in the impact zone) in comparison with the overset analysis, where the flotsam impacted the membrane (in the standard mesh) with no clear change in the velocity for about 0.0005 s (Figure 4.12). In contrast, for the overset mesh simulation, the managed velocity of 4 m/s was deactivated one time step before impact. That is why the results of the simulation discretized by the overset mesh (Figure 4.23 and Figure 4.26) show smaller displacements in comparison.

In detail, the impact zone of the membrane experienced a maximum total displacement of 2.03 cm and a maximum displacement in X direction of 1.806 cm at the impact time, respectively (Figure 4.11).

After an impact time of 0.104 s, the membrane deformed further so that a maximum total displacement of 28.83 cm and a maximum displacement in X direction of 27.83 cm in the impact zone could be observed (Figure 4.13). In fact, there are increases of 26.8 cm and 26.024 cm in the total displacement and the maximum displacement in X direction (during impact), respectively.

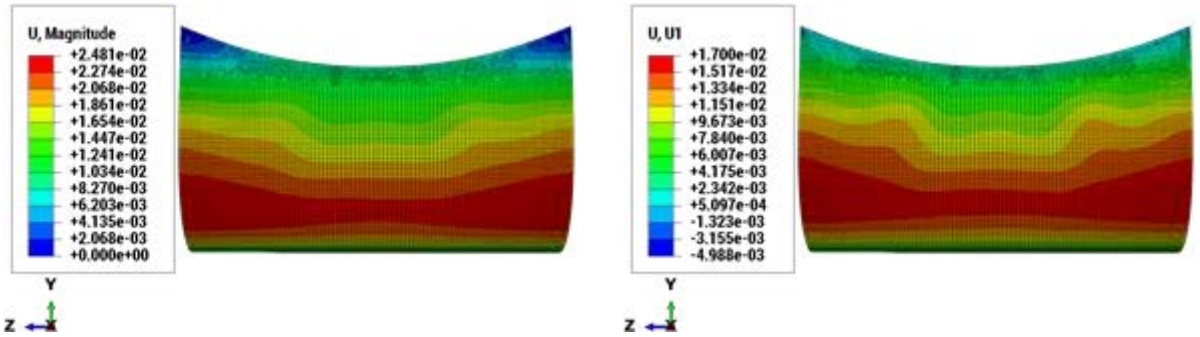

Figure 4.10: The total displacement (left) and the displacement in X direction for the prototype after preload step (The corresponding values for U and U1 are in meter).

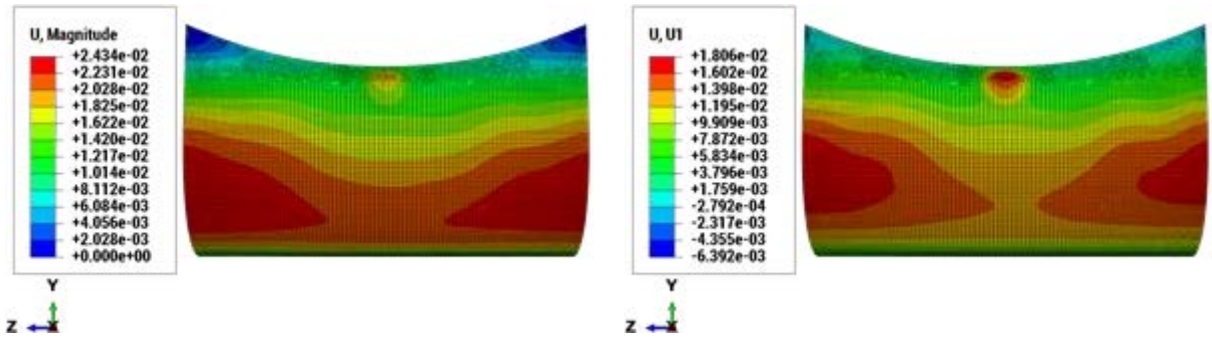

Figure 4.11: The total displacement U (left) and the displacement U1 in X direction for the prototype at the time of the impact (The corresponding values for U and U1 are in meter).

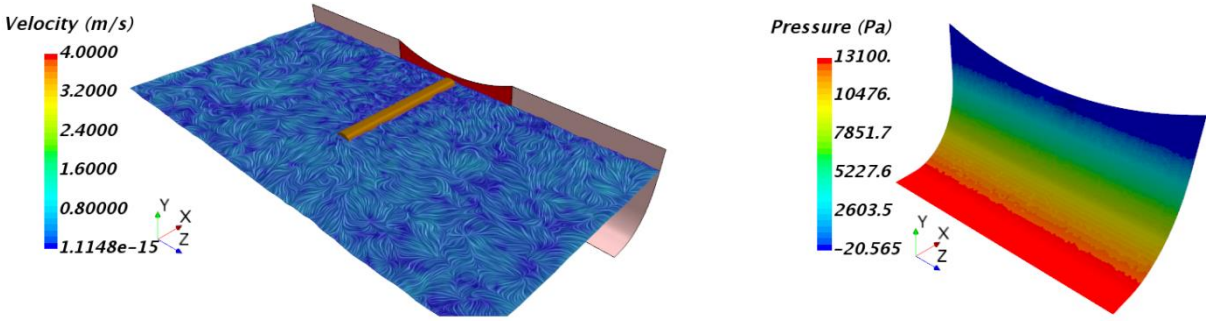

Figure 4.12: The velocity field on the water free surface (left) and the relative pressure load on the prototype at the time of the impact

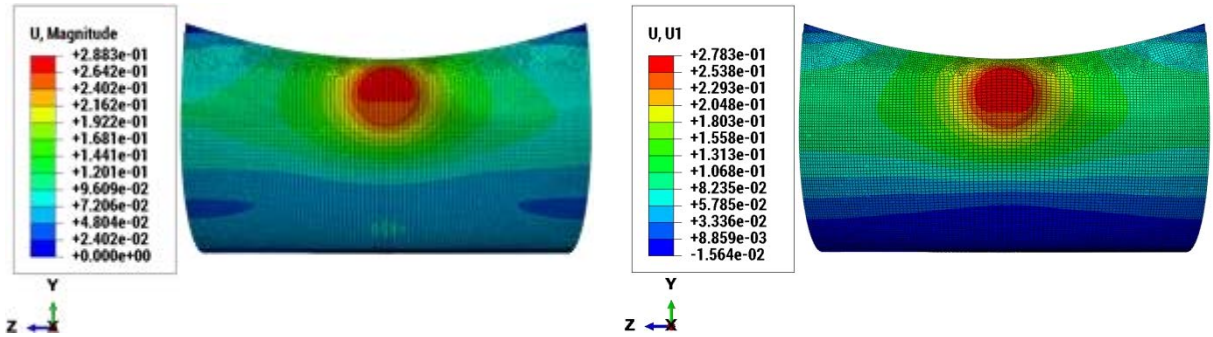

Figure 4.13: The total displacement (left) and the displacement in X direction for the prototype at 0.104 s after impact (The corresponding values for U and U1 are in meter).

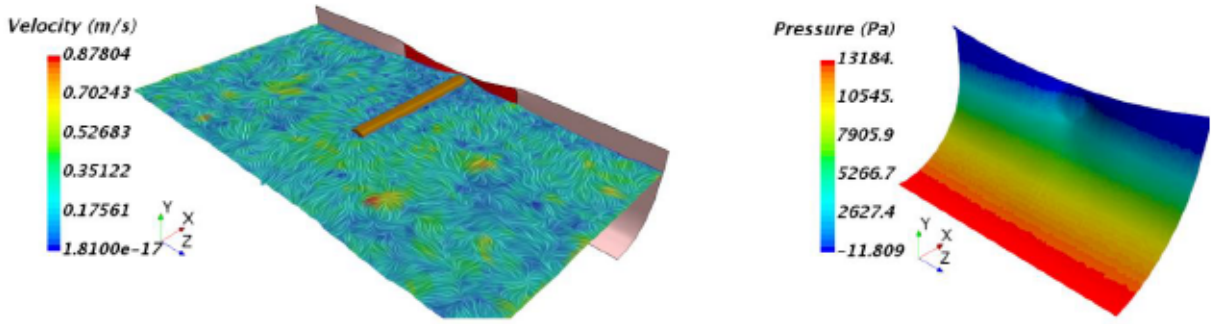

Figure 4.14: The velocity field on the water free surface (left) and the relative pressure load on the prototype at 0.104 s after impact

4.2.2 Overset mesh

When the flotsam moved from 70 cm far away the light membrane, especially if coming into contact with each other, the fluid mesh between them had to be squeezed (Figure 4.8 and Figure 4.9 in section 4.2.1). To meet the criteria beyond which the morpher began to generate poor quality cells, the flotsam was wrapped by an overset mesh. In general, an overset mesh works effectively without remeshing after generating the initial mesh, providing greater flexibility in comparison with the standard meshing techniques as a consequence. Moreover, a minimum distance between the structures approaching each other can be reduced. Last but not least, it is most suitable for optimization studies. In this technique, the overset part had to be assigned to a segregated region, but the initially constructed part as the fluid domain in section 4.2 (before subtraction of the flotsam as implemented in section 4.2.1) still could be used to define the further region (the background region).

Two different scenarios could be applied for the background: one-region based or two-region based.

In the former, some areas of the overset region extended beyond the channel wall (membranes and baffles) when the flotsam impacted the membrane within the structural model. The issue was not inevitable in spite of the lag between the flotsam counterparts because the deformation of the membrane after impact was hugely nonuniform. The overset region extending over the channel wall had been partially filled with the water flow, while the ambient air had to occupy the baffles exterior and these areas of the overset region as a result. In fact, the baffles created in the background region could not be distinguished within the overset region (refer to Figure 4.15 and Figure 4.16).

As a result, the water flow diffused into the ambient air within the overset region. The issue has been exhibited clearly in Figure 4.16. The blue color behind the mem-

brane represents the permeation of the water flow into the other side, which is not physically correct

In Figure 4.15, the left top shows the overset cell type for a section on the water level within the background region, where the left bottom zooms the cross section in the vicinity of the membrane. Moreover, the right top exhibits the overset cell type on the X-Y plane on the middle of the membrane within the background region, where the right bottom enlarges a detail of the overset cell type on the mentioned plane in the vicinity of the membrane. The cells over the membrane in the air side of the background are covered by the overset mesh, which means that the water can penetrate in the air.

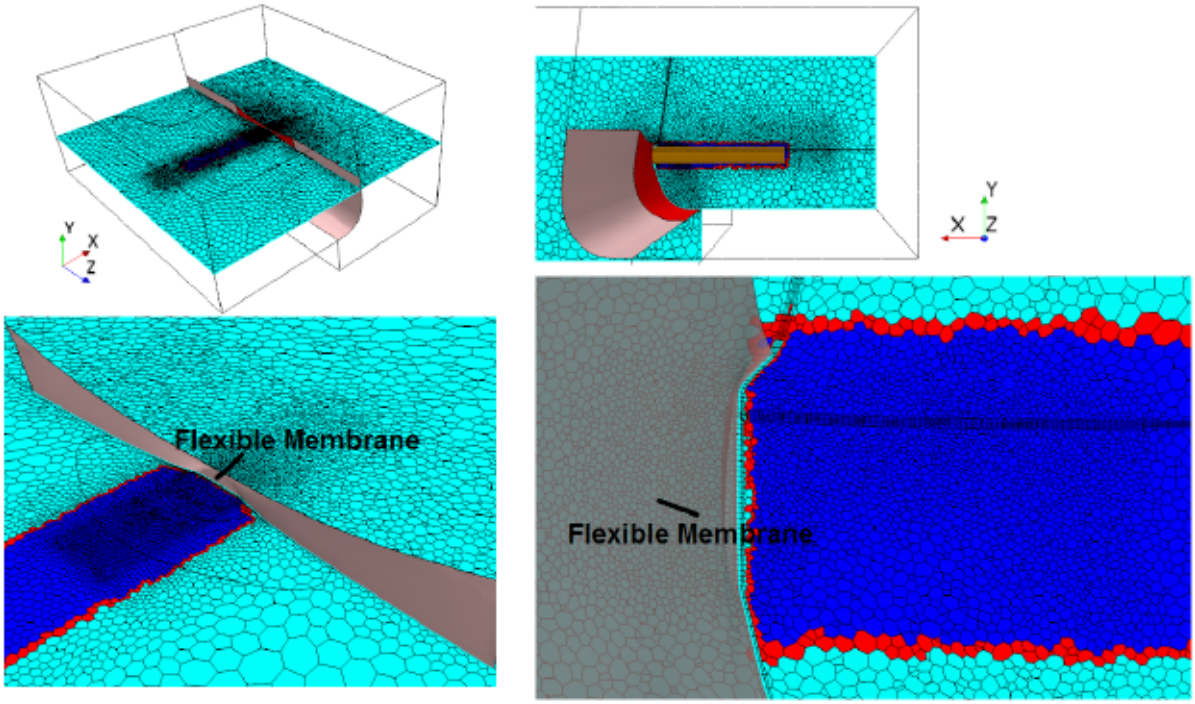

Figure 4.15: Overset cell type for one region with 2 active layers for the membrane in both sides at 0.018 s after impact (active (aqua), inactive (dark blue), and acceptor (red)) (In the bottom, the membrane is represented by red color with opacity 0.1 to make the overset mesh be seen).

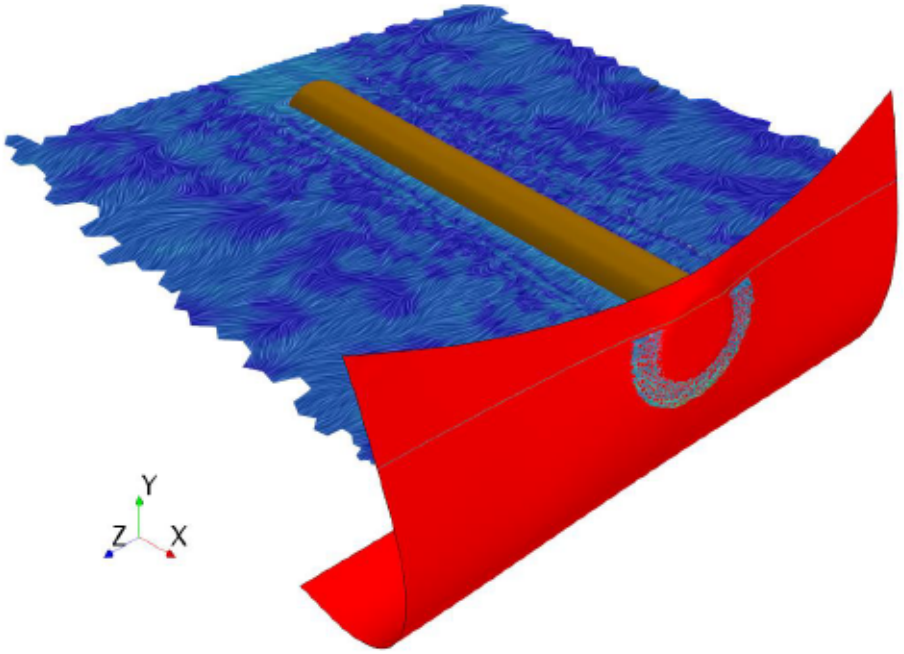

Figure 4.16: One region with 2 active layers for the membrane in both sides at 0.018 s after impact

To avoid the resulting unrealistic flow solution, the initially constructed part for the background (before the subtraction) was divided into two parts through internal walls. As a consequence, the VOF channel side and the air side were split thoroughly and attributed to two different regions (two-region based background). The former was selected to be interfaced with the overset region; hence the overset mesh became deactivated when extending over the VOF region. As a consequence, if the overset region expanded over the baffles, the overset region cells located in the air side filled with the ambient air could be deactivated.

As mentioned before, similar to the simulation discretized by the standard mesh, the polyhedral mesh model was used as volume mesh to guarantee a conformal mesh across the interfaces. However, to capture the water free surface, a conformal prismatic layer was enforced to be built at the free surface.

Similar to the standard mesh technique, there was a need for a lag distance for the position of the flotsam within the software of Star CCM+ to follow the motion of the flotsam.

To reduce this distance, both the area surrounding the nose of the flotsam and the route tracked by the flotsam were refined. Finally, the flotsam in the fluid domain lagged only 4 cm behind its counterpart within the structural domain, which is acceptable in engineering applications.

The inlet, the outlet and the side wall of the channel side were not be extruded, in contrast to the previous simulation in order to reduce the computational cost.

As a general requirement for an overset interpolation, the overset mesh boundaries should overlap the background mesh (the mesh covering the channel side) by at least 4-5 cell rows unless they are assigned to work as a wall instead of an overset boundary (Siemens AG 2019) [88].

Flow initialization could be performed by the help of the region index system-defined field functions and the position-dependent user defined field functions.

Within the background region, the side walls, the top and the air environment beneath were defined as symmetry planes (blue), while a wall boundary was specified for the bottom of the channel (grey). With the exception of the inner boundaries (red, pink, and cyan), the remaining boundaries were chosen as inlet (green) and outlet (yellow) boundaries, where typical standard models of velocity inlet and pressure outlet were applied, respectively (Figure 4.17).

In the overset region, the flotsam (brown) was selected as wall boundary, whereas the other boundaries were marked as overset boundaries (shown in Figure 4.17).
The red point exhibits the position of the node within the Abaqus interfacing with the brown flotsam surfaces.

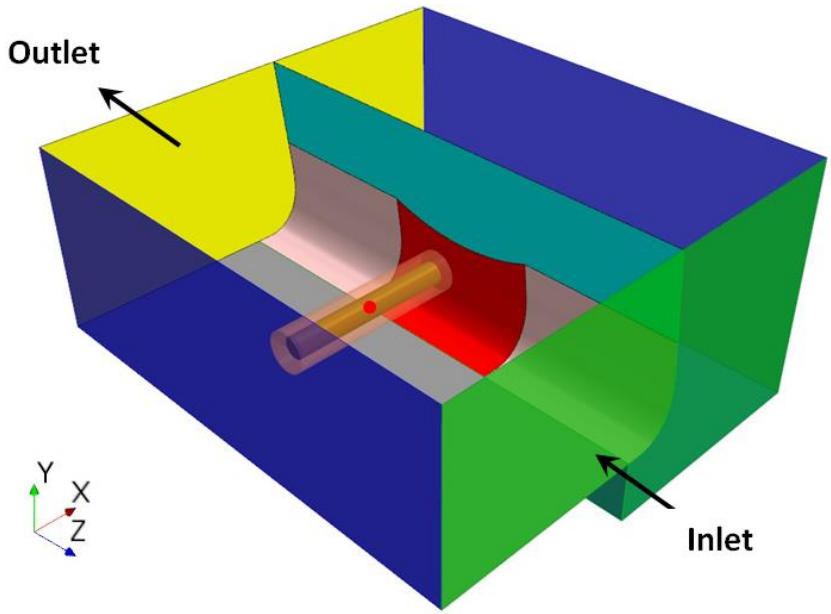

Figure 4.17: Schematic of the fluid model: the coupled membrane (red), the baffle (pink), mimicking the channel wall, the flotsam (brown) surrounded by a cylinder which represent the overset region, bottom of the channel (grey), inlet (green), outlet (yellow), symmetric sides (blue), internal wall (cyan)

Akin to the standard mesh technique, a morphing motion model (refer to Figure 4.18) had to be assigned to the regions. As a result, the coupled components between two software were permitted to track the movement according to their counterparts within the Abaqus. The red point exhibits the position of the node (within the Abaqus) interfacing with the grey flotsam surfaces.

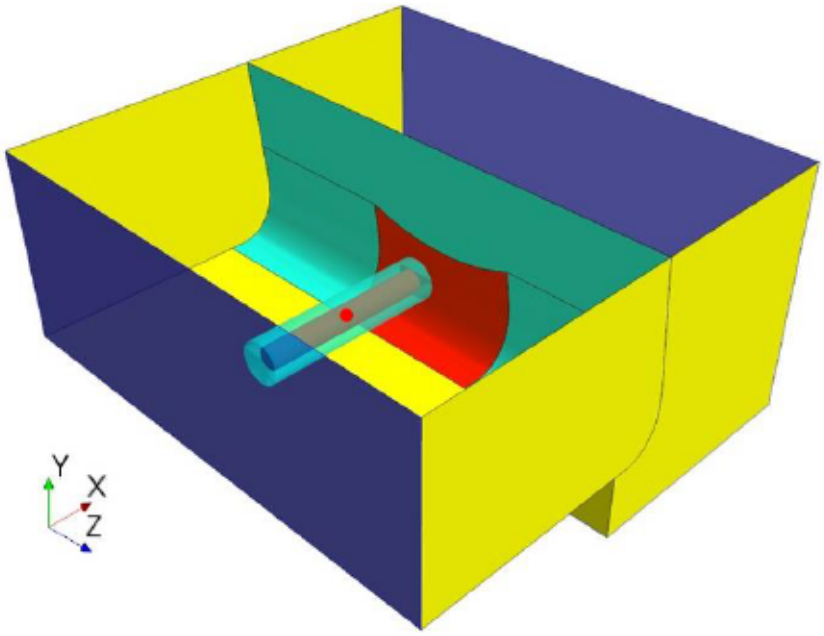

Figure 4.18: Morphing motion model specification: displacement by the co-simulation method (the red membrane and the grey flotsam), fixed model (yellow), symmetric sides (blue), floating model (cyan)

On account of the fact that the moving flotsam intended to impact the physical boundary of the channel (the membrane), the overset interface could be substituted with the overset mesh zero gap (refer to section 2.5).

To gain a better understanding, how the overset mesh zero gap works, different scenarios with a rigid wall (rather than flexible) were examined. To save time, no physical continuum was attributed to the regions. The flotsam had a velocity of 4 m/s in X direction for all simulations.

The possible issue resulting from the overset mesh zero gap was an elimination of a number of cells within the gap. If less number of cells (compared to the specified criteria) existed, the cells become inactive. The deactivation of cells gave rise to a fatal problem when deformable bodies (here only the membrane) were affected (Figure 4.19). In detail, in a co-simulation analysis, the coupled boundaries between two software have to share the same position and configuration. If a part of the membrane becomes deactivated, the coupled membrane will still not be identical within two software, which stops the simulation from running.

There were also the cases in which the implementation of the overset mesh zero gap had no contribution on the hole-cutting process, where the flotsam could not approach further towards the membrane. In other words, the simulation with the overset mesh zero gap encountered detrimental issues with the hole-cutting process at the same time when the simulation conducted by the overset mesh failed to proceed.

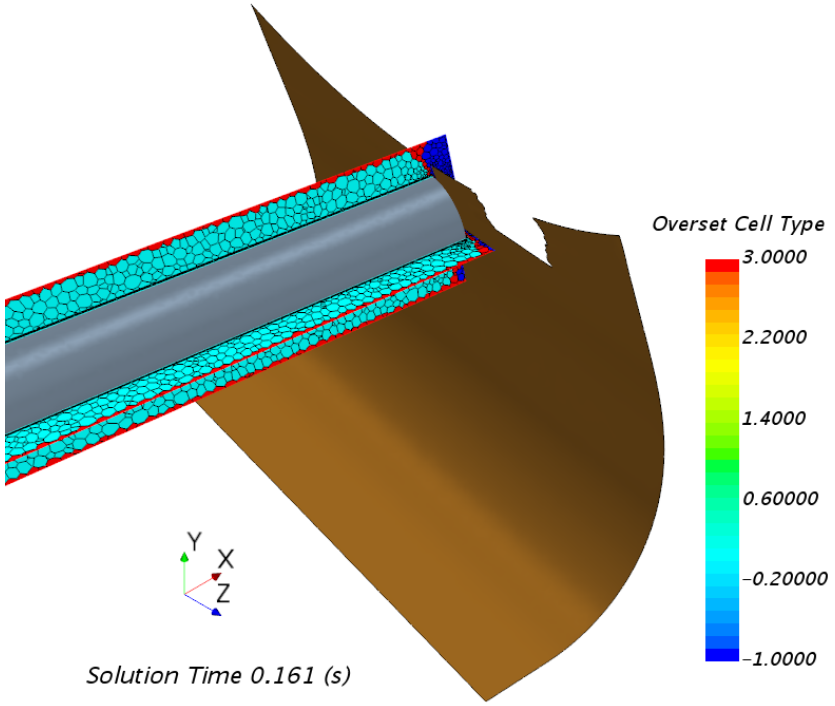

Figure 4.19: Overset cell type for two regions with 8 zero gap layers for the flotsam and 2 zero gap layers for the membrane: active (aqua), inactive (dark blue), and acceptor (red) (The torn part on the membrane is deactivated due to a zero gap with the flotsam).

Moreover, in order to gain a deeper insight through the impact of the geometrical parameters of the flotsam when using the overset mesh zero gap, the shape of the flotsam was partly altered.

In this regard, the cylindrical flotsam was exchanged with a conic form at the front boundary approaching the membrane (Figure 4.20 and Figure 4.21).

First, a simulation was executed upon the replaced geometry with 3 prism layers and 2 zero gap layers for both the flotsam and the membrane. After a solution time of 0.1691 s, the surface of the flotsam was somewhat deactivated, but the simulation could run further until the time of 0.16925 s, when the surface of the membrane was also partially deactivated and the simulation stops running at the time of 0.1701 s.

In detail, the flotsam moved 0.6 mm further (After a solution time of 0.1691 s) and approached the membrane more closely, leading to a partly deactivation of the

membrane surface. A further decrease of 3.4 mm in the gap closure was achieved until the simulation failed to be run due to an error at the time of 0.1701 s.

In fact, the flotsam can approach the membrane 4 cm more closely when the shape of the front boundary (the nose) is changed to the conic form.

An important finding to emerge from the last two simulations is the fact that a change in the geometry of the flotsam from a cylinder to a conic cause the flotsam to be able to approach the membrane 3.6 cm more closely without any deactivation of the membrane surfaces.

In case of a small gap between a moving body in the overset region and a wall, another possible option has recently been added, which enabled the prism layer shrinkage to morph the cells within the small gap.

However, the prism layer shrinkage works as a default with an overset mesh interface and an overset zero gap interface when five prism layers are defined on each wall boundary that forms the gap. This number of prism layers can be reduced to at least four prism layers if the number of (zero) gap layers are altered from 3 (default number) to 2.

Moreover, the prism layer shrinkage behavior can be specified or setup as automatically. With shrinkage behavior as automatic, only prism layers at wall boundaries will be shrunk whereas shrinkage behavior set to specified alters the default behavior. In the latter case, shrinking takes place for that boundary even when it is not a wall boundary.

In order to control the gap closure behavior, the maximum stretch factor has to be setup for an overset mesh interface, while for an overset mesh zero gap either the maximum stretch factor or the minimum gap distance has to be specified.

It is recommended (Siemens AG 2019) [88] that the layer reduction percentage (within the specified mesh) has to be changed to zero when the cells within the gap at sharp edges and corners have to be shrunk.

To compare the influence of a shrinkage on the overset cell type, two simulations were conducted, where the former (Figure 4.20) and the latter (Figure 4.21) represented the scenarios without activation of shrinkage, and with enabled shrinkage, respectively.

As mentioned before, for a case with enabled shrinkage, zero gap interface and default setup (three zero gap layers), at least five prism layers on each wall boundary

within the gap closure (between the flotsam and the membrane) were necessary to be defined (Figure 4.21). Likewise, another case with disabled shrinkage followed this requirement (5 prism layers and 3 zero gap layers for both the flotsam and the membrane) in order to make comparable results (Figure 4.20).

With regard to both cases, there was no possibility to run the simulation further and the simulation stopped due to mesh criteria issues. Neither the flotsam nor the membrane was deactivated partially regarding the case without shrinkage, while parts of the flotsam were deactivated in the case with enabled shrinkage.

However, the latter (shrinkage is active) allowed the prism layers defined on the membrane to be shrunk. As a consequence, the simulation could be further executed compared to the former, which implied that the flotsam could approach the membrane more closely when shrinkage was activated (Figure 4.21).

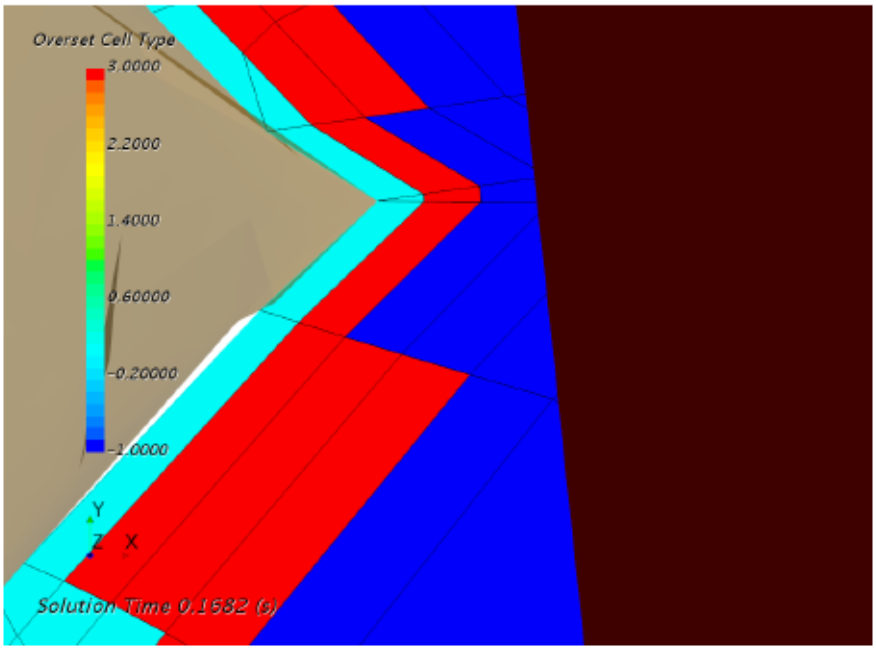

Figure 4.20: Overset Cell Type for two regions with 5 prism layers and 3 zero gap layers for both the flotsam and the membrane (active (aqua), inactive (dark blue), and acceptor (red))

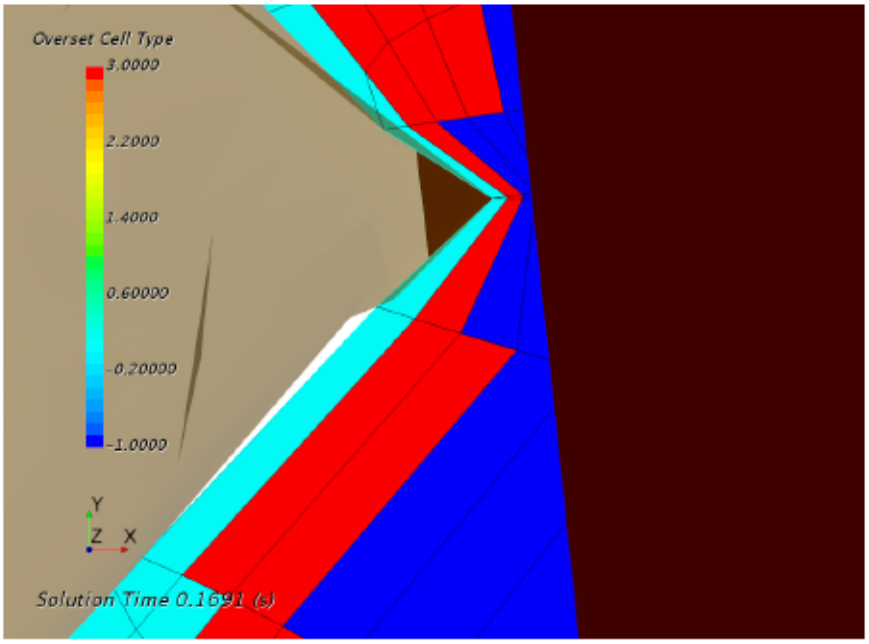

Figure 4.21: Overset Cell Type for two regions with 5 prism layers, enabled shrinkage and 3 zero gap layers for both the flotsam and the membrane (active (aqua), inactive (dark blue), and acceptor (red))

In this regard, five prism layers (Figure 4.20 and Figure 4.21) were accommodated within the prism layer total thickness of 1 cm which was also implemented for the simulation with three prism layers and two zero gap layers. It implies that a finer mesh was applied within the boundary layer by the new mesh setup (Figure 4.20 and Figure 4.21). Nonetheless, Figure 4.20 and Figure 4.21 have illustrated that a narrower gap closure can not be achieved only by refinement of the prism layers. In particular, the flotsam with three prism layers across the gap closure could approach the membrane 4.2 mm more closely than the case in which five prism layers on each wall boundary within the gap closure (Figure 4.20) was used. However, the gap could be reduced by 3.6 mm when shrinkage was activated (Figure 4.21), which is still 0.6 mm larger than the case in which three prism layers on each wall boundary and two zero gap layers within the gap closure were implemented.

4.3 Co-simulation model setup and results

Three co-simulation zones were specified, including two surface-to-surface couplings and one surface-to-point coupling.

The co-simulations had to be performed in two co-simulation steps, albeit with a preload step before the first co-simulation step was released. In the former co-simulation step, the flotsam was accelerated towards the membrane based on tabular amplitude. On the contrary, the acceleration source had to be removed from the

flotsam in the latter step; however, the flotsam moved forwards in a short time span before it rebounded.

The data were exchanged between two Star CCM+ boundaries on the imported deformed membrane (the inner and outer surfaces of the membrane) and two corresponding Abaqus surfaces where the identical positions, configurations, and orientations of the coupled surfaces had to be ensured. Any contradiction in the configuration of the membrane in both software either stopped the co-simulation from working or enabled only partial data mapping at least. The boundary representing the flotsam within the fluid domain was earmarked for a movement according to the reference node of the rigid flotsam inside of the structure domain. In contrast, there was no need for a similarity in either the position or the configuration of the flotsam in two codes as a result of a surface-to-point coupling. Hence, the flotsam could be located in the fluid domain a little behind its position in the structure domain to prevent the execution from a failure when two structures maintained contact.

The identical geometry for the co-simulation coupled membrane within the fluid and the structure domain permitted the reference configuration for mappers to be set as the original coordinates (as against to the current coordinates) which needed less computational cost in comparison with the current coordinates. Within the mapper setting, the normal vectors of the surfaces were checked to guarantee that the Star CCM+ boundary was appropriately orientated toward the corresponding Abaqus surface.

To follow an instruction in the Star CCM+ user guide (Siemens AG 2019) [88] when utilizing shell elements for the discretization of a structure model, rotations were conversely not mapped. The coupled surfaces, the coupled node, the exchanged fields, and co-simulation steps had to be defined by co-simulation commands and co-simulation controller appended to the Abaqus input file.

The automatic thin-out Cl factor as residual basis functions (RBF) parameter was decreased to 0.5, with the intention of increased morpher sensitivity to the mesh deformation.

The co-simulation was executed in an implicit iterative manner and a sequential order.

The Star CCM+ was preferred as a mapper of both directions, while the Abaqus was selected as the leading software in the coupling scheme (recommended for FSI analysis (Siemens AG 2019) [88]). The selection of the Abaqus for leading a co-simulation added more stability in comparison with the alternative (the Star CCM+ as the leading

software) with the same computational cost since the fluid mesh could be synchronized with the structure mesh instead of lagging by an iteration. The coupling step which is the period between two consecutive synchronized exchanges was defined at the commencement of the co-simulation and set as fixed to 0.00005 s.

Moreover, the minimum number of exchange within co-simulation was set to 15 with the minimum inner iterations per exchange of 3. Likewise, the stopping criteria stopped the exchanges within each time step (the inner iterations) if both the minimum inner iterations per time step of 45 and the co-simulation displacement residual of 0.0001 were satisfied. On the other hand, the maximum inner iterations per time step of 180 enabled more exchanges per time step until the co-simulation displacement residual of 0.0001 was ensured.

A common approach to prevent the co-simulation from destabilization was to allow the flow to be developed around the coupled boundary. For this purpose, the co-simulation was initialized with the solution achieved by deactivated co-simulation and mesh morpher solvers, which imparted a rigid characteristic to the flexible structure. Once the flow tended to be stable, the co-simulation was launched with both the enabled co-simulation and mesh morpher solvers, and a cleared solution history.

Furthermore, the stresses in the structure could not be restored in the simulation with deformed parts due to the type of the used elements. That provides an explanation why a preload step was defined in the co-simulation input file before the former co-simulation step started to work.

Consequently, a mesh morpher solver was allowed to be activated within the initialization process, which made it possible for the resulting deformations in the preload step to be mapped on the interfaces within the fluid domain.

The restart frames were managed to be written in the Abaqus output file in specified intervals synchronized with the auto save settings within the Star CCM+ so that an Abaqus restart could be executed to continue the analysis from the previous saved state. In such a way, some calculated data could be retrieved in case the analysis was terminated. Besides, a restart frame needed to exist definitely at the time when the flotsam hit the membrane. The inevitability of the restart step stemmed from the fact that two co-simulation steps were not permitted to be defined in the Abaqus input file, while the acceleration source (here velocity boundary type for the flotsam) had to be switched from enabled to disabled within the sequential co-simulation steps.

Figure 4.22 until Figure 4.29 represent the numerical results captured by the overset mesh technique.

The displacement fields on the membrane after the preload step which takes 1s before the co-simulation starts are depicted in Figure 4.22. In this interval, no coupling took place between two software.

Also, Figure 4.23 and Figure 4.25 represent the displacement fields for the membrane, the velocity field on the water free surface and the relative pressure field on the membrane respectively when the flotsam tended to impact the membrane.
As a result of the coupling with the fluid domain, a subtle increase in the membrane deformation and the relative pressure load on the membrane can be seen.

In detail, the maximum total displacement increased from 2.484 cm (Figure 4.22) to 2.564 cm (Figure 4.23) when co-simulation started to work. In the meanwhile, there was an increase in the maximum displacement in X direction from 1.892 cm (Figure 4.22) to 1.989 cm (Figure 4.23). Moreover, the impact zone on the membrane deformed almost 1.496 cm totally and 0.907 cm in X direction at the time of impact, respectively.

The maximum displacement of the membrane, which is illustrated in Figure 4.26, was achieved after 0.104 s contact with the flotsam. The figure exhibits a big difference for the membrane deformation compared to Figure 4.22 and Figure 4.23, which ensued from the impact with a heavy moving flotsam.

In other words, the membrane experienced a maximum total displacement of 28.81 cm and a maximum displacement in X direction of 27.78 cm after an impact time of 0.104 s (Figure 4.26).

In fact, there were increases of 27.314 cm and 26.873 cm in the total displacement and the maximum displacement in X direction (during impact), respectively. For the same time duration, the membrane deformed 26.8 cm and 26.024 cm in the total displacement and the maximum displacement in X direction using the standard mesh, respectively. Clearly, the membrane which was simulated with the overset mesh exhibited more deformation than the membrane modeled with the standard mesh (section 4.2.1).

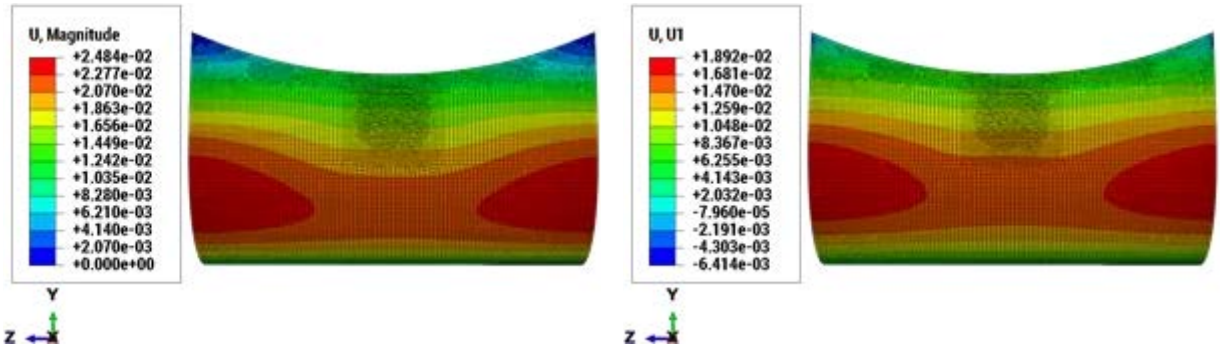

Figure 4.22: The total magnitude of the displacement (left) and the displacement in X direction (right) after preloading (The corresponding values for U and U1 are in meter).

Figure 4.24 and Figure 4.27 exhibit the overset cell type immediately before impact and after impact time of 0.104 s, respectively. In these figures, the left top shows the overset cell type for a section on the water level within the background region, where the left bottom magnifies the view in the vicinity of the membrane. Furthermore, the right top exhibits the overset cell type on the X-Y symmetric plane of the overset region, where the right bottom enlarges a detail of the overset cell type on the mentioned plane in the neighborhood of the membrane.

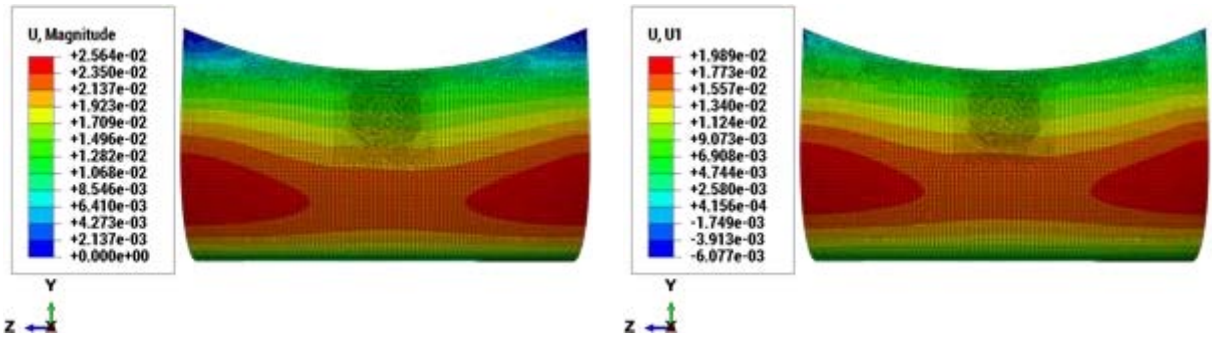

Figure 4.23: The total magnitude of the displacement (left) and the displacement in X direction (right) at the time of impact (The corresponding values for U and U1 are in meter).

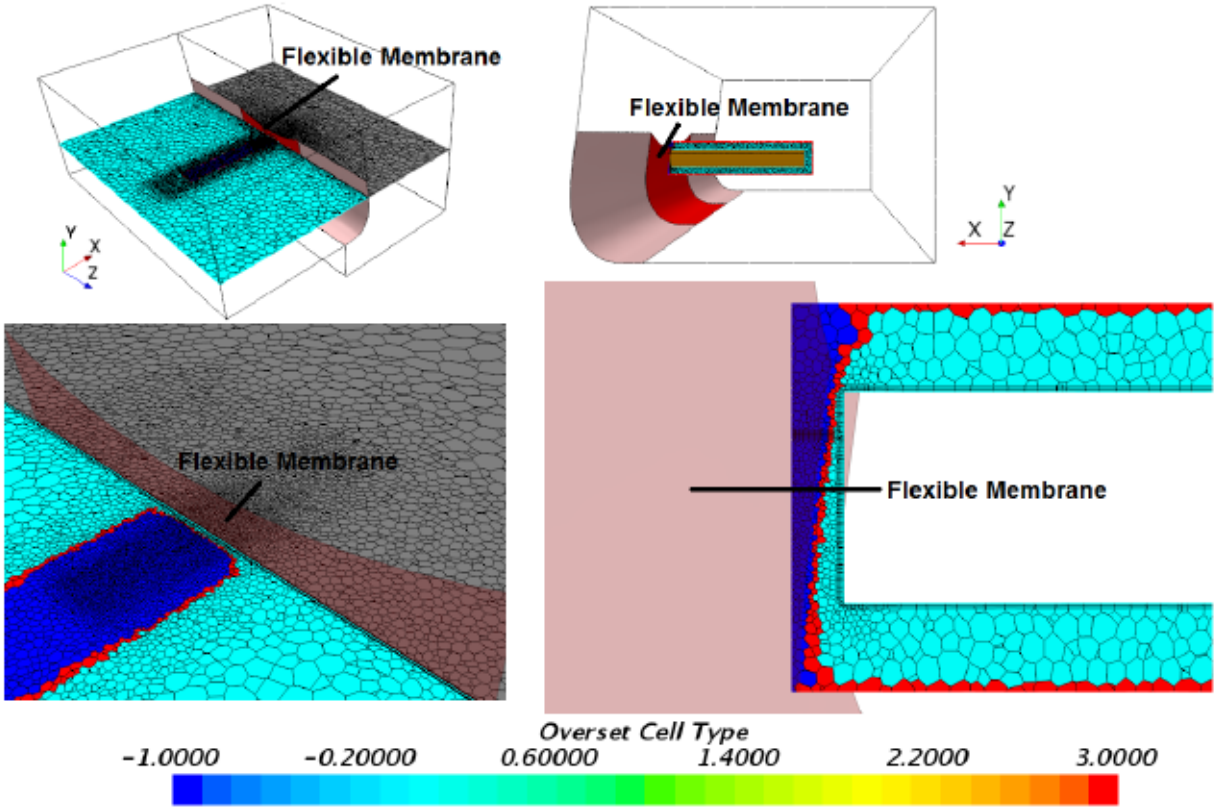

Figure 4.24: Overset cell type at the time of impact (active (aqua), inactive (dark blue), and acceptor (red)) (In the bottom, the membrane is represented by red color with opacity 0.1 to make the overset mesh be seen).

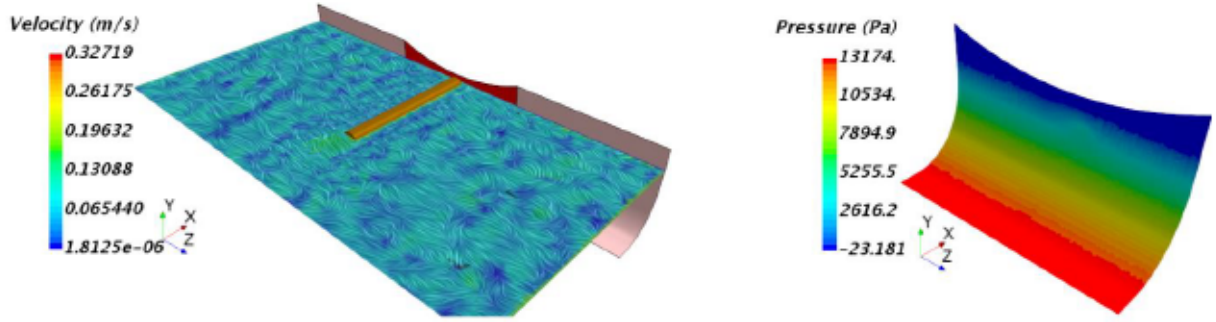

Figure 4.25: The velocity field on the water free surface (left) and the relative pressure load on the prototype (right) at the time of impact

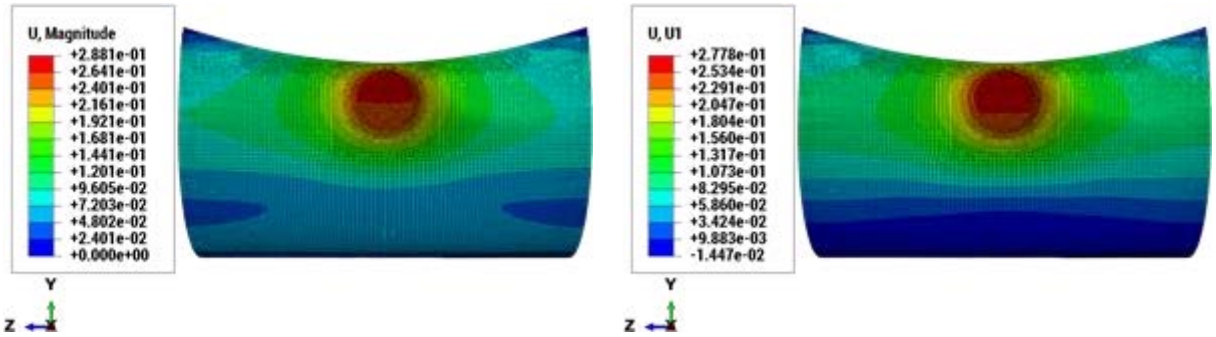

Figure 4.26: The maximum total displacement (left) and the displacement in X direction (right) at 0.104 s after impact

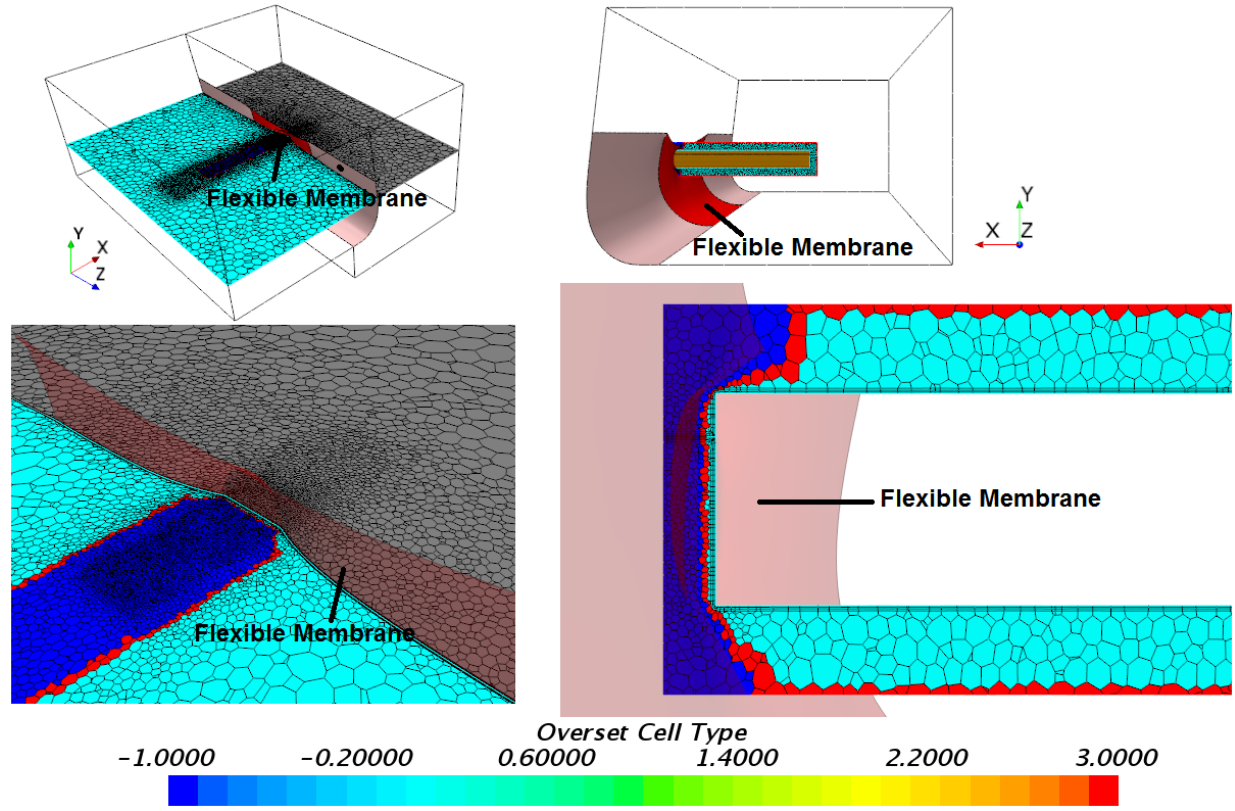

Figure 4.27: Overset cell type at 0.104 s after impact (active (aqua), inactive (dark blue), and acceptor (red)) (In the bottom, the membrane is represented by red color with opacity 0.1 to make the overset mesh be seen).

Moreover, the velocity field on the water free surface and the relative pressure field on the membrane are represented in Figure 4.28. The fluid pressure and the velocity fields are more or less similar to the hydrostatic state when the moving flotsam is either in the immediate vicinity of the membrane (Figure 4.25) or even in contact with the membrane (Figure 4.28).

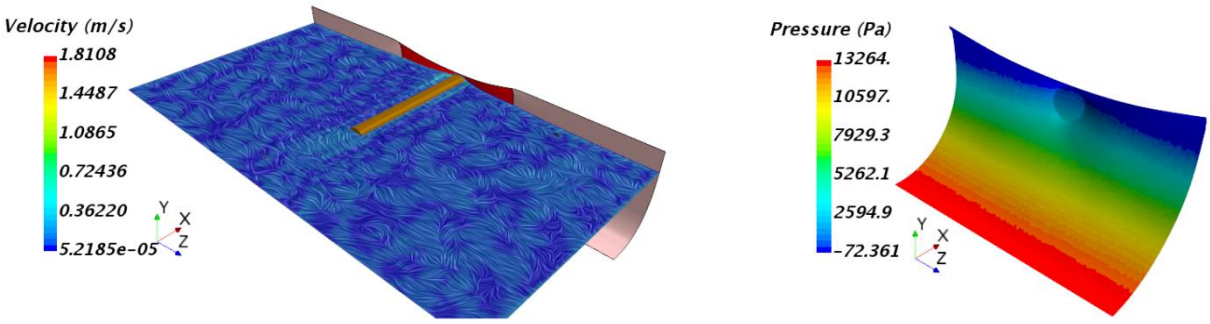

Figure 4.28: The velocity field on the water free surface (left) and the relative pressure load on the prototype (right) after 0.104 s after impact

Since the numerical findings contradict strongly the everyday experience (overpressure nearby the impact zone), a further simulation with the same geometry, mesh, and physics within the fluid domain was conducted in order to verify the accuracy of the model setup for the fluid domain. Nonetheless, the membrane was modeled as a rigid structure in the latter model (refer to Figure 4.29) contrary to the former one. The comparison between the two results justifies why the former fluid case and hydrostatic state resemble each other, resulting in a negligible difference in the results for the water flow regardless of the applied meshing strategy (either the standard mesh or the overset mesh).

Figure 4.29 exhibited a huge influence of the flotsam on the water flow velocity and the relative pressure on the membrane (especially an overpressure in the contact zone) when the membrane was represented as a rigid thin structure. In fact, the deformation of the flexible membrane as a result of the impact mitigated the effect of the impact between two structures on the water flow even in the contact zone.

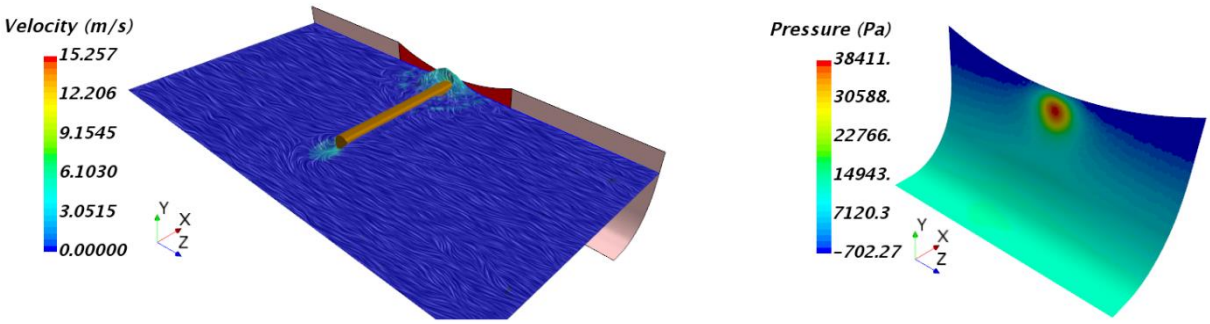

Figure 4.29: The velocity field on the water free surface (left) and the relative pressure load on the prototype (right) for the flotsam in an immediate distance of the rigid wall (rather than flexible wall as in Figure 4.28)

4.4 Concluding remarks

The model was validated through experimental impact tests where the flotsam was made to impact the membrane at inbound velocities of approximately 4 m/s.

The material properties like the density, the Young's modulus, the Poisson's ratio and the thickness of the membrane were measured experimentally (Table 4.1) and applied for the numerical model. Moreover, the reinforcing steel cord on the upper boundary of the numerical model membrane was set up based on the manufacturing material specification (Table 4.2)

Furthermore, Table 4.3 represents the dimensions and the impact velocity of the flotsam, which were applied for both numerical and experimental investigations.
In addition to the similarity in the material characteristics, the numerical model and the experimental membrane shared common boundary conditions, which enabled a valid comparison between numerical and experimental results.

Density	1500 kg/m^3
Young's modulus	1400 MPa
Poisson's ratio	0.1
Thickness	0.075 mm

Table 4.1: Material specification for flexible PVC

Density	7850 kg/m^3
Young's modulus	2100 GPa
Poisson's ratio	0.3
Diameter	10 mm

Table 4.2: Material specification for steel circular stringer on the upper boundary

Mass	330 kg
Diameter	0.4 m
Length	3 m
Velocity at the time of impact	4 m/s

Table 4.3: Material for flotsam

The experimental impact test represented a maximum displacement of 30 cm for the membrane (Figure 4.30), validating well the three numerical models (the standalone Abaqus analysis (the results are presented in chapter 7), the co-simulations with both

the standard mesh technique and the overset mesh technique for the fluid region discretization).

Figure 4.30: Displacements of the membrane for four time stages during the experimental impact investigation in Glauchau (Germany) conducted by the professorship of light structure at TU Chemnitz (Hesse 2017) [109] (The maximum displacement is shown in the third time stage (from left), while the last time stage represents the membrane when returning to its initial form).

The results computed by three different numerical analyses have shown minor discrepancy, which were in well agreement with the experimental outcomes.

Figure 4.31 draws a comparison between the numerical displacement of the memebrane (computed by co-simulations with the overset mesh technique) and the experimental displacement of memebrane when the displacements reached their peak. Evidently, the numerical result is in good agreement with the experimental measurement. Nevertheless, there are subtle differences which can be explained by the difference in boundary condition for two hanging points on the upper edge, the error involved when measuring the material properties of the membrane, the impact velocity, and the impact angle in addition to the numerical errors due to the applied algorithms for solvers, and the discretization approaches.

The slight impact of the methods on the behavior of the membrane stems from the fact that the flotsam was managed artificially to move and hit the membrane with the desired velocity and impact direction in both the experimental and numerical studies, where the fluid medium was somehow in hydrostatic equilibrium.

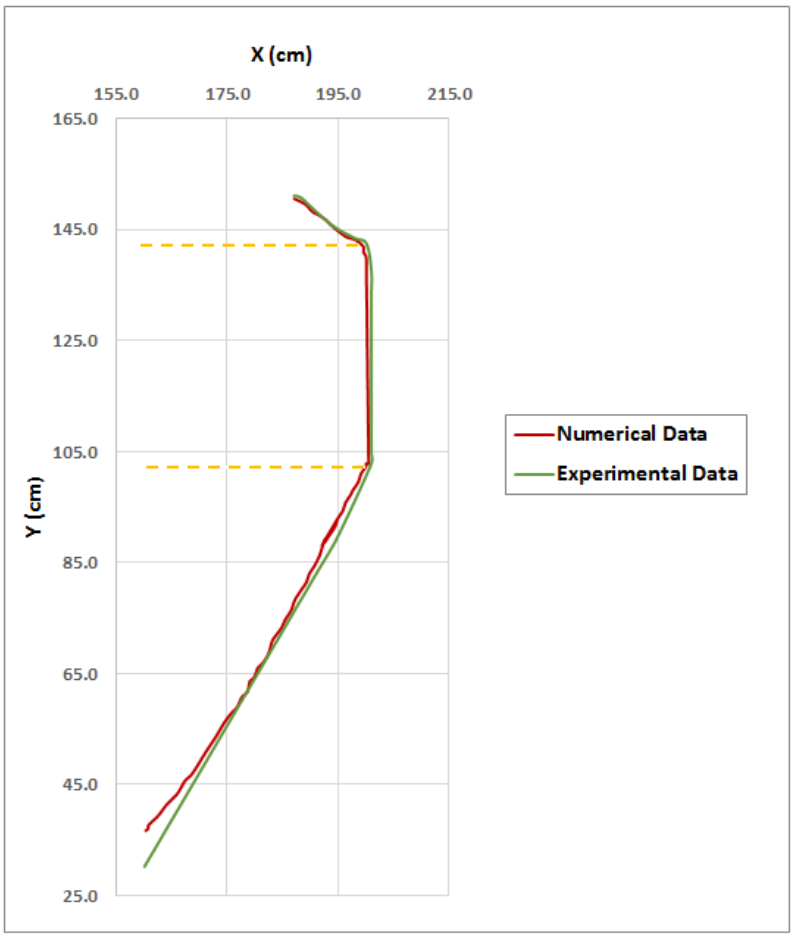

Figure 4.31: Comparison between the numerical (red) and experimental (green) results for the deformation of the membrane 0.104 s after impact (orange dash lines represents the flotsam).

The effect of the fluid flow versus hydrostatic load on the membrane was far less than the extent affected by the impact between the membrane and the flotsam; however, in reality, the fluid domain brought the flotsam to hit the membrane, while the flotsam was managed artificially to move with a high velocity in both the experimental and numerical studies. It implies that a two-way FSI analysis is inevitable when a real impact scenario is investigated.

The most remarkable result to emerge from the comparison between the behavior of the membrane modeled as either rigid or flexible is that the representation of the flexible membrane as a rigid one leads to wrong results due to a significant influence of the membrane behavior on the fluid. In other words, an impact simulation of the behavior of a flexible membrane can be conducted by a standalone Abaqus analysis at the cost of accuracy if the effects of fluid domain on the structures can be defined by mathematical formulations. In contrast, valid results for the fluid domain can be

achieved unless the membrane is simulated as a flexible structure whose deformations have to be computed and transferred to the fluid domain in specific intervals.

The success in stabilizing the FSI simulation dealing with a huge impact on the flexible slender structure interacting with the heavy water medium is a great motivation to conduct further research for a comprehensive study of a more complicated phenomenon where the statistical flood information is incorporated into the dynamic behavior of the fluid domain. To guarantee a reliable performance for the flood protection system against a possible impact, the financial and time investments on more research have to be also economically justified.

However, in order to realize the above scenario numerically, preliminary numerical analyses are required to provide insights into the behavior of light structures in interaction with high Reynolds number water flows and water waves.

For these purposes, the behavior of the down-scale model in response to hydrodynamic loads will be numerically investigated (chapter 6), where motions of a wooden body within a numerical wave channel simulate a one-way piston-type wavemaker. The results will also be compared against experimental findings to verify the accuracy of the numerical model setups and applied numerical algorithms.

The reason why the numerical analysis will be performed on the down-scale model is the space limitation regarding the experimental investigation on the original membrane.

Furthermore, experimental analysis of the interaction between the membrane and hydrodynamic loads is more convenient by motion of a piston-type wavemaker within a channel closed from two ends compared to water flows with high Reynolds number. Indeed, performing a laboratory experiment with water flow requires a pump to circulate water flow. It provides an explanation why the experiment is carried out with water waves instead.

5 Numerical wave generation

In order to ensure a reliable performance for the flood protection system, a further research is required to investigate the interaction between a flexible structure and dynamic high Reynolds number water flows.

In this regard, numerical and experimental analyses will be performed on the down-scale model membrane (chapter 6), which investigate the behavior of the down-scale model in response to hydrodynamic loads. Moreover, the hydrodynamic loads will result from the waves which are generated by translational motion of a wooden body within a numerical wave channel, representing a semi piston movement.

The investigations will be conducted on the down-scale model due to the space limitation related to the experimental investigation on the original membrane.
Although an experimental analysis of the interaction between the membrane and hydrodynamic loads can be carried out in the presence of a high velocity water flow, the generation of a water wave forming a dynamic high Reynolds number water flow adds more convenience for the experimental investigation.

In fact, a water wave can be generated by the translational movement of a piston-type wavemaker within a channel which is closed from two ends. With this setup, in contrary to the case when a high velocity water flow is selected, there is no need to use a pump to circulate the water flow. In addition, an experimental investigation subjected to a water wave can be conducted in a comparable shorter water channel which saves cost and time.

Nevertheless, to capture the water free surface and consequently maintain the wave shape, there are some parameters like the type of the wavemaker, the discretization model, the reflection of the water wave from boundaries, and the appropriate time step which need special attention.

As mentioned before, conducting a numerical simulation in which the interaction between a light structure and a heavy fluid domain is inherently a time consuming task. What makes the target case even worse is the fact that the generation of water waves is not a straightforward matter.

That explains why a preparatory simulation is needed to shed light on the numerical wave generation before proceeding with investigating the behavior of the membrane interacting with the water wave.

This chapter aims at providing an overview of methods and investigations featuring a free surface to explain the requirements as well and finally to compare numerical results for an exemplary case against theoretical findings.

To produce waves in water tanks, flap-type, plunger-type, and piston-type wavemakers are common to use, which are distinct from each other solely based on their motion.

The piston-type wavemaker consists of a vertical board with translation in the horizontal direction (back and forth) (Figure 5.1).

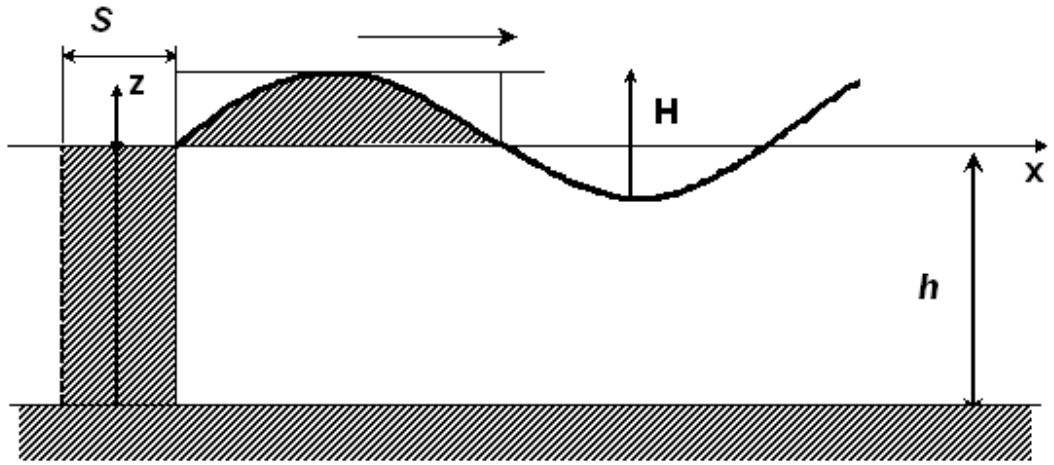

Figure 5.1: The piston-type wavemaker (Kusumawinahyu et al. 2006) [110]

In Figure 5.1, X and Z stand for axes of a three-dimensional Cartesian coordinate system. Moreover, S, h, and H represent the stroke of the wavemaker, the water depth, and the wave height, respectively.

In shallow water, it is more efficient to generate the waves by a piston wavemaker because the piston motion is more similar to the water particle trajectories under the waves, where the horizontal velocities of the water wave particle over the water column remain almost constant. Moreover, evanescent standing waves have less influence on results compared to the flap wakemakers and the plunger wavemakers. Also, a piston wavemaker needs a shorter wavemaker stroke than a flap wavemaker to achieve an identical wave height. While a flap-type wavemaker is the hinged board revolving around a rotation, a plunger-type wavemaker comprises the solid body oscillating vertically around the mean water level, where the displacement of the fluid by means of the vertical motion contributes to the wave motion.

In contrast, in deeper water, the flap wavemakers and the plunger wavemakers are more convenient devices to generate waves on account of the fact that the wave motions are restricted to near the surface. In fact, a piston wavemaker demands more energy to move in deep water.

At the current work, the generation of the waves by a piston wavemaker will be followed because a shorter wavemaker stroke is required to capture an identical wave height which results from a flap wavemaker. It is evident that a shorter wavemaker stroke implies a shorter water wave channel which makes savings in the cost of the numerical and experimental analyses.

Linearized wavemaker theory contributes to the estimation of the amplitude of the progressive wave (the desired wave) radiating away from the wavemaker, and the shape of the evanescent modes which exist near the wavemaker.

The surface tension at the air-water interface is assumed to be negligible, which is typically a valid simplification for free water surface flows without capillarity, cavitation, and droplets.

The free surface is featured to satisfy two requirements; the kinematic and the dynamic free surface conditions (Faltinsen 1993) [111]. The former enforces a particle on the free surface to remain on the free surface, while the latter imposes the equality between the water pressure and the atmospheric pressure at the free surface.

Free surface treatment methods are divided into two main categories, namely interface tracking methods and interface capturing methods.

In the interface tracking methods, a sharp interface (boundary) represents the free surface needed to be followed during the solution. In the interface tracking methods, the mesh has typically to be updated to accommodate new free surface shapes.
The interface tracking techniques work according to the deforming spatial domain/stabilized space time (DSD/SST) formulation, where the interface-tracking might require sometimes an overwhelming mesh generation, perhaps too complex or time consuming, which makes it disadvantageous be implemented.

The interface capturing techniques are formulated typically over non-moving meshes, which incorporate an advection equation to the flow equations. The interface function presenting the location of the interface during the solution time evolves from the advection equation. The volume of fluid (VOF) approach, monitoring a volume within a fixed domain which encircles the free surface, belongs to the category of interface capturing methods.

The VOF approach implements the function of C, where a value of one stands for filled with fluid and zero represents empty. The free surface solution can be captured by solving the following equation.

$$\frac{\partial C}{\partial t} + \nabla \cdot (vC) = 0 \tag{5.1}$$

Where t, C and v stand for time, the phase fraction function and velocity at the interface, respectively.
Moreover, symbols of $\cdot$ and $\nabla \cdot$ represent the scalar product operator and the divergence operator applying on a vector field, which produces a scalar field, respectively.

The implementation of the kinematic and dynamic free surface conditions in the VOF method is affected by the approach defining the two phase flow.

Hirt and Nichols (1981) [112] solved the flow equations only for the liquid phase, where a pressure interpolation scheme enforced the kinematic and dynamic free surface conditions on the correct boundary location.

In Muzaferija's approach (Muzaferija and Peric 1999) [113], both the air and water phases were assumed as a single fluid with varied properties (like pressure, viscosity) in accordance with the volume fraction, where the kinematic and dynamic free surface conditions were imposed implicitly on the solution.

Discontinuities regarding the VOF method necessitate some special care for the discretization of the convection term and the time step as well as to capture a sharp interface. The issue with regard to the first order upwind is a false diffusion, while the higher order schemes, such as second order central differencing or Crank-Nicholson suffer from an unboundedness problem.

The high resolution interface capturing (HRIC) scheme (Muzaferija and Peric 1999) [113] have succeeded in the elimination of issues with the convective transport of immiscible fluid phases based on the normalized variable diagram (NVD), which makes it a proper scheme to follow sharp interfaces.

The normalized variable diagram (NVD) approximates the normalized cell face value in conjunction with the Courant number by a correlation between the cell face with three neighboring cells in the downwind, central, and upwind positions.

From mathematical viewpoint, the Courant-Friedrichs-Lewy (CFL) condition is a necessary condition for convergence in the numerical solution of certain partial differential equations (usually hyperbolic PDEs) by explicit time integration schemes.

For the one-dimensional case, the CFL condition is defined as follows:

$$CO = v\frac{\Delta t}{\Delta x} \leq CO_{max} \tag{5.2}$$

where CO, v, Δt and Δx denote the dimensionless Courant number, the magnitude of the velocity, the time step, and the length interval, respectively.

The CFL imposes consequently a limitation on the time step so that the time step must be less than a certain time in many explicit time-marching numerical schemes; otherwise stability issues or incorrect results are inevitable.
The value of CO_{max} is dependent on the applied discretization, especially if the method is explicit or implicit. For an explicit time-marching method, CO_{max} can typically set to 1. Implicit time-marching procedures exhibit more numerical stability, where larger values of CO_{max} may be tolerated.

The research on waves is conducted also empirically, for instance by Ursell et al. (1960) [114], Keating et al. (1977) [115], and Patel and Ionnaou (1980) [116] for piston and flap-type wavemakers.

Ursell et al. (1960) [114] conducted experimental measurements on the waves generated by a piston type wavemaker for different wave steepnesses.
Their results exhibited that the measured wave heights (for large wave steepnesses) are typically 10 % less than the values estimated on the basis of the linear wave theory.

The first theory on linear forced waves was introduced by Havelock (1929) [117] with the assumption of inviscid water flow with finite depth for piston-type and flap-type wavemakers. Biesel and Suquet (1951) [118] presented later linearized solutions for both flaps and piston-type wavemakers.

To analyze the generation of long waves, classical linear wave theory was developed to second-order accuracy by Madsen (1971) [119].

The high discrepancy in the wave troughs predicted for large waves based on the second-order wave theory promoted the development of higher order solutions (Dean and Dalrymple, 1991) [120].

The third order theory proposed by Borgman and Chappelear (1957) [121] and fifth order theory developed by Fenton (1985) [122] are typical examples.

Nevertheless, the extension of the wave theory to higher orders was extremely complicated. Consequently, waves have been studied numerically as an alternative approach.
Numerical investigation facilitates many researches which can not be carried out by analytical methods, for instance the study of surface waves in the interaction with an arbitrary shaped solid object.
Every approach to capture the free surface has been implemented by many researchers. Exemplary works will be presented as follows:

Kim et al. (2001) [123] simulated numerically 3-D nonlinear multi-directional waves by the help of a finite difference method and a modified marker-and-cell (MAC) method. To dissipate the reflected outgoing waves, an artificial damping zone at the end of the tank was devised.

Sun and Faltinsen (2006) [124] developed a 2-D numerical tank using the boundary element method in order to simulate the coupling between an elastic cylindrical shell and the water free surface flow.

A three-dimensional higher order boundary element model (HOBEM) was implemented by Ning and Teng (2007) [125] to investigate a fully nonlinear irregular wave tank. The model was further developed by Ning et al. (2008) [126] to simulate nonlinear regular and focused waves for an infinite water depth. The dissipation of the outgoing waves was achieved by imposing a spatially varying artificial damping on the free surface. This method was used later by Yan and Liu (2011) [127] to study nonlinear wave-wave and wave-body interactions within a 3-D numerical wave tank.

Wu and Hu (2004) [128] applied the velocity potential theory in addition to a FEM formulation within the numerical tank equipped with a wavemaker in order to simulate the mutual influence for water waves and a floating cylinder. Moreover, a combination of a damping zone and the Sommerfeld condition was implemented in the backside of the tank to deal with wave reflection issues.

Hadžić et al. (2005) [129] used the commercial CFD code of Comet to study the motion of a floating rigid body (with 6 degrees of freedom) subjected to large amplitude waves inside a 2-D NWT, where the body movement and the CFD code solution communicated by user-coding interfaces.

The CFD code of Comet was later utilized by Agamloh et al. (2008) [130] to develop a 3-D numerical wave tank, where fluid-structure interaction of a water wave and a cylindrical ocean wave energy device was of interest.

Sriram et al. (2006) [131] used a numerical piston type wavemaker for the generation of 2-D nonlinear waves, where the finite element approach along with a cubic spline approximation was implemented to solve the governing equations. Their investigation aimed at modeling sloshing and wave interaction with a submerged obstacle.

Liang et al. (2010) [132] studied experimentally and numerically (using the commercial CFD software of Fluent) a piston type wavemaker for the generation of an irregular wave train.

Lal and Elangovan (2008) [133] investigated linear water waves generated by a flap type wavemaker by means of the finite volume based package of Ansys CFX, where the NWT was equipped with a beach at the end of the tank to damp a reflected wave.

Prasad et al. (2017) [134] used the commercial CFD software of Ansys CFX to simulate the waves generated by a piston-type wakemaker in a 3-D numerical wave tank (NWT). The numerical results were compared against the experimental data, where the experimental setup consisted of a turbine.

Spence's work (2014) [135] on his thesis was carried out by the CFD software of Star CCM+ on the interaction between the free surface flow and vessels, representing a satisfactory result for a ship resistance prediction.
Gomes and his co-workers (2009) [136] suggested two different numerical methodologies to generate regular gravity waves by a piston-type movement, where the Fluent solved the free surface flow.

In the first approach, a user defined function (UDF) controlled a change in the velocity of a moving wall, where the wall motion was defined based on a equation proposed by Liu et al. (2008) [137].

The second approach developed by Horko (2007) [138] imposed an entry velocity (velocity inlet) on the wave generator by means of a user defined function (UDF). The velocity was modified based on the equations describing the motion of the free surface in Stokes second order theory.

Quân (2009) [139] presented in his master thesis a mathematical formulation for the wave generation using a piston-type and a flap-type wavemaker in a basin, as follows and achieved results by the Python programming language.

If the horizontal displacement of the wavemaker is defined as:

$$x = \frac{S(Y)}{2} sin(\sigma t) \tag{5.3}$$

where $S(Y)$, σ and t denote the stroke of the wavemaker, the angular frequency of the wavemaker and time, respectively.

Moreover, the stroke of the wavemaker would be described as follows.

$$S(Y) = \begin{cases} S, & piston\ motion \\ S\left(1 + \frac{Y}{h_w}\right), & flap\ motion \end{cases} \tag{5.4}$$

where Y and h_w are the vertical coordinate with the origin on the water free surface and the water depth, respectively.

To generate water waves by means of a wavemaker, several evanescent standing waves would be produced in addition to the desired progressive wave.

In the next section, the theoretical formulations for the water waves generated by either a piston wavemaker or a flap wavemaker will be discussed.

5.1 Theoretical estimation of the waves

By applying the linearized form of the dynamic and kinematics free surface boundary conditions, the governing equations can be achieved.

$$\sigma^2 = g k_p \, tanh(k_p h_w) \tag{5.5}$$

$$\sigma^2 = -g k_s \, tan(k_s h_w) \tag{5.6}$$

where g, k_p, k_s and σ are the gravitational acceleration, the wave number for the progressive wave, the wave numbers for the standing waves and the angular frequency of the wavemaker.
The subscripts p and s on k indicate progressive and standing waves, respectively.

The angular frequency of the wavemaker (σ) can be related to the period of the desired water wave (T), as follows:

$$\sigma = \frac{2\pi}{T} \tag{5.7}$$

Eq. (5.5) represents the dispersion relationship for the progressive wave, whereas eq. (5.6) defines the wave numbers for the standing waves which have exponentially decreasing amplitudes in proportion to the distance from the wavemaker.

To approximate graphically the roots for the equations of (5.5) and (5.6), they can be written as eq. (5.8) and eq. (5.9), respectively.

When $\frac{\sigma^2 h_w}{g} = 1$, the new equations can be solved as shown in Figure 5.2 and Figure 5.3, respectively.

In Figure 5.2, two different curves which represent respectively the left and right sides of eq. (5.8) are plotted versus $k_p h_w$. The intersection of the curves contributes to the wave number for the progressive wave (k_p).

$$\frac{\sigma^2 h_w}{g} . \frac{1}{k_p h_w} = tanh\left(k_p h_w\right) \tag{5.8}$$

$$\frac{\sigma^2 h_w}{g} . \frac{1}{k_s h_w} = -\, tan(k_s h_w) \tag{5.9}$$

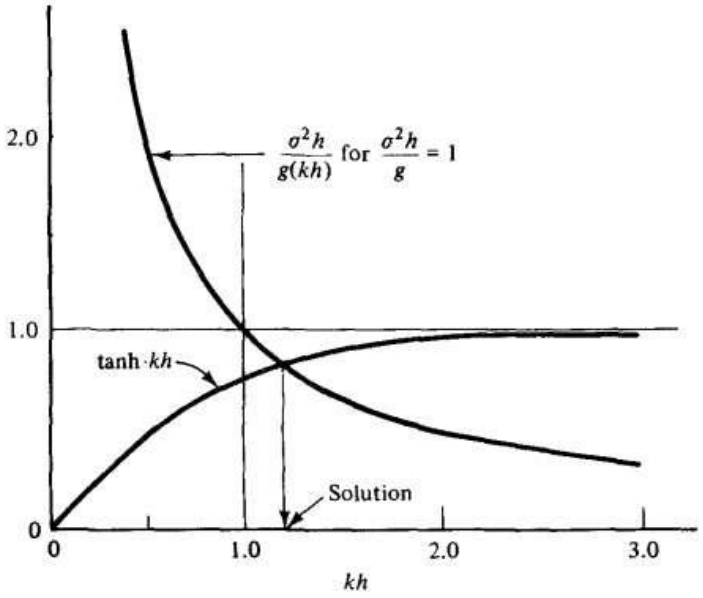

Figure 5.2: The solution for the progressive wave (Here h represents the water depth, where the horizontal axis is in m and the vertical axis in m^{-1}) (Quân 2009) [139].

Likewise, the left and right sides of eq. (5.9) are exhibited by two different curves (Figure 5.3) plotted relative to $k_s h_w$, where their intersections result in the wave numbers for the standing waves (k_s).

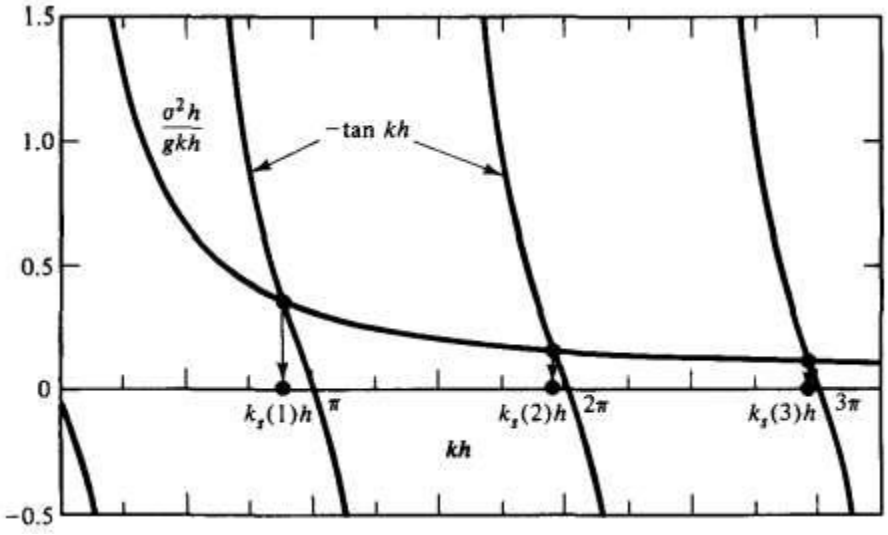

Figure 5.3: The solutions for the standing waves (Here h represents the water depth, where the horizontal axis is in m and the vertical axis in m^{-1}) (Quân 2009) [139].

By given parameters like the desired wave height of H (refer to eq. (5.13) and eq. (5.14)), the wave period of T (the wavemaker angular frequency of σ as a result), and the depth of the water wave (h_w), eq. (5.5) obtains only one solution, which implies the generation of one progressive wave. In contrast, eq. (5.6) gives an infinite number of solutions, where there is an exponential decrease in the amplitude of the countless standing waves with an increase in the standing wave number (k_s). That is why some smallest roots, for example three first roots have to be found.

By means of a formulation proposed by Fenton and McKee (1990) [140] (eq. (5.10)) for the wave length (L), the root of eq. (5.5) for the progressive wave, namely k_p, can be approximated as follows.

$$L = L_\infty \left(tanh\left(\frac{\sigma^2 h_w}{g} \right)^{\frac{3}{4}} \right)^{\frac{2}{3}} \tag{5.10}$$

$$L_\infty = g\frac{T^2}{2\pi} \tag{5.11}$$

$$\Rightarrow k_p = \frac{2\pi}{L} \tag{5.12}$$

For k_s, three starting estimates of three roots can be made from Figure 5.3 as $\frac{\pi}{\mathrm{h_w}}$, $\frac{2\pi}{\mathrm{h_w}}$ and $\frac{3\pi}{\mathrm{h_w}}$, respectively.

The stroke of the piston and the wave height are correlated as follows (Dean and Dalrymple 1991) [120]:

For flap wavemaker:

$$\frac{H}{S} = 4\frac{sinh(k_p h_w)}{k_p h_w} \cdot \frac{k_p\, h_w sinh(k_p h_w) - cosh(k_p h_w) + 1}{sinh(2k_p h_w) + 2k_p h_w} \tag{5.13}$$

For piston wavemaker:

$$\frac{H}{S} = \frac{2\left[cosh(2k_p h_w) - 1\right]}{sinh(2k_p h_w) + 2k_p h_w} \tag{5.14}$$

where H, S, k_p, and h_w are the wave height, the stroke of the piston type wavemaker, the wave number for the progressive wave and the water depth, respectively.
The following study only focuses on the precision of the waves generated by a piston type wavemaker within the overset mesh framework, which will be used in the next chapter in a more complicated simulation. Next section presents a numerical model setup for a simple geometry which provides a good perspective for the target FSI numerical investigation. In order to generate a water wave, a piston wavemaker is preferred because the piston motion is more suitable in shallow water. In addition, evanescent standing waves affect results to a lower extent in comparison with the flap wakemakers and the plunger wavemakers. Also, a piston wavemaker needs a shorter wavemaker stroke than a flap wakemaker to achieve an identical wave height, which results in less required space for an experimental analysis.

5.2 Numerical wave tank setup

The piston type wavemaker was represented as a moving boundary (paddle) at the left end of the NWT, where it moves horizontally with a constant velocity and a sinusoidal functional speed, respectively. The motion of the paddle produced the waves propagating perpendicularly to the paddle surface

To generate waves, the wave characteristic parameters, such as the wave period and the wave height are of importance. Knowing these parameters, the motion of the piston would be estimated based on theoretical formulations.

The motion of the paddle inside the fluid flow was prescribed with the stroke, the water depth and the wave period of 5.8 cm, 15 cm and 1s, respectively.

To alleviate the effect of an upper boundary on the formation of the surface waves, the upper boundary was located in a far distance from the free surface. For this rea-

son, the height of the NWT was selected as 1 m, while the width of the tank was small to save the computational cost.

In order to save the simulation cost, the channel was firstly discretized with a coarse pattern. However, the applied coarse meshes were not able to resolve the wave shape. To capture the wave shape, the mesh refinement was implemented on the discretized model so that the guideline of Siemens AG (2019) [88] regarding waves was observed. In detail, 80 cells in the wavelength and 20 cells for the elevations of the wave crest relative to free surface enabled the wave shape to be resolved.

Two different simulations were conducted based on the moving boundary motion with a constant velocity and a sinusoidal functional speed, respectively, where the total length of the NWT was modeled as 7.26 m, which was about 6.6 times the wave length. A further simulation according to the moving boundary motion with a constant velocity was carried out to investigate the effect of the channel length and mesh refinement on the results. The total length of the NWT was increased to 13.26 m, where a mesh refinement was implemented along with the water flow direction.
Despite efforts at the simulation with the standard mesh technique in the Star CCM+, piston-type wave generation could not be modeled with such a discretization method. Therefore, the movement of the wall boundary, which replicates a piston type motion, was performed by using the overset mesh technique.

The overset region was constructed to accommodate the modeling of the piston type wavemaker. The region shared dimensional characteristics of the background region, with the exception of the length which was 15 cm.

The immiscible water-air flow in a channel was modeled by the volume of fluid multiphase model (VOF model) and the realizable k-ε two-layer turbulence model.

The Star CCM+ solved the Navier Stokes equations in the discretized form based on the finite volume approach, where the high resolution interface capturing (HRIC) scheme was responsible to capture sharp interfaces between the phases.

For the background region, all boundaries except both the bottom and the moving boundary were modeled as symmetry planes, where the excluding boundaries were represented as slip walls (Figure 5.4).

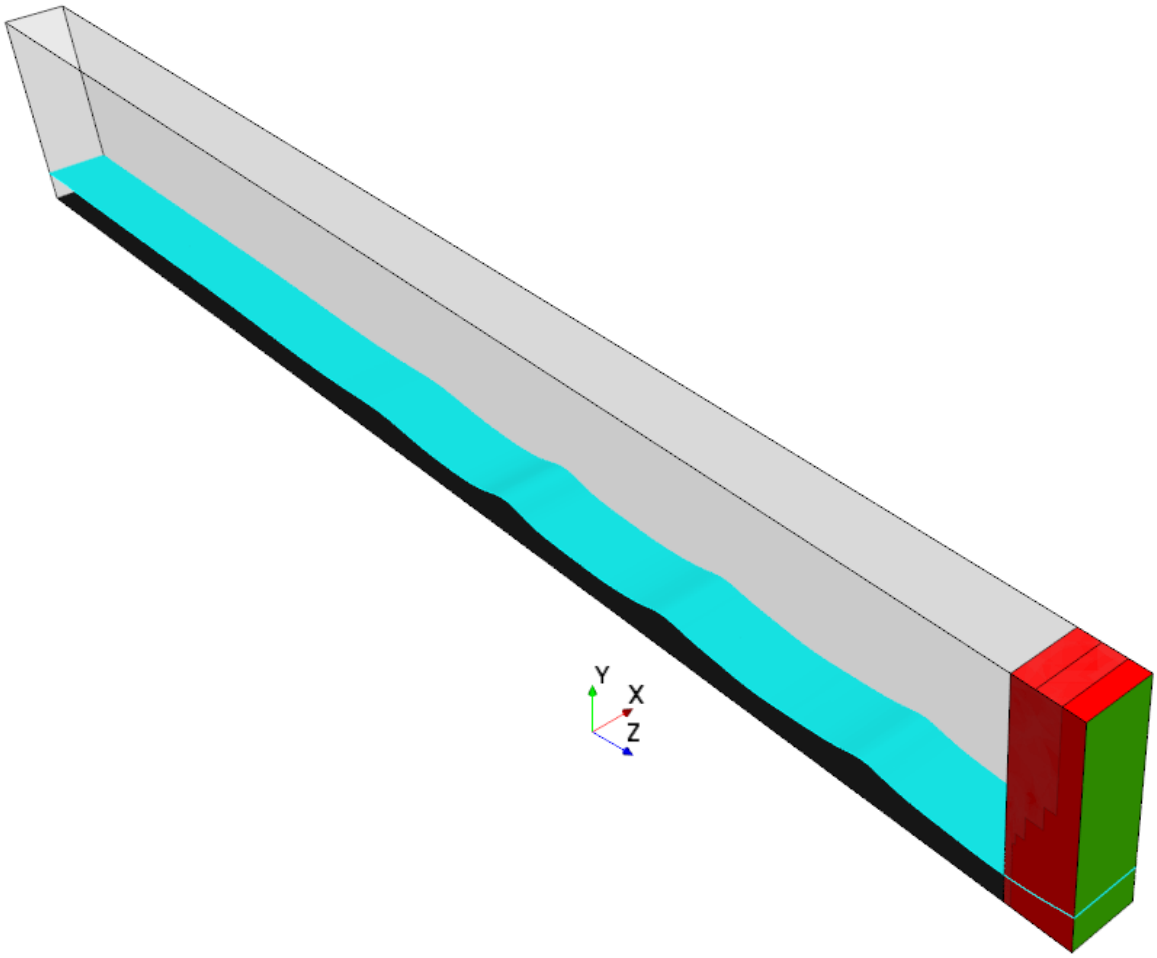

Figure 5.4: The numerical representation and the boundary conditions of the numerical wave tank (NWT) with a wave maker (green paddle): the symmetric boundaries overlapping with the overset region (red), wall boundary for the bottom of the channel (black), the wall boundary for the tank end overlapping with the paddle (green), symmetric boundary for the remainder (grey), (The water wave is represented by cyan).

Within the overset region, all boundaries in contact with the boundaries of the background region shared the same boundary condition, i.e. the side walls, the bottom, the top and the moving end, whereas the only remainder boundary depicted overset interface (Figure 5.5).

For computational domain discretization, a trimmed cell mesher and a prism layer mesher were used (Figure 5.6). In Figure 5.6, the discretized water tank is depicted in the bottom, where the top enlarges a detail of the mesh in the vicinity of the water wave represented by cyan color.

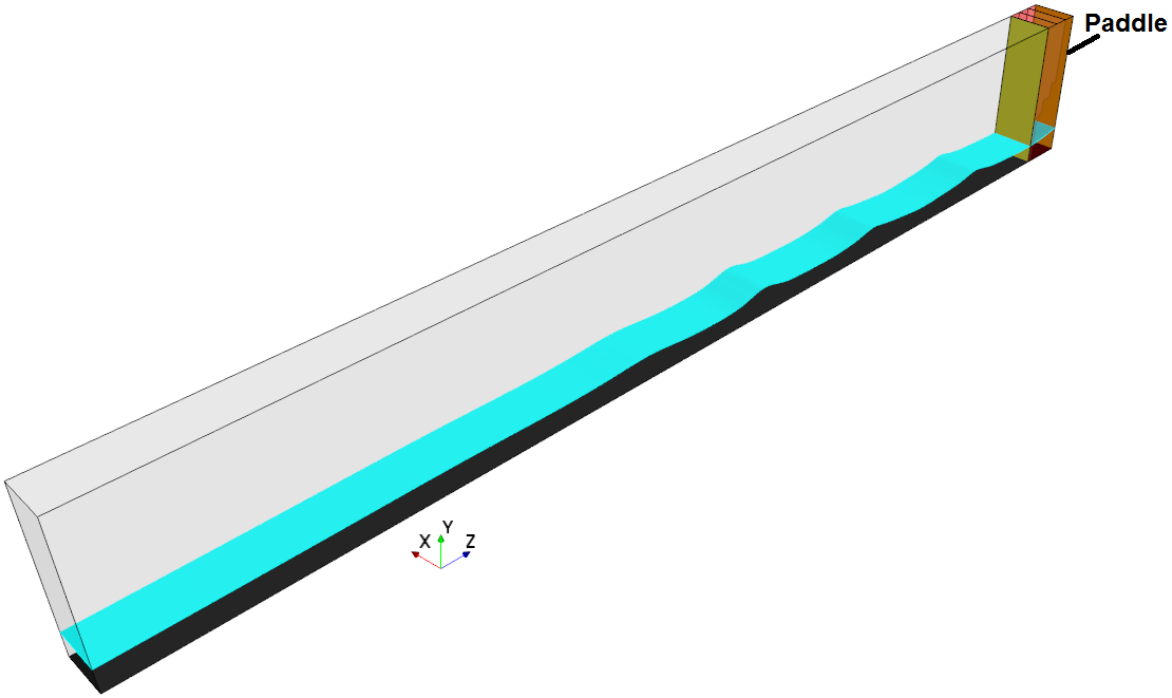

Figure 5.5: The boundary conditions setup for the overset region: the overset interface (olive green), wall boundary for the bottom of the overset region (black), moving wall for the paddle (parallel to the yellow interface), symmetric boundary for the red boundaries within the overset region in conformity with the grey symmetric boundaries within the background region (The water wave is represented by cyan).

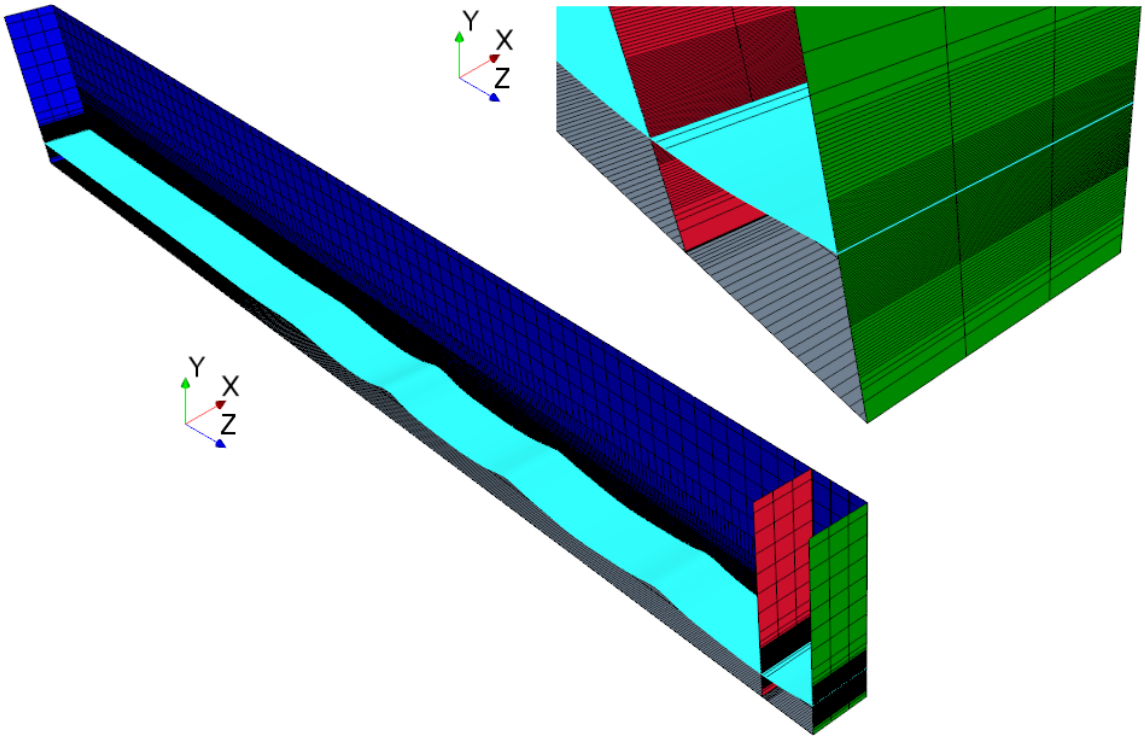

Figure 5.6: The discretization of the numerical wave tank with trimmer mesh, on the symmetric walls (blue), on the paddle (green), on the overset interface (red) and a zoom of the refinement of the mesh nearby the water level (top)

The overset mesh type is represented in Figure 5.7, where the overset cell type of -1 (dark blue), 0 (cyan), 1 (green), 2 (yellow), and 3 (red) indicate inactive cells, active cells, donor cells, active intermediate cell layers used by the hole-cutting process, and overlapping cells, respectively.

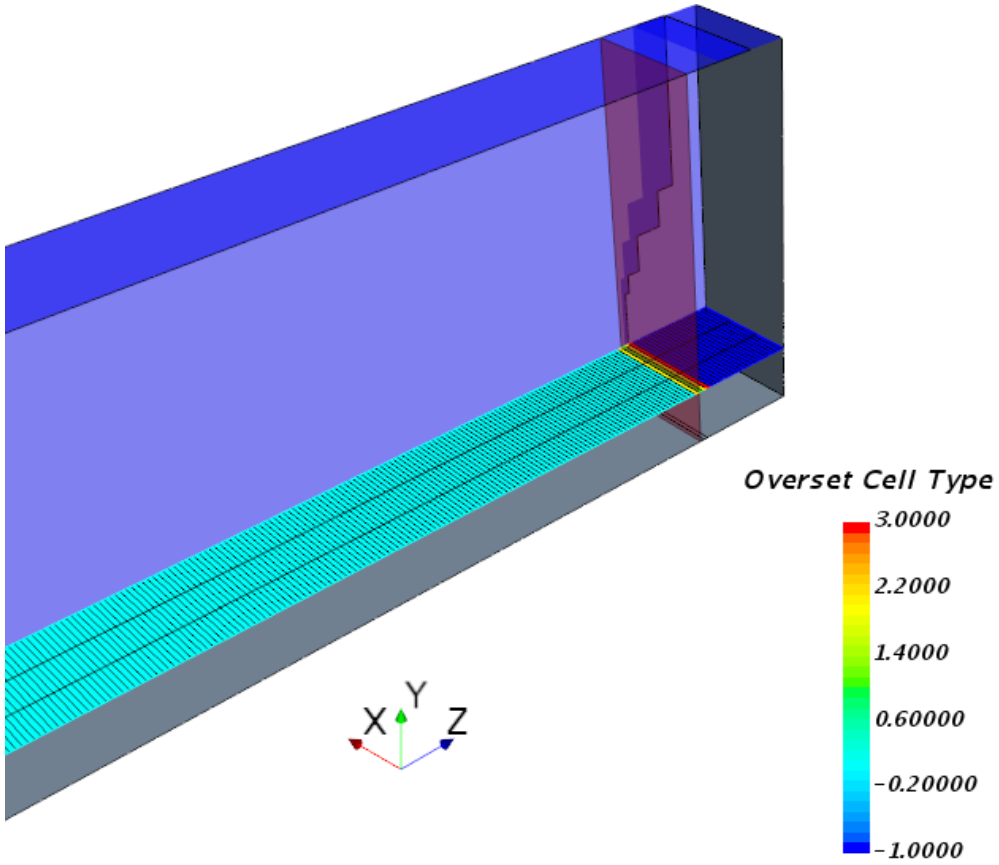

Figure 5.7: The overset cell type

5.3 Results

The formation of a wave chain as it travels from right to left is depicted in Figure 5.8 to Figure 5.12. It takes the wave about 6.6 s (6.6 T) and 12 s (12 T) in the simulations without and with the mesh refinement along with the water flow direction, respectively to reach the back wall at the left. As expected, the waves will be dissipated with the highest rate when the channel is extended and meshed finer (red lines).

For all the simulations, the wave height was monitored and compared with the estimated wave height based on the theory. The theoretical equations presented in section 5.1 (for a sinusoidal moving boundary) contributed to compute the wave height and wave length of 4.959 cm and 1.1041 m, respectively.
In detail, the theoretical equations predict the wave chain whose peaks and troughs are located in the heights of 0.175 cm and 0.125 cm, respectively.

The identical model was executed three times, where there were distinctions in the piston movement and the mesh refinement.

The first and second results (shown by blue and red lines, respectively) were captured by a piston movement with a constant velocity. The second simulation represented the wave shapes for the simulation with refined mesh in the flow direction, where the piston moved with the same velocity as the first one.

The third simulation was discretized as similar as the first one, but the piston motion was defined by a sinusoidal function as described by eq. (5.3) (the results were plotted by yellow lines).

After one period, the waves generated by the piston movements with two different paces share the troughs in common, which are almost similar to the estimated theoretical magnitude of 2.5 cm deeper than the water level. However, the waves' crests are totally different from each other and they are far lower than the estimated wave crest based on theoretical equations, where the numerical results predict a higher crest for the wave generated by the sinusoidal piston motion compared to the constant velocity piston movement. In detail, a peak of 0.1638 m versus a maximum of 0.1564 m is achieved for the sinusoidal piston motion and the constant velocity piston movement, respectively (Figure 5.8).

After 2 s (the second period), the waves die out at the front, as expected. In comparison with the theoretical computed amplitudes, the generated waves during the second period have higher amplitudes at the crests of the waves and lower amplitudes at the troughs. The numerical waves share more analogy in troughs compared to the crests. The wave generated by the sinusoidal piston motion (yellow line) meets better with the theoretical wave at the trough, while the wave generated by constant pace and fine mesh (blue line) has more similar amplitude compared to the theoretical data at the crest. The most deviation from the theoretical magnitude for the amplitude at the crest is represented by the wave generated by sinusoidal piston motion (yellow line) (Figure 5.9).

The generated wave by sinusoidal piston motion during the third period (yellow line) has the higher and less amplitude than the theoretical wave at the crest and trough, respectively. Nevertheless, the other numerical waves (blue and red lines) are in good agreement with amplitude computed by theoretical formulations at the crest, albeit with less amplitude compared to theoretical data and even the generated wave by sinusoidal piston motion (yellow line). Moreover, a similarity for the numerical waves

with constant velocity (red and blue lines) can be observed, where the waves have more in common at their crests (Figure 5.10).

Importantly, the waves nearby the moving boundary are also affected by standing waves.

In the figure representing the results for 4 s after the piston movement (Figure 5.11), the numerical waves gain in amplitudes in their troughs in comparison with the other results (Figure 5.8 to Figure 5.10, and Figure 5.12), while their amplitudes at crests have decreased. As a result, the highest agreement between theoretical and numerical waves can be seen (especially regarding sinusoidal movement after one wave length away from the piston and in the downstream of the damping zone).

Further movement of the piston triggers more side effects on the progressive waves, which results in a decrease in similarity between the numerical and theoretical progressive waves (Figure 5.12).

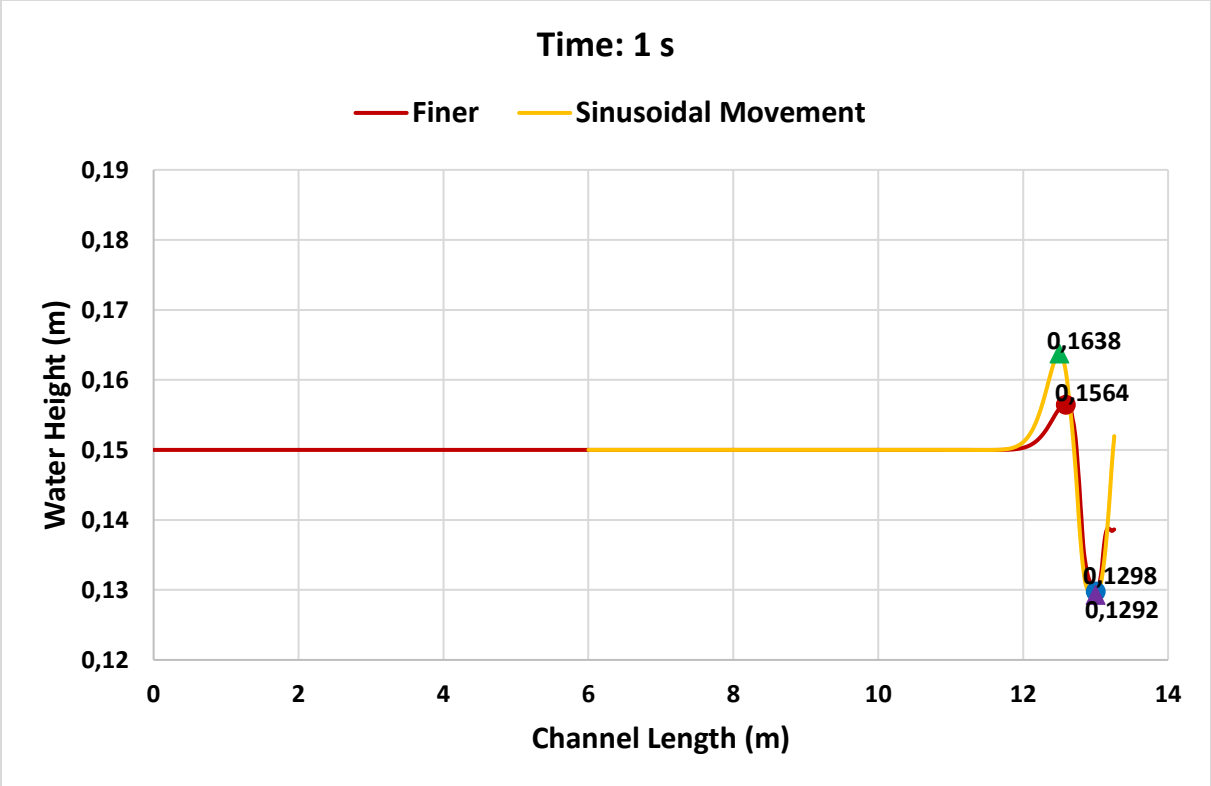

Figure 5.8: The comparison between the numerical wave shapes 1 s after the piston movement

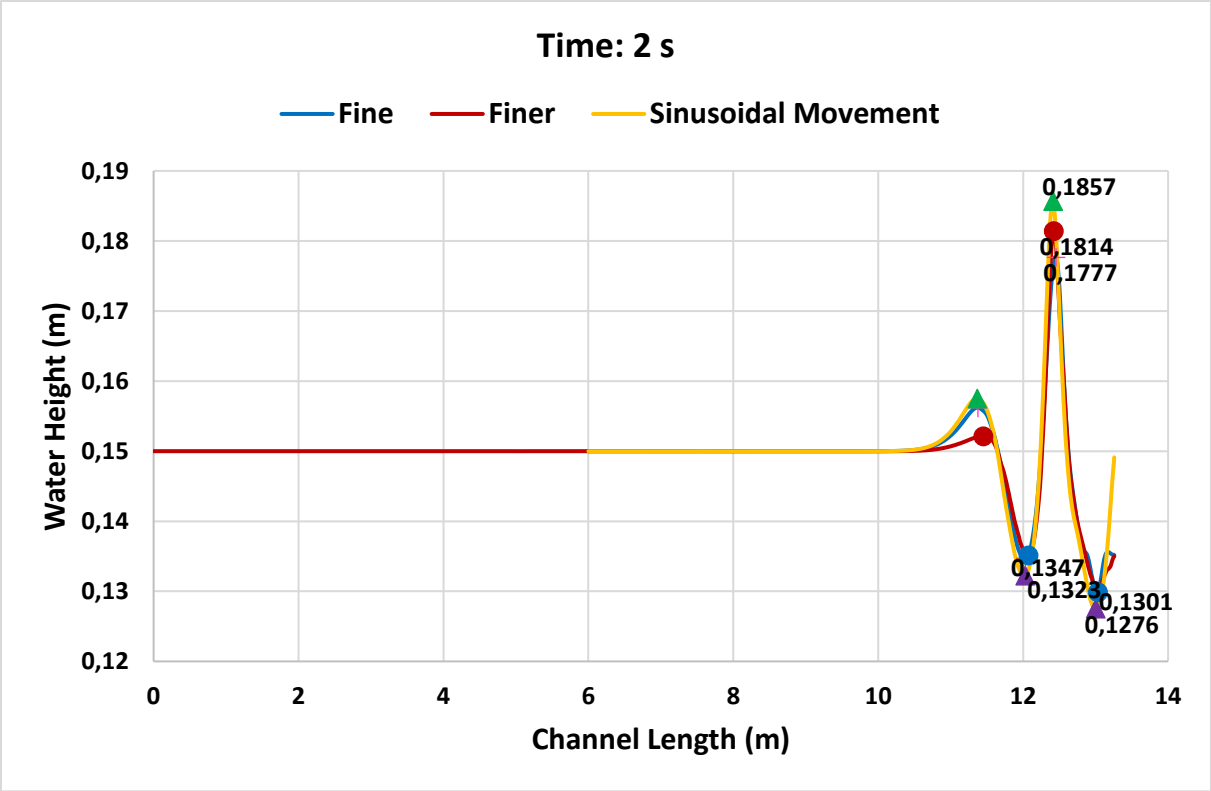

Figure 5.9: The comparison between the numerical wave shapes 2 s after the piston movement

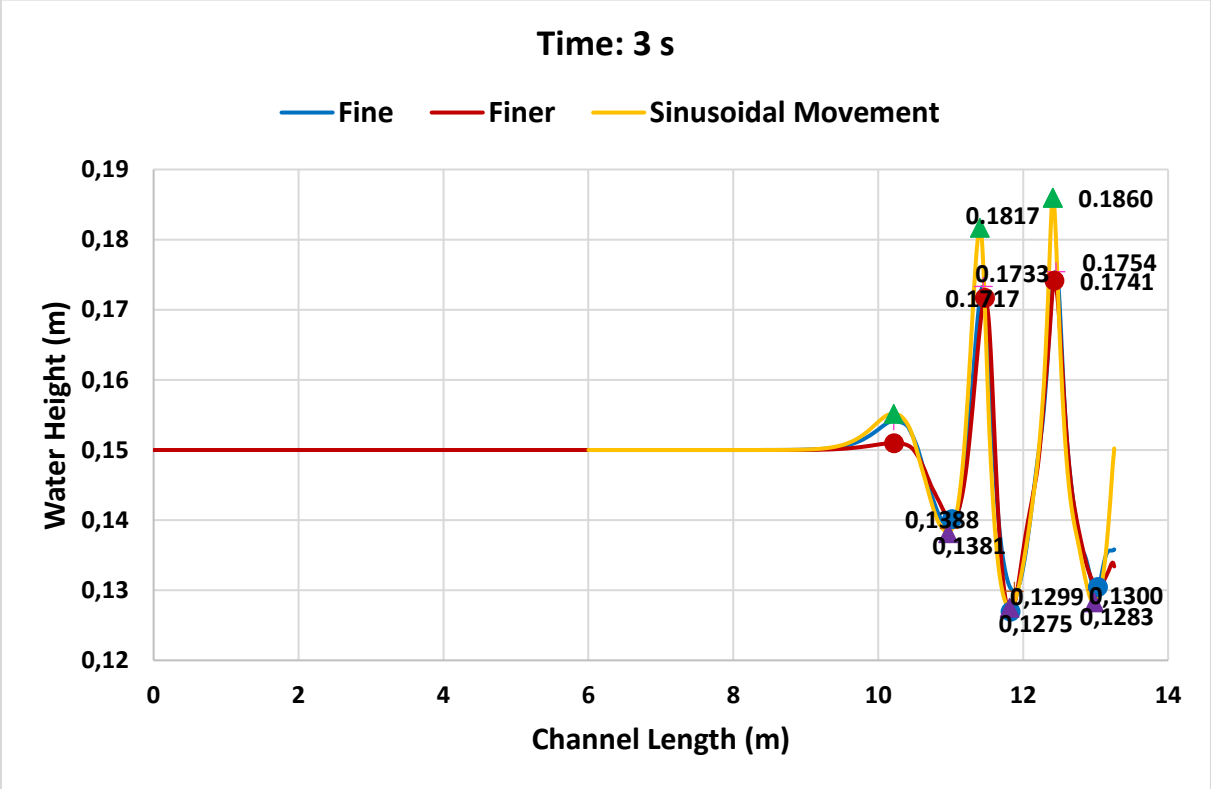

Figure 5.10: The comparison between the numerical wave shapes 3 s after the piston movement

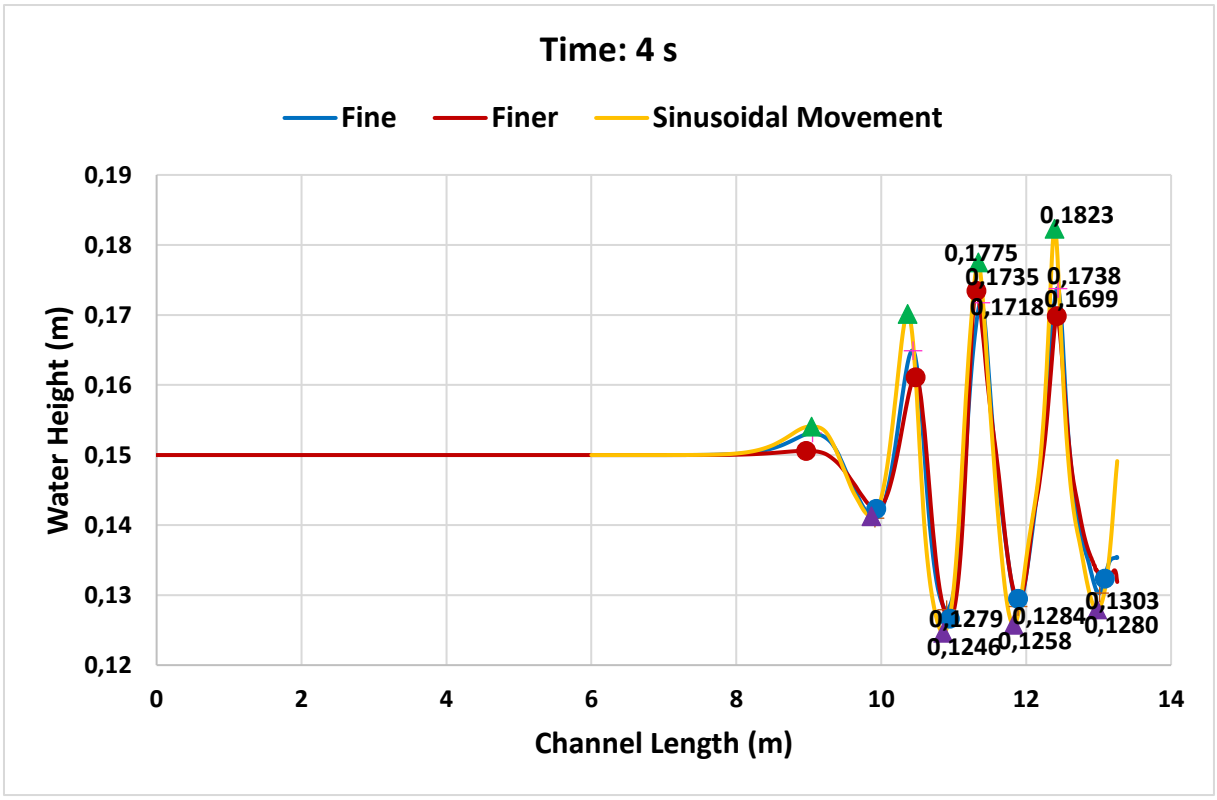

Figure 5.11: The comparison between the numerical wave shapes 4 s after the piston movement

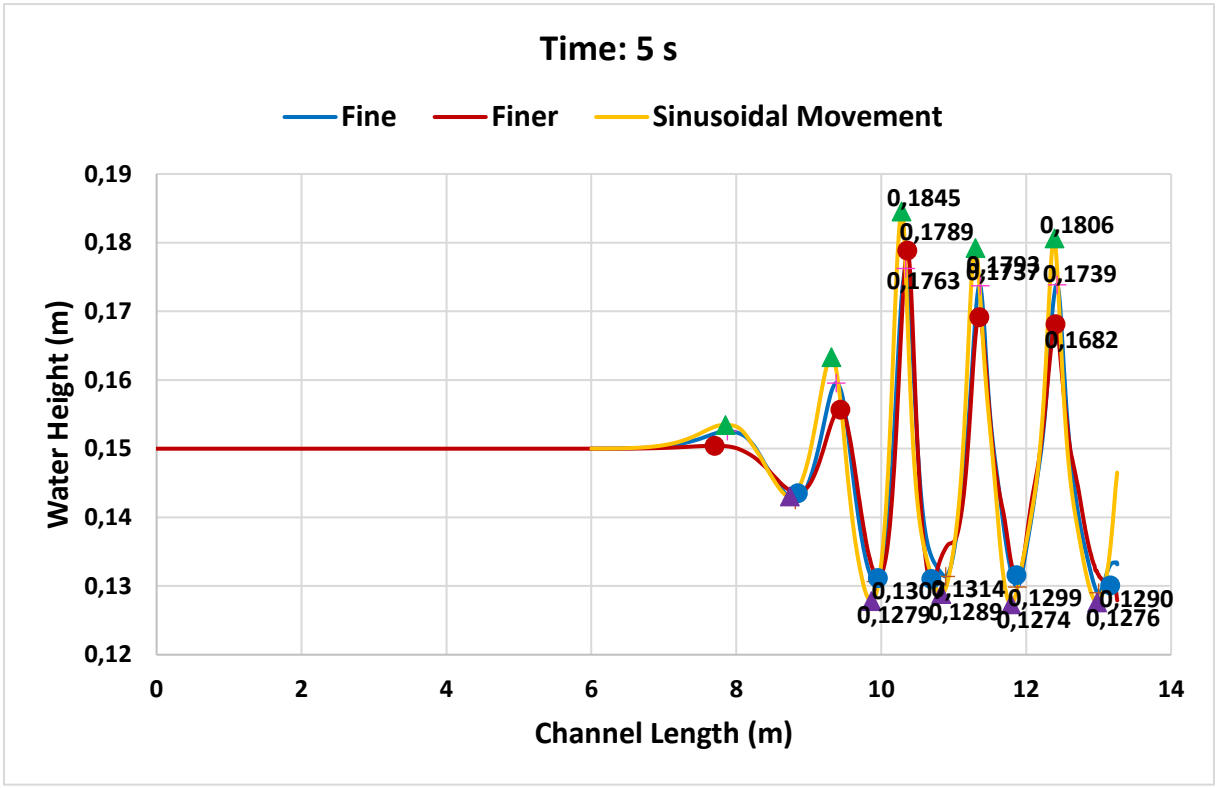

Figure 5.12: The comparison between the numerical wave shapes 5 s after the piston movement

5.4 Concluding remarks

This chapter offered an overview of the water wave models, the methods to capture water wave efficiently or to prevent the reflection of the water wave. Moreover, the theoretical formulations to compute the water wave generated by either a flap wavemaker or a piston wavemaker were presented. Finally, different numerical simulations for the piston wavemaker were conducted, where the results were compared against theoretical data. The reason why the piston wavemaking was numerically investigated is that the piston-type water wave, which is more favored for shallow water flows, will be later in chapter 6 studied.

The simulations exhibit that there exist some discrepancies between the theoretical wave shape and the numerical waves. Similarly, distinctions between the theoretical wave shape and the numerical waves were observed in many other researches conducted on the NWT.

Furthermore, a minor difference between the shapes of the generated wave can be noticed when the discretization of the model was refined. The fact indicates that a further mesh refinement does not improve the results precision.

Nonetheless, the exemplary simulations to capture the waves generated with the piston-type wavemaker were not further followed for different reasons. The first reason is the high computational cost because high cell numbers were needed to capture the shape of waves. Moreover, in our target model represented in chapter 6, capturing an exact shape for the generated water wave is not our main concern. In fact, a compromise between the computational cost and the precision to catch the wave shape has to be forged.

Lessons learned from performing the simulation for the numerical wave tank illuminated preparatory conditions needed for a numerical model setup dealt with a water wave generation.

For instance, the numerical simulations for the waves generated with piston-type wavemaker revealed impossibility for the discretization of the fluid domain with standard mesh models when these types of water waves are of interest. Instead, overset mesh techniques have to be employed to model piston-type water wave generators.

Moreover, some criteria like the minimum number of cells per wavelength and wave amplitude, as well as the time step which are required to be observed were examined. These criteria will be discussed in depth in chapter 6.

Promising numerical results promotes conducting further research in which rigid channel walls are replaced by the down-scale flexible membrane. To save computational cost, this scenario is simplified in a numerical water channel which is enclosed by one flexible membrane connected to the other rigid glasses building the channel walls.

6 Validity of the model with dynamic pressure

Gaining experience with previous numerical investigations such as the structural analysis of the down-scale model, piston-type wavemakers, the co-simulation impact analysis of the full-scale prototype encouraged a further interesting numerical simulation which investigated the interaction between a flexible structure and dynamic water flows.

Moreover, space limitations regarding a laboratory investigation on the original membrane enforced the numerical analysis to be carried out on the down-scale model.

The first simulations for a survey on the fluid-structure interaction for the down-scale model under high Reynolds number water flow were executed in accordance with the experimental model conducted by Schade et al. (2016) [105]. Figure 6.1 depicts Schade et al.'s experimental water channel.

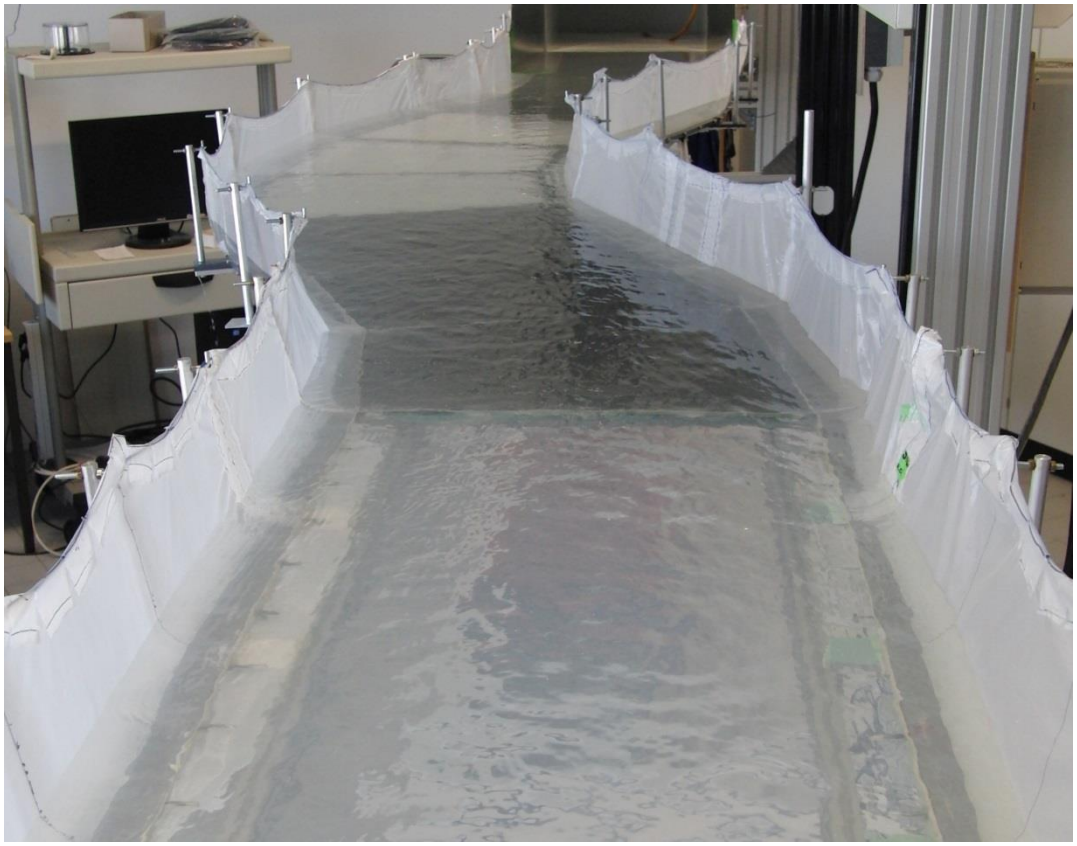

Figure 6.1: Illustration of Schade et al.’s down-scale channel (Schade et al. 2016) [105]

However, the numerical analysis of the model was not successful and terminated even before the velocity change effects reached the membrane (Figure 6.2). The problem ensued from the representation of the baffles (violet) connected to the flexible membrane (grey) within the numerical simulation. The baffles behaved as semi rigid boundaries and floated in conformity with the membrane control points from

one side and the fixed boundaries (inlet boundary (red) and outlet boundary (orange)) on the other side. Due to the fact that they did not deform (in contrast to the physical model) in the way that the fluid domain dictated, the connection between the fluid and the structure was disturbed and finally disrupted.

To eliminate the problem, a further numerical simulation was needed to be conducted, where the model setup had to be adjusted. In the new design, the channel boundaries attached to the target membrane within the numerical simulation had to replicate the structural behavior exhibited in the experimental analysis without the need of a strong coupling with the fluid domain. In other words, with this physical model setup, the boundaries attached to the membrane in the numerical water channel were represented as rigid structures which were in conformity with the physical walls.

Furthermore, an experimental analysis of the interaction between the membrane and hydrodynamic loads can be conducted in the presence of either a high velocity water flow or a water wave. For convenience reasons, the latter was preferred, where the water wave was generated by the movement of a piston-type wavemaker within a channel closed from two ends. In fact, the requirement for a pump to circulate the water flow was eliminated via this selection. Moreover, by the chosen model setup, the experiment can be conducted in a comparable shorter water channel which saves cost and time.

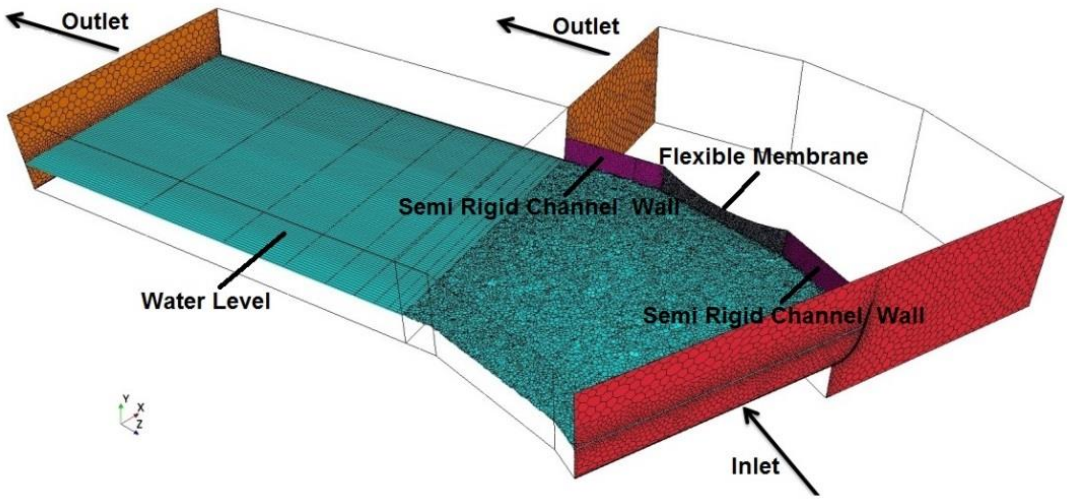

Figure 6.2: Illustration of the model: the coupled flexible membrane (grey); the baffle mimicking the semi rigid channel walls (violet); Inlet (red); outlet (orange); water free surface (aqua)

The numerical model was analyzed by the Abaqus and Star CCM+ co-simulation, which necessitated a new setup for both the fluid and structure domains to accom-

modate properly the inner and outer surfaces of the flexible membrane as the interfaces. The dynamic pressure effects were imposed on the membrane by the water waves which resulted from a translational motion of a body in a free surface water flow.

In order to verify the accuracy of the model, the numerical results were compared against the data collected by the experimental analysis on the physical wave tank. The physical wave tank was constructed so that its representation within the numerical simulation satisfied the boundary requirements for a convergent simulation.

6.1 Wave tank

Generally, waves in numerical water tanks can be produced either with the help of the inlet velocity profile method or the wavemaker method. In the former method, the VOF waves can be incorporated to the flow model. An alternative approach is to define the inlet velocity different from the initial water flow velocity.

The Star CCM+ offers different VOF waves models for the simulation of surface gravity waves on the interface between a light fluid and a heavy fluid, which represents a steadily-progressing periodic motion.

A detailed overview of the available VOF waves models is provided as follows:

Modeling VOF Waves

There are two main theories to model VOF waves in the framework of steady wave problems: Stokes theory and cnoidal theory.
The cnoidal theory took its name from the Jacobian elliptic functions cn() which exist in the description for a nonlinear and exact periodic wave solution (cnoidal wave) of the Korteweg-de Vries equation (Korteweg and de Vries 1895) [141].

The former theory is more suitable to model waves in deeper water, where the steepnesses of waves are assumed to be low.
Nevertheless, the latter is used for the prediction of wave's behavior in shallower water flows, where the ratio of the wavelength to the water depth is greater than ten.

The Star CCM+ offers a variety of VOF wave models: flat wave, first order partial wave, fifth order wave, superposition wave, cnoidal wave and irregular wave.

The cnoidal wave is approximated with the cnoidal theory for shallow water applications, while the remainders (deep water problems) are most appropriately modeled by the Stokes theory.

While a flat wave can be used to model calm water flows, a first order wave generates waves with a regular periodic sinusoidal shape based on a first order approximation to the Stokes theory. The order of the wave can be increased up to five terms in the calculation, where the terms higher than the defined order are ignored.

Likewise, a real wave would be better generated with a fifth order approximation to the Stokes theory of waves than a first order approximation.

There are scenarios involving more complicated patterns for waves when water waves progress from one weather system in spite of a change in wind direction, resulting in a dangerous state with two traveling oblique waves (cross sea). To model the above mentioned waves or spectral waves, a superposition wave model superposes linearly different first order waves.

Moreover, a short-term sea state induced by the vertical displacement sea surface for example can be estimated by an irregular wave.

The water depth, the wave height, the wave length or the wave period and the current flow height are the parameters defining the wave shape and the wave phase of a first order wave or a fifth order wave, while the order of a cnoidal wave is the further parameter which is needed to be prescribed to model the cnoidal wave.

In order to characterize superposition waves, the amplitude, the phase, and the wave length/the wave period for every included first order partial wave have to be known.

The influential factors to feature irregular waves are the height of the significant wave, the peak wave period, and the spectrum type. Either the Pierson-Moskowitz spectrum or the JONSWAP spectrum „Joint North Sea Wave Observation Project “ can be selected to describe irregular waves (Veritas 2010) [142].

A certain issue with physical wave tanks is the reflection of waves from the boundaries, which has to be prohibited from influencing the results.

Reflection is not solely an undesired effect within experimental measurements, but it is of concern in the framework of NWT. Nonetheless, there are some approaches to alleviate the undesired effect of the reflection on boundaries, which prevent any interference with the exact solution. For example, the problem can be handled when wave tanks are provided with tunable beaches or a slope at the back wall of a NWT, as used by many researchers mentioned in chapter 5.

The method suggested by Maguire and Ingram (2009) [143] takes advantage of the periodic boundary condition, where the values of variables on one vertical boundary are copied to those on the other vertical boundary.

Furthermore, reflected waves can be eradicated when an artificial damping zone (sponge layer) at the back wall of a NWT is devised.

The other solution proposed by Larsen and Dancy (1983) [144] incorporates an absorbing beach to impose an artificial counteracting pressure on the dynamic free surface condition over a given area.

A further free of reflection condition for the single wave propagation was suggested by Orlanski (1976) [145], where the Sommerfeld radiation condition on the boundary was enforced.

Apart from the above mentioned approaches, reflections for incident waves from the back wall of a NWT can be decreased by mesh refinement techniques. By producing a coarser grid size in the area nearby the back wall, reflected waves would be dissipated.

Park et al. (2004) [146] employed a combination of an artificial beach and a gradual increase in the mesh size from the wavemaker to the back end to fulfill a reflection free condition.

Within the Star CCM+, the VOF Waves model enjoys both wave forcing and wave damping capabilities.

VOF wave forcing

To run long-lasting simulations on a reduced domain, the upstream-propagating waves would be dissipated by the VOF wave forcing before approaching the inlet boundary.

VOF wave damping

A VOF wave can be damped in a user-specified distance from selected boundaries to alleviate wave oscillation near those boundaries.
The theory behind this technique is deduced by the work of Choi and Yoon (2009) [147], where a resistance term was appended to the velocity component normal to the free surface. The added term promoted the dissipation which decreased exponentially away from the boundary, resulting in zero damping in a user defined damping distance away from the boundary.

When applying VOF waves in a model, an appropriate wave theory has to be implemented as an input in addition to the wave elevation and other relevant parameters. VOF damping or VOF forcing are optional to choose based on the simulation model. The initial conditions for the volume of fraction, the velocity, and the pressure are defined based on VOF waves. Furthermore, the specifications of the volume of fraction, the velocity, and the pressure on the basis of VOF waves are enforced on the inlet boundary and the outlet boundary. As a direct consequence, 3-D Navier-Stokes equations are intended towards the solution implemented by a simplified theory for a selected VOF wave.

Coming back to the topic of piston-type wave generation, a comprehensive view on the waves predefined in the Star CCM+ supports the following conclusions.

The VOF waves models are applicable to model surface gravity waves on the interface between a light fluid and a heavy fluid when a steadily-progressing periodic wave train is generated. However, the assumption applied for the generation of the waves propagating steadily with a constant pattern was not suited to simulate the wave generated during our conducted experimental analysis. In other words, what is aimed to be modeled is a transient case where the wave has to be first generated and propagated during the time.

The fact gave rise to a numerical generation of the wave by the motion of a moving boundary which replicated the movement of the wooden body within the experimental water channel.

Moreover, a common issue which appears when simulating waves is the reflection of the waves. As mentioned in chapter 5, mesh coarsening capability provided an effective possibility to dissipate undesired reflected waves from the boundaries.

The implementation of a gradual mesh coarsening sufficed for the targeted simulation for many reasons.

First, the simulation was needed to be executed for a short time duration until the wave left the flexible membrane. In other words, the interaction between the flexible wall and the progressive wave in this interval was of importance.

Furthermore, the channel was sufficiently long, which prevented any disturbances from permeating in the target progressive wave during the desired simulation time.

6.2 Structure domain

The structure domain consisted of three parts assembled in Abaqus CAE, comprising two deformable parts and one rigid.

Similar to the case mentioned in the chapter 4, two different deformable parts were defined to avoid the problem regarding the presence of beam elements on the shared boundary in the co-simulation. The deformable structures were constructed with CAD tools within the Star CCM+ (refer to the section 6.3 for the detail) and imported to the Abaqus with the stl format and then tied together.

The geometry feature was made with the help of a virtual topology within the mesh module. The generated geometry enabled the model to be remeshed.

Both the membrane and the reinforcing stringer shared the same materials (refer to Figure 6.5) as the model structure in chapter 3, while they were constructed (Figure 6.3) and constrained in a different manner, as shown in Figure 6.4.

There are changes in the boundary conditions for the membrane relative to the model described in chapter 3. In this regard, two hanging points on the stringer (red), the bottom edge of the membrane (orange), and two side edges of the membrane were constrained in three directions (Figure 6.4).

Moreover, the boundary condition for the ground level represented as a three-dimensional discrete rigid part remained constant as fixed completely without any rotational freedom.

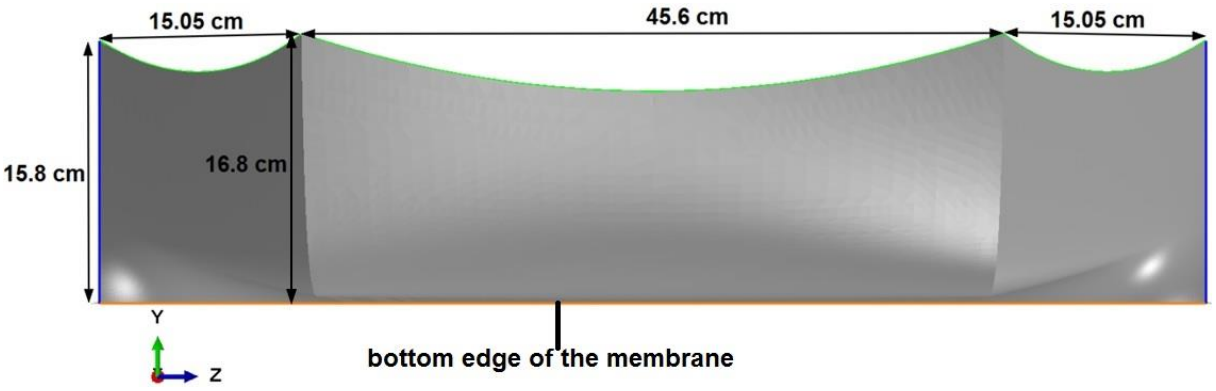

Figure 6.3: Dimension of the model membrane

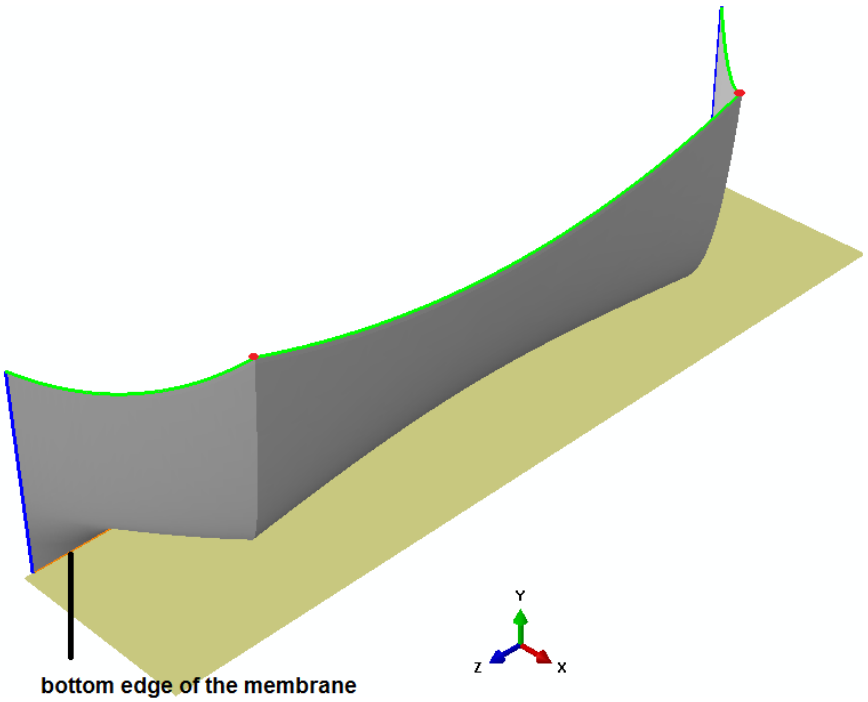

Figure 6.4: Boundary condition: Two hanging points (red), the bottom edge of the membrane represented also in Figure 6.3 (orange) and two side edges of the membrane (blue) as fixed boundary conditions in three directions

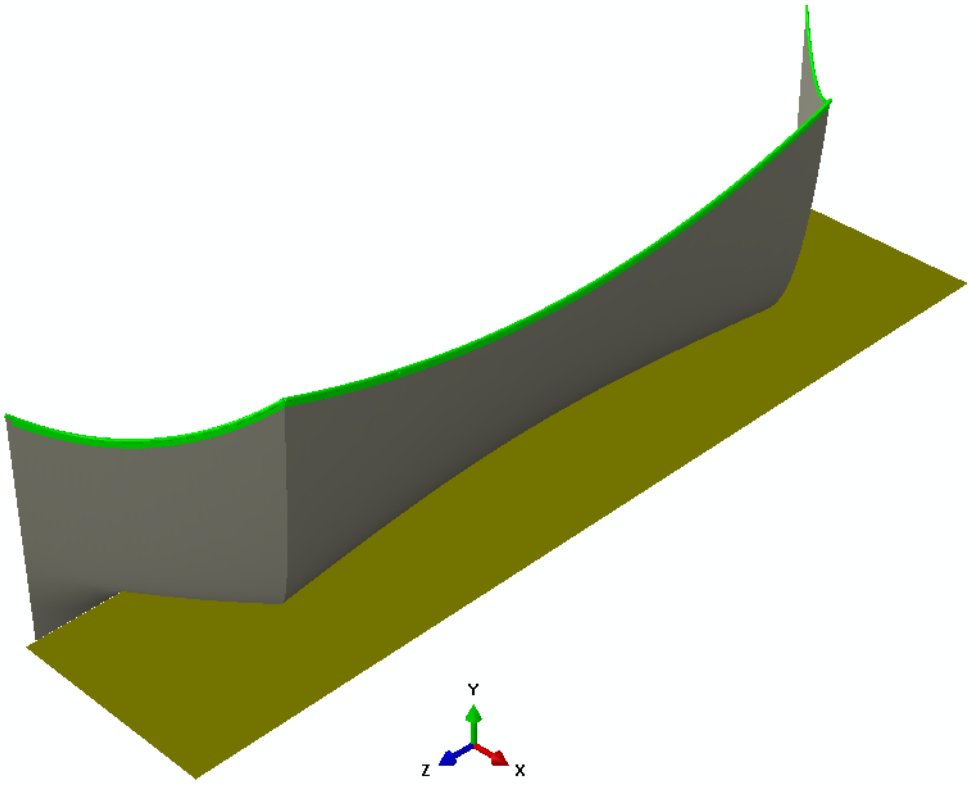

Figure 6.5: Material specification: The flexible PE membrane (grey), the steel stringer on the upper edge of the membrane (green)

The discretization model included M3D4 (a three-dimensional membrane element with four nodes) or M3D3 (a three-dimensional membrane element with three nodes) for the PE membrane and its tied band, linear interpolated beam elements of B31 for the stringer, and three-dimensional rigid elements of R3D4 with 4 nodes for the ground level (Figure 6.6).

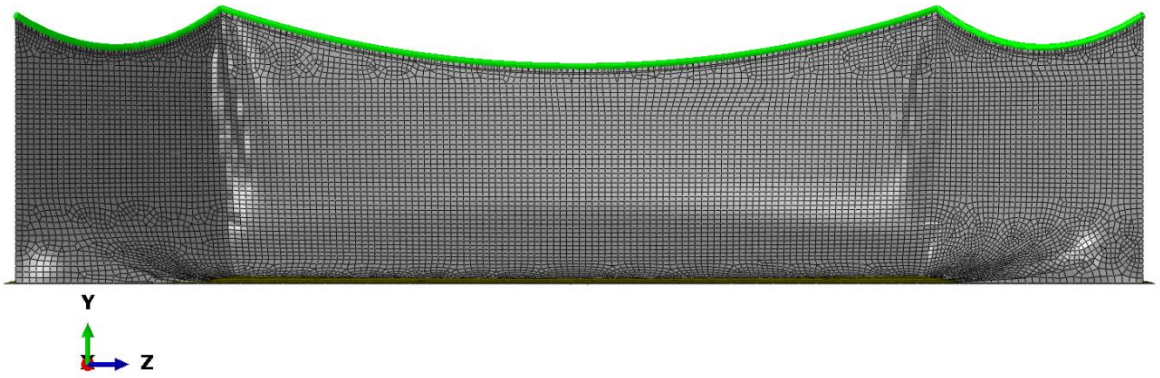

Figure 6.6: Deformed mesh after preload step: M3D4 or M3D3 elements for the PE membrane (grey) and B31 for the stringer (green)

Within the new model setup, the stringer at the upper boundary did not initially locate in a plane. As a result, the n_1 orientation for the stringer was not straightforward to find. To eliminate the warning regarding the disorientation of the stringer, the stringer was split to new small stringers pertinent to the generated discretization on the main steel cord (beam elements). Then, the orientations of the new small stringers were computed mathematically based on the relevant grid coordinates and entered further within the model, which was a demanding manual task.

One surface-to-surface contact model was accounted for the contact between the membrane and the bottom of the channel with a friction coefficient of 0.1, constrained by the penalty contact method with the applied finite sliding.

The default Hughes-Taylor implicit time integration method with second order accuracy and the enabled time increment sub-cycling was accounted for the execution of the structure domain, where the same initial and maximum increment sizes of 0.0001 s were applied.

The enabled time increment sub-cycling let the Abaqus implicit impose its own time incrementation which ensure the stability of the simulation. As a result, the defined

time increment is shortened if there are the nonlinear events needing a smaller increment size.

6.3 Fluid domain

The fluid domain depicting the numerical water wave tank and the surrounding ambient air was designed by CAD tools within the Star CCM+.

The numerical water tank was composed of 3 sections, where the first and the last sections were modeled as rigid walls on both sides of the water tank. The middle section owned the flexible membrane on one side and the rigid wall on the other side.
The middle section had different width due to the flexible membrane (more than 40 cm wide), while the other sections have constant cross sections with a width of 40 cm.
However, a change in the cross section of the tank rendered the experimental and the numerical constructions strenuous.

To overcome the barrier, the tank was first established experimentally by a try and error procedure so as to fit the membrane with the boundary constraints. Then, the lengths of the membrane were measured in the different cross sections.

In order to build the geometry of the main deformable structure within the numerical simulation, the three dimensional coordinates of the grids on the stringers were defined based on the position of hanging points, the length of the stringers and the catenary equation in a three-dimensional Cartesian coordinate system (Figure 6.7). The shape of the membrane was generated by the creation of the different 3-D curves which were constrained by the grids on the bottom of the channel and computed shape for stringers on the upper boundaries. The profiles for the 3-D curves were also plotted so that the measured lengths in the relevant cross sections were satisfied. The final shape for the membrane was formed by the loft operation in CAD tools of the Star CCM+ (Figure 6.8).

The loft operation is a tool to generate a shape by fitting surfaces between a series of profile sketches (at least two start and end sketches), where guide wires can be incorporated to control the generated shape (Figure 6.8).

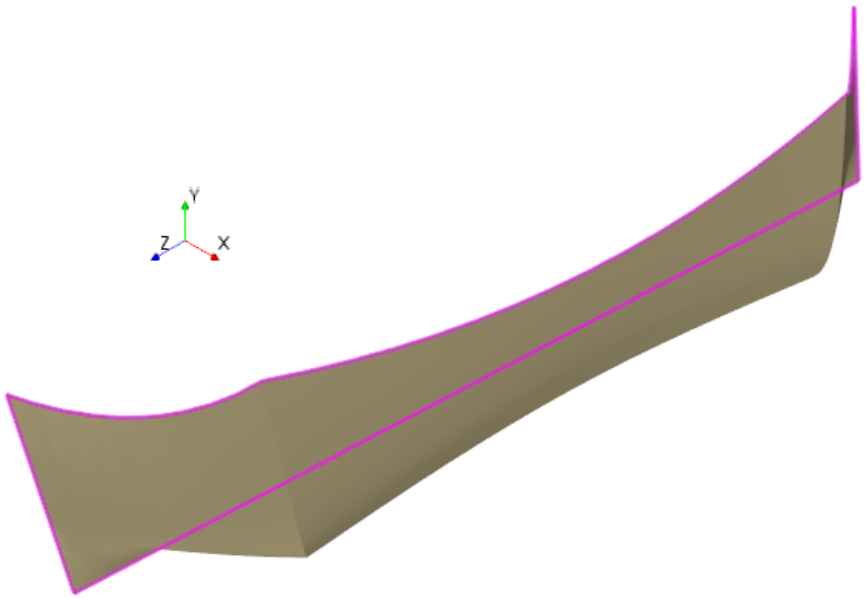

Figure 6.7: The curve on the top (the stringers) and the bottom edge of the membrane as guide wires shown by violet (Two violet sides depicting the fixed boundaries connected to the glass tank walls).

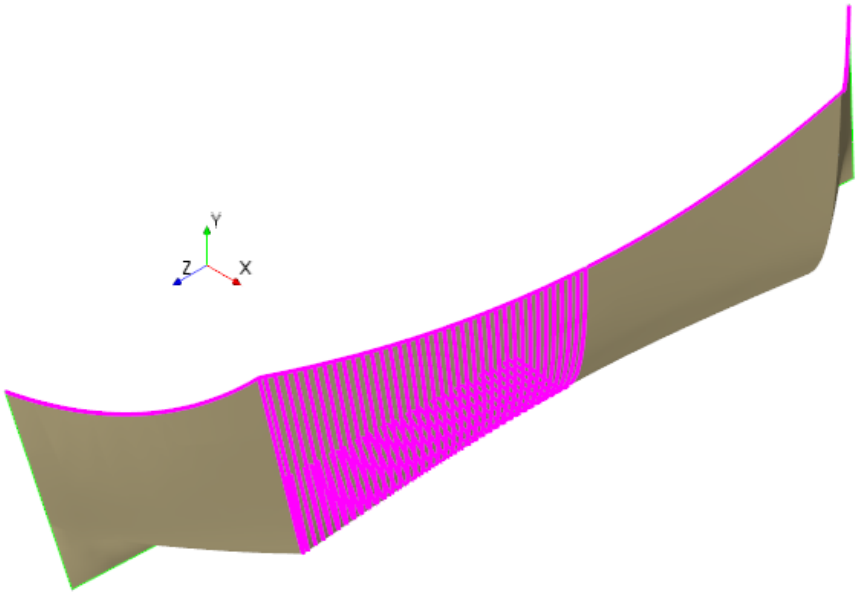

Figure 6.8: Generation of the membrane shape by fitting surfaces between the guide wires (the stringers and the bottom edge of the membrane) and a series of profile sketches (The bottom edge is not plotted).

In the water channel, the wave was generated at the moving boundary (right end) and damped out near the wall boundary at the left end (Figure 6.9).

The applied numerical wave generation replicated the process to form the waves in the experimental analysis. To generate the waves in the experimental water tank, the submerged wooden bulk body which spanned the width of the water tank was dis-

placed by a forward translational movement, representing a semi piston movement. They generated waves which were propagated perpendicularly to the front surface of the wooden body (the paddle surface).

To assign the same motion to the numerical model, the displacement of the body was monitored by a camera during the piston movement in order to define a user defined field function for the velocity of the moving boundary. The overset mesh enabled the same procedure to be reflected, leading to the desired wave model.

The fluid model included two different regions, where the former served as the background region overlapping the latter representing the overset region.

The background region encircled the whole fluids domain (including the immiscible water-air flow inside the channel and surrounding air environment) which was split partwise by the internal fixed rigid walls representing the glass walls of the water tank and the internal flexible membrane.

Within the air side, the lower boundary in the air side was modeled deeper than the ground level. Moreover, one end of the air side connected to the flexible membrane was designed inclined. This construction avoided any possible issues regarding mesh criteria in case either the membrane approached the ground on the air side or it tended to touch the mentioned end boundary (the inclined boundary).

Within the background region, all boundaries were set as the walls (presented by light yellow, orange, red and grey in Figure 6.9) with the exception of the top boundary together with the bottom and the side boundaries on the side representing the air environment (exhibited by green in Figure 6.9), which were defined as symmetry planes. For the overset region (blue), all boundaries excluding the boundary on the front of the moving body were assigned to walls, while the excluded one was selected as an overset interface. In detail, the boundaries of the overset region coinciding with or sliding on the boundary of the background region had to share the same boundary type as the relevant boundaries in the counterpart region (Figure 6.9).

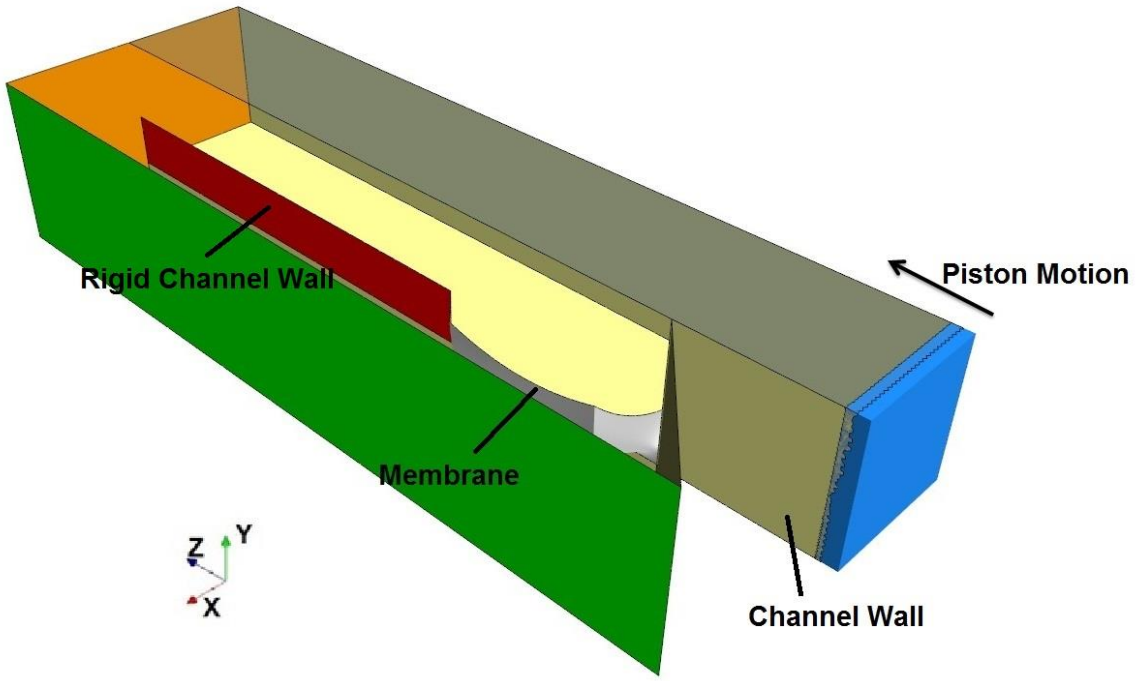

Figure 6.9: Illustration of the model: the coupled membrane tied with the red wall (grey), the rigid wall mimicking the channel glass wall (red), the part of the background region connected by the overset region (blue), fixed plane wall boundary (orange), symmetric boundaries (green), the bottom plane representing the ground level of the channel (light yellow), the rest flat boundaries as fixed wall boundaries (They are represented with light yellow color but with an opacity of 10 % to make other boundaries visible).

Mesh movement within the background region was enforced by specifying the morphing motion to the region motion, which allows the coupled flexible membrane (grey) to conform the structural deformation. The upwind end wall boundary (orange) was constrained as a fixed plane, which needs less computational effort, while the further walls (yellow and red) were fixed (Figure 6.9).

All wall boundaries within the background region and the overset region were assumed as non-slip walls.

In addition, the motion specification for the overset region was represented by a translation along the tank length, where the field function for the velocity of the wooden body was determined based on the monitored data for the corresponding velocity within the experimental investigation.

To alleviate the effect of the upper boundary on the formation of the surface waves, the upper boundary was located in a far distance from the free surface.
To prevent the wave reflection resulting from either non-conformal or non-smooth mesh, a fully conformal polyhedral mesh was implemented.

Furthermore, the polyhedral mesh was so refined that a smooth transition between different cell sizes was maintained. It was attempted to minimize the grid refinement, while still preserving the important flow characteristics, in order to reduce computation costs.

To resolve the wave shape, the mesh was refined with more than 70 cells in the wavelength and 18 cells for the elevations of the wave crest relative to free surface. For fulfillment of the latter condition, one internal surface in an elevation higher than the water free surface was appended to the model, which allowed a conformal prismatic layer within the desired span. It also enhanced the solver efficiency as a result of the cells faces which were perpendicular to the main gradients of the flow.

Siemens AG (2019) [88] has published a guideline to capture waves for free surface flows, which include some recommendations for the minimum number of cells per wavelength and wave amplitude, as well as the time step.

The procedure issued by the international towing tank conference (ITTC 2011) [148] is another resource which supplied practical guidelines for ship CFD application (version 2011) to gain useful guidelines regarding the required minimum number of cells per wave amplitude and wavelength and the appropriate time step for free surface flow simulations.

The following table lists the minimum requirements for the number of cells per wave amplitude and wavelength and compares them on the basis of the Star CCM+ user guide (Siemens AG 2019) [88] and the ITTC recommendation (ITTC 2011) [148].

	Cells number per wave length	Cells number per wave amplitude
Star CCM+	40-100 (80 is recommended)	20-40 (40 is recommended)
ITTC	40	10

Table 6.1: Comparison between recommended criteria by the Siemens AG and the ITTC for mesh resolution to capture free surface in water flow

What is an interesting point regarding Table 6.1 is the fact that the Star CCM+ mesh resolution recommendations are introduced in a conservative manner, where the minimum requirements proposed by Siemens AG are twice as demanding as the ITTC guidelines.

As mentioned, there is a criterion for the time step, which is based on the Courant number requirement.

Two different formulations were proposed by the Star CCM+ and the ITTC for the maximum time step, as follows:

$$\Delta t_{Star\ CCM+} = \frac{Wave\ Period}{Number\ of\ Cells\ per\ Wave\ Length \times 2.4} \tag{6.1}$$

$$\Delta t_{ITTC} = 0.005 \sim 0.01\ \frac{L}{V} \tag{6.2}$$

The guidance proposed by ITTC was deduced from Spence's thesis (2014) [135].
He mentioned in his thesis that there is no explicit definition for the characteristic length and the velocity found in Equation (6.2). Nevertheless, he assumed that L and V stand for the wavelength and the wave propagation speed, respectively.

The Star CCM+ equation for the time step depicts clearly that an increase in the mesh resolution (decline in the mesh size) has to be followed by a decrease in the time step, where both the mesh size and the time step go hand in hand.

The guidelines presented by either the Star CCM+ user guide or the ITTC were limited to free surface waves application.
In addition, the ITTC recommended the time step for an implicit temporal discretization scheme, while the Star CCM+ preferred a 2nd order time integration model and an implicit unsteady solver to improve the model setup.

To improve the accuracy for an overset interpolation (during the data exchange), every boundary within the overset region had to overlap the background mesh (here namely VOF) by at least 4-5 cell rows unless it was assigned to work as a wall instead of an overset boundary (Siemens AG 2019) [88].

The free surface was captured using the VOF method and high resolution interface capturing (HRIC) scheme.

As given in the Star CCM+ manual (Siemens AG 2019) [88], an additional source term was also needed to be imposed on the pressure correction equation, which enhanced the convergency together with the precision of results (refer to section 2.5).

The flow initialization could be performed by means of cell surface parts, an extraction of the pertinent cell ID as tabular data, a generation of cell sets, and finally user defined field functions, as described in the section 4.2.2.

The following figure depicts the mesh after a forward translational movement of the wooden body. As mentioned before, the wall in the air side has an incline relative to

X-Y plane in order to prevent any mesh issues resulted from the displacement of the flexible membrane.

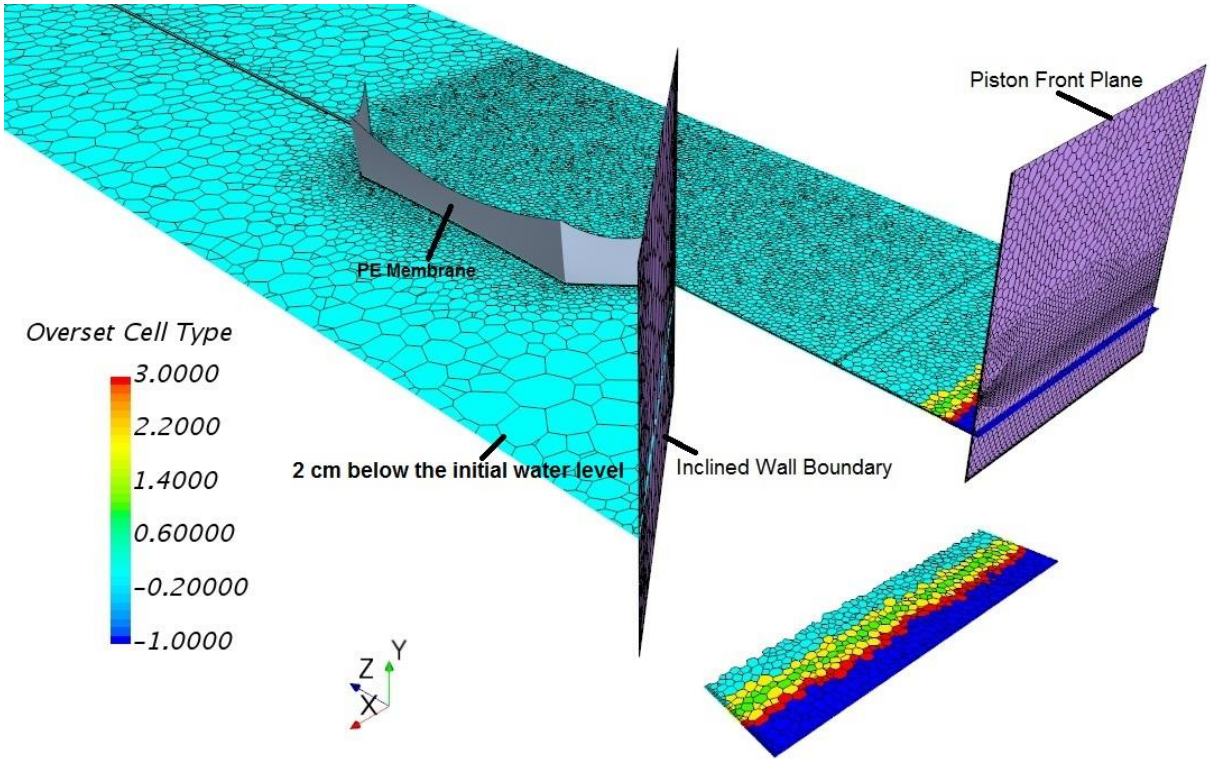

Figure 6.10: Discretization configuration on a surface parallel to the initial water wave (2 cm below the initial water level) with the depiction of the overset cell type: the inactive cells residing outside of the background mesh (dark blue), the active cells (aqua), the donor cells (green), the active, intermediate cell layers used by the hole-cutting process (yellow) and the acceptor cells (red) (The flexible membrane is represent in grey color and the piston front plane and the inclined wall boundary used in air side are shown in light violet).

Within the background region, the areas which were passed by the overset region became deactivated as shown with dark blue in Figure 6.10. In other words, the mesh cells (within the background region) coinciding no longer with the overset region were excluded from the analysis unless they were located in upside of the overset boundary.

6.4 Co-simulation model setup

Two co-simulation zones with a surface-to-surface coupling model were specified. A proper exchange of the mechanical data (fully data mapping) between relevant boundaries was enabled by the identical positions, the configurations and the orientations of the coupled surfaces.

Some parameters including the coupled surfaces, the exchanged fields and the co-simulation step had to be specified in the Star CCM+ and the Abaqus, where the cor-

responding co-simulation commands to control the co-simulation were written in the Abaqus input file and inputted within the Star CCM+ for the further communication.

The original coordinates as a reference configuration for mappers could be used because of the equal geometries for the coupled boundaries. The discretization of the flexible membrane by means of the membrane elements within the structure model required the rotations not to be mapped to the fluid domain.

The computed deformation of the coupled boundaries within the Abaqus exerted a change in the mesh within the background region (by the attribution of the morphing motion with automatic thin-out Cl factor of 0.5 to the region).

The Star CCM+ and the Abaqus were selected as a mapper of both directions and the leading software for the coupling scheme, respectively. The co-simulation was executed in an implicit iterative manner and a sequential order with the coupling step of 0.0001 s. Moreover, the minimum number of exchange within the co-simulation was set to 10 with the minimum inner iterations per exchange of 3. The stopping criteria stopped the exchange at each time step if both the minimum inner iterations per time step of 30 and co-simulation displacement residual of 0.0001 were satisfied. On the other hand, the maximum inner iterations per time step of 180 enabled more exchange per time step until the co-simulation displacement residual of 0.0001 was ensured.

The development of the flow field around the coupled boundary was again performed before the co-simulation and mesh morpher solvers were activated. In order to save computational time, a preload step was performed for 1.2 s before the co-simulation step without any data exchange between two software. A long preload step of 1.2 s was required to allow the membrane to deform based on the hydrostatic pressure.

In case the simulation was terminated, the restart frames had to be written in an Abaqus output file in the specified intervals in sync with the automatic save settings within the Star CCM+ to proceed the new simulation from each saved state.

6.5 Experimental approach

To investigate the deformation of the membrane in the laboratory, a water tank was built and the measurement instruments were installed. The water channel comprises of three parts tied with each other. The main parts of the channel had a rectangular shape with a total length of 252 cm, a width of 40 cm and a depth of 19 cm. The water channel was closed from two ends of the tank, while it is exposed to ambient air.

The channel was thoroughly made of glass plates, with the exception of the side comprising the flexible membrane in the middle (the left side in Figure 6.11).

An illustration of the water channel, the measurement equipments and methods of the measurement method will be discussed, as follows.

Two different cameras were installed in the left and right sides of the water tank to monitor the membrane and the wooden body, respectively.

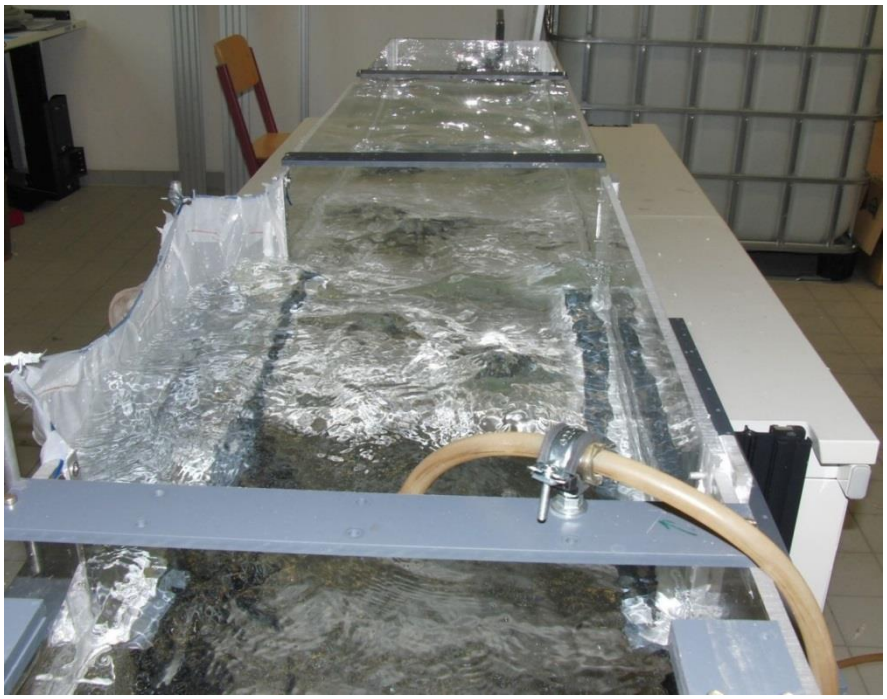

Figure 6.11: Photo of the water channel

The optical method applied for the determination of the deformation works similar to the particle image velocimetry method (PIV).

For the membrane, the applied tracking method followed the movement of two different points (on the membrane) with the radius 1 mm during the measurement time. The positions of the selected points were monitored by the way of consecutive captures using a Basler acA2040 180km camera with a resolution of 2048x2048 pixels and a maximum capturing rate of 180 frames per second.

The position tracking of the selected points did not happen simultaneously within a single experiment. Instead, the experimental measurements were performed within two different investigations, where there was a difference in the camera setup for each specified point.

In the first experiment, the camera monitoring the membrane was positioned horizontally perpendicular to the flow in order to measure the displacements in Y and Z

directions of a selected point (Figure 6.12). Also, the selected point was initially located on the middle of the membrane, 1 cm below the steel stringer.

The change in the camera setup resulted from the fact that each point has to be tracked in different directions.

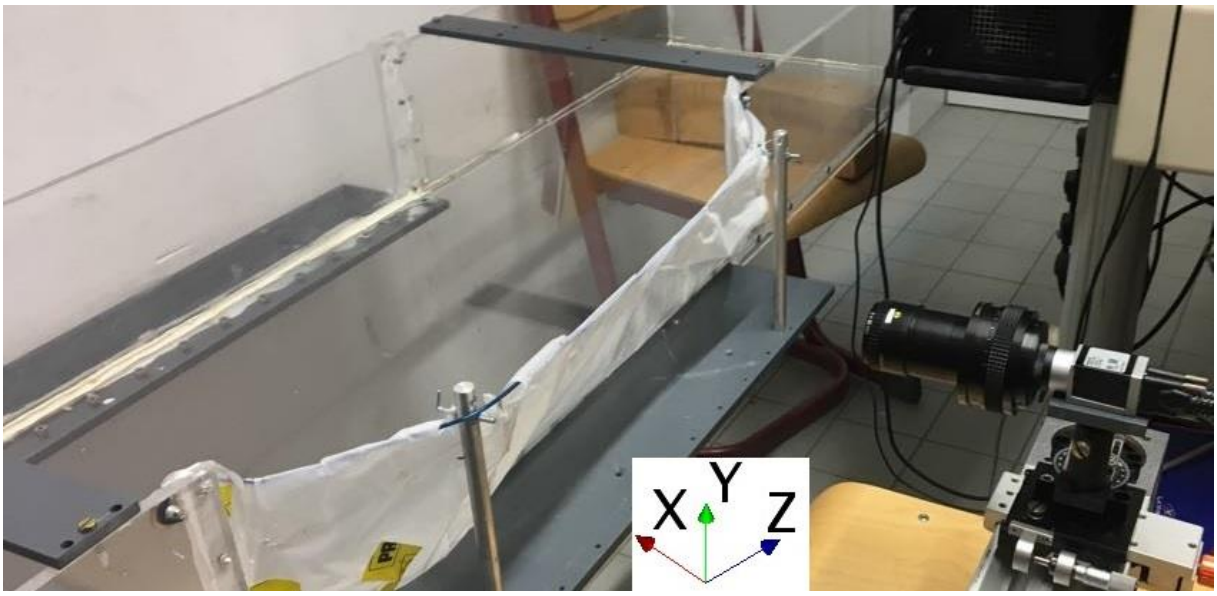

Figure 6.12: Horizontal positioning of the Basler camera

In the latter experiment, the camera was placed vertically (as shown in Figure 6.13) to measure the displacement in the X direction for the other marked point.
The new point was chosen again on the middle of the membrane but directly on the stringer.

In order to correctly track the positions of the points, a scaling plane was placed on the capturing plane parallel with the camera (Figure 6.14). The scaling plane is used to calibrate the Lavision software which is a tool to collect, process and report the data. Then, the camera was scaled with the help of the Lavision software which made the motion of the marked points to be properly tracked.

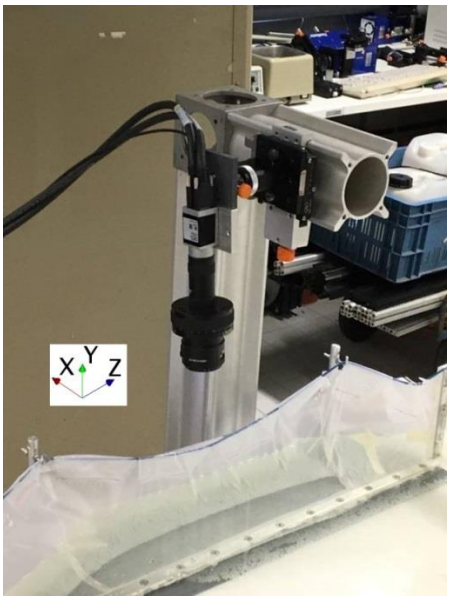

Figure 6.13: Vertical positioning of the Basler camera

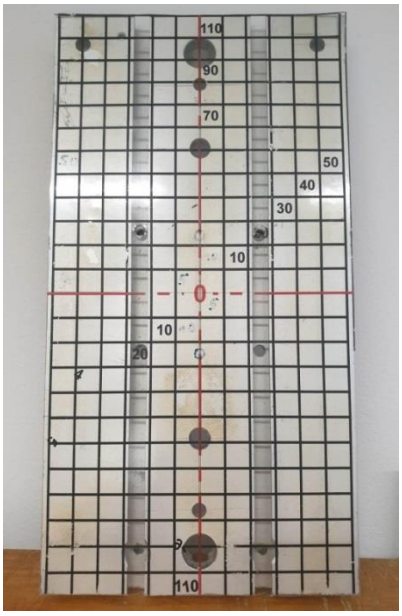

Figure 6.14: Scaling plane used for calibration of the Lavision software

Afterwards, the points on which the displacements had to be measured were marked. Whereas the measurement for the displacements in X direction was performed on a point in the middle of the membrane directly on the stringer, a point in the middle of the membrane, 1 cm below the steel stringer was flagged for the measurement which recorded the displacements in Y and Z directions.

In order to track the displacement of each marked point within a time period, the consecutive frames captured with the desired time interval (here 0.125 s) have to be precisely compared.

Moreover, on the rigid side of the water tank (right side), a commercial camera was installed to measure the velocity of the piston movement in Z direction. In this regard, a meter scale was placed at the same side of the water tank to follow the position of the wooden body (Figure 6.15).

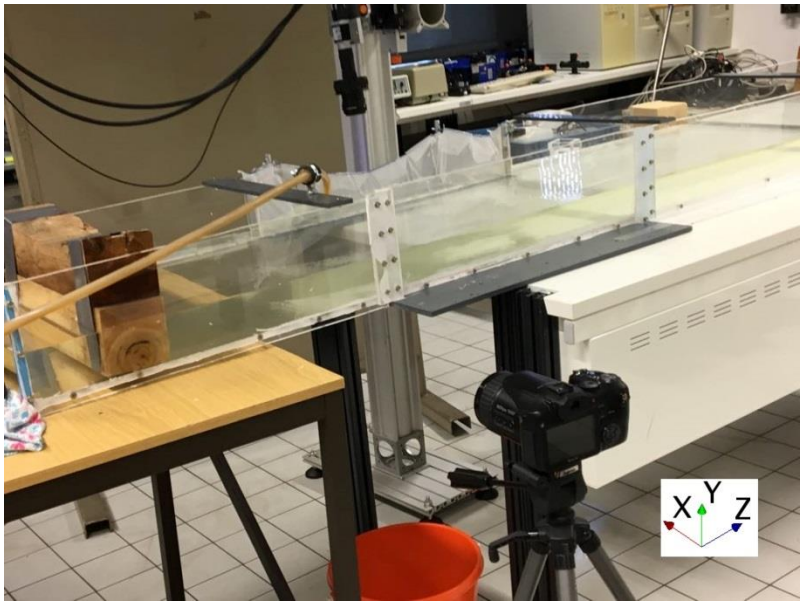

Figure 6.15: Positioning of the commercial camera

Given the wooden body position and the time intervals (specified by the frame capturing rate of the commercial camera), the velocity of the wooden body in Z direction can be measured.

6.6 Results

The comparisons between the wave heights generated within the numerical and experimental investigations have been drawn in Figure 6.16 to Figure 6.30, where side 1 and side 2 represented the tank sides which were completely rigid and partially flexible, respectively. Evidently, the middle stands for the plane which is perpendicular to the cross section of the water tank (in the section surrounded by rigid structures in both sides) and originated from the cross section center.

As a result, the experimental data monitored from the right side of the water tank are comparable with the numerical wave profile at the side 1. The wave profiles in the other planes are plotted to compare the influence of the presence of the flexible wall on the wave shapes.

The experimental data were captured by a commercial camera for a water depth of 70 cm, followed by a calculation on an excel sheet.

The mentioned figures demonstrate the motion of a wave in conformity with the piston-type movement of the wooden body within a time interval of 0.05 s.

There exists an increase in the numerical wave height after 0.25 s movement of the piston so that it reaches from 96 cm (Figure 6.16) to 117 cm (Figure 6.20) during 0.2 s (an increase of 11 cm). Concurrently, the experimental wave grows in height from 92 cm (Figure 6.16) to 102 cm (Figure 6.20), which experienced in fact a rise of 10 cm.

Afterwards, there is a decline in the difference between the heights of the waves crests generated within the experimental and numerical investigations, respectively (Figure 6.21 to Figure 6.30). The resemblance can be observed clearly in Figure 6.29 when the numerical and experimental waves go hand in hand 0.7 s after the initial piston motion.

There is an analogy between wave heights in different planes represented by side 1, side 2, and middle during 0.55 s since the initial piston movement when the wave reaches the flexible membrane (see Figure 6.26). Then, there is a drop in the height for the wave profile at side 2 relative to the other plane sections. The difference between wave heights reaches a peak first in the wave crest (Figure 6.27 and Figure 6.28) and then also in the wave trough (Figure 6.29 and Figure 6.30).

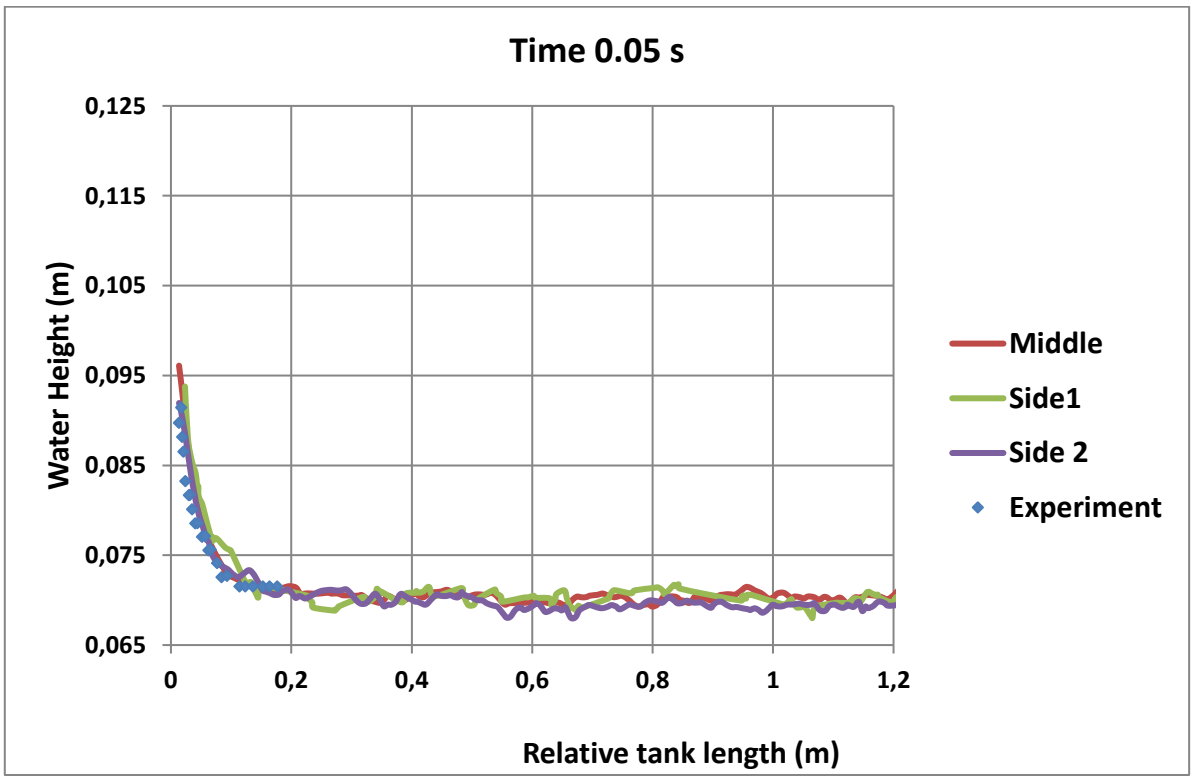

Figure 6.16: Comparison between the numerical and experimental waves 0.05 s after the piston motion

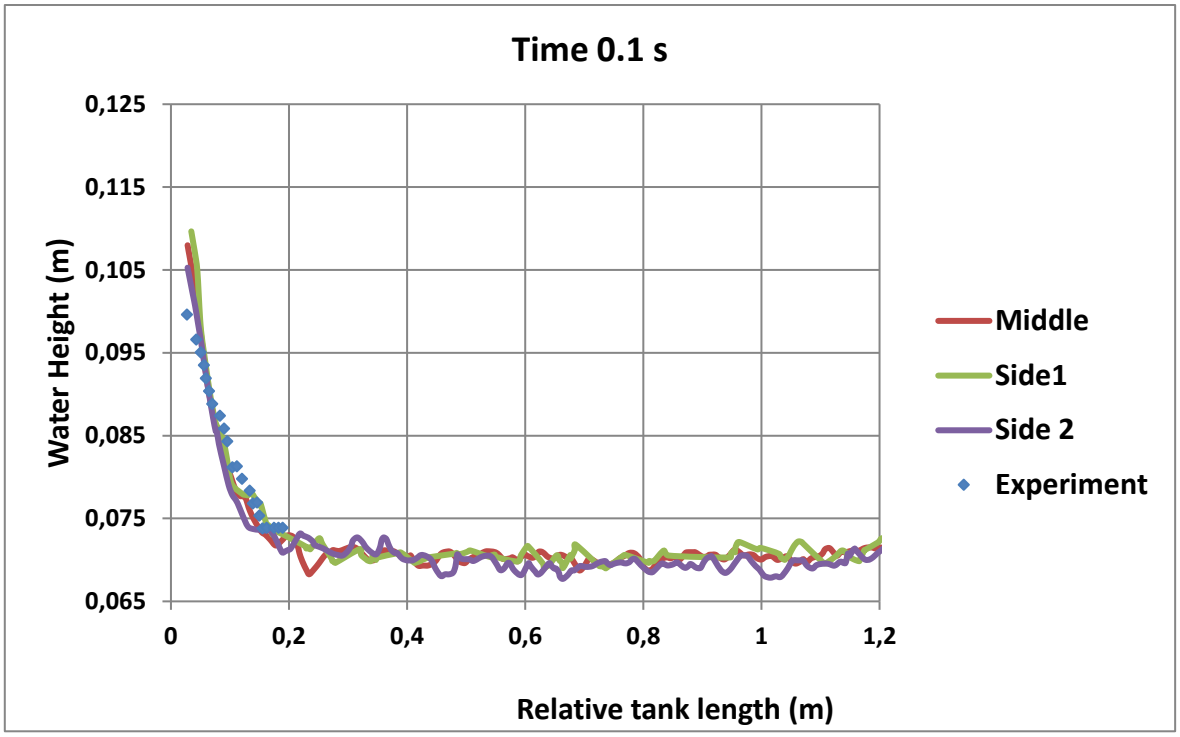

Figure 6.17: Comparison between the numerical and experimental waves 0.1 s after the piston motion

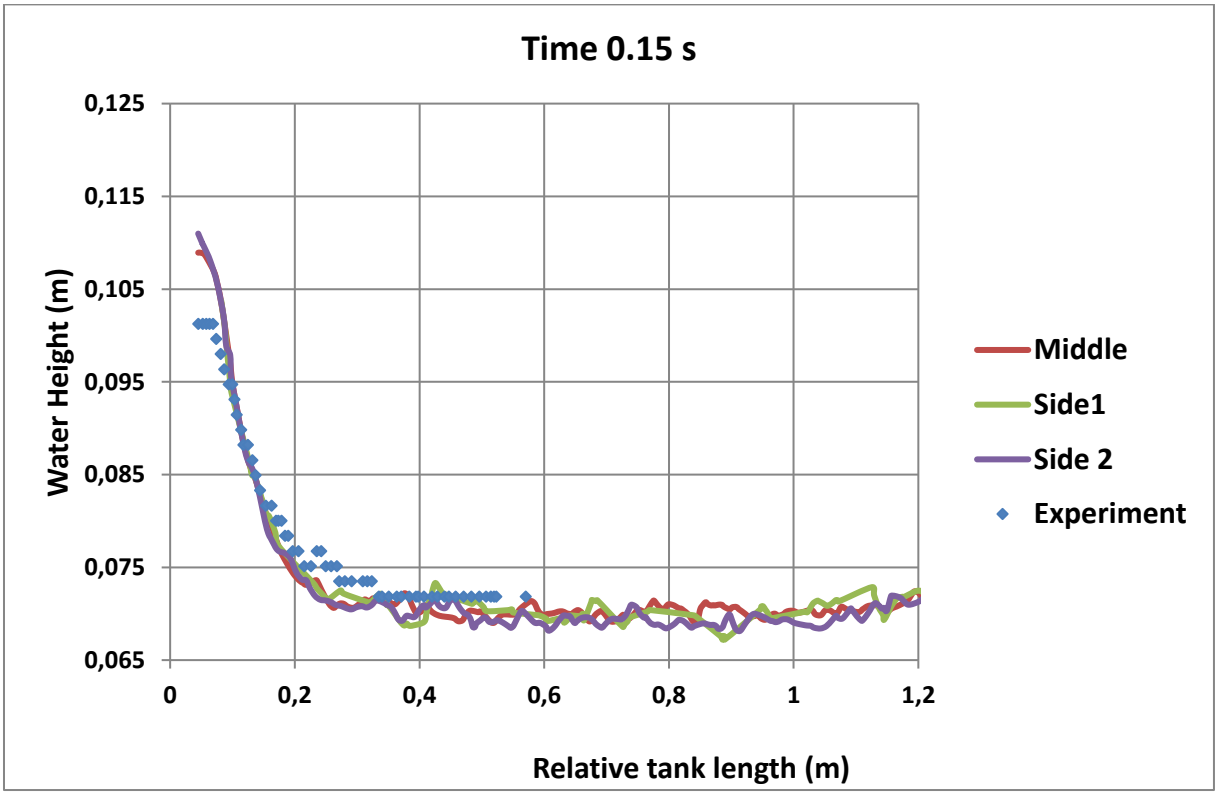

Figure 6.18: Comparison between the numerical and experimental waves 0.15 s after the piston motion

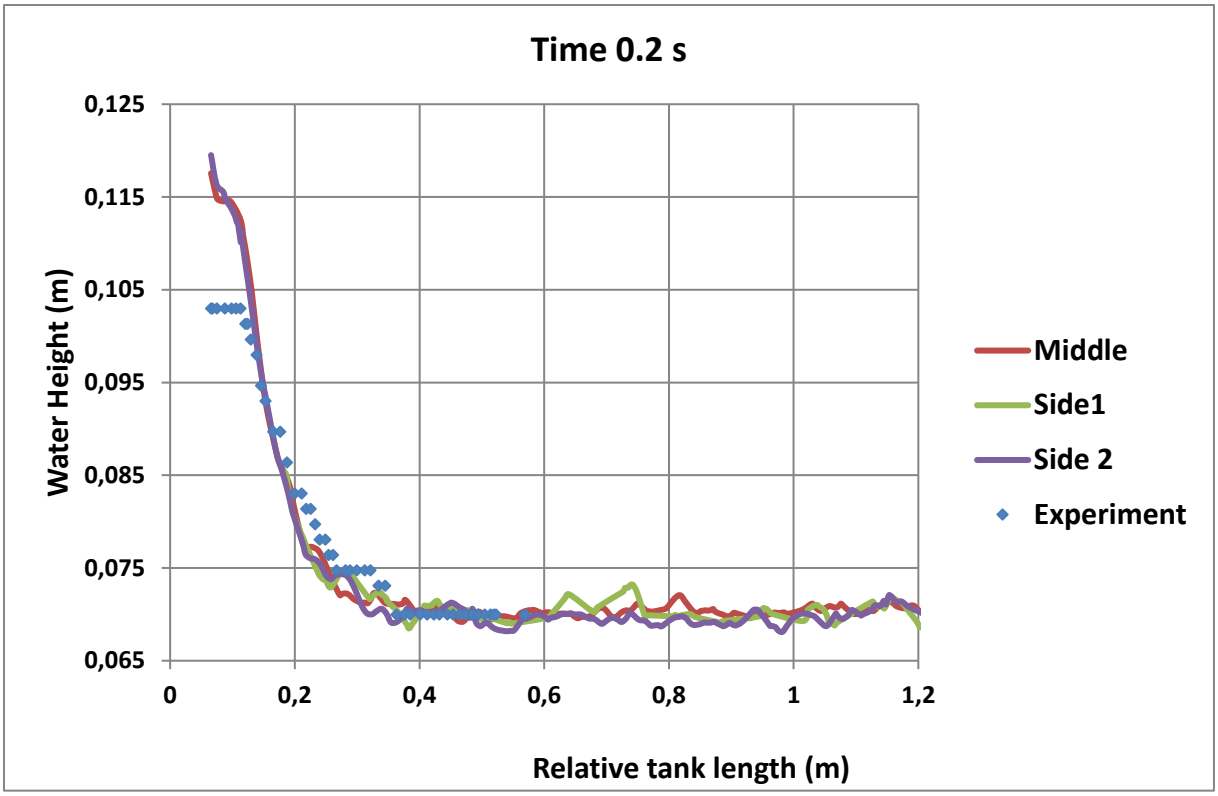

Figure 6.19: Comparison between the numerical and experimental waves 0.2 s after the piston motion

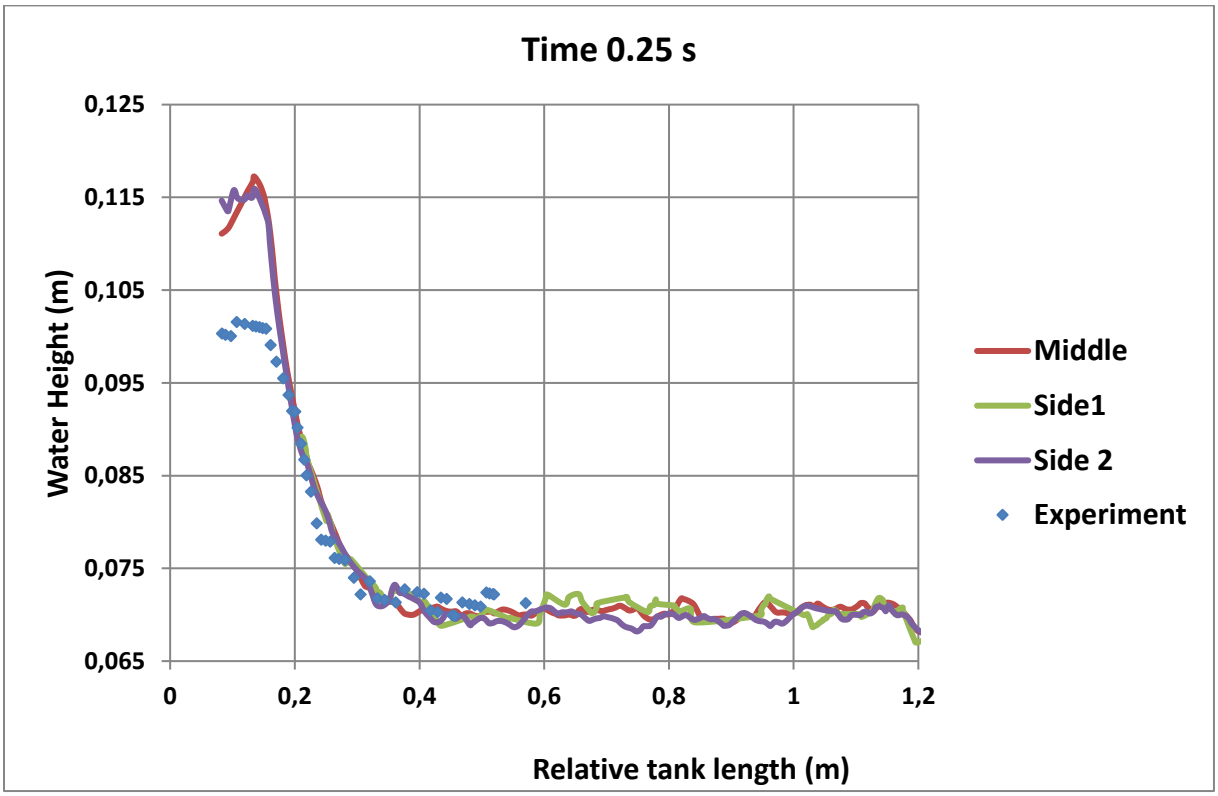

Figure 6.20: Comparison between the numerical and experimental waves 0.25 s after the piston motion

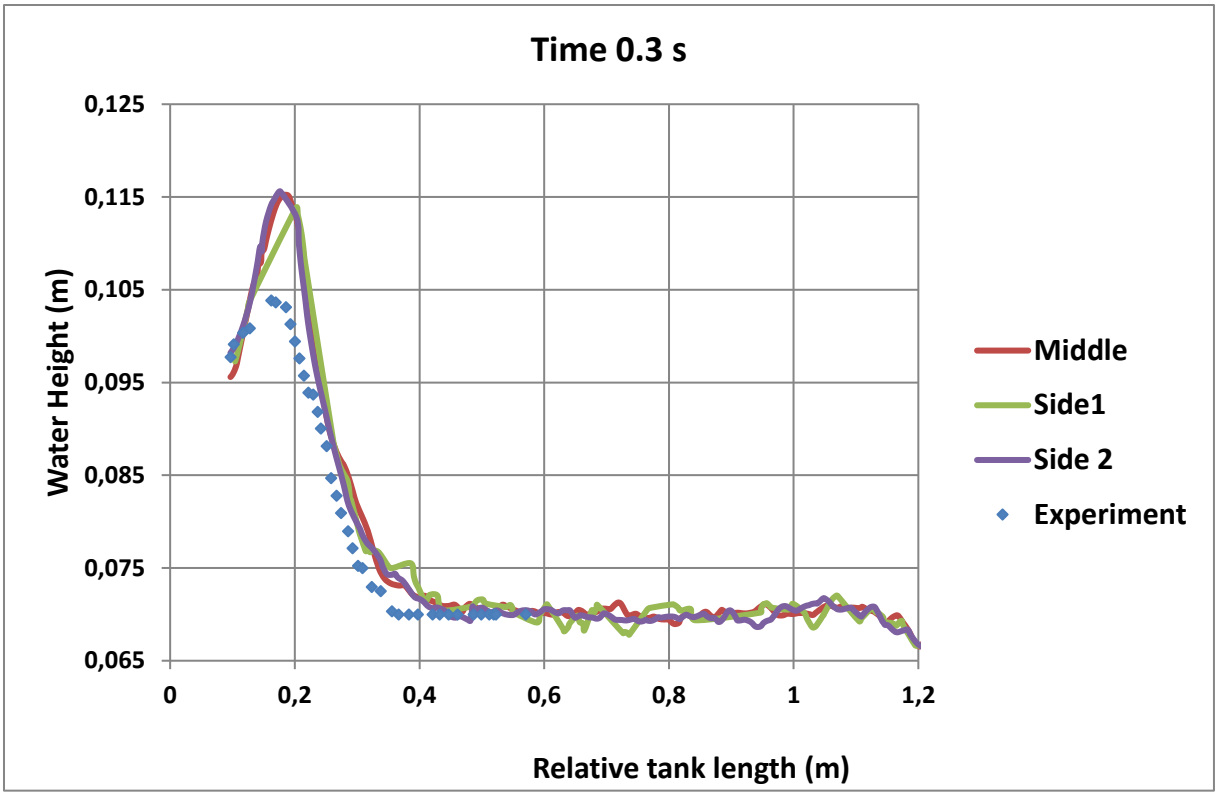

Figure 6.21: Comparison between the numerical and experimental waves 0.3 s after the piston motion

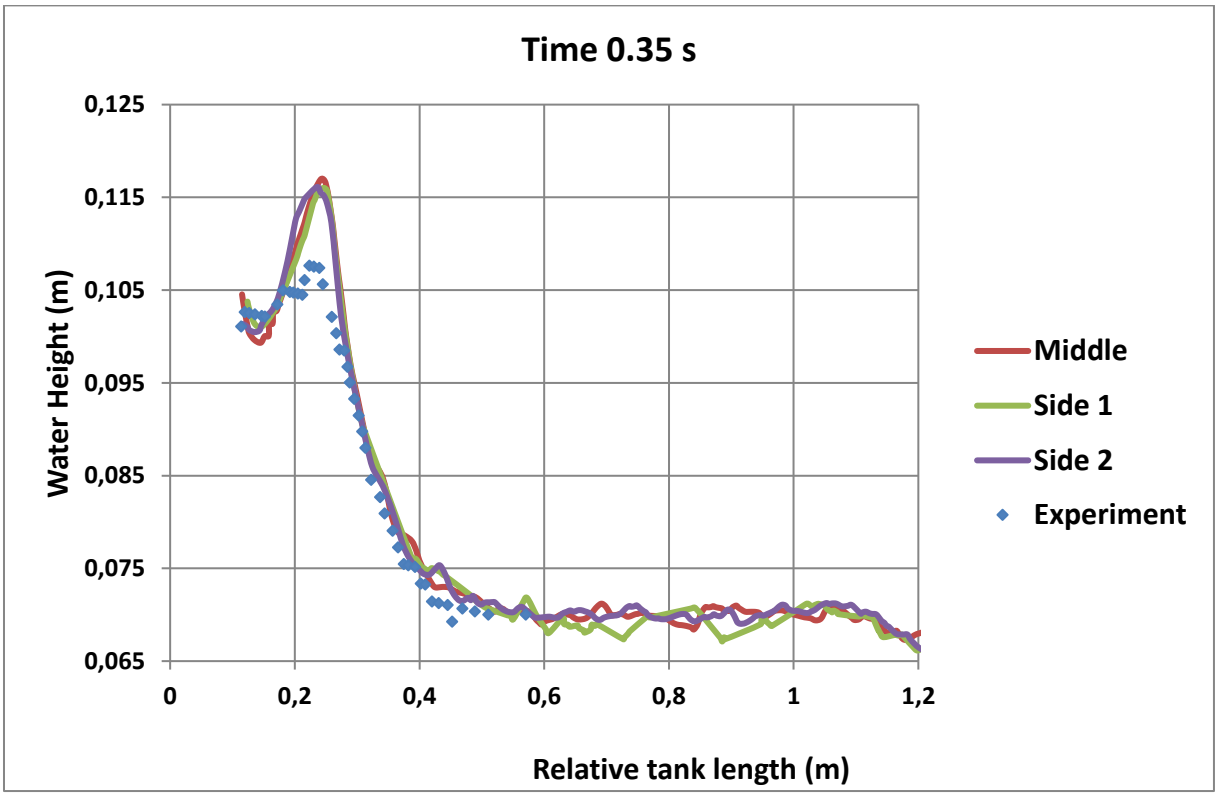

Figure 6.22: Comparison between the numerical and experimental waves 0.35 s after the piston motion

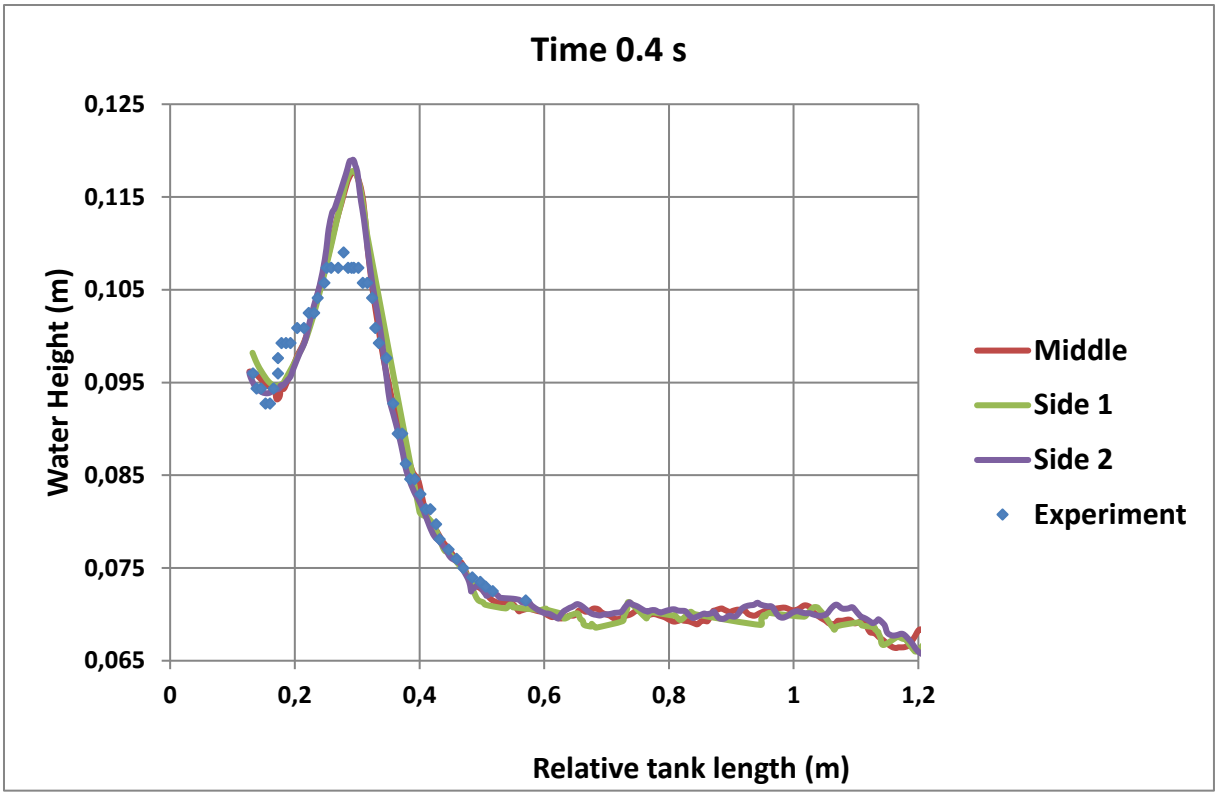

Figure 6.23: Comparison between the numerical and experimental waves 0.4 s after the piston motion

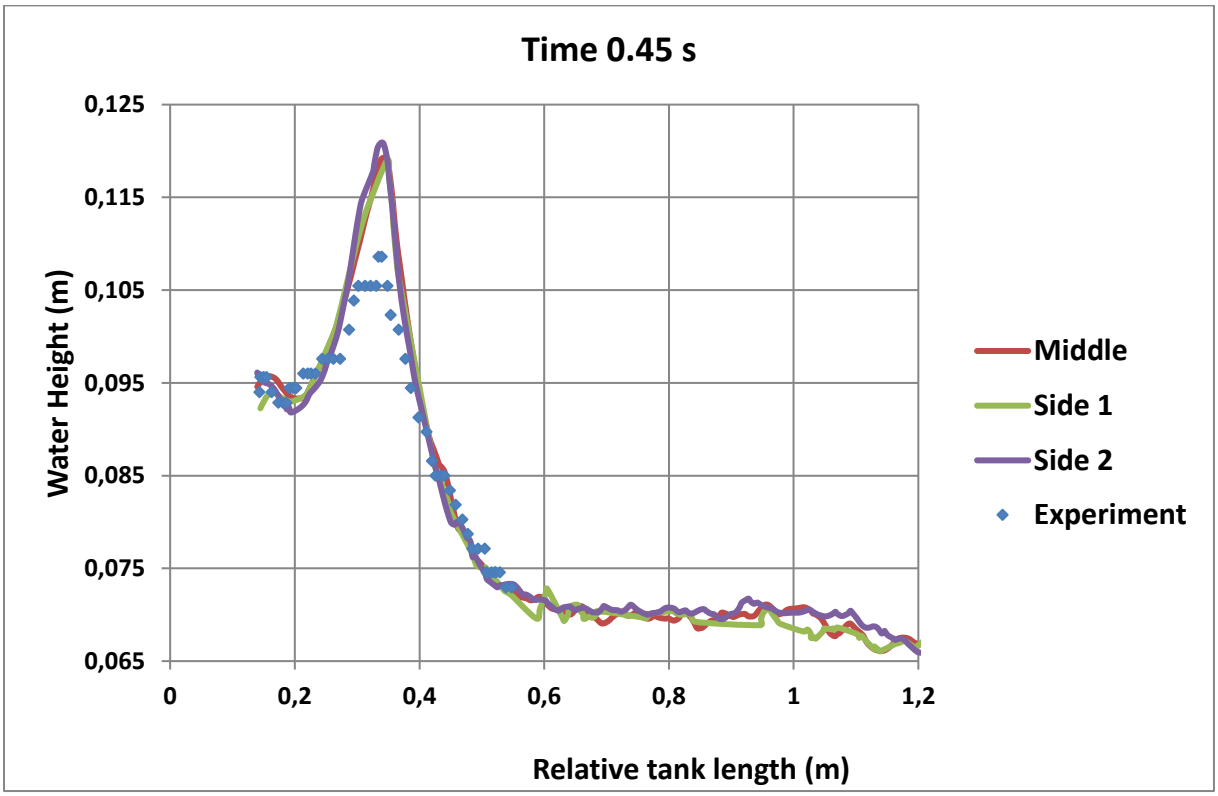

Figure 6.24: Comparison between the numerical and experimental waves 0.45 s after the piston motion

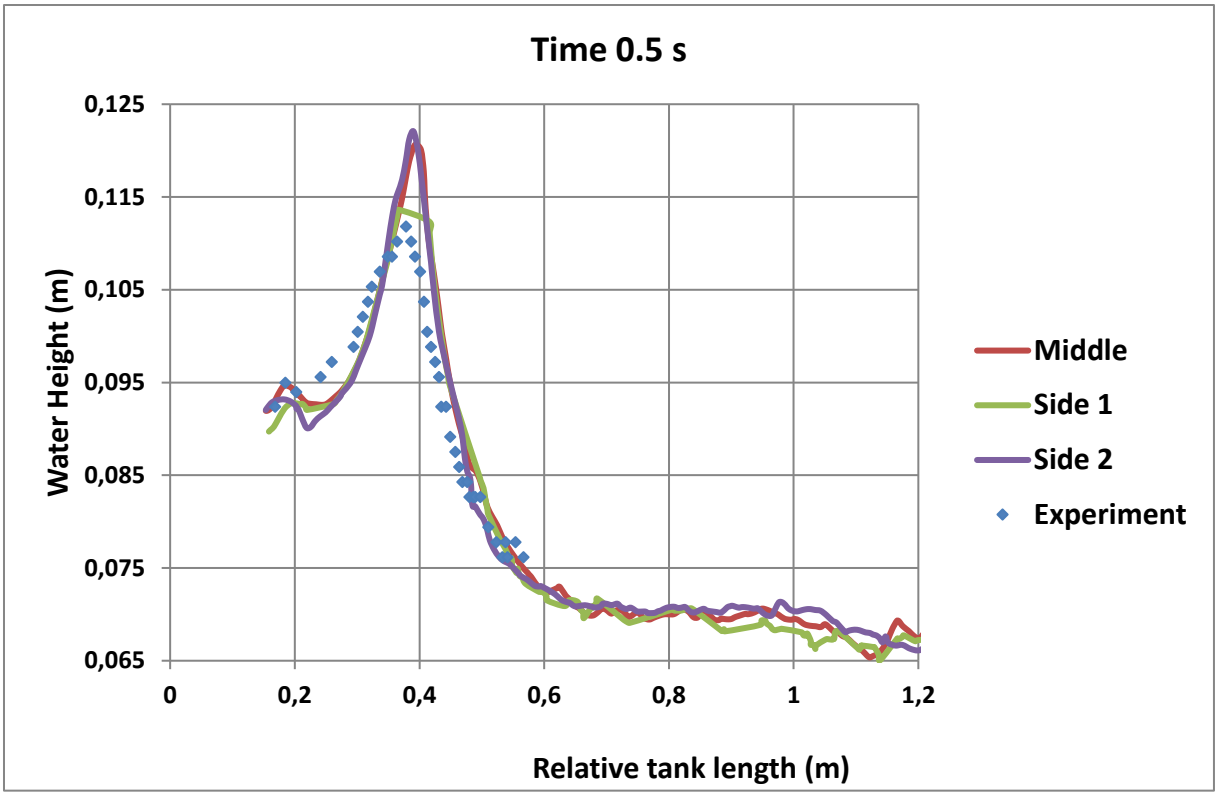

Figure 6.25: Comparison between the numerical and experimental waves 0.5 s after the piston motion

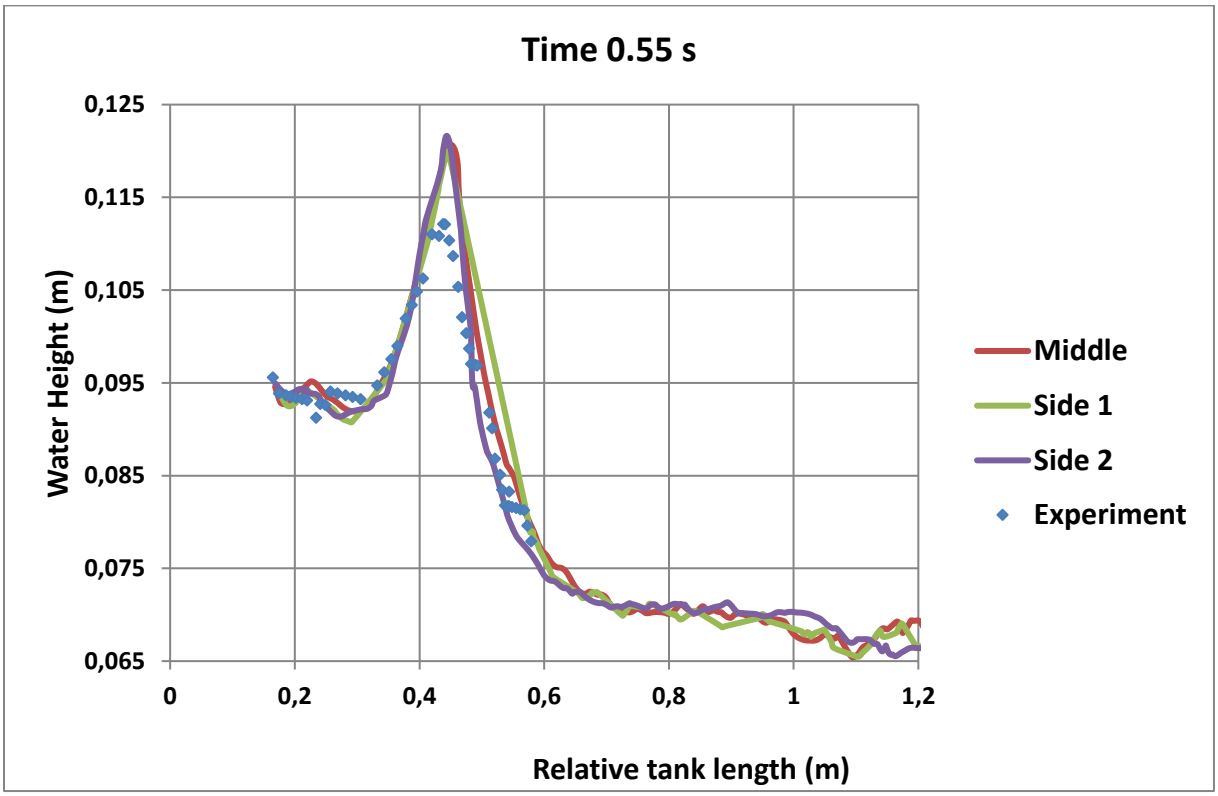

Figure 6.26: Comparison between the numerical and experimental waves 0.55 s after the piston motion

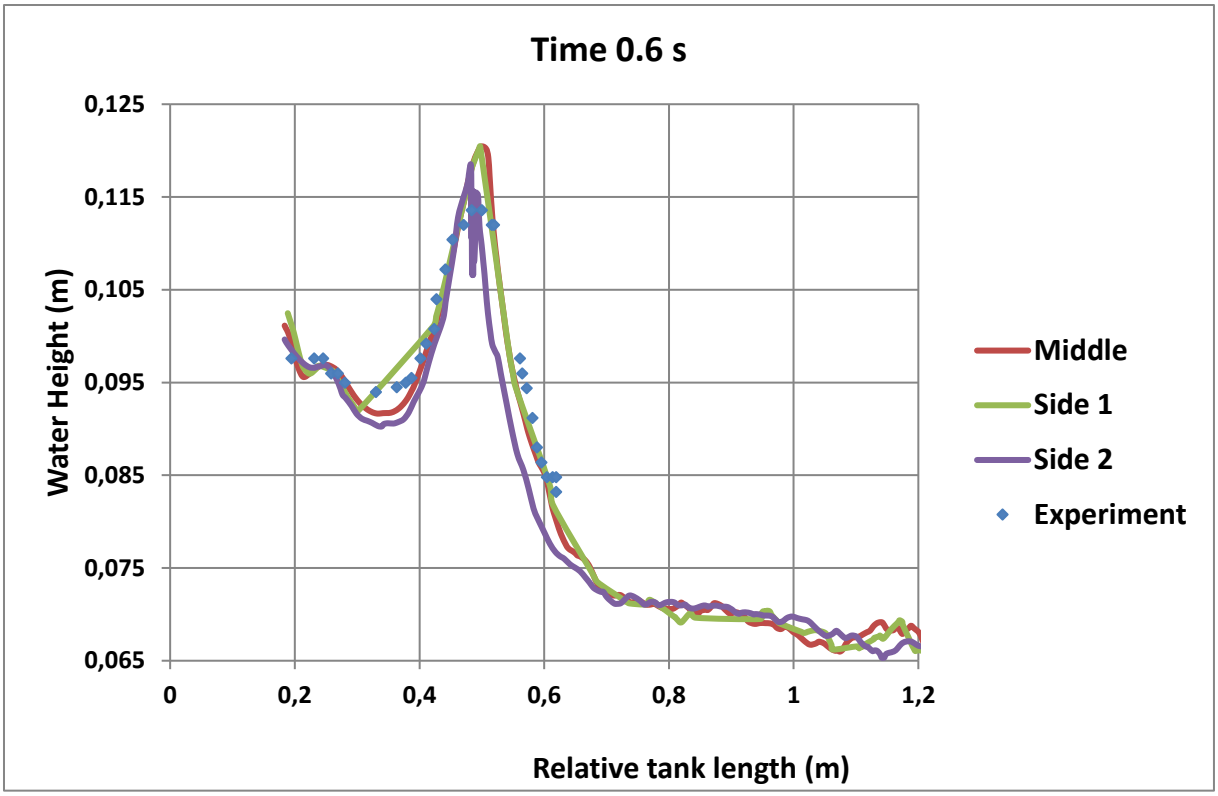

Figure 6.27: Comparison between the numerical and experimental waves 0.6 s after the piston motion

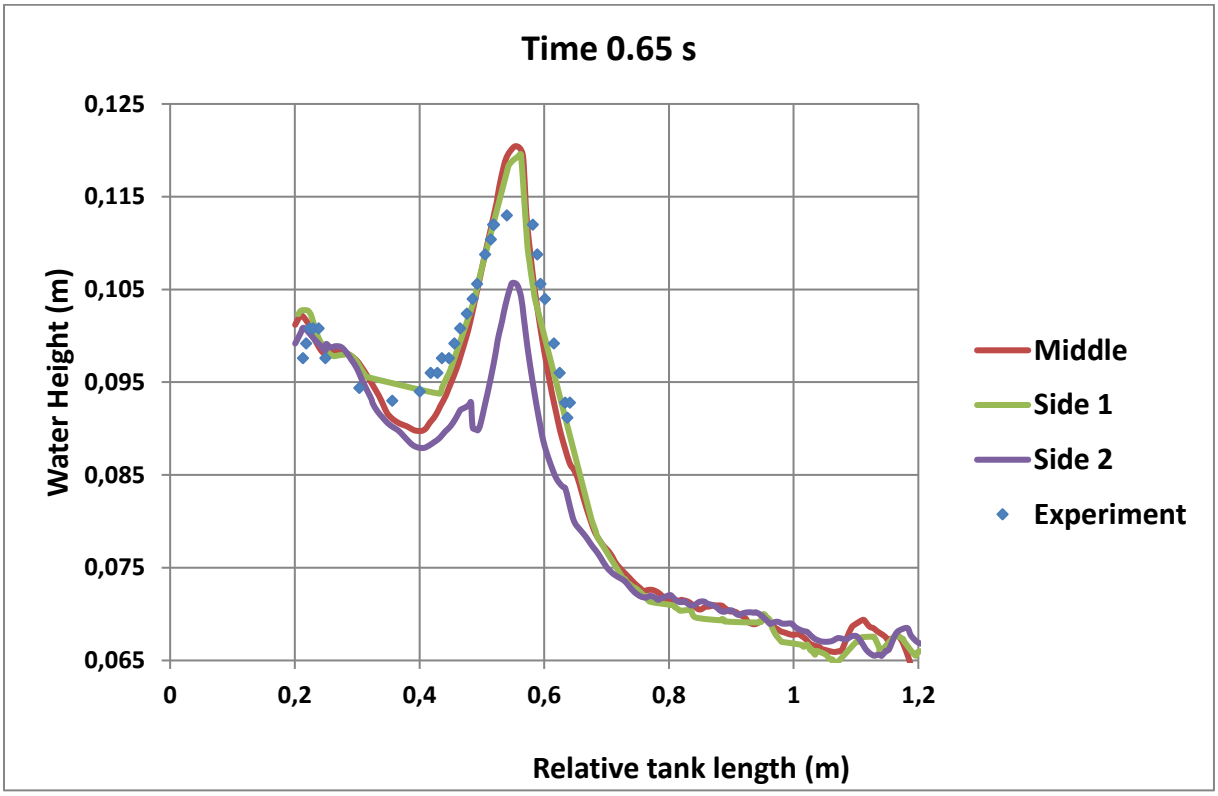

Figure 6.28: Comparison between the numerical and experimental waves 0.65 s after the piston motion

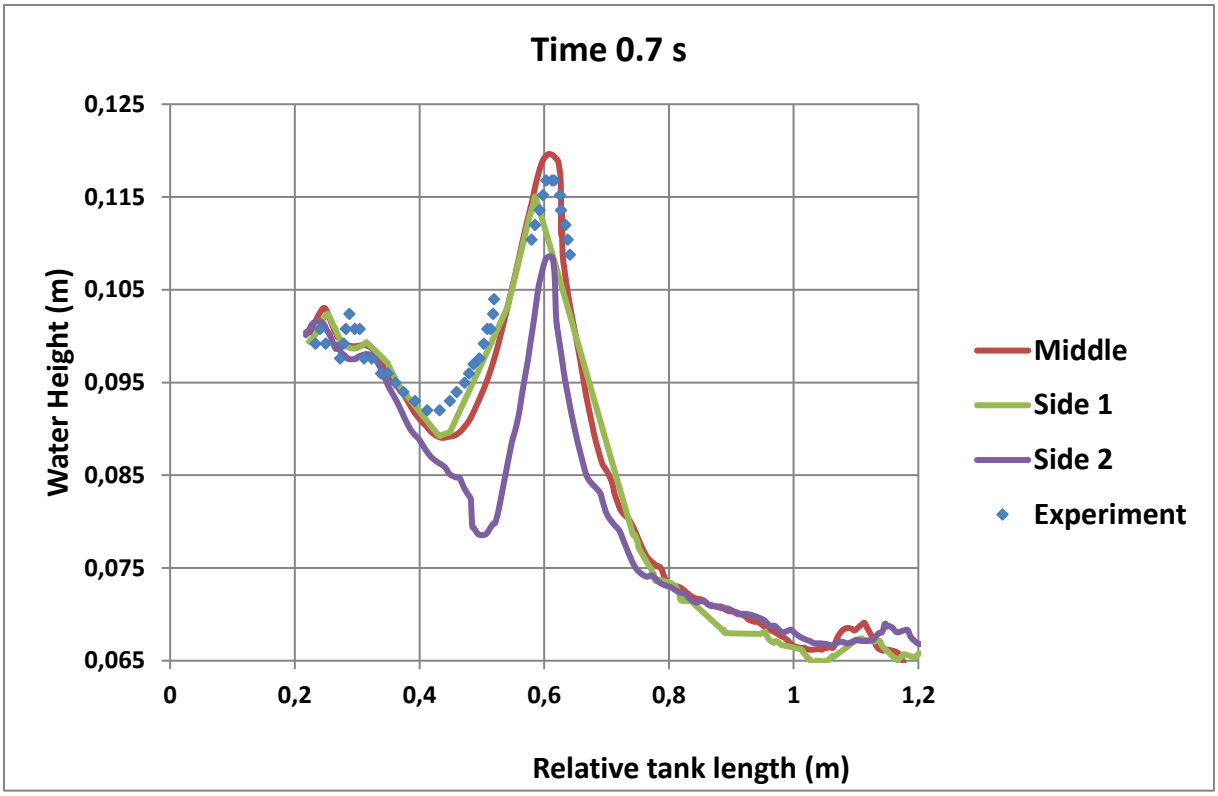

Figure 6.29: Comparison between the numerical and experimental waves 0.7 s after the piston motion

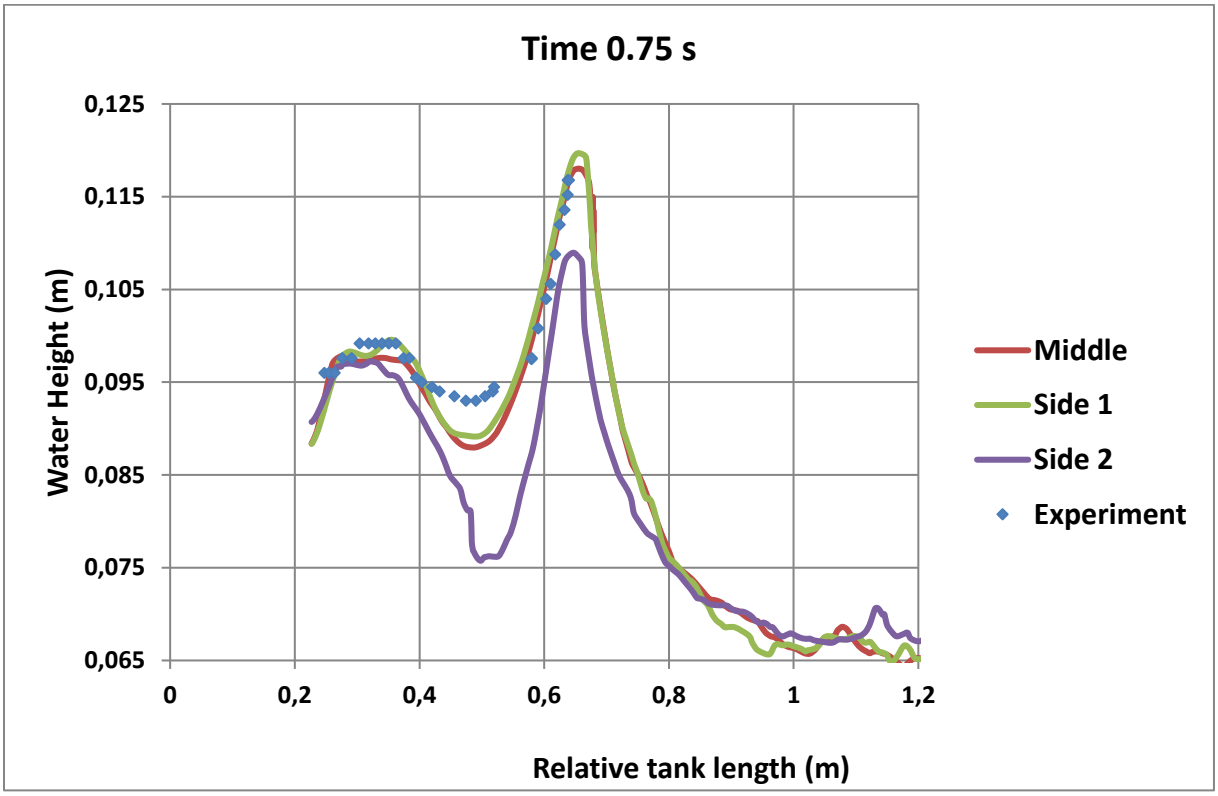

Figure 6.30: Comparison between the numerical and experimental waves 075 s after the piston motion

Furthermore, the numerical and experimental results are exhibited at the time of 0.55 s after the initial movement of the piston in Figure 6.31 and Figure 6.32, respectively.

Figure 6.33 draws a comparison between the numerical wave and the experimentally generated wave at the time of 0.55 s after the initial movement of the piston, which confirms a similarity between the waves. Nevertheless, the numerical analysis predicts a higher peak for the wave which can be justified well considering the water leakage around the piston within the experimental analysis.

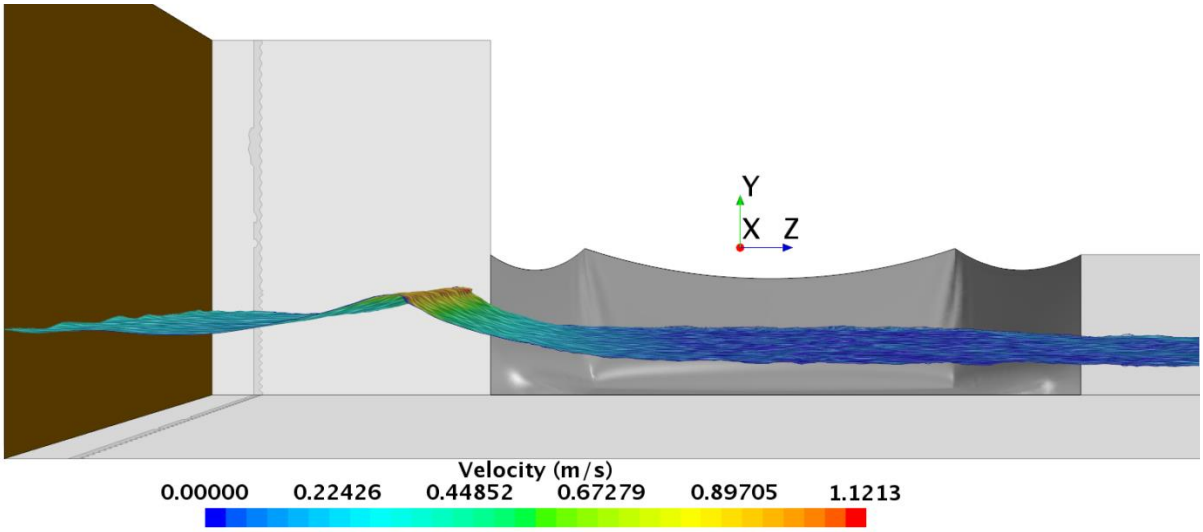

Figure 6.31: The numerical water wave and the wave velocity on the free surface water flow 0.55 s after the piston motion

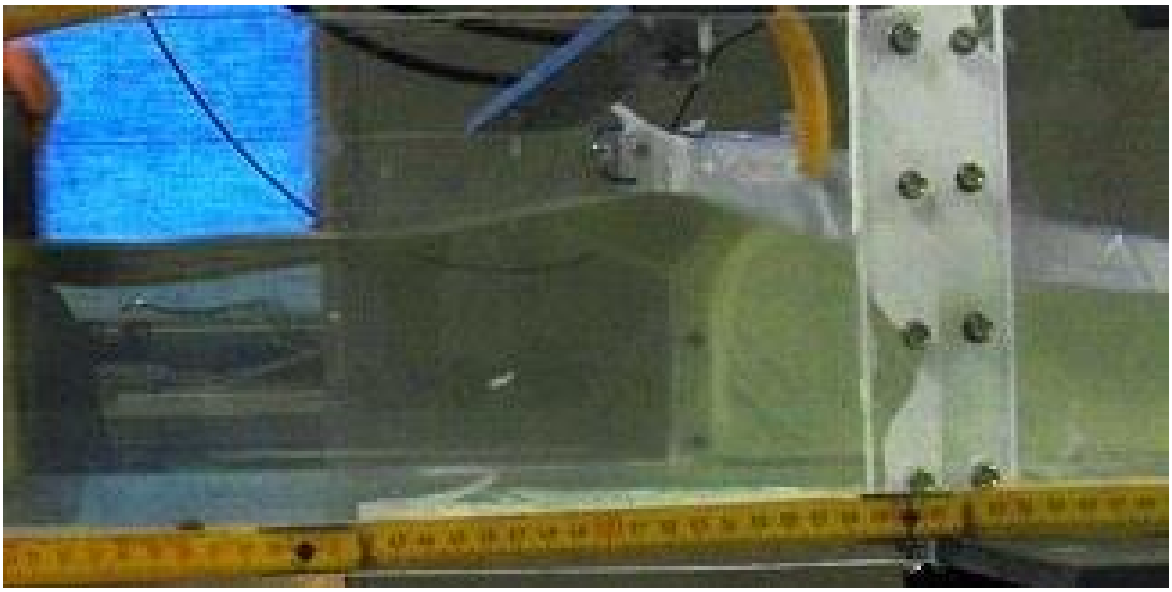

Figure 6.32: The shape of the experimental water wave 0.55 s after the piston motion

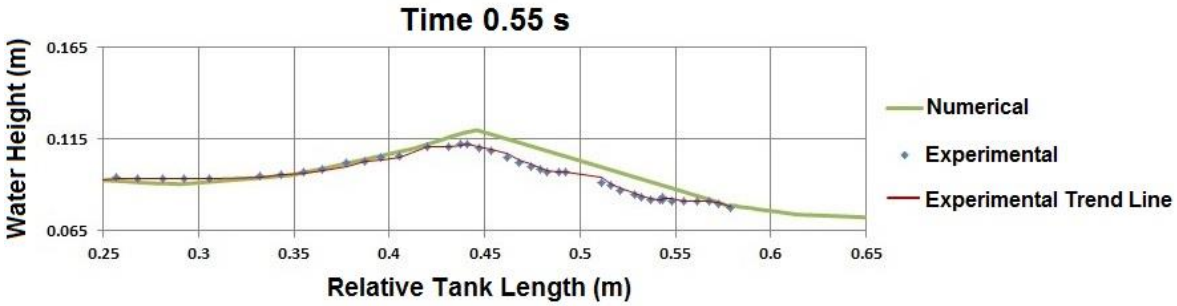

Figure 6.33: The comparison between the shapes of the experimental and numerical water waves 0.55 s after the piston motion

Figure 6.34 to Figure 6.42 exhibit the relative pressure fields and the displacement of the membrane which stem from the wave generated by the translational motion of the moving wooden body within the water tank.

The colormaps on the left hand, up and down represent the relative pressure fields on the overset region boundaries, the outer side of the membrane (exposed to the ambient air) and the inner side of the membrane (the water pressure), respectively (Figure 6.34, Figure 6.37 and Figure 6.40).

Figure 6.34 to Figure 6.36 depict the relative pressure fields, the deformation in X direction (U1) and the vertical deformation of the membrane (U2) 0.0175 s after execution of the co-simulation analysis initialized by a preloading step. The displacements of the membrane (Figure 6.35 and Figure 6.36) resulted from the water pressure load regarding an initial water depth of 7 cm. The movement of the wooden body has generated the wave which forms a peak at the front wall of the wooden body, while the most areas in the channel (nearby the membrane in particular) remain intact (Figure 6.34).

In fact, the fluid domain imposes the identical pressure (in Z direction) on the membrane (Figure 6.34) and the membrane is constrained symmetric in Z direction. That explains well why U1 and U2 exhibit symmetric behaviors in Z direction relative to the middle of the membrane (Figure 6.34 and Figure 6.36).

The same parameters were followed for a further execution time of 0.5325 s when the wave reached the membrane (refer to Figure 6.37 to Figure 6.39).

In Figure 6.37, the water wave has grown in height so that a rise in the maximum relative pressure from 824.68 Pa (Figure 6.34) to 966.14 Pa (Figure 6.37) at the tail of the wave (the colormap on the left) can be observed.

The water height has increased in the areas which are surrounded on both sides by rigid glass walls and their neighborhood, while it has plateaued at the rest of the channel.

Therefore, there exists a clear difference between the relative pressure fields shown by the bottom colormaps in the areas of the membrane influenced by the generated wave and the corresponding relative pressure fields on the areas of the membrane which are not affected by the water wave. While a maximum relative pressure of 887.03 Pa can be seen in the former areas where the water height has increased, the maximum relative pressure in the latter remains constant about 690 Pa.

As a result of a continuous motion of the water wave, the maximum relative pressure for the inner side of the membrane increased from 690.30 Pa (Figure 6.34) to 887.03 Pa (Figure 6.37) after 0.0175 s and 0.55 s since the initial piston motion, respectively.

At this time, the main part of the membrane is still unaffected by the water wave. It explains why an asymmetric relative pressure field could be seen on the membrane, while subtle changes were observed in the membrane deformations (Figure 6.38 and Figure 6.39). In other words, asymmetry in the displacements of the membrane could be noticed to a lesser degree (especially for U2 shown by Figure 6.39).

Figure 6.40 to Figure 6.42 presents the quantities for the relative pressure, the displacements of U1 and U2 respectively when the piston moves for 0.88 s.

There is a further rise in the height of the water wave, which caused an increase in the water pressure on the membrane to a great extent.

The water wave reached a maximum height in an immediate distance of the middle of the membrane after 0.88 s since the initial piston movement (Figure 6.40), which gave rise to a maximum relative pressure of 993.91 Pa for the inner side of the membrane.

At the same time, the maximum X-displacement and the maximum Y-displacement increased by 6 mm (Figure 6.41) and 2.8 mm (Figure 6.42) during 0.33 s, respectively. Furthermore, the membrane exhibited a huge asymmetry for the displacements of U1 and U2, which ensued from the fact that the left half of the membrane was loaded by the water wave, which led to a further change in the other unloaded parts of the membrane (especially in the neighborhood of the stringer).

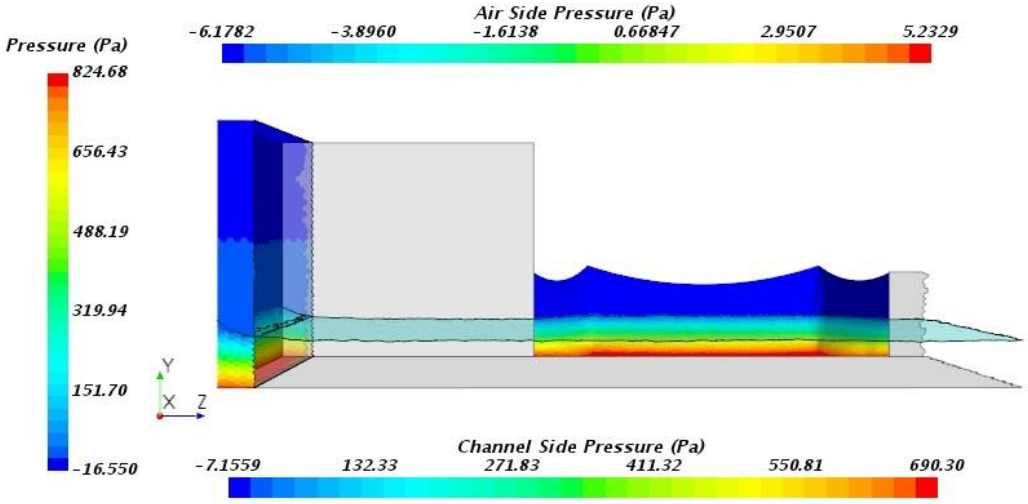

Figure 6.34: Relative pressure fields 0.0175 s after the piston motion

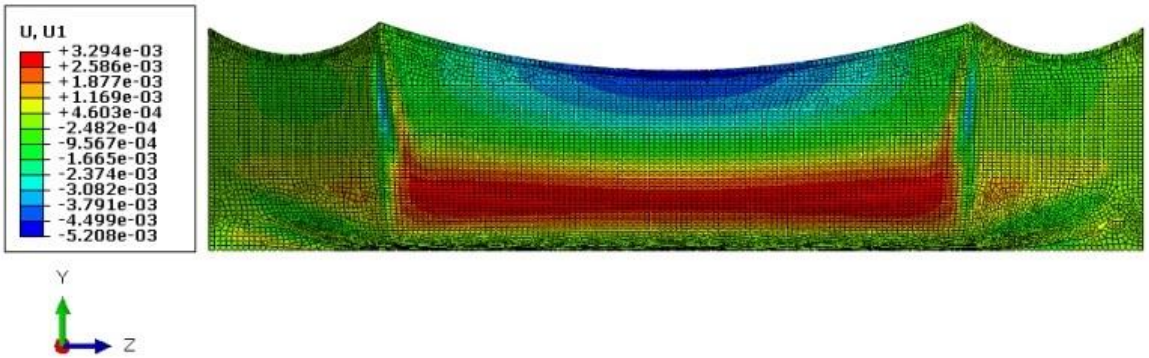

Figure 6.35: Displacements of the membrane in X direction 0.0175 s after the piston motion (The corresponding values for U1 are in meter).

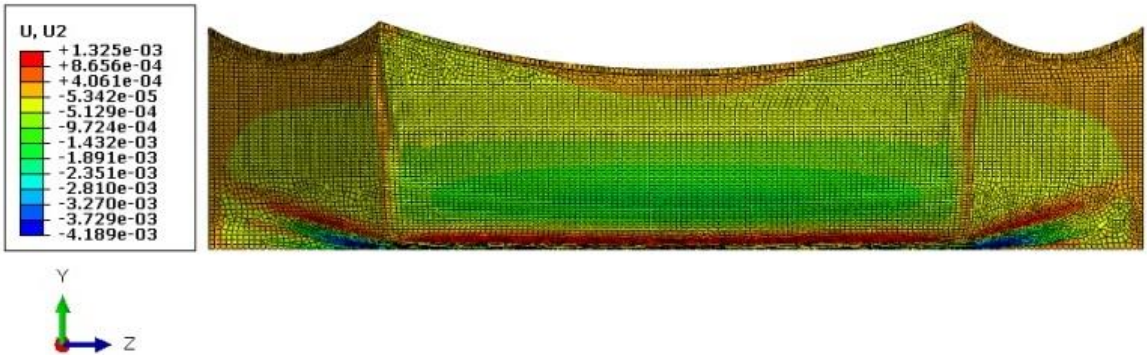

Figure 6.36: Displacements of the membrane in Y direction 0.0175 s after the piston motion (The corresponding values for U2 are in meter).

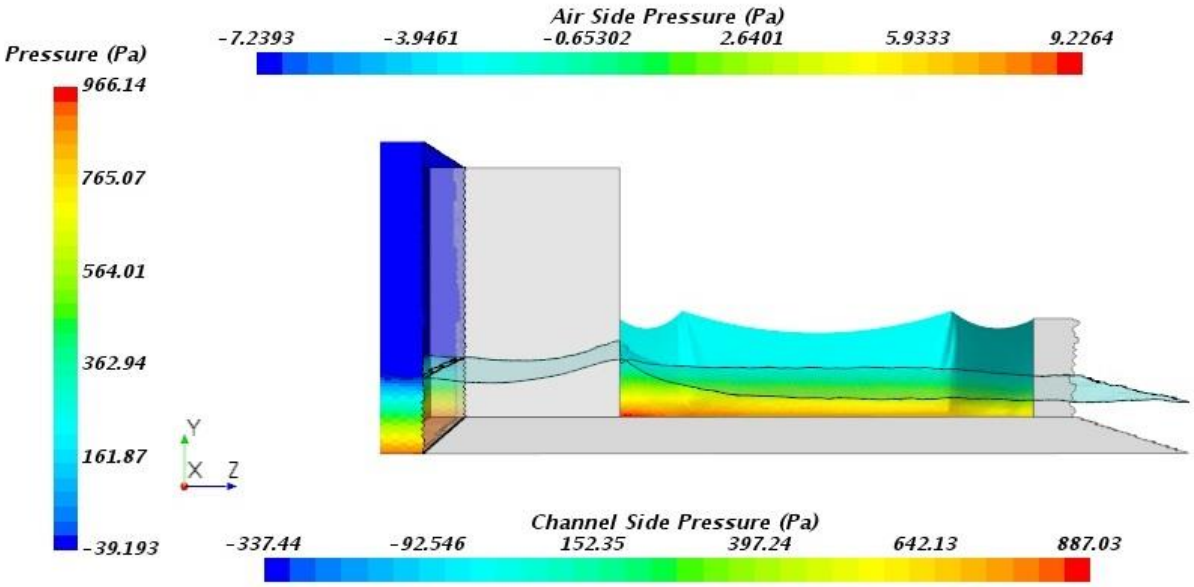

Figure 6.37: Relative pressure fields 0.55 s after the piston motion

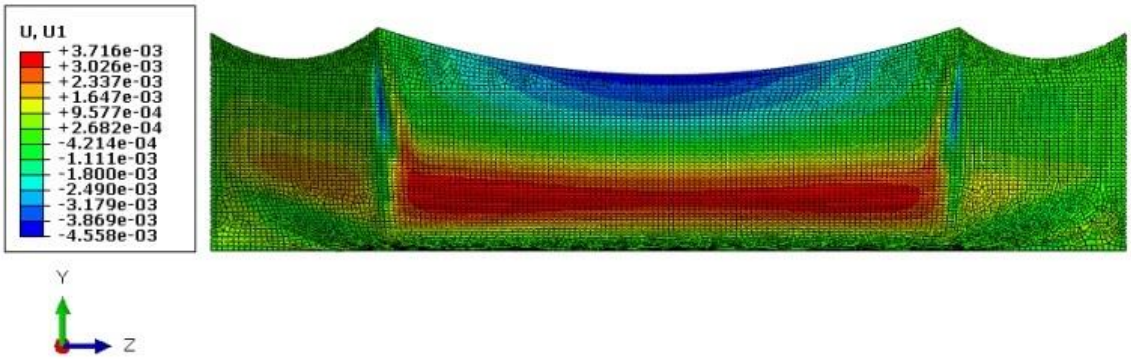

Figure 6.38: Displacement of the membrane in X direction 0.55 s after the piston motion (The corresponding values for U1 are in meter).

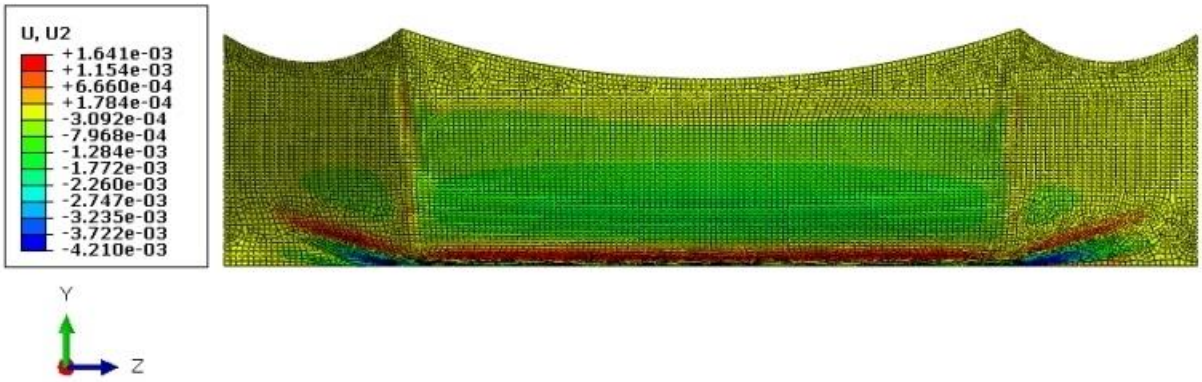

Figure 6.39: Displacement of the membrane in Y direction 0.55 s after the piston motion (The corresponding values for U2 are in meter).

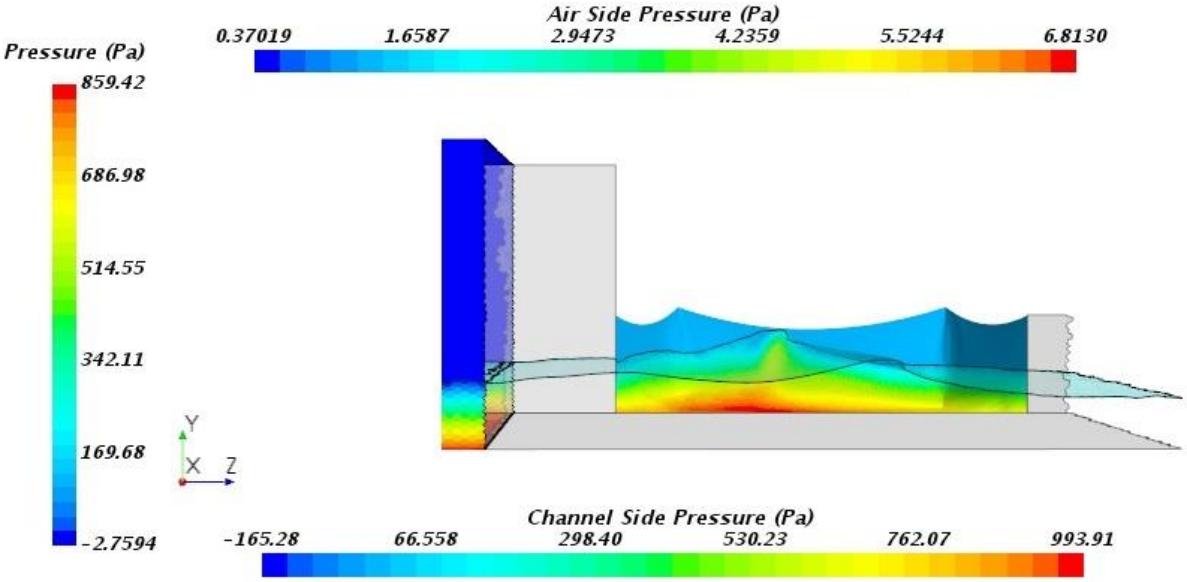

Figure 6.40: Relative pressure fields 0.88 s after the piston motion

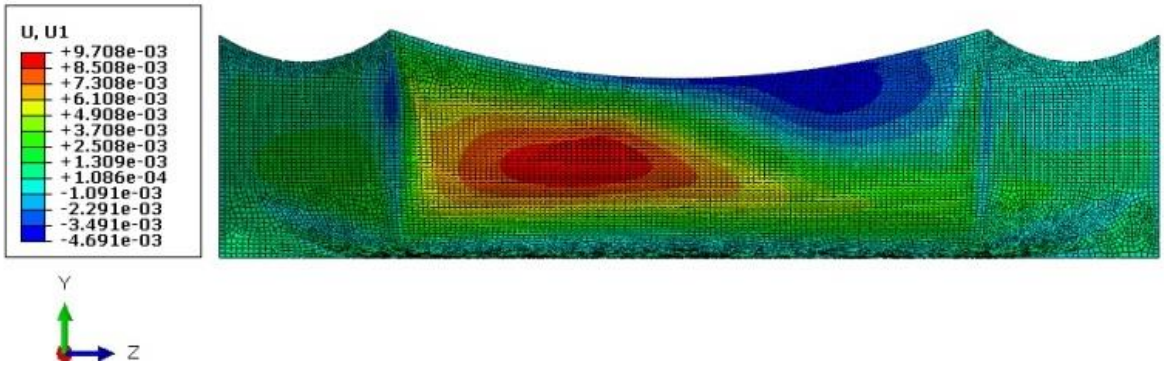

Figure 6.41: Displacement of the membrane in X direction 0.88 s after the piston motion (The corresponding values for U1 are in meter).

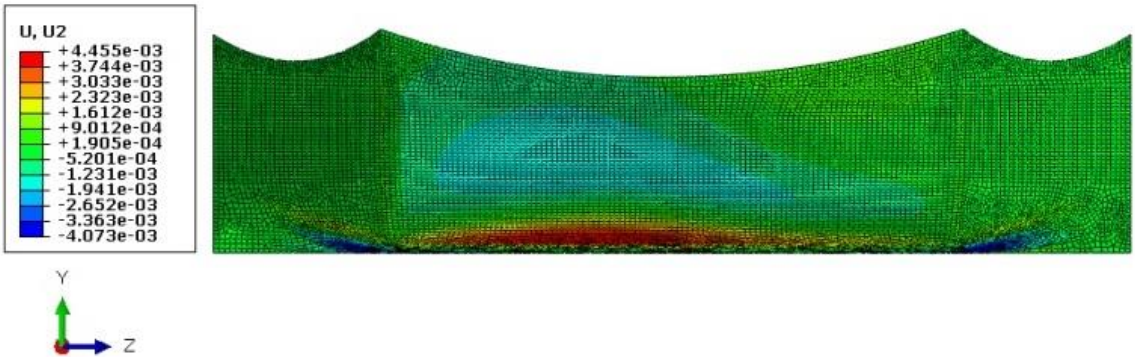

Figure 6.42: Displacement of the membrane in Y direction 0.88 s after the piston motion (The corresponding values for U2 are in meter).

In addition, the displacements results will be numerically and experimentally collected and compared in the sections 6.6.1 to 6.6.3 for the selected points on the membrane (Figure 6.43).

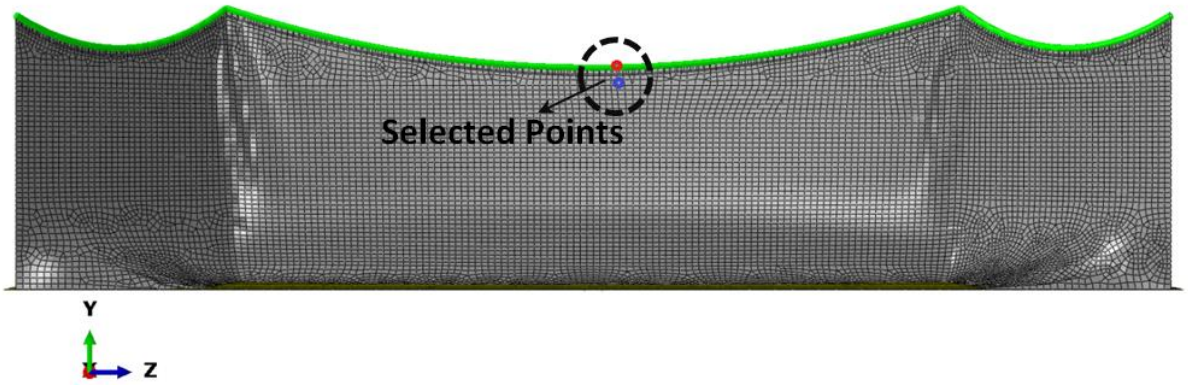

Figure 6.43: The points on the membrane selected for the X-displacement measurement (red) and the displacements in Y and Z directions (blue)

In Figure 6.43, while the point on which the displacements in Y and Z directions are measured is located on the middle of the membrane, 1 cm below the steel stringer (blue), the measurement of the X-displacement is performed on the middle of the membrane directly on the stringer (red). Moreover, the uncertainties in the experimental measurements of the displacements in X, Y and Z directions are ±0.01 mm.

In order to compare differences in X, Y, and Z displacements for the numerical results against experimental data, comparisons for each pair of the numerical and experimental results will be drawn in terms of distributions and similarity.

In this regard, two-sample Kolmogorov-Smirnov test will be performed to measure the similarity in the distributions of the data series. Then, a mathematical function will be derived for each sample by the curve fitting tool in Matlab. Afterwards, the numerical curves for the experimental and numerical results will be compared according to the Frechet distance, and dynamic time warping methods (refer to section 3.2)

In the following sections, the comparisons drawn for the displacements in X, Y, and Z directions are demonstrated.

6.6.1 Similarity tests for the displacement of the membrane in X direction

Similar to what is done in section 3.2, an exponential function as eq. (6.3) fitting best with the experimental data points for the displacement in X direction is expressed, depicted in Figure 6.44. In general, the displacements in X, Y, and Z directions are

measured experimentally in the time interval of 0.125 s (Figure 6.44, Figure 6.50, Figure 6.55), while the numerical analysis recorded the data for the displacements in every 0.001 s (Figure 6.45, Figure 6.49, Figure 6.54). That is why the number of data points for the numerical analysis is much more than the experimental analyses.

$$f(h) = ae^{(bt)} \tag{6.3}$$

Where the coefficients (with 95 % confidence bounds) are as follows:
$a = 0.01408\ (0.005231, 0.02293)$
$b = 5.62\ (4.908, 6.332)$
t: time (s)
f: the displacement in X direction (mm)

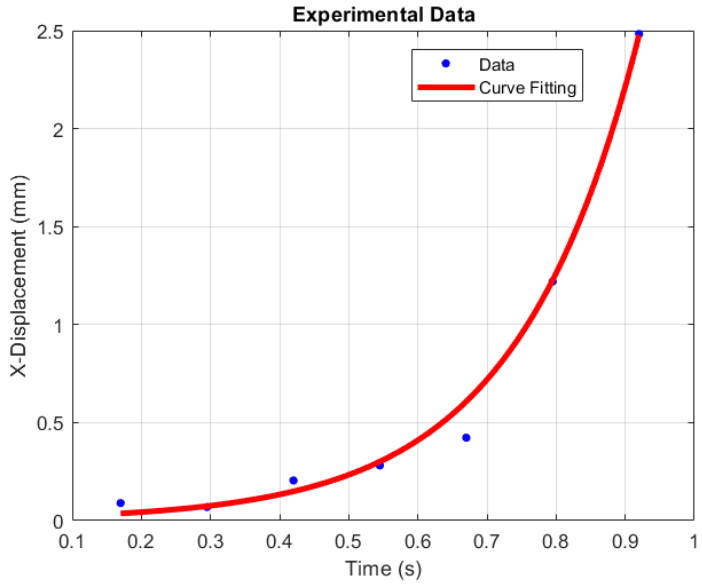

Figure 6.44: The raw data for the experimental result of the displacement in X direction (blue) and the fitting curve (red) (The data is measured for the point on the middle of the membrane, directly on the stringer. The horizontal axis indicates the time after the initial piston movement).

In the same manner, the curve (Figure 6.45) matching the numerical data points introduces an exponential function as eq. (6.3).

Where the coefficients (with 95 % confidence bounds) are as follows:
$a = 0.005745\ (0.005484, 0.006006)$
$b = 6.766\ (6.712, 6.819)$
t: time (s)
f: the displacement in X direction (mm)

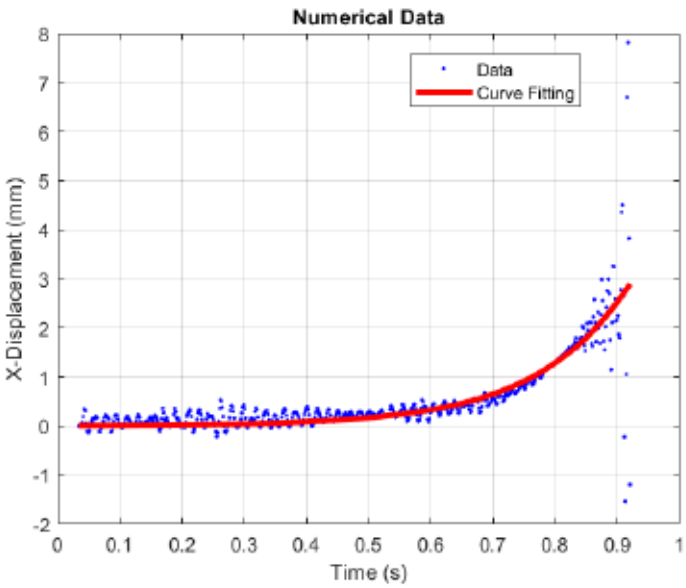

Figure 6.45: The raw data for the numerical result of the displacement in X direction (blue) and the fitting curve (red) (The data is collected for the point on the middle of the membrane, directly on the stringer. The horizontal axis indicates the time after the initial piston movement).

The results for the cumulative distribution function test (ktest2) comparing an analogy for the distributions of the experimental and numerical data points is shown according to eq. (6.4). A similar distribution for both data series (Figure 6.46) are demonstrated, where the computed values for h and p represent the validity of the null hypothesis (similar distribution) and probability of 98.03 % for the similarity. Moreover, the maximum difference for the cumulative distribution function of F(x) equals the k value of 0.1681.

$$[h, p, k] = ktest2(U_1^n, U_1^e) \tag{6.4}$$

$h = 0\ (logical)$
$p = 0.9803$
$k = 0.1681$
U_1^n: numerical data sample for the displacement in X direction
U_1^e: experimental data sample for the displacement in X direction

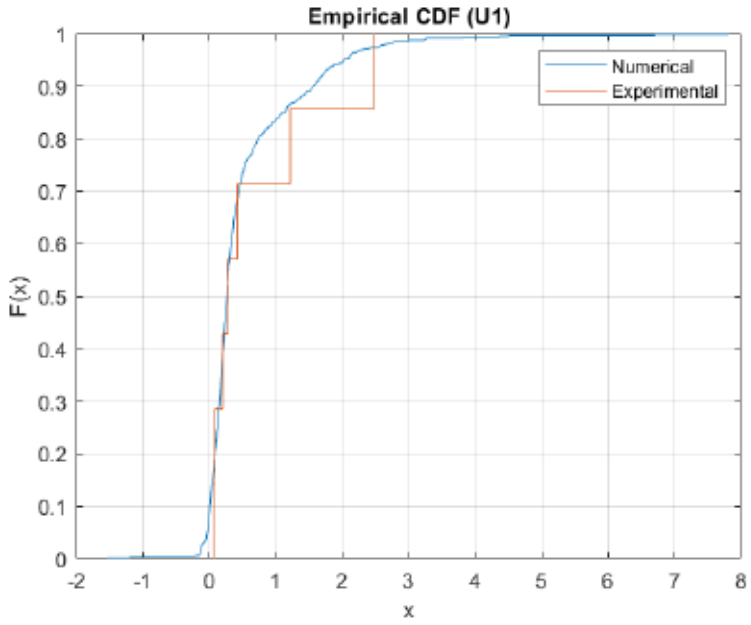

Figure 6.46: Cumulative distribution function (Horizontal and vertical axes exhibit the displacement on X direction, and the cumulative distribution function, respectively).

The Frechet distance determined as the minimum cord-length connecting a point traveling forwards along one curve and one proceeding forwards along another curve is measured between the numerical and experimental curves (Figure 6.47) for the displacement in X direction. The measurement reveals a Frechet distances of 0.4258 mm, where 600 data points on each curve are taken into consideration.

In the same manner, the cumulative distance for 600 points of curves (Figure 6.48) is computed as 4.5820 mm by the dynamic time warping method (DTW), which depicts a similarity between curves.
In addition, DTW is aimed at finding a path (warping path) between two curves minimizing the cumulative distance between points.
By warping according to the warping path, the two curves can be aligned in time (Figure 6.48), which make the original data points be transformed to the warped data points.

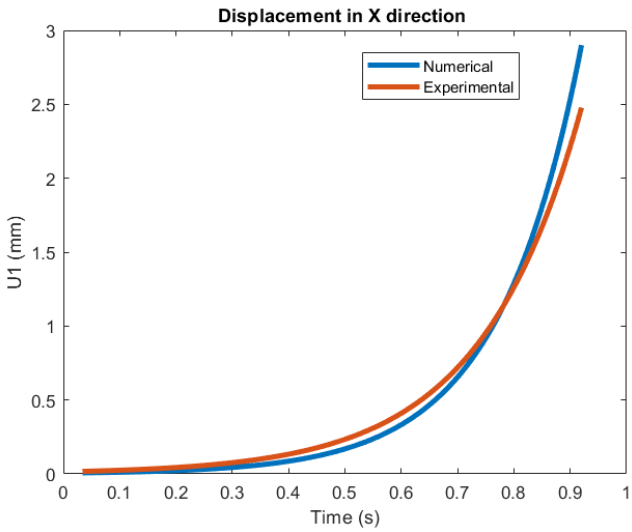

Figure 6.47: Comparison of the displacement of the membrane in X direction between the numerical curve (blue) and the experimental curve (red) (The data is measured for the point on the middle of the membrane, directly on the stringer. The horizontal axis indicates the time after the initial piston movement).

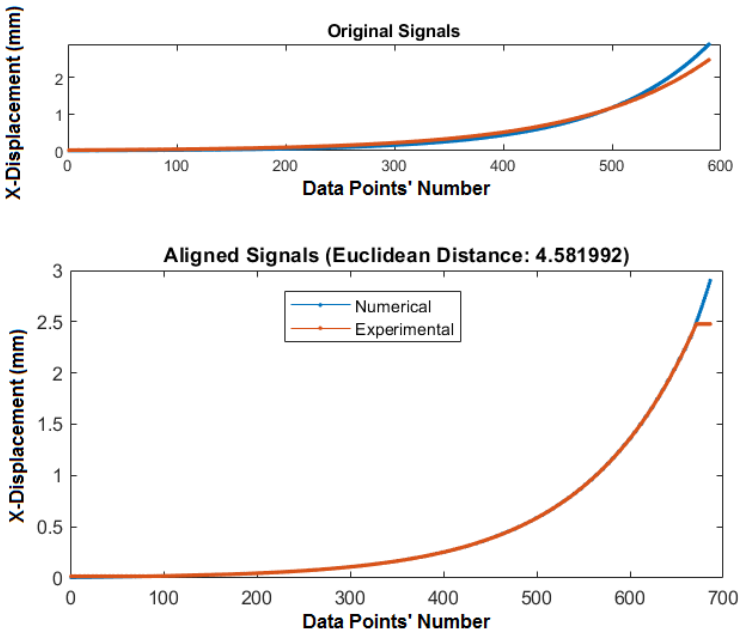

Figure 6.48: Two original sets of four data points (up) and the warped sets of the data points (down) (Horizontal and vertical axes exhibit the data points number, and the X displacement (mm), respectively).

6.6.2 Similarity tests for the displacement of the membrane in Y direction

In addition, a general form of exponential functions best suited to the numerical data points for the displacement in Y direction is described according to eq. (6.5), represented by Figure 6.49.

$$f(h) = ae^{(bt)} + ce^{(dt)} \tag{6.5}$$

Where the coefficients (with 95 % confidence bounds) are as follows:
$a = 0.01706\ (-0.01779, -0.01633)$
$b = 2.161\ (2.052, 2.27)$
$c = -2.951e^{-05}\ (-3.423e^{-05}, -2.478e^{-05})$
$d = 10.94\ (10.77, 11.1)$
t: time (s)
f: the displacement in Y direction (mm)

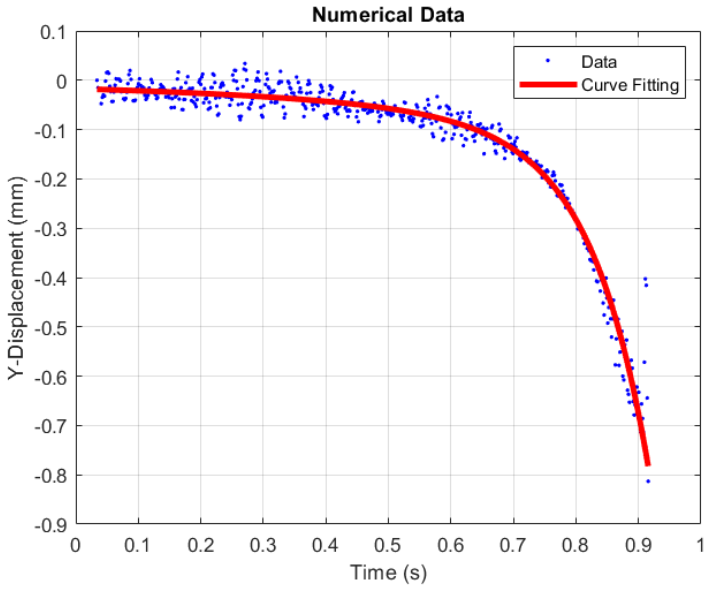

Figure 6.49: The raw data for the numerical result of the displacement in Y direction (blue) and the fitting curve (red) (The data is measured for the point on the middle of the membrane, 1 cm below the steel stringer. The horizontal axis indicates the time after the initial piston movement).

Likewise, the experimental datapoints for the displacement in Y direction can be formulated based on a general form of exponential functions as eq. (6.5), exhibited by Figure 6.50.

Where the coefficients (with 95 % confidence bounds) are as follows:
$a = -0.01646\ (-0.04587, 0.01296)$
$b = 2.344\ (-1.398, 6.085)$
$c = -2e^{-05}\ (-8.406e^{-05}, 4.406e^{-05})$
$d = 11.31\ (8.314, 14.31)$
t: time (s)
f: the displacement in Y direction (mm)

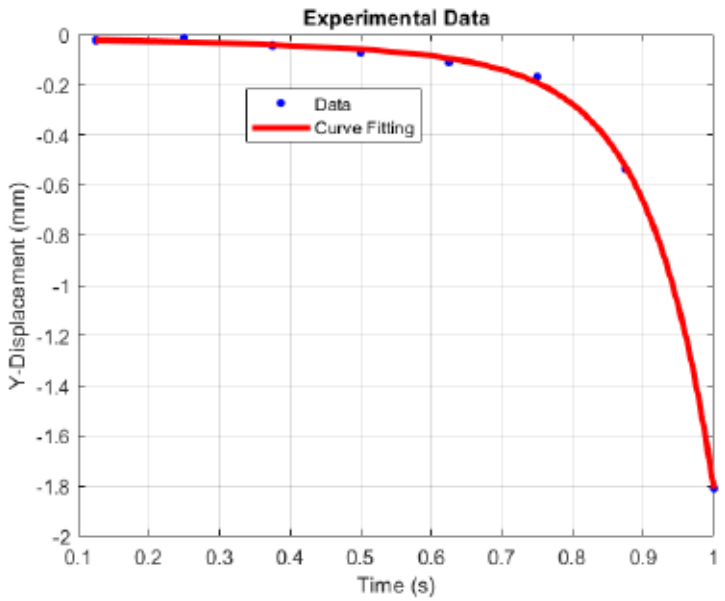

Figure 6.50: The raw data for the experimental result of the displacement in Y direction (blue) and the fitting curve (red) (The data is collected for the point on the middle of the membrane, 1 cm below the steel stringer. The horizontal axis indicates the time after the initial piston movement).

A comparison made for the similarity in the distributions of the experimental and numerical data points by the cumulative distribution function test (ktest2) is illustrated according to eq. (6.6). A similar distribution for both data series (Figure 6.51) is proved, where the computed values for h and p represent the validity of the null hypothesis (similar distribution) and probability of 99.89 % for the similarity.
Moreover, the maximum difference for F(x) equals the k value of 0.1349.

$$[h, p, k] = ktest2(U_2^n, U_2^e) \tag{6.6}$$

$h = 0\ (logical)$
$p = 0.9989$
$k = 0.1349$
U_2^n: numerical data sample for the displacement in Y direction
U_2^e: experimental data sample for the displacement in Y direction

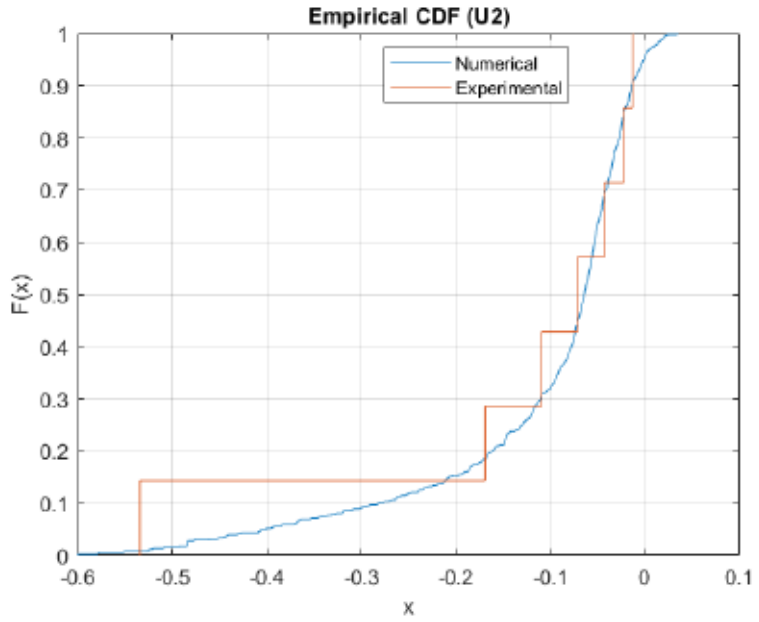

Figure 6.51: Cumulative distribution function (Horizontal and vertical axes exhibit the displacement on Y direction, and the cumulative distribution function, respectively).

In contrast to the displacement in X direction, the Frechet distance of the numerical and experimental results for the displacement in Y direction (Figure 6.52) is evidently lower. In detail, a Frechet distance of 0.0131 mm is computed for 600 data points, which indicates a good similarity between the numerical and experimental results.

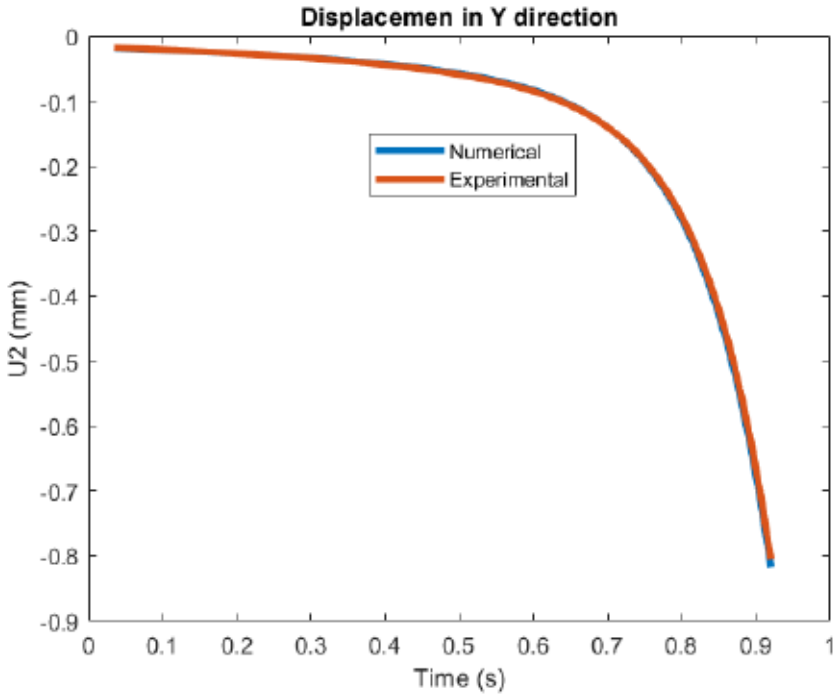

Figure 6.52: Comparison of the displacement of the membrane in Y direction between the numerical curve (blue) and the experimental curve (red) (The data is measured for the point

on the middle of the membrane, 1 cm below the steel stringer. The horizontal axis indicates the time after the initial piston movement).

Likewise, the cumulative distance for 600 points on the curves for the displacement in Y direction (Figure 6.53) is 0.2458 mm which indicates a high degree of similarity between the results.
Moreover, the original data points and the warped data points for the slope are plotted in (Figure 6.53).

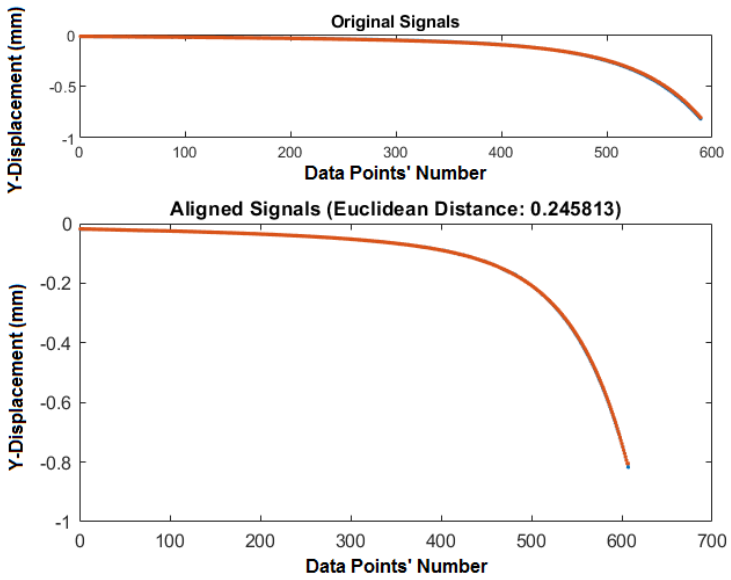

Figure 6.53: Two original sets of four data points (up) and the warped sets of the data points (down) (Horizontal and vertical axes exhibit the data points number, and the Y displacement (mm), respectively).

6.6.3 Similarity tests for the displacement of the membrane in Z direction

Likewise, the numerical datapoints for the displacement in Z direction (Figure 6.54) can be formulated based on a Gaussian model function as eq. (6.7).

$$f(h) = a_1 e^{\left(-((t-b_1)/c_1)^2\right)} + a_2 e^{\left(-((t-b_2)/c_2)^2\right)} + a_3 e^{\left(-((t-b_3)/c_3)^2\right)} + a_4 e^{\left(-((t-b_4)/c_4)^2\right)} \quad (6.7)$$

Where the coefficients (with 95 % confidence bounds) are as follows:
$a_1 = -0.0001194$
$b_1 = 0.1685$
$c_1 = 0.003523$
$a_2 = -6.398e-06$
$b_2 = 0.1804$
$c_2 = 0.0005413$
$a_3 = -0.05981$

$b_3 = 0.8579$
$c_3 = 0.1567$
$a_4 = 0$
$b_4 = 0.3121$
$c_4 = 3.696e^{-06}$
t: time (s)
f: the displacement in Z direction (mm)

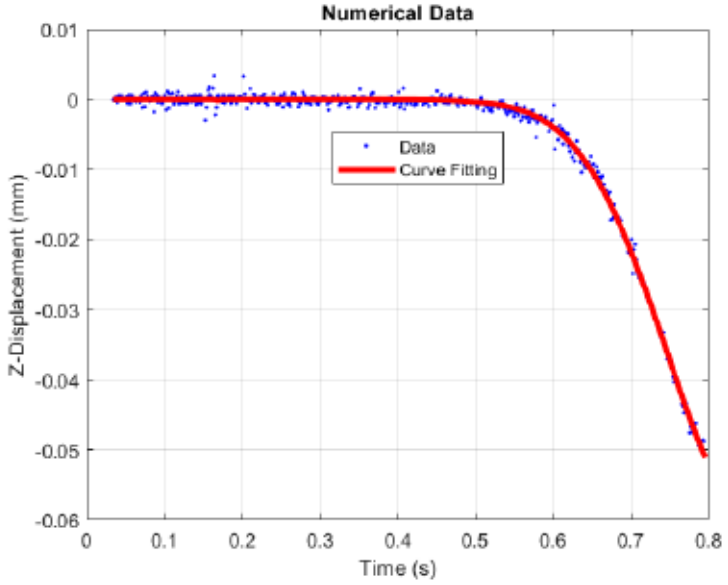

Figure 6.54: The raw data for the numerical result of the displacement in Z direction (blue) and the fitting curve (red) (The data is computed for the point on the middle of the membrane, 1 cm below the steel stringer. The horizontal axis indicates the time after the initial piston movement).

In addition, a Gaussian model function best suited to the experimental data points for the displacement in Z direction (Figure 6.55) is described according to eq.(6.8).

$$f(h) = a_1 e^{\left(-((t-b_1)/c_1)^2\right)} \tag{6.8}$$

Where the coefficients (with 95 % confidence bounds) are as follows:
$a_1 = -1.538e^{+11}\ (-1.262e^{+14}, 1.259e^{+14})$
$b_1 = 5.741\ (-133, 144.5)$
$c_1 = 0.922\ (-11.82, 13.66)$

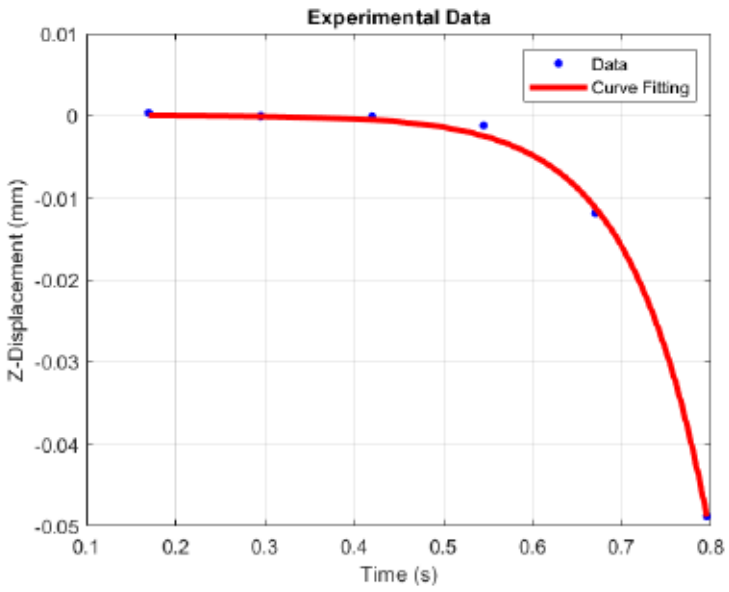

Figure 6.55: The raw data for the experimental result of the displacement in Z direction (blue) and the fitting curve (red) (The data is measured for the point on the middle of the membrane, 1 cm below the steel stringer. The horizontal axis indicates the time after the initial piston movement).

Eq. (6.9) demonstrates a comparison drawn for the similarity in the distributions of the experimental and numerical data points by the cumulative distribution function test (ktest2). The computed values for h and p exhibit the validity of the null hypothesis (similar distribution) and probability of 99.11 % for the similarity, which prove a similar distribution for both data series (Figure 6.56).
In addition, the maximum difference for F(x) equals the k value of 0.168.

$$[h, p, k] = ktest2(U_3^n, U_3^e) \tag{6.9}$$

$h = 0\ (logical)$
$p = 0.9911$
$k = 0.1680$
U_3^n: numerical data sample for the displacement in Z direction
U_3^e: experimental data sample for the displacement in Z direction

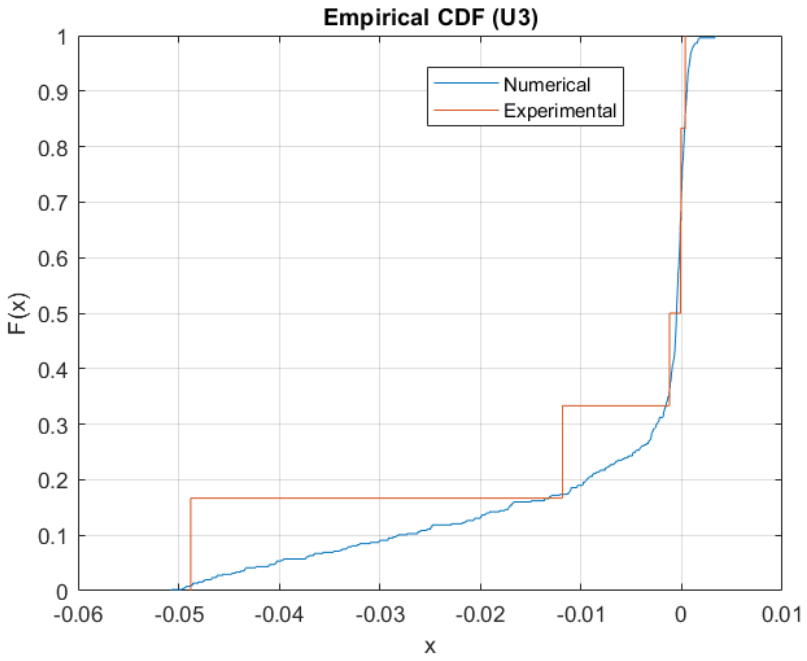

Figure 6.56: Cumulative distribution function (Horizontal and vertical axes exhibit the displacement on Z direction, and the cumulative distribution function, respectively).

In comparison to the displacement in Y direction, the Frechet distance of the numerical and experimental curves (Figure 6.57) for the displacement in Z direction is low. Nevertheless, considering the range of the data for each pair samples, the displacement in Y direction exhibits more similarity. In detail, a Frechet distance of 0.0084 mm is captured for 500 data points.

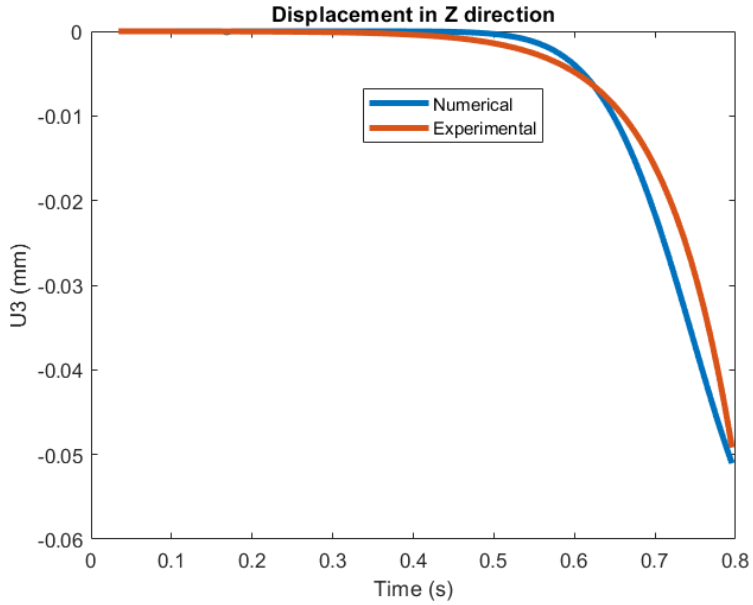

Figure 6.57: Comparison of the displacement of the membrane in Z direction between the numerical curve (blue) and the experimental curve (red) (The data is measured for the point

on the middle of the membrane, 1 cm below the steel stringer. The horizontal axis indicates the time after the initial piston movement).

Likewise, the cumulative distance for 500 points on the curves for the displacement in Z direction (Figure 6.58) is 0.0239 mm which indicates a good analogy between the curves.
Furthermore, the original data points and the warped data points for the slope are plotted in Figure 6.58.

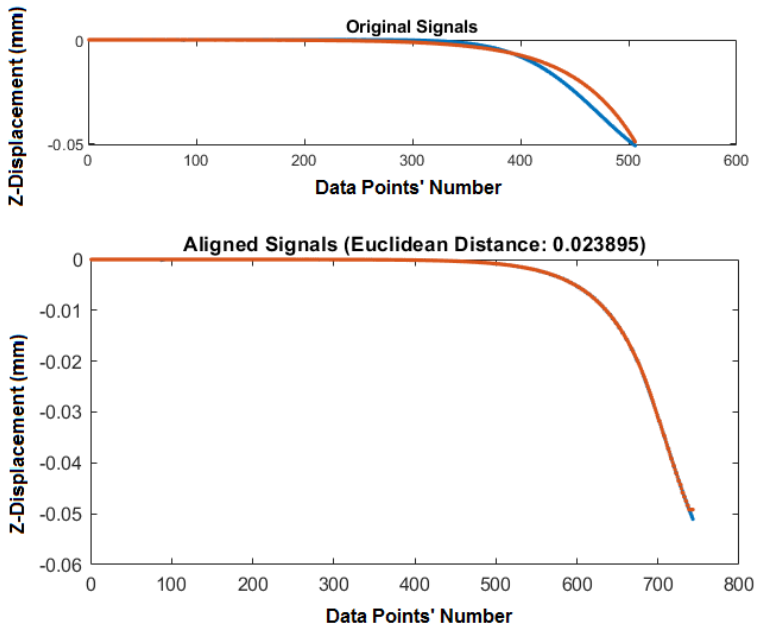

Figure 6.58: Two original sets of four data points (up) and the warped sets of the data points (down) (Horizontal and vertical axes exhibit the data points number, and the Z displacement (mm), respectively).

6.7 Concluding remarks

There are clear similarities in dominant trends for the numerical and experimental wave profiles within each captured frame. Although the wave heights differ from each other in the waves crest before 0.25 s after the piston movement, a tendency for increasing resemblance prevails afterwards for the numerically and experimentally generated waves (depicted in Figure 6.16 to Figure 6.30).

The initial high difference for the predicted numerically and experimentally observed wave heights can be justified by the effects of the leakage around the piston within the experimental analysis.
In fact, the piston fits rarely the tank dimensions exactly, which can not prohibit water from permeating into the backside of the piston. Consequently, it gives rise to

decreases in the wave heights for the experimental investigation in comparison with the numerical wave heights.

The numerically computed deformation in the membrane validates well by drawing a comparison with the experimentally captured deformation for selected points.

There was also an indication of instabilities after 0.92 s, which led to a crash in execution after 1.02 s co-simulation time. In the time of failure, the peak of the wave in side 1 passed the straight part of the membrane and the membrane was thoroughly affected by the wave.

The instability can be attributed to a lack of the stiffness proportional damping coefficient for the Rayleigh damping which is a helpful tool to dissipate disturbances with high frequency rate. The reason why no stiffness proportional damping coefficient was defined was a lack of the proper data regarding the dynamic behavior of the membrane which necessitated a further experimental modal analysis (for the down-scale model).

The loss in dynamic data forced us to set the stiffness proportional damping coefficient for the Rayleigh damping to zero in order not to lose any important dynamic effects.

To prohibit any instability, when maintaining the accuracy, an experimental modal analysis seems to be necessary.

Moreover, the improvement in the structural boundary condition on the upper edge is the other possible option which can contribute to increased convergency and precision.

Until now, the behaviors of the flexible slender structures were numerically studied for different cases and compared against experimental results. While the first scenario was conducted for the membrane loaded by the hydrostatic force in a standalone structural analysis (chapter 3), two way interactions of the membranes and water flows were analyzed within the second and third scenarios (chapters 4 and 6).

In the second case (chapters 4), the impact on the membrane in interaction with the low speed water flow was investigated, whereas the membrane was interacted with a high velocity water wave in the third case (chapters 6).

Moreover, the first and third analyses were carried out for the down-scale model membrane, while the original membrane was investigated in the second case.

In this context, the question is raised whether a correlation between the behavior of the original membrane and the down-scale model can be found. The next chapter demonstrates the circumstances upon which a correlation can be drawn between the behavior of the original membrane and the down-scale model.

7 Similarity

In this chapter, similitude analysis is used as a powerful engineering tool to study the interaction between fluids and structures together with an impact test.
Application of similarity laws permits a quantitative evaluation of the behavior of the full scale prototype based on the data for the down-scale model.

In order to correlate the response of the down-scale model to the original prototype, the similarity conditions will be established based on the Buckingham π theorem.
The comparison between the results of the numerical simulations for the full-scale prototype and the down-scale model paves the way to verify accuracy of the similitude analysis.

In this regard, the accuracy of the dimensionless numbers will be investigated numerically and discussed.
In detail, two numerical analyses will be conducted within the Abaqus standard for the full-scale prototype and the down-scale model, respectively.

7.1 Motivation

On account of the present-day high computational power combined with enhanced numerical algorithms, numerical analysis has aroused growing interest to study complex phenomena. However, experimental tests should be conducted in order to validate the applied methods and approximations within numerical models. Nevertheless, an experimental investigation on a full-scale prototype is generally expensive, time consuming and perhaps impossible due to space limitations. Hence, an experiment on a down-scale model is a more proper alternative. The condition to be able to downscale the model is physical similarity.

The similitude concept, which relates a down-scale model to a full-scale prototype, is of great importance in the design of complex structures for many engineering applications. The aim is to predict how the prototype behaves based on the results from the scaled model. As a consequence, the scaled model is targeted to replicate the behavior of the prototype, which saves considerable time, material and cost pertinent to an experimental setup for the original system. Similarity in the response of the model and the prototype implies an equality of the dimensionless numbers representing the characteristic behavior of the systems.

In many circumstances, a complete similarity between a model and a prototype is impossible to be satisfied due to geometrical factors, material characteristics, environmental conditions, and so on. A distorted model is captured with partial similarity

unless all the similarity requirements are met. The accuracy for the distorted model depends upon the appropriate dimensionless numbers which are observed when the model is fabricated and loaded.

For free surface flows, gravitational, viscous, inertial forces, and surface tension are of importance. Therefore, the Froude number, the Reynolds number, and the Weber number will be regarded as significant similarity parameters.

The Froude number deals with the relationship between gravity and inertial forces, enforcing the requirement which will be met by eq. (7.1).

$$\frac{u_p}{\sqrt{g_p l_p}} = \frac{u_m}{\sqrt{g_m l_m}} \overset{g_p=g_m}{\Longrightarrow} \frac{u_m}{u_p} = \sqrt{\frac{l_m}{l_p}} \tag{7.1}$$

where l, g and u are the characteristic length of the fluid domain, the gravity acceleration and the fluid speed, respectively.
In this chapter, subscripts of p and m represent the prototype and the model, respectively.

On the other hand, the Reynolds number relates the frictional and inertial forces. To govern the conditions of the Reynolds number and the Froude number similarity, the following equation has to be satisfied.

$$\frac{\rho_p u_p l_p}{\mu_p} = \frac{\rho_m u_m l_m}{\mu_m} \overset{g_p=g_m}{\Longrightarrow} \frac{\nu_m}{\nu_p} = \left(\frac{l_m}{l_p}\right)^{3/2} \tag{7.2}$$

where ρ, μ, and ν are the fluid density, the fluid dynamic viscosity and the fluid kinematic viscosity, respectively.

The working fluid for the prototype and model is normally either freshwater or seawater and the length scale is small. Consequently, it is impossible to satisfy simultaneously both dimensionless numbers, leading to a distortion in the dynamic similarity between the model and the prototype in interaction with the free surface flow.

The problem will be more complicated if surface tension effects are taken into account. Considering surface tension effects, the requirement for the identical Weber numbers imposes the following condition.

$$\frac{\rho_p u_p^2 l_p}{\sigma_p} = \frac{\rho_m u_m^2 l_m}{\sigma_m} \Rightarrow \frac{\sigma_m/\rho_m}{\sigma_p/\rho_p} = \frac{u_m^2 l_m}{u_p^2 l_p} = \frac{l_m^2}{l_p^2} \tag{7.3}$$

The above relation for the kinematic surface tension (σ/ρ) exhibits clearly that the same fluid cannot be used for the model and the prototype.

Therefore, the decision on which forces are more dominant on the system plays important role on the solution. Fortunately, in our target problem, both the surface tension and the viscous forces affect the free surface flow considerably less than the gravity force.

As a result, a strict adherence to the Froude number similarity has to be achieved with the expense of the ignored Weber and Reynolds number similarity.

Nevertheless, with the reduction in the depth of the flow, the surface tension effect gains in importance, sparking a matter of concern.

In order to eradicate surface tension effects from the model, different horizontal and vertical length scales can be applied; however, it initiates a geometric distortion, which must be usually considered by increasing the model surface roughness. Then, the model surface roughness must be so adjusted that an agreement between the model and the prototype would be met.

Although fluid-structure interactions have been studied by many researchers as reviewed in chapter 1, there are limited works which investigated impact analysis for FSI problems. Furthermore, similitude concept is implemented to a lesser extent for FSI problems.

In Schade et al.'s work (2016) [105], similarity laws were derived based on experimental results for a down-scale flexible channel interacting with a water flow. Nonetheless, the similitude study carried out in this work was limited to the fluid mechanics aspect.

In this chapter, the similarity conditions relating the response of the down-scale model to the original prototype will be built on the basis of Buckingham π theorem and their accuracy will be discussed. The scaling law will be implemented on the membrane subjected to a hydrostatic pressure and a high velocity impact load with an emphasis on the structural aspect. The numerical analysis will be utilized to verify the validity of the applied dimensional analysis.

The behavior of a physical system depends on many parameters, i.e. the geometry, the material behavior, the dynamic response and the energy characteristics of the system.
To determine the influential parameters, the governing physical phenomena should be understood.

In this respect, the governing equations of thin wall plates will firstly be expressed, which provide guidance in the selection of key variables for down scaling of the target structure.

7.2 Governing equations

On account of the important role of the water pressure and the impact load on the deformation of the thin flexible structure, a bending load can be regarded as a dominant load.

Since the thin flexible membrane is reinforced with a steel stringer on the upper border, two groups of equations have been established to characterize the response of the beam and the membrane to the bending load.
Pozrikidis (2009) [87] have used the linear constitutive eq. (7.4) for the bending moments to compute flow-induced deformation of an elastic two-dimensional membrane adhering to a wall.

$$m = B_M(K - K_R) \tag{7.4}$$

where m, K and K_R are the bending moments, the curvature of the membrane in the two-dimensional plane, and the curvature of the membrane in a resting configuration, respectively. Moreover, the theory of thin plates contributes to estimate the bending stiffness of the membrane (B_M) by the following relation (Fung 1965) [149].

$$B_M = \frac{E_M t^3}{12(1-\nu^2)} \tag{7.5}$$

where t, E_M and ν are the thickness, the Young modulus and the poisson ratio of the membrane, respectively.

Furthermore, based on the theory of beams, Fung (1965) [149] has used the following equation to define the bending moment (m) for beams.

$$m = \frac{E_s I}{R} \tag{7.6}$$

where R and $E_s I$ are the radius of the beam curvature after bending and the bending stiffness of the beam, respectively.

For the steel beam with a circular cross section (with the radius of r), the bending stiffness (B_{beam}) can be calculated based on eq. (7.7).

$$B_{beam} = E_s I = E_s \left(\frac{\pi r^4}{4}\right) = E_s \frac{A_s^2}{4\pi} \tag{7.7}$$

Also, A_s, E_s, and I represent the cross section area, the Young modulus, and the moment of inertia of the steel cord with the circular cross section, respectively.

7.3 Buckingham Pi theorem

The behavior of any physical phenomena can be measured fundamentally according to dimensions such as length, mass, time, temperature, electric charge and so on. The equations governing conditions on physical problems can be expressed as follows:

$$F(X_1, X_2, \ldots, X_k) = 0 \tag{7.8}$$

where $X_1, X_2, \ldots, X_k$ are k physical variables.

The above equation can be transformed in the form of eq. (7.9).

$$G(\pi_1, \pi_2, \ldots, \pi_{k-r}) = 0 \tag{7.9}$$

where $\pi_1, \pi_2, \ldots, \pi_{k-r}$ are dimensionless products of the k physical variables and r refers to the number of the fundamental dimensions (here M (mass), L (length), T (time)) dominating within the physical problem.
The equality of the π terms between the scaled model and the original one is termed as the similitude requirement.

7.4 Dimensionless numbers

At this point, the step-by-step approach adopted to determine dimensionless numbers for the target impact analyses is explained. It is aimed at finding how the prototype interacting with both water flow and a heavy flotsam behaves when the data for its downscaled model is available (Figure 7.1).

The prototype membrane and the relevant projectile were modeled with the same geometrical, material and boundary conditions as defined in chapter 4.
A scale factor of 10 (the scale factor S=10) was introduced as the ratio of the geometrical dimensions in the prototype membrane to the corresponding geometrical parameters in the model membrane. To maintain the geometrical similarity, both the prototype and the down-scale model share the same boundary condition.

Moreover, the working fluid for the prototype and the model was assumed as water with similar density.

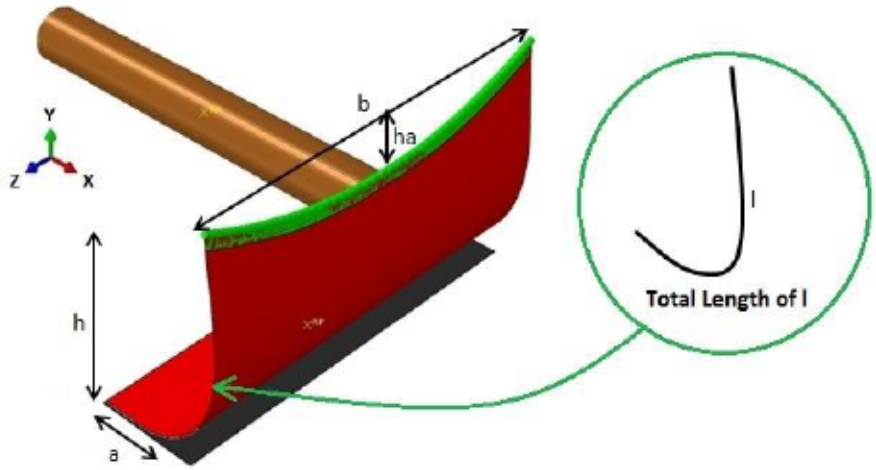

Figure 7.1: Illustration of the model: the membrane (red); the steel cord (green); the flotsam (brown); the bottom of the channel (dark grey)

The governing equations on the system like eq. (7.4) to eq. (7.7) contribute to the proper selection of key parameters. Then, the procedure to derive the dimensionless groups by means of the Buckingham π theorem is as follows.

First, all the variables involved in the problem can be listed as l, C, B_M, W_M, B_{beam}, P, W_s, M, A, h, b, a, ha and t.

While B_M and W_M stand for the bending stiffness and the weight per area of the membrane, B_{beam} and W_s denote the bending stiffness and the weight per length of the steel cord. L, h, b, a, ha, and t represent the geometrical parameter of the flexible structure, whereas A, M and C are the cross section area, the mass and the initial velocity of the projectile. Furthermore, the water hydrostatic pressure is termed as P.

The water hydrostatic pressure: $P = \rho_w g h_w$

The weight of the membrane per area: $W_M = \rho_M t$

The weight of the steel cord per length: $W_s = \rho_s A_s$

where ρ_M and ρ_s are the density of the membrane and the density of the steel cord, respectively. The thickness of the membrane and the circular cross section of the steel cord are represented by t and A_s, respectively. Moreover, ρ_w and h_w denote the water density and the water level, respectively.

Then, the variables are decomposed in terms of the basic dimensions (M, L, and T), where M, L, and T represent fundamental dimensions of mass, length, and time, respectively. Next, the repeating variables, namely l, B_M, B_{beam} are selected as a set of r dimensional variables which include all the primary dimensions. Finally, an attempt

has been made to form π terms (the dimensionless groups) for each non-repeating variable in combination with repeating variables.

Similitude requirement

The dynamic similarity conditions between the prototype and the down-scaled model were derived from the structural viewpoint based on the dimensional analysis theory, whereby six dimensionless groups must be met, excluding the geometrical similarity.

$$\pi_1 = \frac{W_M l^3}{B_M} \tag{7.10}$$

$$\pi_2 = \frac{B_{beam}}{B_M l} \tag{7.11}$$

$$\pi_3 = \frac{P l^3}{B_M} \tag{7.12}$$

$$\pi_4 = \frac{W_s l^2}{B_M} \tag{7.13}$$

$$\pi_5 = \frac{M C^2}{B_M} \tag{7.14}$$

$$\Rightarrow \pi_{42} = \frac{\pi_4}{\pi_2} = \frac{W_s l^3}{B_{beam}} \tag{7.15}$$

For a 1/10th scaled down model, all the geometrical parameters of the model should be scaled by a factor (S), i.e. $l_m = l_p/S$, where the suffix m and p denote the model and the prototype, respectively.

$$\pi_6 = \frac{A}{l^2} \tag{7.16}$$

$$\pi_7 = \frac{h}{l}, \qquad \pi_8 = \frac{b}{l}, \qquad \pi_9 = \frac{a}{l}, \qquad \pi_{10} = \frac{ha}{l} \tag{7.17}$$

The water hydrostatic pressure depends on the height and the density of water, leading to the following relation with the assumption of an identical density for two samples.

$$\frac{P_p}{P_m} = \frac{h_{wp}}{h_{wm}} = S \tag{7.18}$$

As a result, to achieve a similarity, the hydrostatic pressure has to be scaled by 10.

To meet the third dimensionless term:

$$\frac{B_{M,p}}{B_{M,m}} = S^4 \Rightarrow \left(\frac{E_M t^3}{(1-\nu^2)}\right)_p = S^4 \left(\frac{E_M t^3}{(1-\nu^2)}\right)_m \tag{7.19}$$

In order to satisfy the second dimensionless term:

$$\frac{B_{beam,p}}{B_{beam,m}} = S^5 \Rightarrow (E_s A_s^2)_p = S^5 (E_s A_s^2)_m \tag{7.20}$$

By exerting the forth dimensionless number:

$$W_{S,p} = S^2\, W_{S,m} \Rightarrow (\rho_s\, A_s)_p = S^2 (\rho_s\, A_s)_m \tag{7.21}$$

As a result, we cannot use the same material for the cord in the down-scale model. In detail, the materials for the prototype and the down-scale model have to share common density, albeit with different Young modulus.

The first dimensionless number leads to:

$$W_{M,p} = S\, W_{M,m} \Rightarrow (\rho_M t)_p = S(\rho_M t)_m \tag{7.22}$$

To maintain the fifth dimensionless term:

$$(MC^2)_p = S^4 (MC^2)_m \tag{7.23}$$

Because of the buoyancy effect, the density of the projectile should stay constant.

$$\Rightarrow (VC^2)_p = S^4 (VC^2)_m \tag{7.24}$$

V is the volume of the projectile.

7.5 Simulation setup

To verify the accuracy of the dimensional analysis, two structures have been prepared. The former represented the original structure with the same geometrical and material characteristics as described in chapter 4, while the latter was geometrically downscaled as 1:10. Both models were constructed, meshed, and prepared within the Abaqus CAE, where the flexible parts were imported from the simulation of the full-scale prototype to the other simulation and downscaled by a scale factor of 10.

Moreover, the material properties assigned to the down-scale model were followed the requirements imposed by the gained dimensionless numbers. In detail, the density and the Poisson ratio of both the membrane and the stringer remained constant, whereas the Young's moduli for both of them were reduced 10 times. Furthermore,

the thickness of the membrane and the diameter of the stringer for the model were downscaled as 1:10. As a result, the plastic behaviors of the flexible materials have to be different. The yield stress and the applied stresses resulting in plastic deformations for the membrane within the down-scale model were reduced by a factor of 10 for the same strain rates which were introduced within the prototype.

For the full-scale prototype, the representation for the flotsam was made by a cylindrical three-dimensional discrete rigid part with a diameter of 0.4 m, a length of 3 m, and a mass of 330 kg at the flotsam center of gravity.
In contrast, a cylindrical three-dimensional discrete rigid part with a diameter of 0.04 m, a length of 0.3 m, and a mass of 3.3 kg was attributed to the flotsam for the down-scale model.

The water hydrostatic pressure with regard to a water level of 135 cm was imposed on the prototype by the user defined subroutine of DLOAD, updated in accordance with the deformed shape during the solution.
A new user defined subroutine of DLOAD based on a water level of 13.5 cm was applied to depict the updated hydrostatic pressure distributions for the down-scale model in every time step.

Each of the simulations was performed in two steps, where the flotsam was accelerated towards the membrane during the former step, followed by the elimination of the acceleration within the latter step.
To accelerate each of the flotsams, a velocity boundary condition was imposed on each of the flotsams, where the velocity was altered from 4 m/s for the full-scale prototype to 0.4 m/s for the down-scale model.

7.6 Results

Figure 7.2 to Figure 7.13 demonstrate the results for both membranes before they make contact with the pertinent heavy accelerated flotsam.

The displacement fields in X-direction are shown in Figure 7.2 and Figure 7.3 for the down-scale model and the full-scale prototype, respectively.
While both figures exhibit symmetric displacements in X-direction relative to X-Y plane, the latter represents the displacement field in X-direction which is about 10 times bigger than the corresponding displacements field in the former, as expected.
For instance, the maximum X-displacement for the down-scale model is in the range between 2.11 mm and 2.3 mm when the full-scale prototype deforms with a peak of 20.48 mm in X direction.

The same trend can be seen in Figure 7.4 and Figure 7.5, which represent the displacement fields in Y-direction for the down-scale model and the full-scale prototype, respectively.

In detail, symmetric displacements in Y-direction relative to X-Y plane stand out for both cases. Similarly, the ratio of 10 to 1 is maintained for the displacement in Y-direction between the prototype and the down-scale model.

Although displacements in Z-direction seem not to be similar relative to X-Y plane, the same displacements in Z-direction but in opposite directions are resulted for both the down-scale model and the full-scale prototype (refer to Figure 7.6 and Figure 7.7). Likewise, a ratio of 10 to 1 for the displacement in Z-direction between the prototype and down-scale model is still valid.

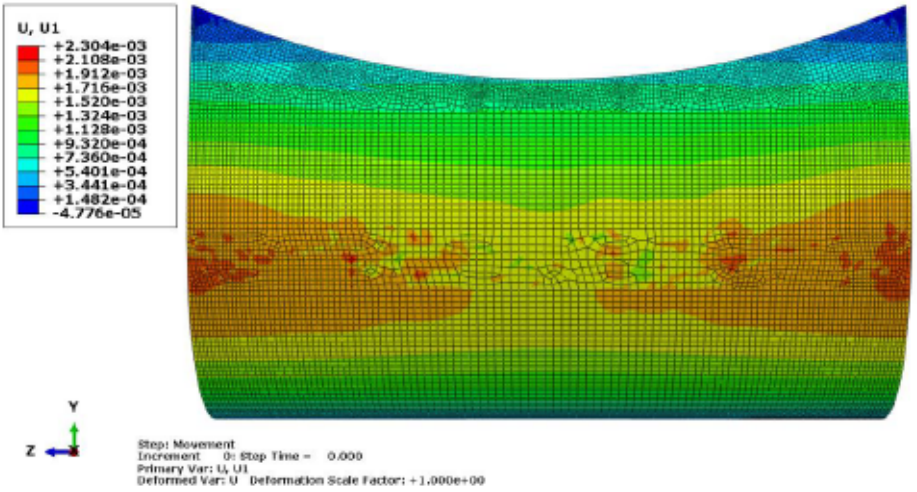

Figure 7.2: Displacement in X direction before impact for the down-scale model (The corresponding values for U1 are in meter).

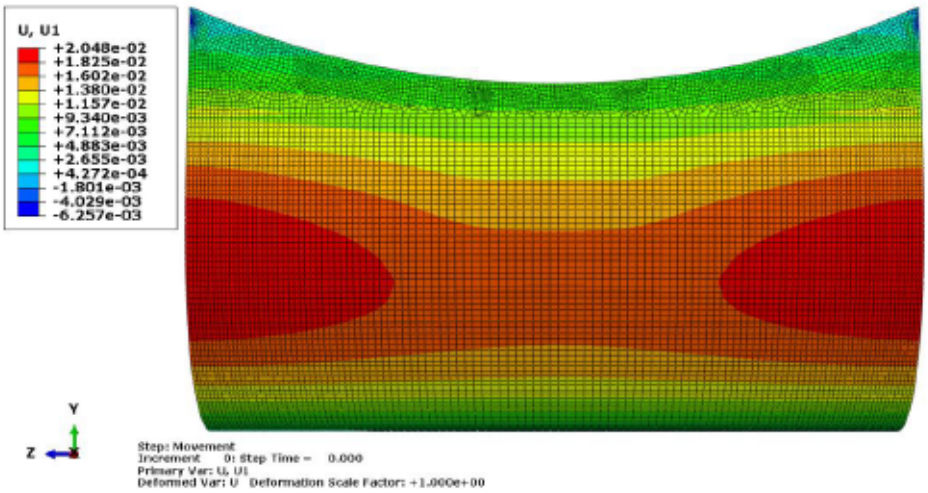

Figure 7.3: Displacement in X direction before impact for the full-scale prototype (The corresponding values for U1 are in meter).

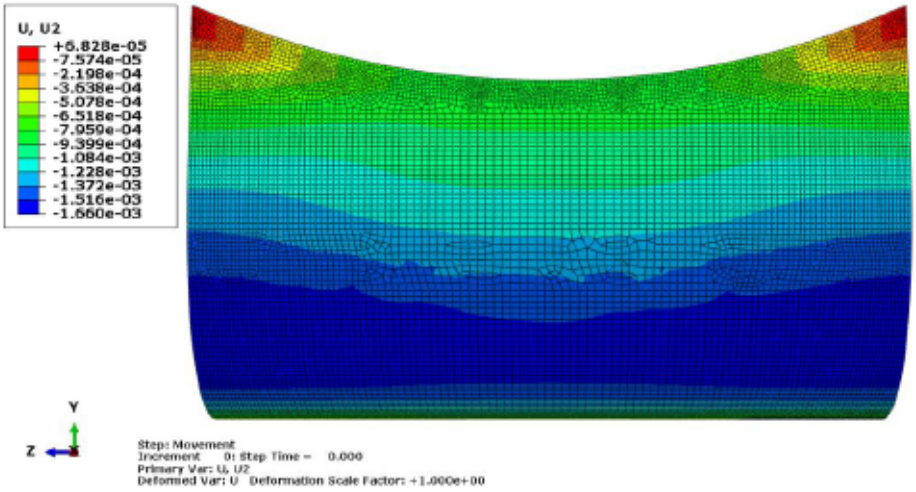

Figure 7.4: Displacement in Y direction before impact for the down-scale model (The corresponding values for U2 are in meter).

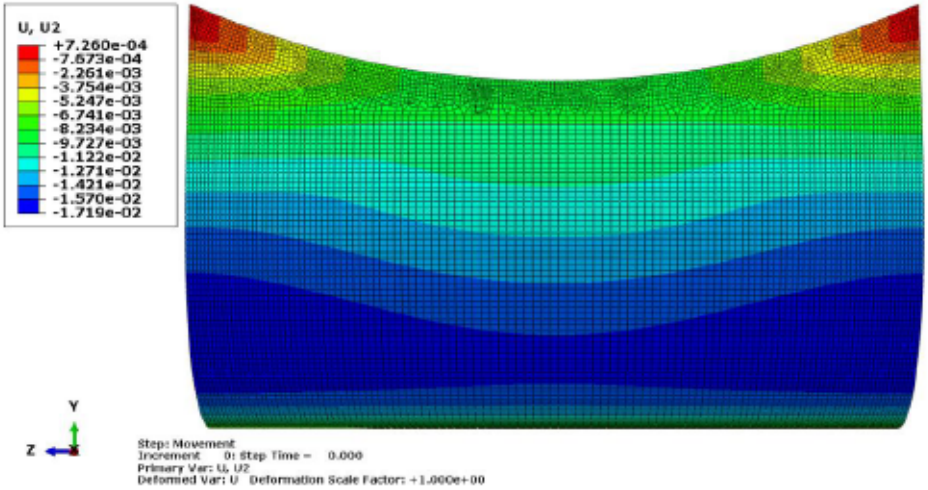

Figure 7.5: Displacement in Y direction before impact for the full-scale prototype (The corresponding values for U2 are in meter).

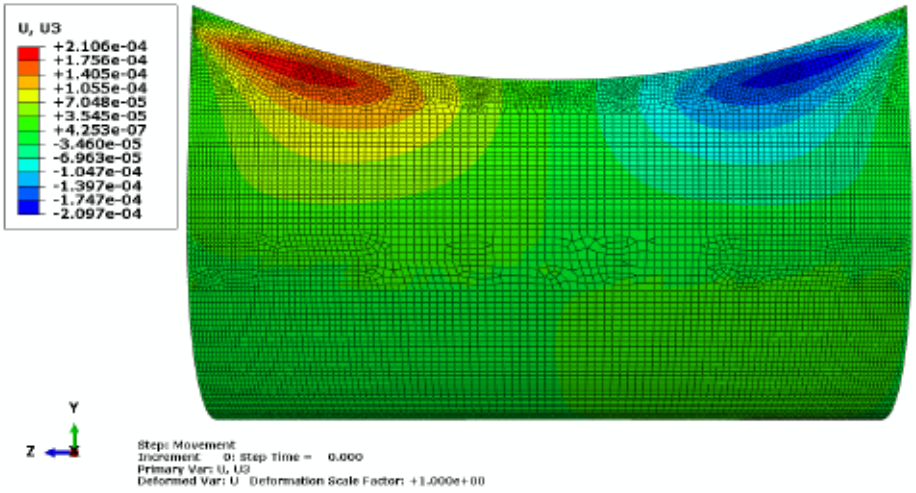

Figure 7.6: Displacement in Z direction before impact for the down-scale model (The corresponding values for U3 are in meter).

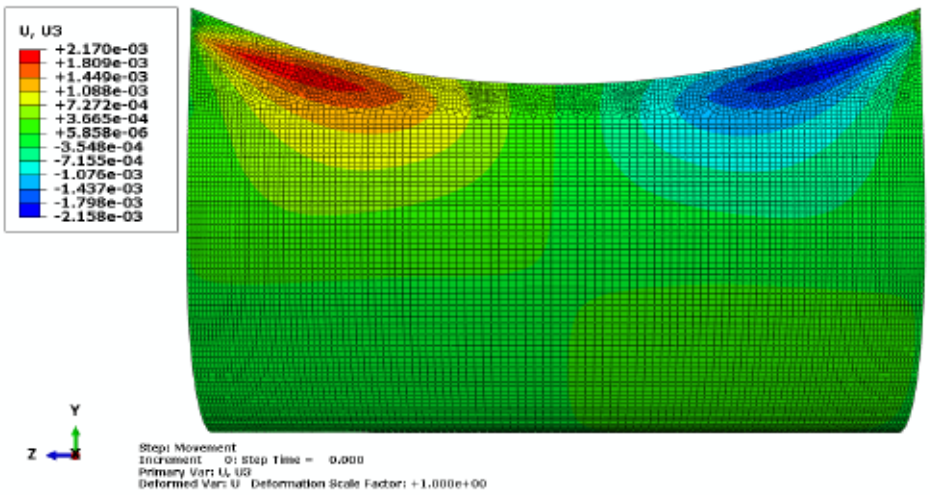

Figure 7.7: Displacement in Z direction before impact for the full-scale prototype (The corresponding values for U3 are in meter).

There is also a relation between the Von Mises stresses for the down-scale model and the full-scale prototype, where the ratio of the former to the latter is about 1/10 (Figure 7.8 and Figure 7.9). For example, the main part of membranes is under the Von Mises stress of 1.047 MPa and 10.50 MPa, respectively.

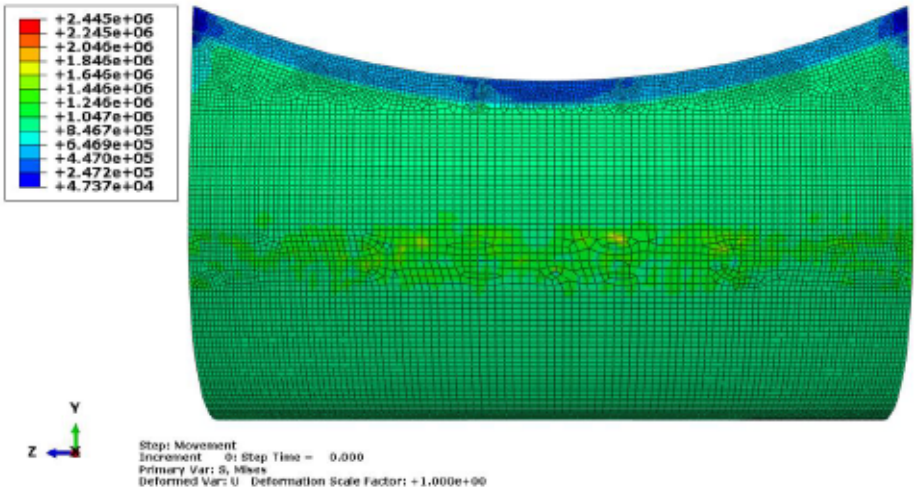

Figure 7.8: Von Mises stress before impact for the down-scale model prototype (The corresponding values for Von Mises stress are in Pa).

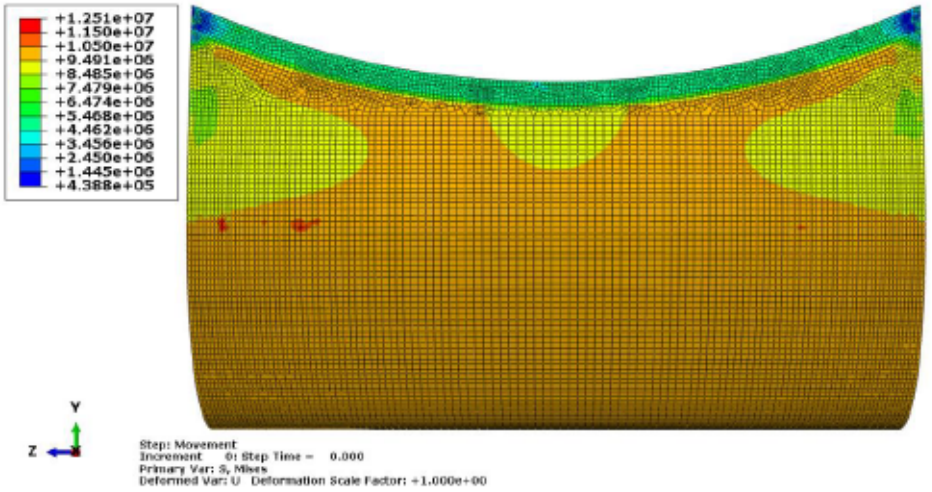

Figure 7.9: Von Mises stress before impact for the full-scale prototype (The corresponding values for Von Mises stress are in Pa).

Since strain is a dimensionless parameter, the maximum in-plane principal plastic strain and the plastic strain in X direction for the down-scale model (Figure 7.10 and Figure 7.12, respectively) are of the same order as the full-scale prototype (Figure 7.11 and Figure 7.13, respectively). The symmetric patterns relative to X-Y plane are here also preserved.

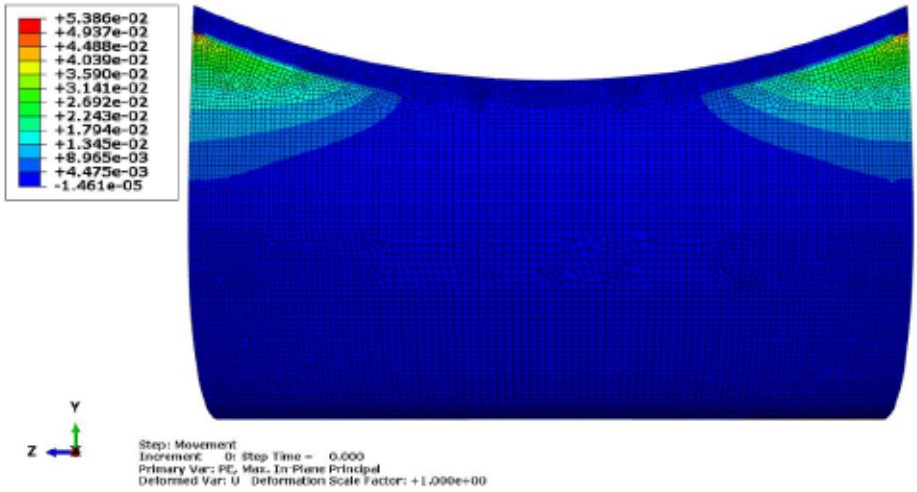

Figure 7.10: Maximum in-plane principal plastic strain before impact for the down-scale model

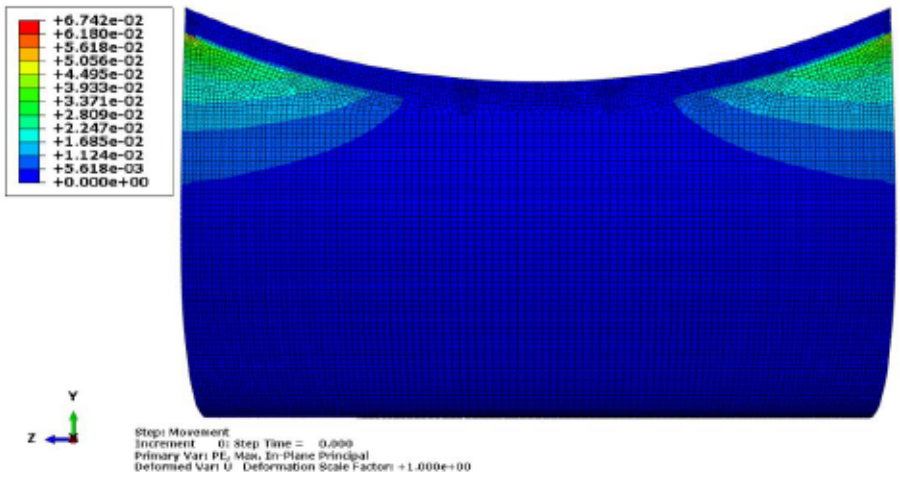

Figure 7.11: Maximum in-plane principal plastic strain before impact for the full-scale prototype

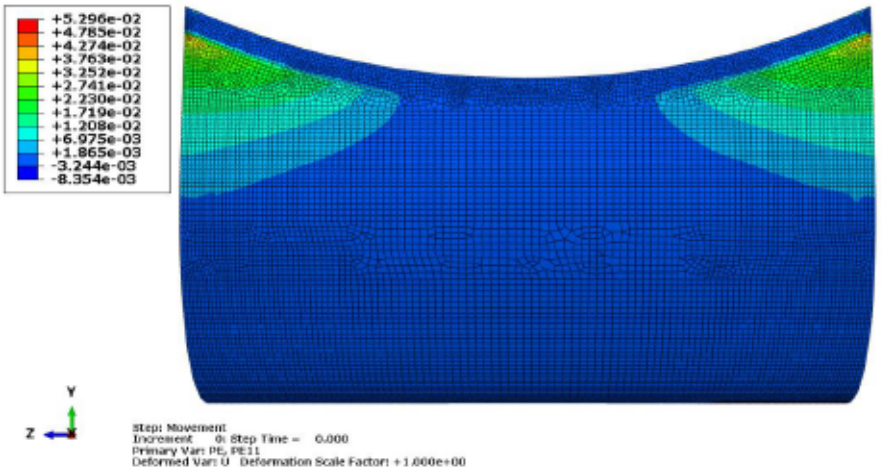

Figure 7.12: Plastic strain in X direction before impact for the down-scale model

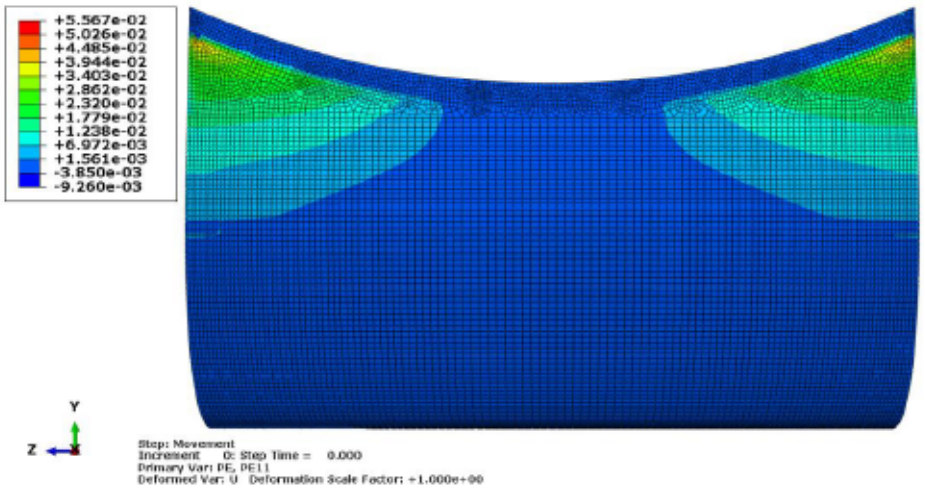

Figure 7.13: Plastic strain in X direction before impact for the full-scale prototype

The results for both membranes impacted by corresponding heavy accelerated flotsam for 0.1044 s are depicted in Figure 7.14 to Figure 7.25. In fact, during 0.1044 s after impact, maximum deformations for both membranes can be observed.

The results captured after impact show the same tendency exhibited by the results before impact. In other words, the deformation ratios and symmetrical patterns for both the down-scale model and the full-scale prototype before impact remains intact after the light structures are attacked by the corresponding flotsams. The maximum displacements in X, Y and Z directions are 2.792 cm, 7.634 mm and 0.8657 mm, respectively, for the down-scale model (Figure 7.14, Figure 7.16 and Figure 7.18).

Likewise, the same parameters reach 27.83 cm, 77 mm and 8.586 mm for the full-scale prototype (Figure 7.15, Figure 7.17 and Figure 7.19).

In Figure 7.14 and Figure 7.15, more or less uniform displacements in X-direction for the membrane in the impact zone (the circular areas in the membrane which are impacted by the flotsam) can be seen. Moreover, the effect of the impact on the displacements in the impact zone propagates in all directions. Notwithstanding the fact that the displacements grow symmetric relative to X-Y plane, the displacement propagated by the impact affect the membrane to a lesser extent in Y-direction.

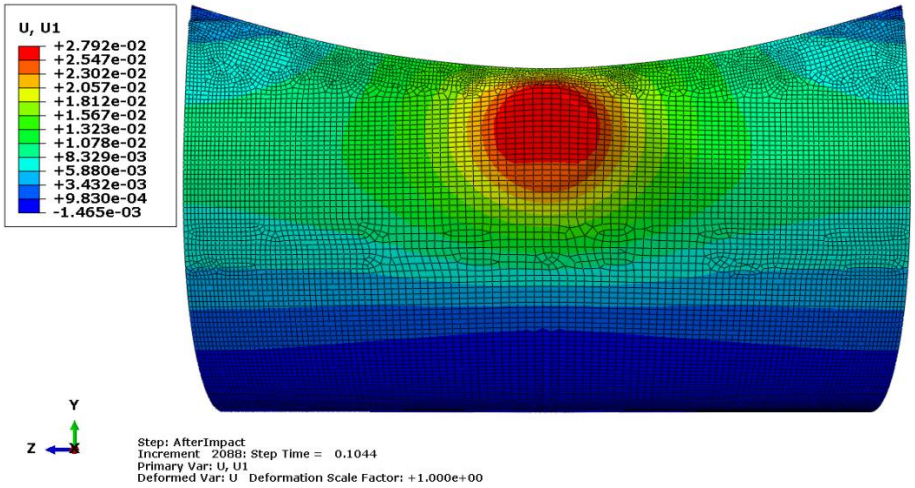

Figure 7.14: Maximum displacement in X direction in 0.1044 s after impact for the down-scale model (The corresponding values for U1 are in meter).

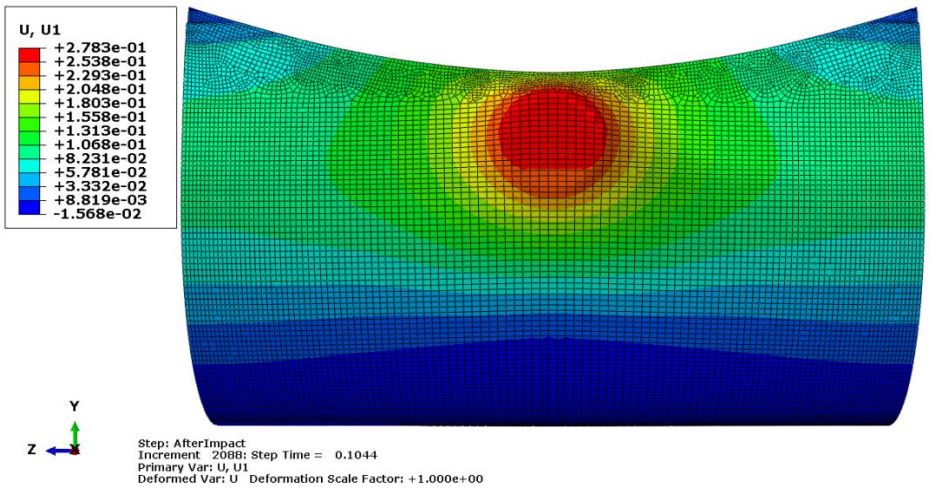

Figure 7.15: Maximum displacement in X direction in 0.1044 s after impact for the full-scale prototype (The corresponding values for U1 are in meter).

The displacements in Y-direction are to a great degree less than the displacements in X-direction so that the maximum displacement in Y-direction is about 27 percent of the maximum displacement in X-direction (Figure 7.16 and Figure 7.17).

In these figures, two different areas with significant extents in displacement can be distinguished. The former has a maximum amount in the upper areas of the impact zone and the latter originates from the bottom of the membrane. The increases in displacements in both areas propagate in all directions. Whereas rises in the displacements in the bottom of the membrane distribute completely in the Z-direction, the propagation of the displacement in the upper of the impact zone is more limited to the impact zone.

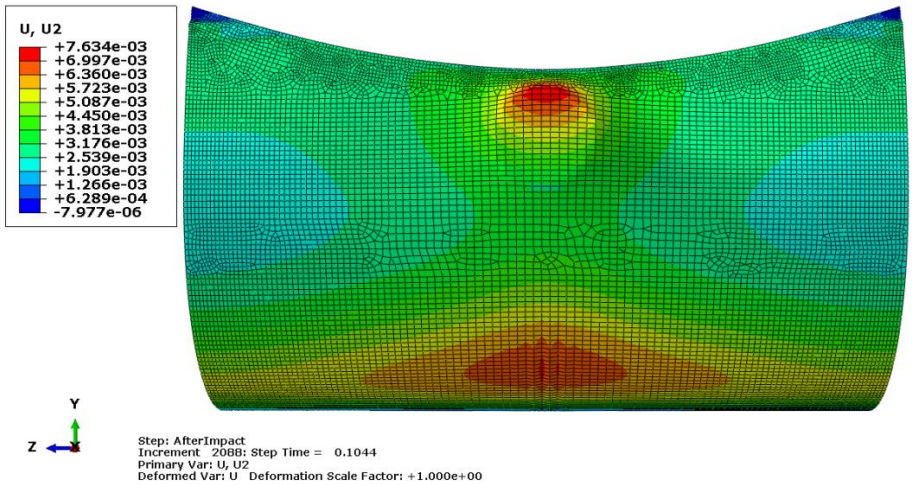

Figure 7.16: Displacement in Y direction in 0.1044 s after impact for the down-scale model (The corresponding values for U2 are in meter).

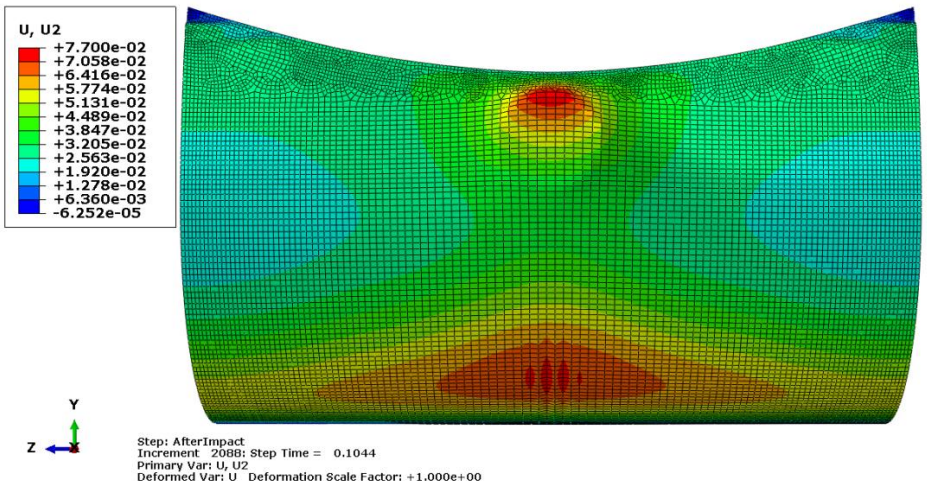

Figure 7.17: Displacement in Y direction in 0.1044 s after impact for the full-scale prototype (The corresponding values for U2 are in meter).

Despite the fact that four distinguishing areas can be recognized in Figure 7.18 and Figure 7.19, the displacements in Z direction are low in the range of -0.86 mm to 0.87 mm. The maximum displacements in Z direction are 8.9 times and 32.3 times less than maximum displacements in Y-direction and X-direction, respectively. Furthermore, the displacements in Z direction are symmetric relative to X-Y plane, but in the opposite directions. That is why the Z-displacement contours are displayed in different colors with regard to X-Y plane.

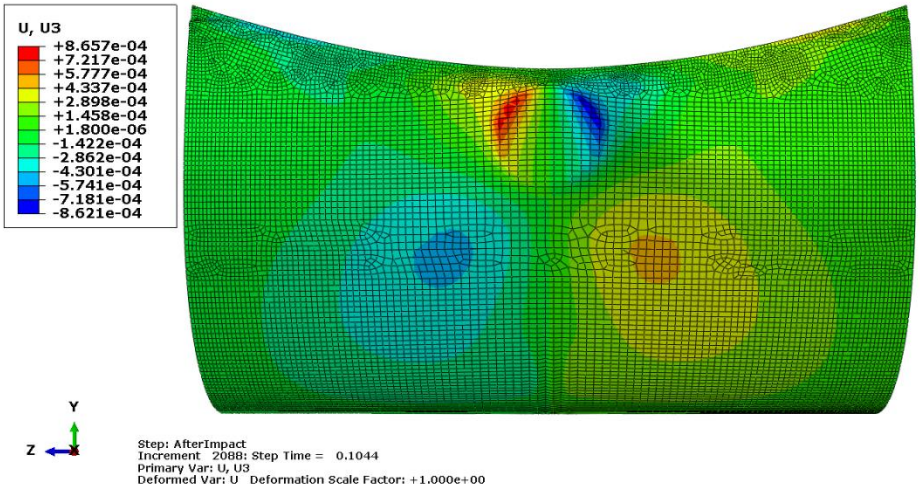

Figure 7.18: Displacement in Z direction in 0.1044 s after impact for the down-scale model (The corresponding values for U3 are in meter).

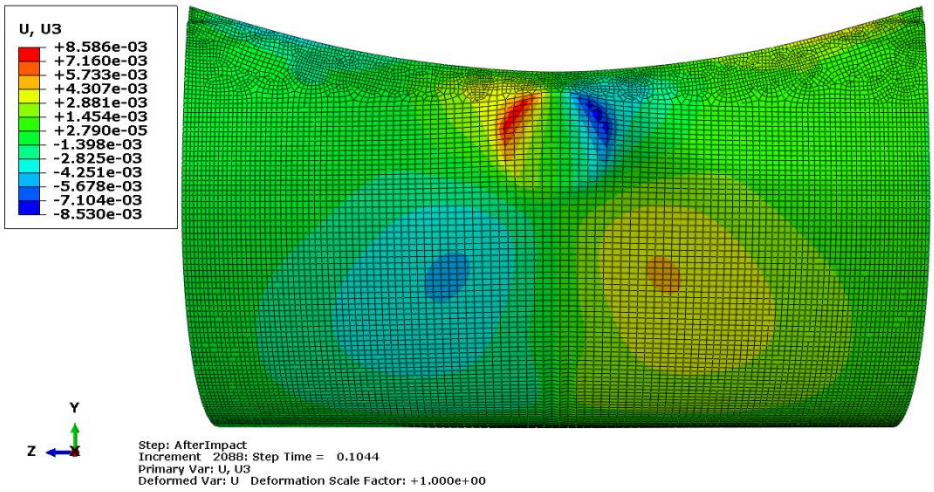

Figure 7.19: Displacement in Z direction in 0.1044 s after impact for the full-scale prototype (The corresponding values for U3 are in meter).

As it can be seen in Figure 7.20 and Figure 7.21, the Von Mises stresses are totally varying in the impact zone. Likewise, the effect of the impact on the membrane triggers the maximum Von Mises stress in the upper areas of the impact zone, which propagates throughout the membrane. However, it makes the membrane be affected to a greater extent in Y-direction. Also, the Von Mises stress within the down-scale model is 10 times less than the full-scale prototype.
To be more precise, the maximum Von Mises stress of 7.115 MPa is captured for the down-scale model (Figure 7.20), while the full-scale prototype is under a maximum Von Mises stress of 70.10 MPa (Figure 7.21).

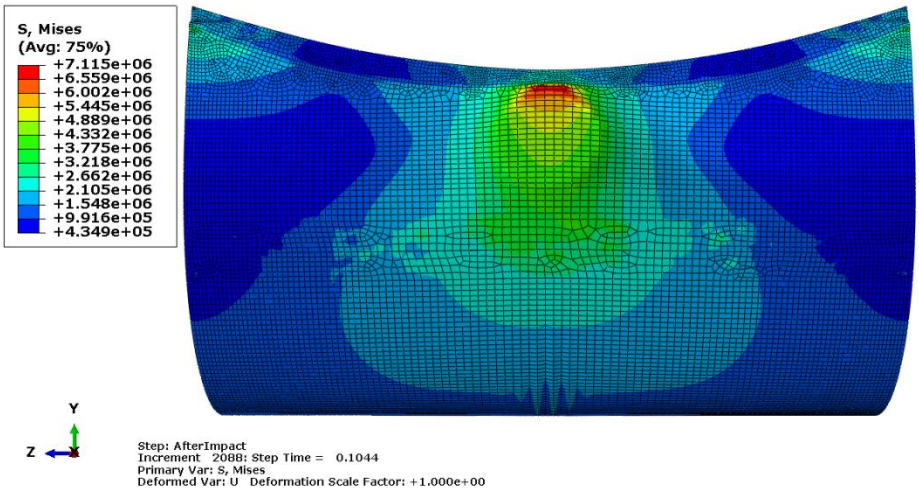

Figure 7.20: Von Mises stress in 0.1044 s after impact for the down-scale model (The corresponding values for Von Mises stress are in Pa).

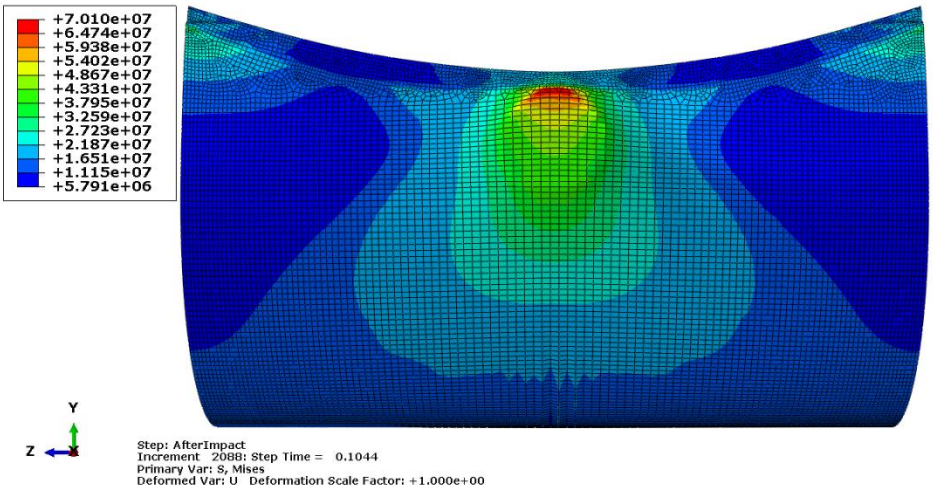

Figure 7.21: Von Mises stress in 0.1044 s after impact for the full-scale prototype (The corresponding values for Von Mises stress are in Pa).

Furthermore, Figure 7.22 to Figure 7.25 depict the maximum strains in the upper areas of the impact zone, which propagate throughout the membrane in Y-direction in much larger degrees than in in Z-direction.

The maximum in-plane principal plastic strain and the plastic strain in X direction are 0.09663 and 0.09650 for the down-scale model (Figure 7.22 and Figure 7.24) and of the same order as their counterparts for the full-scale prototype, which are 0.09644 and 0.09607(Figure 7.23 and Figure 7.25).

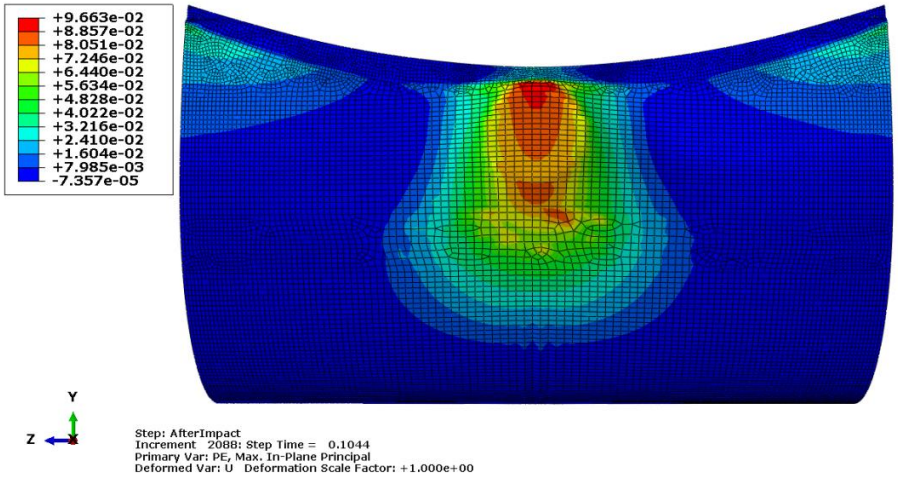

Figure 7.22: Maximum in-plane principal plastic strain in 0.1044 s after impact for the down-scale model

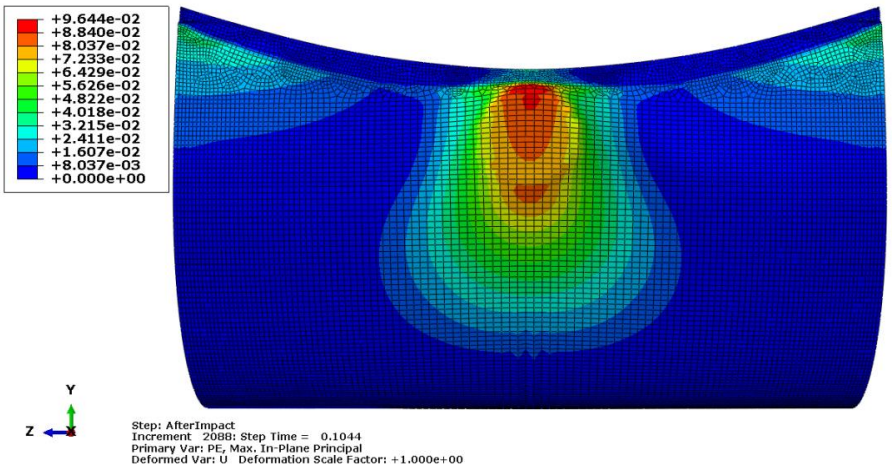

Figure 7.23: Maximum in-plane principal plastic strain in 0.1044 s after impact for the full-scale prototype

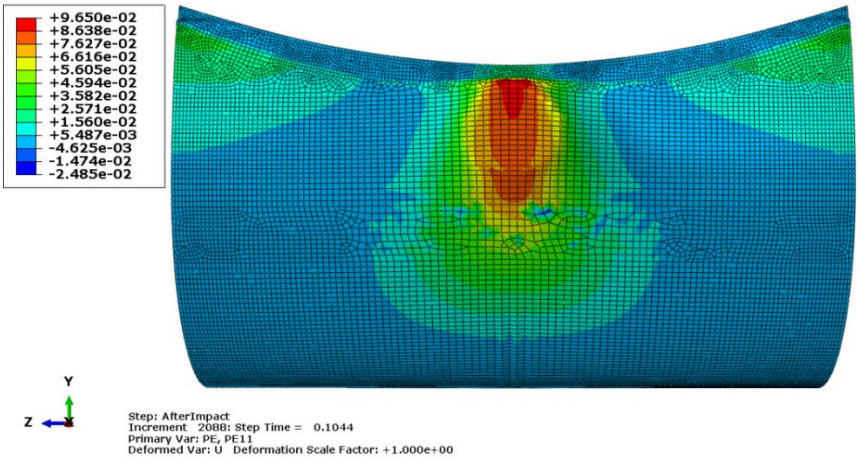

Figure 7.24: Plastic strain in X direction in 0.1044 s after impact for the down-scale model

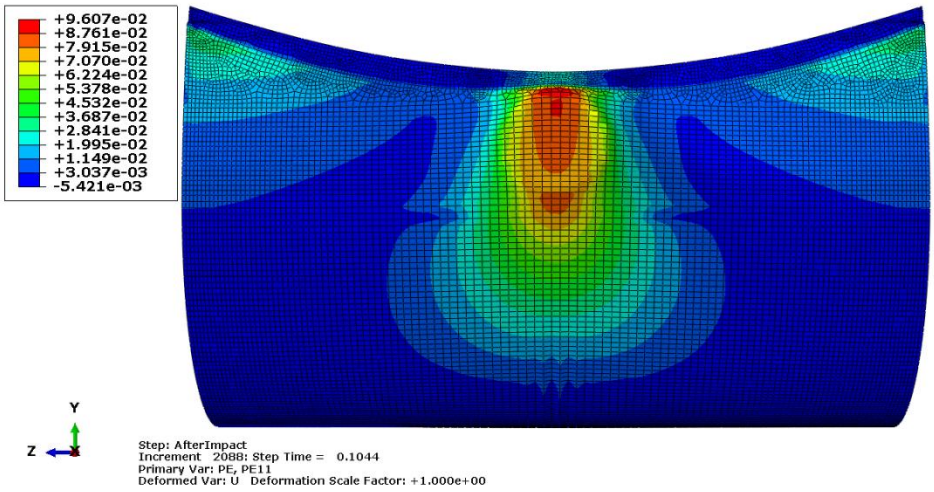

Figure 7.25: Plastic strain in X direction in 0.1044 s after impact for the full-scale prototype

7.7 Concluding remarks

The results show an excellent correlation between both the prototype and the model. The numerical results have exhibited that the displacements and the stresses of the down-scale model are 10 times less than the corresponding displacements and the stresses in the prototype (before impact and after impact). Moreover, the strains are of the same order for the prototype and the model.

As a result, the numerical results captured by the similitude theory were in good agreement with the predictions for the parameters, such as the displacements, the stresses, and the strains based on the dimensionless analysis, which validate the accuracy of the dimensionless approach.

As mentioned before, the similarity was studied from a structural viewpoint, where there exists a weak interaction between water flow and the light structure impacted by a heavy flotsam. In other words, the effect of the water pressure was imposed on the light structure by a subroutine, where water pressure field on the membrane was affected by a change in the water heights resulting from the membrane deformations.

Nevertheless, the implementation of optimization measures accelerating the computation time for two-way co-simulations together with cluster computing opens the way to investigate numerically two-way fluid-structure interactions in a cost-effective way. It can in turn lead to comprehensive similarity analyses on the FSI problems.

8 Summary, conclusions and outlook

This thesis presents the numerical findings regarding the fluid-structure interaction, comprising flexible slender shaped structure, free surface flow, and potentially interacting rigid structures, using the commercial software of Star CCM+ for computational fluid dynamics and Abaqus for finite element analyses.

Notwithstanding the current work deals with solutions for the design of a light temporary installable textile flood control structure, the findings can also contribute to solve other practical problems in industries, such as marine, aircraft, automotive industry, medicine, and entertainment industry.

In the first chapter, the relevant literatures on numerical approaches to solve fluid-structure interaction problems have been reviewed, where the works dealing with fluid-structure interface treatments have been emphasized.
In this respect, two main classes of methods for FSI numerical procedures were covered. Whereas the former discussed immersed methods implementing non-conforming mesh, partitioned approaches were topics of debate in the latter.
Taking strengths and weaknesses into consideration, a partitioned approach was followed for different reasons. The main reason why the partitioned approach was implemented is its higher degree of flexibility in spatial meshing which allows the detailed physics along the fluid-structure interface to be captured. Furthermore, a continuous data transfer between domains permits a solution for the whole fluid and structure domains to be achieved, where different proper algorithms and discretization models are applied for each corresponding domains.

In the second chapter, the pros and cons of different partitioned approaches such as single FV, and coupled FV-FE frameworks were discussed. Furthermore, the difference between the time integration approaches as explicit or implicit was explained. Moreover, coupling schemes which are important factors influencing the FSI analysis were demonstrated.

In this respect, the fluid domain was analyzed by a 2nd order time integration model and an implicit unsteady solver in all conducted simulations

However, the dynamic explicit scheme which can well handle with inherently highly nonlinear problems was firstly selected to provide a solution for the structural domain (as implemented in chapter 3).

Nevertheless, convergency issues with regard to added mass effect resulting from a loosely coupled (explicit) algorithm for two-way co-simulations enforced an inevitable switch in the coupling scheme from explicit to implicit (applied in chapters 4 and 6).

However, a change in the coupling scheme affects the algorithm solving the structural domain due to incompatibility between a dynamic explicit solver (for structure) and an implicit coupling scheme.
Moreover, the discretization techniques or models which were widely used like structural elements of beam, membrane and the overset mesh for the fluid domain were reviewed.

Likewise, the turbulence models incorporated into the physics of the fluid domain were compared, where the realizable two-layer K-Epsilon turbulence model were selected as an appropriate model for the target application.
Several relevant theories behind the analysis of the light structures performance, such as damping models were also presented. The damping models appended into the physics of the structure are responsible to dissipate any oscillations in the structure.
Viewed from this aspect, the damping models are important factors which have to be taken into consideration. Otherwise, a convergent simulation can not be ensured.

What was investigated in the third chapter was the behavior of the down-scale thin flexible membrane exposed to the hydrostatic pressures, where a dynamic explicit solver provided the solution for the structural domain.
Next, the numerical results had to be compared against the experimental findings, which was a crucial step to verify the accuracy of the numerical algorithms and the structural model setup parameters.

In this regard, comparisons were made between the numerical and experimental results for the downscale model loaded by the hydrostatic pressure, where changes in the water level imposed different pressures on the membrane.

Except for the slight differences resulting from simplifications, the parameter setup, measurement errors, and the applied numerical solvers, the numerical results met well the experimental data.

Promising numerical results provided the motivation for further researches investigating other possible scenarios whose levels of complexity were extremely raised.

To estimate the deformation of the light flexible structure due to the impulsive force arising from broken pieces of wood brought by the flood, the impact was numerically analyzed in chapter 4.

The impact analysis was executed at the presence of the free surface water flow which interacted with both the rigid and flexible structures. The flexible structure

representing the full-scale prototype membrane deformed notably when impacted by an accelerated heavy flotsam.

The impact analysis on the full-scale prototype was executed for two co-simulation cases, where a difference in the discretization techniques for the fluid domain was a distinguishing feature. The former was discretized with a standard mesh, while the overset mesh technique added more flexibility to the latter case.

Moreover, to reduce an inevitable gap between the flotsam within the fluid domain and its counterpart in structural domain, the effect of different parameters like the shape of the flotsam, the overset mesh zero gap, shrinkage were investigated.

The maximum numerical deformation for the membrane was compared against the experimental impact test where the flotsam was made to attack the membrane at inbound velocities of 4 m/s.
The experimental impact test captured a maximum displacement of 30 cm (Figure 4.30), for the membrane, which represented a good agreement with the numerical result (28.81 cm in Figure 4.26).

Furthermore, there exist minor differences between the results captured by three different numerical analyses (the standalone Abaqus analysis (the results are presented in chapter 7), the co-simulations with both the standard mesh technique and the overset mesh technique for the fluid region discretization)
The slight differences between results rooted at the fact that the flotsam was accelerated artificially to move and hit the membrane with the specified velocity and impact direction in both the experimental and numerical studies, where a hydrostatic equilibrium was somehow dominant on the fluid medium.

In fact, the effect of the coupling between the fluid and the membrane was far less than the extent influenced by the impulsive contact between the membrane and the flotsam. Nonetheless, in reality, the fluid domain caused the flotsam to hit the membrane, while the flotsam was managed artificially to impact the membrane in both the experimental and numerical studies. It suggested that a real impact scenario (without artificial forces) has to be studied inevitably by a two-way coupled FSI simulation.

The results extracted from a comparison between the behavior of the membrane modeled as either rigid or flexible exhibited that the representation of the flexible membrane as a rigid one give rise to wrong results. In other words, a standalone Abaqus impact simulation is able to provide a solution for the flexible membrane at the cost of accuracy provided that the effects of fluid domain on the structures can

be defined by mathematical formulations. In contrast, due to a significant effect of the membrane behavior on the fluid domain, no valid results for the fluid domain can be captured if the membrane is simulated as a rigid structure.

The successful FSI simulations addressing a huge impact on the flexible slender structure interacting with the heavy water medium encourage a numerical analysis of a more complicated phenomenon in which the statistical flood information determines the dynamic behavior of the fluid domain.

However, before proceeding with such a complicated scenario, preparatory numerical analyses are needed to enhance understanding of the behavior of light structures in interaction with high Reynolds number water flows and water waves.
With this intension, the interaction between the down-scale model and hydrodynamic loads was numerically investigated (chapter 6), where movements of a wooden body within a numerical wave channel replicated a one-way piston-type wavemaker. In addition, the results had to be validated against experimental data.

The rationale behind the numerical analysis on the down-scale model lay in the space limitation and costs regarding the experimental investigation on the original membrane.
Likewise, in order to investigate the influence of the dynamic water pressure on the light slender deformable structure, a piston-type wave maker was preferred to generate a shallow water wave for different reasons. First, the generation of a wave can be conducted in a channel closed from two ends which is a plus regarding space limitation in a laboratory investigation. Second, it saves costs related to long piping lines and a circulation pump.
In this regard, the experimental investigation was performed in the water tank equipped with a wooden body, where the wooden body moved translationally to produce the desired wave.

Furthermore, a numerical water tank was needed to be designed based on the geometric parameters of the physical water tank, which allowed making a comparison between the experimental and numerical results for the generated wave shape and the deformation of the down-scale model membrane.
Nevertheless, a numerical investigation on the interaction between a light structure and a heavy fluid domain has its own inherent cost and complication which will be worsened if numerical water waves are also aimed to be generated.

To gain an insight into the numerical generation of the water wave, another numerical water tank with a simple shape (a rectangular water tank) was designed in chapter

5 to generate waves with a piston-type wavemaker, where the results were compared against the theoretical estimations for the wave.
Lessons learned from performing the simulation for the numerical wave tank revealed the certain criteria which must be observed when the target numerical simulation dealt with a water wave generation.

By way of illustration, the numerical simulations for the waves generated with piston-type wavemaker elucidated that the fluid domain can not be discretized with standard mesh models when piston-type water wave making is desired. As an alternative, overset mesh techniques can be applied to model piston-type water wave generators. Furthermore, it established some criteria like the minimum number of cells per wavelength and wave amplitude, as well as the time step which have to be met.

Then, the numerical water tank modeled according to the physical water tank surrounded by the down-scale membrane was investigated. At the beginning of the simulation, the numerical and experimental wave's profiles shared a lot of characteristics in common, while there was a discrepancy in the numerical wave crest height compared to the experimental data. Nevertheless, an increasing analogy between the numerical and experimental results could be observed with regard to the wave crests with the passage of time.
In fact, the wave crest heights observed in experimental investigation were clearly less than the numerical wave crest height in a wave generation duration of 0.25 s, which can be explained by the effects of the leakage around the piston within the experimental analysis.
Furthermore, comparisons were drawn for the deformations of the membrane, which revealed that the numerically computed deformations were in good agreement with the data gathered from the physical model.

Finally, the similarity requirements regarding structural aspects were investigated. The constraints achieved by the theoretical findings were imposed on the prototype and the model. The great correlations between the results for both the prototype and the model validated well the accuracy of the dimensionless analysis.
The numerical results have exhibited the same ratio of 1 to 10 for the displacements and the stresses of the down-scale model relative to the respective displacements and the stresses in the prototype (before impact and after impact). As anticipated, the strains for the prototype and the model are also in the same order of magnitude

On the whole, the success in stabilizing the FSI investigation dealing with the huge impact of an accelerated massive flotsam on the flexible slender structure (the full-scale prototype) in interaction with a heavy water medium is of great importance.

In addition, the simulation of the flexible down-scale model interacting with a water wave flow exhibited promising results in spite of occurrence subtle instabilities after a wave generation duration of 0.92 s. In fact, a good agreement between the numerical results and the experimental findings mitigates the concern due to the instability issue.
Nonetheless, the instabilities appeared suddenly when the dynamic rate of events increased. The issue would be justified by a lack of the stiffness proportional damping coefficient for the Rayleigh damping which is a helpful tool to dissipate disturbances with high frequency rate. The reason why no stiffness proportional damping coefficient was defined was a lack of the proper data regarding the dynamic behavior of the membrane which necessitated a further experimental modal analysis (for the down-scale model). In fact, the stiffness proportional damping coefficient is a sensitive factor which needs special considerations. Improper setup for the stiffness give rise to lose important dynamic effects, which leads to wrong results as a consequence. For this reason, an experimental modal analysis is required to prohibit any instability, while maintaining the accuracy.

Future work is still needed to provide an improved structural model and obviously a stable, robust solution for the FSI numerical analysis of the target project aimed at market-orientated research on highly demanding protective systems as mentioned.

In this regard, for instance, the boundary condition for two hanging points on the upper edge, which was assumed as fixed in every direction for simplicity, can be improved. As a consequence, supports and other pertinent components have to be appended to the structural model to include small displacements for the hanging points into the analysis.

Within the fluid domain, more investigations are needed to increase the stability of simulations together with decreasing computational cost, without any accuracy sacrifice.

Moreover, surveys on the durability of the light flexible structures under environmental effects, such as corrosion and erosion deserve special attention.

Last but not least, the investigations on the similarity law arouse a great interest when the fluid aspect is also taken into account. As mentioned before, the similarity analysis performed in this work placed more focus on the structural viewpoint. In other words, the water pressure imposed on the light structure was defined by a subroutine, where water pressure field depends on the water height arising out of the membrane deformations. Nevertheless, a comprehensive view makes significant contributions towards the solutions for many practical applications. That is a great moti-

vation for further studies to optimize the models so that a comprehensive study on the similarity law would be feasible and economical.

List of figures

List of tables

References

[1] S. Hoppe, “Siebtes Opfer nach Hochwasser-Katastrophe,” *Lahrer Zeitung*, 2016. [Online]. Available: https://www.lahrer-zeitung.de/inhalt.deutschland-nach-ueberschwemmungenkatastrophenalarm-inniederbayern.e5423af8-b7e6-4cc5-92de-fdd0ae6e7b7e.html.

[2] H. Wibbeler, “AquaWand is the latest development in mobile flood protection,” *Aquaburg Hochwasserschutz GmbH*, 2016. [Online]. Available: https://www.aquaburg.com/category/aquawand120/.

[3] H. J.-P. Morand and R. Ohayon, “Fluid structure interaction-Applied numerical methods,”Wiley, Chichester, England, 1995.

[4] S. K. Chakrabarti, “Numerical models in fluid-structure interaction,”WIT Press, Ashurst Lodge, England, 2005.

[5] R. Mittal and G. Iaccarino, “Immersed boundary methods,” *Annual Review of Fluid Mechanics*, vol. 37, pp. 239–261, 2005.

[6] G. Hou, J. Wang, and A. Layton, “Numerical methods for fluid-structure interaction—a review,” *Communications in Computational Physics*, vol. 12, no. 2, pp. 337–377, 2012.

[7] A. Leonardi, F. K. Wittel, M. Mendoza, R. Vetter, and H. J. Herrmann, “Particle–fluid–structure interaction for debris flow impact on flexible barriers,” *Computer-Aided Civil and Infrastructure*, vol. 31, no. 5, pp. 323–333, 2016.

[8] R. A. Gingold and J. J. Monaghan, “Smoothed particle hydrodynamics: theory and application to non-spherical stars,” *Monthly Notices of the Royal Astronomical Society*, vol. 181, no. 3, pp. 375–389, 1977.

[9] L. B. Lucy, “A numerical approach to the testing of the fission hypothesis,” *The Astronomical Journal*, vol. 82, pp. 1013–1024, 1977.

[10] M. Schörgenhumer, P. G. Gruber, and J. Gerstmayr, “Interaction of flexible multibody systems with fluids analyzed by means of smoothed particle hydrodynamics,” *Multibody System Dynamics*, vol. 30, no. 1, pp. 53–76, 2013.

[11] W. Hu, W. Pan, M. Rakhsha, Q. Tian, H. Hu, and D. Negrut, “A consistent multi-resolution smoothed particle hydrodynamics method,” *Computer Methods in Applied Mechanics and Engineering*, vol. 324, pp. 278–299, 2017.

[12] S. Tiwari, S. Antonov, D. Hietel, J. Kuhnert, F. Olawsky, and R. Wegener, “A meshfree method for simulations of interactions between fluids and flexible structures,” in *Meshfree Methods for Partial Differential Equations III*, Springer-Verlag, Berlin Heidelberg, Germany, pp. 249–264, 2007.

[13] C. S. Peskin, “Numerical analysis of blood flow in the heart,” *Journal of Computational Physics*, vol. 25, no. 3, pp. 220–252, 1977.

[14] S. Ghosh, J. R. Edwards, and Y.-I. Choi, “Numerical simulation of the effects of mesoflaps in controlling shock/boundary-layer interactions,” *Journal of Propulsion and Power*, vol. 28, no. 5, pp. 955–970, 2012.

[15] J. Sigüenza, S. Mendez, D. Ambard, F. Dubois, F. Jourdan, R. Mozul, and F. Nicoud, “Validation of an immersed thick boundary method for simulating fluid–structure interactions of deformable membranes,” *Journal of Computational Physics*, vol. 322, pp. 723–746, 2016.

[16] J. Mohd-Yusof, “Combined immersed boundaries/B-splines methods for simulations of flows in complex geometries,” *Annual Research Briefs, Center for Turbulence Research, Stanford University*, pp. 317–327, 1997.

[17] R. J. Leveque and Z. Li, “Immersed interface methods for Stokes flow with elastic boundaries or surface tension,” *SIAM Journal on Scientific Computing*, vol. 18, no. 3, pp. 709–735, 1997.

[18] Z. Li and M.-C. Lai, “The immersed interface method for the Navier–Stokes equations with singular forces,” *Journal of Computational Physics*, vol. 171, no. 2, pp. 822–842, 2001.

[19] A. Mark and B. G. M. van Wachem, “Derivation and validation of a novel implicit second-order accurate immersed boundary method,” *Journal of Computational Physics*, vol. 227, no. 13, pp. 6660–6680, 2008.

[20] R. Glowinski, T.-W. Pan, T. I. Hesla, and D. D. Joseph, “A distributed Lagrange multiplier/fictitious domain method for particulate flows,” *International Journal of Multiphase Flow*, vol. 25, no. 5, pp. 755–794, 1999.

[21] R. Glowinski, T.-W. Pan, T. I. Hesla, D. D. Joseph, and J. Periaux, “A distributed Lagrange multiplier/fictitious domain method for the simulation of flow around moving rigid bodies: application to particulate flow,” *Computer Methods in Applied Mechanics and Engineering*, vol. 184, no. 2–4, pp. 241–267, 2000.

[22] R. Glowinski, T.-W. Pan, T. I. Hesla, D. D. Joseph, and J. Periaux, “A fictitious domain approach to the direct numerical simulation of incompressible viscous

flow past moving rigid bodies: application to particulate flow," *Journal of Computational Physics*, vol. 169, no. 2, pp. 363–426, 2001.

[23] N. A. Patankar, "A formulation for fast computations of rigid particulate flows," *Center for Turbulence Research Annual Research Briefs*, pp. 185–196, 2001.

[24] Z. Yu, "A DLM/FD method for fluid/flexible-body interactions," *Journal of Computational Physics*, vol. 207, pp. 1–27, 2005.

[25] Z. Yu and X. Shao, "A direct-forcing fictitious domain method for particulate flows," *Journal of Computational Physics*, vol. 227, no. 1, pp. 292–314, 2007.

[26] F. P. T. Baaijens, "A fictitious domain/mortar element method for fluid–structure interaction," *International Journal for Numerical Methods in Fluids*, vol. 35, no. 7, pp. 743–761, 2001.

[27] J. De Hart, G. W. Peters, P. J. Schreurs, and F. P. Baaijens, "A two-dimensional fluid-structure interaction model of the aortic valve [correction of value]," *Journal of Biomechanics*, vol. 33, no. 9, pp. 1079–1088, 2000.

[28] J. De Hart, G. W. M. Peters, P. J. G. Schreurs, and F. P. T. Baaijens, "A three-dimensional computational analysis of fluid–structure interaction in the aortic valve," *Journal of Biomechanics*, vol. 36, no. 1, pp. 103–112, 2003.

[29] R. van Loon, P. D. Anderson, and F. N. van de Vosse, "A fluid–structure interaction method with solid-rigid contact for heart valve dynamics," *Journal of Computational Physics*, vol. 217, no. 2, pp. 806–823, 2006.

[30] R. Van Loon, P. D. Anderson, F. N. Van de Vosse, and S. J. Sherwin, "Comparison of various fluid–structure interaction methods for deformable bodies," *Computers & Structures*, vol. 85, no. 11–14, pp. 833–843, 2007.

[31] X. Wang and W. K. Liu, "Extended immersed boundary method using FEM and RKPM," *Computer Methods in Applied Mechanics and Engineering*, vol. 193, no. 12–14, pp. 1305–1321, 2004.

[32] L. Zhang, A. Gerstenberger, X. Wang, and W. K. Liu, "Immersed finite element method," *Computer Methods in Applied Mechanics and Engineering*, vol. 193, no. 21–22, pp. 2051–2067, 2004.

[33] D. Kamensky, M.-C. Hsu, D. Schillinger, J. A. Evans, A. Aggarwal, Y. Bazilevs, M. S. Sacks, and T. J. R. Hughes, "An immersogeometric variational framework for fluid–structure interaction: Application to bioprosthetic heart valves," *Computer Methods in Applied Mechanics and Engineering*, vol. 284, pp. 1005–

1053, 2015.

[34] H. Zhao, J. B. Freund, and R. D. Moser, “A fixed-mesh method for incompressible flow–structure systems with finite solid deformations,” *Journal of Computational Physics*, vol. 227, no. 6, pp. 3114–3140, 2008.

[35] C. H. Tai, Y. Zhao, and K. M. Liew, “Parallel computation of unsteady incompressible viscous flows around moving rigid bodies using an immersed object method with overlapping grids,” *Journal of Computational Physics*, vol. 207, no. 1, pp. 151–172, 2005.

[36] C. H. Tai, K. M. Liew, and Y. Zhao, “Numerical simulation of 3D fluid–structure interaction flow using an immersed object method with overlapping grids,” *Computers & Structures*, vol. 85, no. 11–14, pp. 749–762, 2007.

[37] G. Starius, “Composite mesh difference methods for elliptic boundary value problems,” *Numerische Mathematik*, vol. 28, no. 2, pp. 243–258, 1977.

[38] G. Starius, “On composite mesh difference methods for hyperbolic differential equations,” *Numerische Mathematik*, vol. 35, no. 3, pp. 241–255, 1980.

[39] J. L. Steger, F. C. Dougherty, J. A. Benek, and A. C. G. Scheme, “Advances in grid generation,” *presented at Applied Mechanics, Bioengineering, and Fluids Engineering Conference, Houston, Texas, U.S.A, ASME FED*, vol. 5, pp. 59–69, 1983.

[40] J. A. Benek, P. G. Buning, and J. L. Steger, “3-D chimera grid embedding technique.,” *presented at the 7th Computational Physics Conference, Cincinnati, OH, U.S.A., AIAA85-1523*, pp. 322–331, 1985.

[41] G. Chesshire and W. D. Henshaw, “Composite overlapping meshes for the solution of partial differential equations,” *Journal of Computational Physics*, vol. 90, no. 1, pp. 1–64, 1990.

[42] K. Luo, Z. Wang, and J. Fan, “A modified immersed boundary method for simulations of fluid–particle interactions,” *Computer Methods in Applied Mechanics and Engineering*, vol. 197, no. 1–4, pp. 36–46, 2007.

[43] R. Ghias, R. Mittal, and T. Lund, “A non-body conformal grid method for simulation of compressible flows with complex immersed boundaries,” *presented at the 42nd AIAA Aerospace Sciences Meeting and Exhibit, Reno, Nevada, U.S.A, AIAA 2004-80*, pp. 1–10, 2004.

[44] G. Iaccarino and R. Verzicco, “Immersed boundary technique for turbulent flow

simulations," *Applied Mechanics Reviews*, vol. 56, no. 3, pp. 331–347, 2003.

[45] C. Farhat and V. K. Lakshminarayan, "An ALE formulation of embedded boundary methods for tracking boundary layers in turbulent fluid–structure interaction problems," *Journal of Computational Physics*, vol. 263, pp. 53–70, 2014.

[46] F. Schäfer, S. Müller, T. Uffinger, S. Becker, J. Grabinger, and M. Kaltenbacher, "Fluid-structure-acoustic interaction of the flow past a thin flexible structure," *AIAA Journal*, vol. 48, no. 4, pp. 738–748, 2010.

[47] G. Link, M. Kaltenbacher, M. Breuer, and M. Döllinger, "A 2d finite-element scheme for fluid–solid–acoustic interactions and its application to human phonation," *Computer Methods in Applied Mechanics and Engineering*, vol. 198, no. 41–44, pp. 3321–3334, 2009.

[48] R. Wüchner, A. Kupzok, and K. U. Bletzinger, "Simulation of fluid-structure-interaction with free form membrane structures using an implicit coupling scheme with adaptive under relaxation," *presented at the European Conference on Computational Fluid Dynamics, TU Delft, The Netherlands, ECCOMAS CFD 2006*, pp. 1–17, 2006.

[49] M. Breuer, G. De Nayer, and M. Münsch, "Fluid–structure interaction of a flexible structure in a turbulent flow using LES," in *Direct and Large-Eddy Simulation VIII*, Springer-Verlag, Netherlands, pp. 449–454, 2011.

[50] S. Sotelo, "Investigation of multiscale fluid structure interaction modeling of flow in arterial systems," Master Thesis, University of Central Florida, Department of Mechanical and Aerospace Engineering, Orlando, Florida, U.S.A, 2013.

[51] D. P. De Andrade, "Interaction fluid structure on the laminar flow in curved pipes," Master Thesis, Instituto Superior Técnico, Department of Aerospace Engineering, Lisbon, Portugal, 2014.

[52] H. Lee, M.-C. Song, J.-C. Suh, and B.-J. Chang, "Hydro-elastic analysis of marine propellers based on a BEM-FEM coupled FSI algorithm," *International Journal of Naval Architecture and Ocean Engineering*, vol. 6, no. 3, pp. 562–577, 2014.

[53] P. C. Gomes, "Numerical study of 2-D rigid and deformable fluid-structure interaction cases," Master Thesis, Instituto Superior Técnico, Department of Mechanical Engineering, Lisbon, Portugal, 2014.

[54] B. Landvogt, "Fluid-structure interaction of racing car spoilers," *presented at*

NAFEMS European Conference: Multiphysics Simulation, Copenhagen, Denmark, pp. 117–120, 2016.

[55] P. Pasolini, R. Savino, F. Franco, and S. De Rosa, "Preliminary validation of fluid-structure interaction modeling for hypersonic deployable Re-entry systems," *FDMP: Fluid Dynamics & Materials Processing*, vol. 11, no. 3, pp. 301–324, 2015.

[56] M. P. Handeland, "Importance of fluid-structure interaction on dropped lifeboats-a parametric study used to explore the importance of hydroelasticity on complex low rigidity structures using decision factors," Master Thesis, Norwegian University of Science and Technology, Department of Marine Technology, Trondheim, Norway, 2015.

[57] A. L. Bloxom, "Numerical Simulation of the Fluid-Structure Interaction of a Surface Effect Ship Bow Seal," PhD Thesis, Virginia Polytechnic Institute and State University, Department of Aerospace Engineering, Blacksburg, VA, U.S.A, 2014.

[58] D. Oliveira, A. Santiago, and C. Rigueiro, "Fluid Structure Interaction in Offshore Environment," *presented at the 5th International Conference on Integrity-Reliability-Failure, Porto, Portugal*, pp. 635–646, 2016.

[59] C. J. Jesse, J. C. Kennedy, and G. L. Solbrekken, "Fluid-Structure Interaction (FSI) Modeling of Thin Plates," *presented at the 16th International Topical Meeting on Nuclear Reactor Thermalhydraulics, Chicago, IL, U.S.A*, pp. 7993–8006, 2015.

[60] S. Neumann, "Fluid-structure interaction of flexible lifting bodies with multi-body dynamics of order-reduced models and the actuator-line method,"epubli Gmbh, Berlin, Germany, 2016.

[61] M. R. Lied, "A numerical study of exercise induced laryngeal obstruction using fluid-structure interaction," Master Thesis, The University of Bergen, Department of Physics and Technology, Bergen, Norway, 2017.

[62] S. Brown, "Displacement extrapolations for CFD+ CSM aeroelastic analysis," *presented at the 38th Structures, Structural Dynamics, and Materials Conference, Kissimmee, FL, U.S.A., AIAA-97-1090*, pp. 291–300, 1997.

[63] R. Onishi, T. Kimura, Z. Guo, and T. Iwamiya, "Coupled aero-structural model-Approach and application to high aspect-ratio wing-box structures," *presented at the 7th AIAAIUSAFINASA/ISSMO Symposium on Multidisciplinary Analysis and Optimization, St. Louis, MO, U.S.A., AIAA-98-4837*, pp. 1004–1010, 1998.

[64] J. Cebral, R. Loehner, J. Cebral, and R. Loehner, “Fluid-structure coupling-Extensions and improvements,” *presented at the 35th Aerospace Sciences Meeting and Exhibit, Reno, NV, U.S.A, AIAA 97-0858*, pp. 1–15, 1997.

[65] J. R. Cebral and R. Lohner, “Conservative load projection and tracking for fluid-structure problems,” *AIAA Journal*, vol. 35, no. 4, pp. 687–692, 1997.

[66] C. Farhat, M. Lesoinne, and P. Le Tallec, “Load and motion transfer algorithms for fluid/structure interaction problems with non-matching discrete interfaces: Momentum and energy conservation, optimal discretization and application to aeroelasticity,” *Computer Methods in Applied Mechanics and Engineering*, vol. 157, no. 1–2, pp. 95–114, 1998.

[67] D. Raveh and M. Karpel, “Structural optimization of flight vehicles with non-linear aerodynamic loads,” *presented at the 7th Symposium on Multidisciplinary Analysis and Optimization, St. Louis, MO, U.S.A., AIAA-98-4832*, pp. 967–977, 1998.

[68] J. Samareh, “Use of CAD geometry in MDO,” *presented at the 6th AIAA/NASA/ISSMO Symposium on Multidisciplinary Analysis and Optimization, Bellevue, WA, U.S.A., AIAA Paper 96-3991*, pp. 88–98, 1996.

[69] J. A. Samareh, “Aeroelastic deflection of NURBS geometry,” *presented at the 6th International Conference on Numerical Grid Generation in Computational Field Simulation, University of Greenwich, Avery Hill Campus, London, UK*, pp. 727–736, 1998.

[70] J. A. Samareh, “A novel shape parameterization approach,” Technical Report of NASA Langley Research Center, NASA Contract No. TM-1999-209116, Hampton,VA, U.S.A., 1999.

[71] J. Samareh, “A survey of shape parameterization techniques,” *presented at CEAS/AIAA/ICASE/NASA Langley International Forum on Aeroelasticity and Structural Dynamics, Williamsburg, VA, U.S.A., NASA/CP-1999-209136*, pp. 333–343, 1999.

[72] K. Appa, “Finite-surface spline,” *Journal of Aircraft*, vol. 26, no. 5, pp. 495–496, 1989.

[73] G. P. Guruswamy and C. Byun, “Direct coupling of Euler flow equations with plate finite element structures,” *AIAA Journal*, vol. 33, no. 2, pp. 375–377, 1995.

[74] R. Kapania, M. Bhardwaj, E. Reichenbach, and G. Guruswamy, “Aeroelastic analysis of modern complex wings,” *presented at the 6th*

AIAA/USAF/NASA/ISSMO Symposium on Multidisciplinary Analysis and Optimization, Bellevue, WA, U.S.A., AIAA 96-4011, pp. 258–265, 1996.

[75] G. Hou and A. Satyanarayana, "Analytical sensitivity analysis of a static aeroelastic wing," *presented at the 8th AIAA/USAF/NASA/ISSMO Symposium on Multidisciplinary Analysis and Optimization, Long Beach, U.S.A., AIAA Paper 2000-4824*, pp. 1–15, 2000.

[76] C. Farhat, K. G. Van der Zee, and P. Geuzaine, "Provably second-order time-accurate loosely-coupled solution algorithms for transient nonlinear computational aeroelasticity," *Computer Methods in Applied Mechanics and Engineering*, vol. 195, no. 17–18, pp. 1973–2001, 2006.

[77] W. Zhang, Y. Jiang, and Z. Ye, "Two better loosely coupled solution algorithms of CFD based aeroelastic simulation," *Engineering Applications of Computational Fluid Mechanics*, vol. 1, no. 4, pp. 253–262, 2007.

[78] J. A. Vierendeels, K. Riemslagh, E. Dick, and P. R. Verdonck, "Computer simulation of intraventricular flow and pressure gradients during diastole," *Journal of Biomechanical Engineering*, vol. 122, no. 6, pp. 667–674, 2000.

[79] J. A. Vierendeels, E. Dick, and P. R. Verdonck, "Hydrodynamics of color M-mode doppler flow wave propagation velocity V (p): a computer study," *Journal of the American Society of Echocardiography*, vol. 15, no. 3, pp. 219–224, 2002.

[80] D. P. Mok, W. A. Wall, and E. Ramm, "Accelerated iterative substructuring schemes for instationary fluid-structure interaction," *presented at the First M.I.T. Conference on Computational Fluid and Solid Mechanics, Massachusetts Institute of Technology, Cambridge, U.S.A., Computational Fluid and Solid Mechanics*, vol. 2, pp. 1325–1328, 2001.

[81] J. Vierendeels, L. Lanoye, J. Degroote, and P. Verdonck, "Implicit coupling of partitioned fluid–structure interaction problems with reduced order models," *Computers & Structures*, vol. 85, no. 11–14, pp. 970–976, 2007.

[82] J. Vierendeels, K. Dumont, and P. R. Verdonck, "A partitioned strongly coupled fluid-structure interaction method to model heart valve dynamics," *Journal of Computational and Applied Mathematics*, vol. 215, no. 2, pp. 602–609, 2008.

[83] J. Degroote, P. Bruggeman, R. Haelterman, and J. Vierendeels, "Stability of a coupling technique for partitioned solvers in FSI applications," *Computers & Structures*, vol. 86, no. 23–24, pp. 2224–2234, 2008.

[84] B. M. Irons and R. C. Tuck, "A version of the Aitken accelerator for computer

iteration," *International Journal for Numerical Methods in Engineering*, vol. 1, no. 3, pp. 275–277, 1969.

[85] J. Degroote, A. Swillens, P. Bruggeman, R. Haelterman, P. Segers, and J. Vierendeels, "Simulation of fluid–structure interaction with the interface artificial compressibility method," *International Journal for Numerical Methods in Biomedical Engineering*, vol. 26, no. 3-4, pp. 276–289, 2010.

[86] S. Badia, F. Nobile, and C. Vergara, "Fluid–structure partitioned procedures based on Robin transmission conditions," *Journal of Computational Physics*, vol. 227, no. 14, pp. 7027–7051, 2008.

[87] C. Pozrikidis, "Flow-induced deformation of an elastic membrane adhering to a wall," *International Journal of Solids and Structures*, vol. 46, no. 17, pp. 3198–3208, 2009.

[88] Siemens AG, "User guide: Star CCM+," Version 2019.3.1, 2019.

[89] W. P. Jones and B. E. Launder, "The prediction of laminarization with a two-equation model of turbulence," *International Journal of Heat and Mass Transfer*, vol. 15, no. 2, pp. 301–314, 1972.

[90] W. Rodi, "Experience with two-layer models combining the k-ε model with a one-equation model near the wall," *presented at the 29th Aerospace Sciences Meeting, Reno, Nevada, U.S.A., AIAA 91-0216*, 1991.

[91] T.-H. Shih, W. W. Liou, A. Shabbir, Z. Yang, and J. Zhu, "A new k-ε eddy viscosity model for high Reynolds number turbulent flows," *Computers & Fluids*, vol. 24, no. 3, pp. 227–238, 1995.

[92] D. C. Wilcox, "Turbulence modeling for CFD," vol. 2,DCW industries, La Canada, CA, U.S.A, 1998.

[93] F. R. Menter, "Two-equation eddy-viscosity turbulence models for engineering applications," *AIAA Journal*, vol. 32, no. 8, pp. 1598–1605, 1994.

[94] I. Chowdhury and S. P. Dasgupta, "Computation of Rayleigh damping coefficients for large systems," *The Electronic Journal of Geotechnical Engineering*, vol. 8, no. 0, pp. 1–11, 2003.

[95] Dassault Systèmes, "Abaqus: CAE user's guide," Version 6.13, 2013.

[96] M. Azaouzi, A. Makradi, and S. Belouettar, "Deployment of a self-expanding stent inside an artery: A finite element analysis," *Materials & Design*, vol. 41,

pp. 410–420, 2012.

[97] H. Baek and G. E. Karniadakis, “A convergence study of a new partitioned fluid–structure interaction algorithm based on fictitious mass and damping,” *Journal of Computational Physics*, vol. 231, no. 2, pp. 629–652, 2012.

[98] T. Liaghat, F. Guibault, L. Allenbach, and B. Nennemann, “Two-Way Fluid-Structure Coupling in Vibration and Damping Analysis of an Oscillating Hydrofoil,” *presented at the ASME 2014 International Mechanical Engineering Congress & Exposition, Montreal, Quebec, Canada, IMECE2014-38441*, pp. 1–10, 2014.

[99] P. Causin, J.-F. Gerbeau, and F. Nobile, “Added-mass effect in the design of partitioned algorithms for fluid–structure problems,” *Computer Methods in Applied Mechanics and Engineering*, vol. 194, no. 42–44, pp. 4506–4527, 2005.

[100] R. Löhner, “Robust, vectorized search algorithms for interpolation on unstructured grids,” *Journal of Computational Physics*, vol. 118, no. 2, pp. 380–387, 1995.

[101] M. S. Milgram, “Does a point lie inside a polygon?,” *Journal of Computational Physics*, pp. 134–144, 1989.

[102] H. Alt and M. Godau, “Computing the Fréchet distance between two polygonal curves,” *International Journal of Computational Geometry & Applications*, vol. 5, no. 1 & 2, pp. 75–91, 1995.

[103] C.-Y. Yang, P.-Y. Chen, T.-J. Wen, and G. E. Jan, “IMU consensus exception detection with dynamic time warping—A comparative approach,” *Sensors*, vol. 19, no. 10, pp. 1–19, 2019.

[104] C. F. Jekel, G. Venter, M. P. Venter, N. Stander, and R. T. Haftka, “Similarity measures for identifying material parameters from hysteresis loops using inverse analysis,” *International Journal of Material Forming*, vol. 12, no. 3, pp. 355–378, 2019.

[105] K. Schade, O. Sommer, and G. Wozniak, “Experimental investigation of a flexible high-water protection system in a down-scale water channel flow,” *PAMM*, vol. 16, no. 1, pp. 647–648, 2016.

[106] T. Ursell, “Frechet distance calculator,” *MATLAB Central File Exchange*, 2020. [Online]. Available: https://www.mathworks.com/matlabcentral/fileexchange/41956-frechet-distance-calculator.

[107] Z. Danziger, “Discrete frechet distance,” *MATLAB Central File Exchange*, 2020. [Online]. Available: https://www.mathworks.com/matlabcentral/fileexchange/31922-discrete-frechet-distance.

[108] L. S. Caretto, A. D. Gosman, S. V Patankar, and D. B. Spalding, “Two calculation procedures for steady, three-dimensional flows with recirculation,” *presented at the Third International Conference on Numerical Methods in Fluid Mechanics, University of Paris, France, part of the Lecture Notes in Physics book series (LNP, volume 19)*, pp. 60–68, 1973.

[109] F. Hesse, “Temporärer Hochwasserschutz in Leichtbauweise entwickelt,” 2017. [Online]. Available: https://www.bauingenieur24.de/fachbeitraege/forschung/temporaerer-hochwasserschutz-in-leichtbauweise-entwickelt/2915.htm#hohe-biegemomente-fuer-temporaeren-hochwasserschutz-problematisch.

[110] W. M. Kusumawinahyu, N. Karjanto, and G. Klopman, “Linear theory for single and double flap wavemakers,” *Journal of the Indonesia Mathematical Society*, vol. 12, no. 1, pp. 41–57, 2006.

[111] O. Faltinsen, “Sea loads on ships and offshore structures,” vol. 1,Cambridge University Press, Cambridge, England, 1993.

[112] C. W. Hirt and B. D. Nichols, “Volume of fluid (VOF) method for the dynamics of free boundaries,” *Journal of Computational Physics*, vol. 39, pp. 201–225, 1981.

[113] S. Muzaferija and M. Peric, “Computation of free surface flows using interface-tracking and interface-capturing methods,” in *the book of Nonlinear water-wave interaction, Computational Mechanics, WIT Press, Southampton, England*, pp. 59–100, 1999.

[114] F. Ursell, R. G. Dean, and Y. S. Yu, “Forced small-amplitude water waves: a comparison of theory and experiment,” *Journal of Fluid Mechanics*, vol. 7, no. 1, pp. 33–52, 1960.

[115] T. Keating, N. B. Webber, and T. H. Havelock, “The generation of periodic waves in a laboratory channel: A comparison between theory and experiment,” *Proceedings of the Institution of Civil Engineers*, vol. 63, no. 4, pp. 819–832, 1977.

[116] M. H. Patel and P. A. Ionnaou, “Comparative performance study of paddle-and wedge-type wave generators,” *Journal of Hydronautics*, vol. 14, no. 1, pp. 5–9, 1980.

[117] T. H. Havelock, “LIX. Forced surface-waves on water,” *The London, Edinburgh, and Dublin Philosophical Magazine and Journal of Science*, vol. 8, no. 51, pp. 569–576, 1929.

[118] F. Biesel and F. Suquet, “Etude theorique d’un certain type d’appareil a houle,” *La Houille Blanche*, vol. 6, no. 2, pp. 152–165, 1951.

[119] O. S. Madsen, “On the generation of long waves,” *Journal of Geophysical Research*, vol. 76, no. 36, pp. 8672–8683, 1971.

[120] R. G. Dean and R. A. Dalrymple, “Water wave mechanics for engineers and scientists,” vol. 2,World Scientific Publishing Company, Sigapore, Malaysia, 1991.

[121] L. E. Borgman and J. E. Chappelear, “The use of the Stokes-Struik approximation for waves of finite height,” *Coastal Engineering Proceedings*, vol. 1, no. 6, pp. 252–280, 1957.

[122] J. D. Fenton, “A fifth-order Stokes theory for steady waves,” *Journal of Waterway, Port, Coastal, and Ocean Engineering*, vol. 111, no. 2, pp. 216–234, 1985.

[123] M. H. Kim, J. M. Niedzwecki, J. M. Roesset, J. C. Park, S. Y. Hong, and A. Tavassoli, “Fully nonlinear multidirectional waves by a 3-D viscous numerical wave tank,” *Journal of Offshore Mechanics and Arctic Engineering*, vol. 123, no. 3, pp. 124–133, 2001.

[124] H. Sun and O. M. Faltinsen, “Water impact of horizontal circular cylinders and cylindrical shells,” *Applied Ocean Research*, vol. 28, no. 5, pp. 299–311, 2006.

[125] D. Z. Ning and B. Teng, “Numerical simulation of fully nonlinear irregular wave tank in three dimension,” *International Journal for numerical methods in fluids*, vol. 53, no. 12, pp. 1847–1862, 2007.

[126] D. Z. Ning, B. Teng, R. E. Taylor, and J. Zang, “Numerical simulation of non-linear regular and focused waves in an infinite water-depth,” *Ocean Engineering*, vol. 35, no. 8–9, pp. 887–899, 2008.

[127] H. Yan and Y. Liu, “An efficient high-order boundary element method for nonlinear wave–wave and wave-body interactions,” *Journal of Computational Physics*, vol. 230, no. 2, pp. 402–424, 2011.

[128] G. X. Wu and Z. Z. Hu, “Simulation of nonlinear interactions between waves and floating bodies through a finite-element-based numerical tank,” *Proceedings of*

the Royal Society of London. Series A: Mathematical, Physical and Engineering Sciences, vol. 460, no. 2050, pp. 2797–2817, 2004.

[129] I. Hadžić, J. Hennig, M. Perić, and Y. Xing-Kaeding, "Computation of flow-induced motion of floating bodies," *Applied Mathematical Modelling*, vol. 29, no. 12, pp. 1196–1210, 2005.

[130] E. B. Agamloh, A. K. Wallace, and A. Von Jouanne, "Application of fluid–structure interaction simulation of an ocean wave energy extraction device," *Renewable Energy*, vol. 33, no. 4, pp. 748–757, 2008.

[131] V. Sriram, S. A. Sannasiraj, and V. Sundar, "Simulation of 2-D nonlinear waves using finite element method with cubic spline approximation," *Journal of Fluids and Structures*, vol. 22, no. 5, pp. 663–681, 2006.

[132] X. Liang, J. Yang, L. I. Jun, L. Xiao, and L. I. Xin, "Numerical simulation of irregular wave-simulating irregular wave train," *Journal of Hydrodynamics, Ser. B*, vol. 22, no. 4, pp. 537–545, 2010.

[133] A. Lal and M. Elangovan, "CFD simulation and validation of flap type wave-maker," *World Academy of Science, Engineering and Technology*, vol. 46, no. 1, pp. 76–82, 2008.

[134] D. D. Prasad, M. R. Ahmed, Y. H. Lee, and R. N. Sharma, "Validation of a piston type wave-maker using Numerical Wave Tank," *Ocean Engineering*, vol. 131, pp. 57–67, 2017.

[135] S. Spence, "Numerical investigation of free surface flows," Master Thesis, Norwegian University of Science and Technology, Department of Marine Technology, Trondheim, Norway, 2014.

[136] M. N. Gomes, C. R. Olinto, L. A. O. Rocha, J. A. Souza, and L. A. Isoldi, "Computational modeling of a regular wave tank," *presented at the 3rd Southern Conference on Computational Modeling, Rio Grande, Brazil, Engenharia Térmica (Thermal Engineering), Vol. 8*, pp. 44–50, 2009.

[137] Z. Liu, B.-S. Hyun, and K. Hong, "Application of numerical wave tank to OWC air chamber for wave energy conversion," *The Eighteenth International Offshore and Polar Engineering Conference*, pp. 350–356, 2008.

[138] M. Horko, "CFD optimisation of an oscillating water column energy converter," Master Thesis, The University of Western Australia, School of Mechanical Engineering, Australia, 2007.

[139] N. H. Quân, “Study on design of 2D ocean wave maker,” Bachelor Thesis, Ho Chi Minh City National University, Faculty of Mechanical Engineering, Ho Chi Minh City, Vietnam, 2009.

[140] J. D. Fenton and W. D. McKee, “On calculating the lengths of water waves,” *Coastal Engineering*, vol. 14, no. 6, pp. 499–513, 1990.

[141] D. J. Korteweg and G. de Vries, “On the change of form of long waves advancing in a rectangular canal, and on a new type of long stationary waves,” *Philosophical Magazine and Journal of Science*, vol. 39, no. 240, pp. 422–443, 1895.

[142] D. N. Veritas, “Environmental conditions and environmental loads,” Technical Report of Recommended Practice (DNV-RP-C205), Hovik, Norway, 2010.

[143] A. Maguire and D. Ingram, “Hydrodynamics and absorption efficiencies of wavemakers,” *presented at the Eighth European Wave and Tidal Energy Conference, Uppsala, Sweden*, pp. 7–10, 2009.

[144] J. Larsen and H. Dancy, “Open boundaries in short wave simulations—a new approach,” *Coastal Engineering*, vol. 7, no. 3, pp. 285–297, 1983.

[145] I. Orlanski, “A simple boundary condition for unbounded hyperbolic flows,” *Journal of Computational Physics*, vol. 21, no. 3, pp. 251–269, 1976.

[146] J. C. Park, Y. Uno, T. Sato, H. Miyata, and H. H. Chun, “Numerical reproduction of fully nonlinear multi-directional waves by a viscous 3D numerical wave tank,” *Ocean Engineering*, vol. 31, no. 11–12, pp. 1549–1565, 2004.

[147] J. Choi and S. B. Yoon, “Numerical simulations using momentum source wave-maker applied to RANS equation model,” *Coastal Engineering*, vol. 56, no. 10, pp. 1043–1060, 2009.

[148] ITTC, “ITTC-Recommended Procedures and Guidelines: Practical Guidelines for Ship CFD Applications,” presented at the 26th International Towing Tank Conference, Rio de Janeiro, Brazil, Technical Report of 26th ITTC Specialist Committee on CFD in Marine Hydrodynamics, 2011.

[149] Y. Fung, “Foundations of solid mechanics,”Prentice-Hall, INC., Englewood Cliffs, New Jersey, U.S.A, 1965.